CHAPTER 3

Spectroscopic Observations

3.1 IMACS Spectroscopy

3.1.1 Mask Design

The vast majority of our spectroscopic data set was acquired with the IMACS spectrograph (Dressler et al., 2011) on the Baade telescope at Las Campanas Observatory. The optical design of the Baade telescope features a 6.5 m parabolic primary mirror, an $f/11$ Gregorian secondary, a flat tertiary, and finally an integral atmospheric dispersion corrector.

We targeted many fields along the expected paths of the Sgr streams with typical field-to-field separations of 5° to 15°, as described in Section 2.1.1. In each field, probable main-sequence stars were selected from (I, $V - I$) color-magnitude diagrams as described in Section 2.2. Naturally, we sought to acquire spectra of as many of these candidate stars as possible. To maximize both the number of spectra per field, and the quality of these spectra, there were several important factors to consider in choosing the ideal configuration of the IMACS spectrograph and the design of the multi-slit masks fabricated for it.

In order to achieve our desired wavelength coverage and spectral resolution all

observations were made using the $f/4.3$ camera and the 600 lines mm^{-1} reflection grating in first order centered at or near 4550 Å. This camera and grating combination produces a dispersion of 0.378 Å pixel^{-1}. However, given the faintness of our target stars, we choose to bin our data 2×2, for an effective dispersion of 0.755 Å pixel^{-1}. The pixel size with this binning choice was $0.''222$ pixel^{-1}. The widths of our target slits were all designed to be $0.''8$. This setup produced spectra with a spectral resolution of 2.7 Å, corresponding to a spectral resolving power of $R \sim 1700$.

The multi-slit masks were designed so that all spectra spanned the wavelength range of at least 3800–5300 Å. This region was chosen to include several Balmer lines as well as absorption lines from Ca II, Ca I, Fe I, and others. Ensuring this spectral coverage meant restricting the the slit locations to lie along the central ∼60% of the dispersion axis. So although the detector in the $f/4.3$ camera has a $15.'4 \times 15.'4$ field of view, the targets were restricted to lie within an area of approximately $15.'4 \times 9'$.

This restriction meant there was a small amount of freedom in choosing the center of each field, since the target candidates were spread over an area of the sky larger than a single multi-slit mask could cover. When designing each mask we searched in a trial and error fashion for the field center coordinates, and sometimes the slit position angle, that maximized the number of target slits on each mask. The spatial distribution on the sky of observed and unobserved candidates for a representative IMACS field is shown in Figure 3.1.

The actual design of the multi-slit masks is facilitated by the `intgui` program, which provides an easy to use graphical user interface for defining all of the necessary

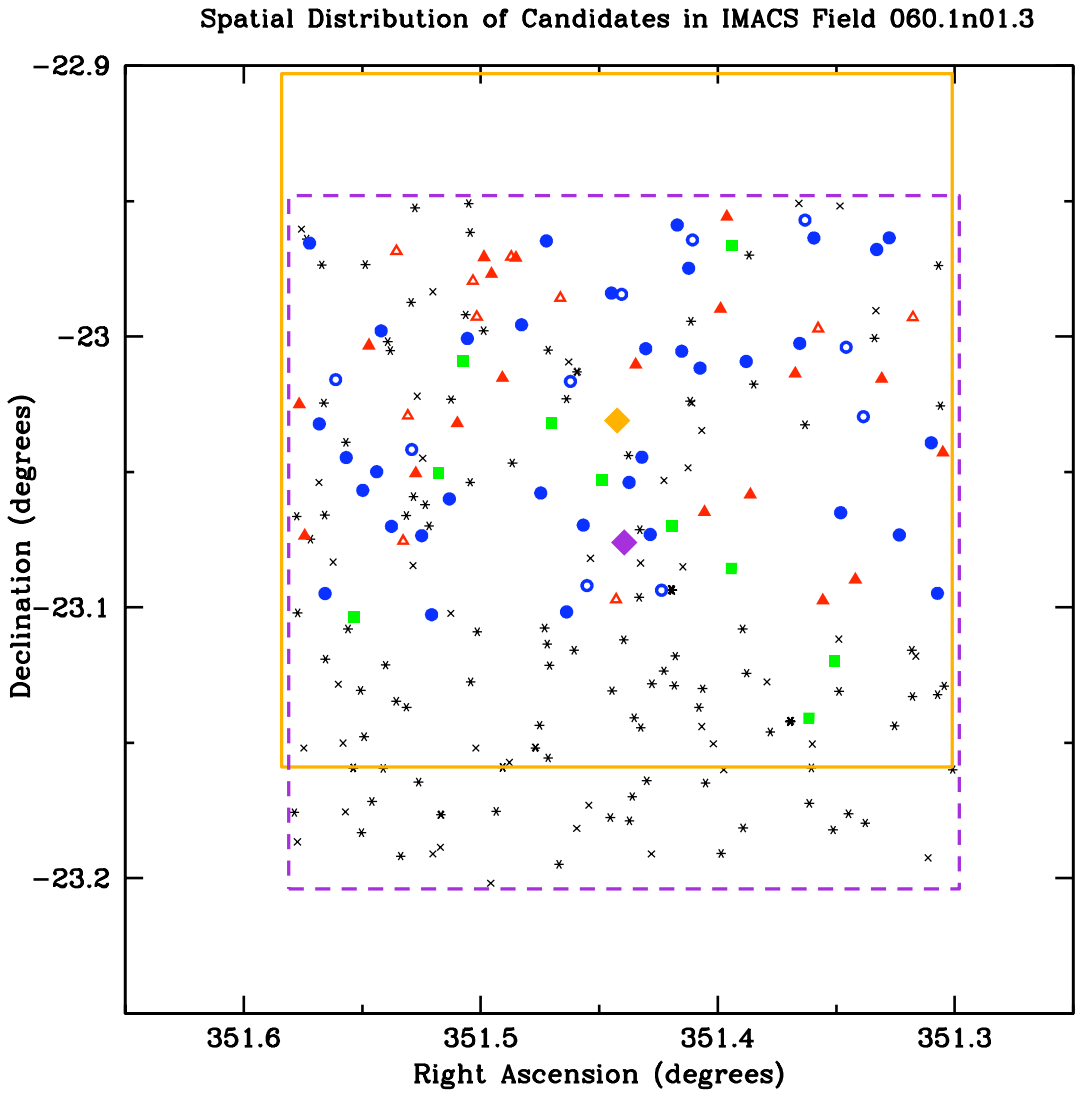

Figure 3.1: Spatial distribution of candidates in a representative IMACS field. The total number of candidate stars in this field, 060.1n01.3, was 227. A total of 153 of them went unobserved. The unobserved candidates from the faint selection box (see Figure 2.11) are marked as black diagonal crosses (N=44). The unobserved stars from the primary selection box (N=109) are depicted as six-pointed stars. The stars with reliable radial velocity measurements (N=45) are shown as solid/open blue circles for the primary/faint selection boxes (N=35/10). Acquired stars that were rejected due to poor velocity measurements (N=29) are represented as solid/open red triangles for the primary/faint selection boxes (N=19/10). The locations of the alignment stars (N=10) are shown as green squares. The large purple square with the dashed-line border represents the field of view of IMACS with the pointing used to acquire the photometry. The center of the field is designated by a diamond of the same color. The large orange square with a solid border represents the field of view of IMACS with the pointing used to acquire the spectroscopy. The center of the field is designated by a diamond of the same color.

parameters and desired specifications for each mask. The command line program `maskgen`, when executed, uses the information specified in `intgui` to optimally assign slits to targets and generate the files necessary to create the masks. Full-size and close-up photographs of a typical IMACS multi-slit mask are shown in Figure 3.2.

To increase the number of Sgr spectra on each mask we sought to remove from the candidate list background galaxies that passed through our color-magnitude selection. To do this, the morphologies of every target were inspected by eye, and extended objects were immediately rejected, leaving only point sources in the candidate list.

Another important consideration when trying to maximize the number of slits per mask is to minimize the lengths of the slits. In designing the masks we insisted that the spectra do not overlap one another, but we also did not enforce a minimum separation between neighboring spectra on the detector. We found $5''$ to be an ideal length for our slits. Given our pixel size, this length corresponds to approximately 24 pixels on the detector. Under typical observing conditions, with seeing of $\sim 1''$, stellar spectra spanned $\sim$5 pixels in the spatial direction, leaving $\sim$9 pixels above and below each spectrum to be used for background sky subtraction.

A final consideration in the design of the masks is the number and locations of the alignment boxes. The alignment boxes are square boxes cut in to the multi-slit masks which are used to correct for the small but unavoidable offset between the astrometry of the targets on the masks and the pointing of the telescope at the time of the observations. Immediately before collecting data, interactive software is used in a two step process to determine and apply larger, and then much smaller, offsets in

Figure 3.2: Photographs of a Multi-Slit mask. The upper panel is a photograph of a multi-slit mask resting comfortably in an armchair. The lower panel is a close-up photograph of the center of the same mask. Many slits can be seen along with several alignment boxes along the top of the photograph. The stainless steel masks are 26 inches in diameter and 0.010 inches thick.

the right ascension, declination, and rotator angle of the telescope. These offsets are calculated so as to center the alignment stars within their square boxes, which, as an intended consequence of this correction, will also center the fainter target stars in both the spatial and spectral directions of their respective slits. Candidate alignment stars typically have magnitudes that range from about two magnitudes brighter than the brightest targets down to the bright limit of the target stars. This allows the software to identify the alignment stars and employ a two-dimensional centering algorithm from a single direct image with a relatively short ($\sim$45 s) exposure time.

The size of the square alignment boxes on our masks ranged from $5\farcs0$ to $5\farcs8$ on a side. It is important to note that, in crowded fields in particular, for each alignment box that is included on a mask the potential number of target slits that can fit on the mask is likely to decrease by one or two due to the requirement that no spectra overlap. When designing the masks, once the field center and slit position angle were chosen so as to maximize the potential number of target slits in the absence of alignment boxes, we then intentionally sought to include candidate alignment boxes that did not conflict with any of the target spectra. If there were an insufficient number of such alignment star candidates, $\lesssim$8, we looked for pairs of alignment stars that would overlap each other on the detector, and thus eliminate only one target slit. Not all fields contained these pairs of alignment stars or contained a sufficient number of them. When necessary we also included alignment boxes that conflicted with, and thus eliminated, a single target slit from the mask, and always avoided including alignment boxes that conflicted with two target slits. Care was also taken to ensure

that the alignment boxes were uniformly distributed throughout the field, with at least a couple falling in each quadrant of the detector, so that accurate offsets in the positioning and rotator angle of the telescope could be determined when aligning the mask on the sky. Our masks had a minimum of 8 alignment boxes, a maximum of 17, and an average of 12.

Note that since the detector is 15.′4 in the spatial direction, the theoretical maximum number of 5″ slits that can fit on the detector without overlapping is ∼184 (ignoring the gap between chips on the detector and the necessity to also include alignment stars on each mask). However, this also assumes perfect packing of the slits, with no space between neighboring slits in the spatial direction. In practice, the highest number of slits we were able to squeeze on to a single mask was 123.

3.1.2 Data Acquisition

Spectroscopic observations of the Sgr streams with IMACS were carried out during nine observing runs over a period of four years, from 2006 June through 2010 April. In total, spectroscopic data from 42 IMACS masks were acquired. Of these, 36 were unique observations, four were repeat observations, and two (one unique, one repeat) were discarded due to problems with the spectroscopy. Information regarding the unique IMACS spectroscopic observations and their multi-slit masks is summarized in Table 3.1. The provided information includes the field name in the first column, the date of the observation in the second column, and the number of exposures and their exposure times in the third column. Also included for each mask is the total number of photometrically identified candidate stars in the field in the fourth column, the

number of target stars (i.e. candidate stars with slits on the mask) and this number expressed as a percentage of the total number of candidate stars in the fifth column, and the number of alignment stars in the seventh column. The total number of target stars that ultimately resulted in reliable radial velocity measurements is provided in column six, along with this number expressed as a percentage of the total number of target stars.

Most of the repeat observations were carried out in the center of Sgr. A total of four masks were created and observed at this location. One of these (field 359.9n01.5) was observed three times, and another (field 000.0n01.6) was observed twice. In addition, there is some overlap of candidate stars amongst these four masks. Specifically, 61 of their collective 475 slits are repeats. One other field, 010.1n03.2, was also repeated. Information about these repeat IMACS spectroscopic observations and their multi-slit masks is provided in Table 3.2, where the columns are as described in the previous paragraph for Table 3.1.

The accurate alignment of each multi-slit mask is absolutely crucial to ensure that the target stars are centered in their slits, and to thus minimize the likelihood of slit effects leading to incorrect wavelength calibrations and velocity measurements. Properly aligning the masks is a three step process, the first of which takes place in the afternoon. At this time, each of the six masks loaded in to the slit-mask server are inserted, one at a time, and a direct image is taken. The ambient light in the dome illuminates the target slits and the alignment boxes of each mask on the CCD detector. An IRAF task called `icbox` is then run on these images to mark and record

Table 3.1: IMACS Spectroscopic Observations

Field	UT Date	Exp. Time (s)	N_{Cands}	$N_{Targets}$(%)	N_{RVs}(%)	N_{Align}
020.1n06.1	2006 Jun 19	4x1800	233	87(37)	72(83)	10
020.5p00.1	2006 Jun 19	4x1800	179	76(42)	68(89)	10
060.0p00.6[a]	2006 Nov 29,30	4x1800	324	85(26)	0(00)	11
060.1n01.3	2006 Sep 21	4x1800	227	74(33)	45(61)	10
075.0p00.9	2007 Oct 6	4x1800	181	62(34)	32(52)	12
075.1n01.1	2006 Sep 21	4x1800	204	61(30)	35(57)	10
090.0n00.7	2006 Nov 27	4x1800	213	68(32)	28(41)	11
090.0p01.3	2007 Oct 5	4x1800	91	44(48)	20(45)	14
090.1n02.7	2007 Oct 7	4x1800	207	73(35)	27(37)	11
105.1n02.3	2007 Oct 6	4x1800	240	73(30)	29(40)	10
119.9p00.0	2007 Oct 5	4x1800	296	69(23)	24(35)	15
135.1p00.5	2007 Oct 7	4x1800	236	58(25)	14(24)	16
139.9n07.6	2007 Oct 6	4x1800	122	51(42)	29(57)	16
147.0n04.5	2007 Oct 7	4x1800	197	71(36)	38(54)	17
150.0n01.1	2008 Feb 5	4x1800	167	63(38)	19(30)	17
150.0n08.9	2007 Oct 5	3x1800,1x1200	206	58(28)	53(91)	16
180.4n11.2	2008 Feb 6	4x1800	404	90(22)	62(69)	17
198.4n10.9	2008 Feb 5	4x1800	240	65(27)	6(09)	17
222.2n09.1	2008 Feb 6	4x1800	113	32(28)	20(63)	16
245.0p01.3	2007 May 10–11	4x1800	223	69(31)	30(43)	10
246.8n05.9	2008 Feb 5	4x1800	113	40(35)	13(33)	8
250.1p01.2	2007 May 11–12	5x1800	109	51(47)	16(31)	11
255.0n00.9	2008 Feb 6	4x1700	207	71(34)	37(52)	12
255.1p03.1	2007 May 13–14	4x1800	211	65(31)	9(14)	10
256.7n04.1	2008 Feb 5,6	4x1800	131	37(28)	28(76)	16
260.0p01.0	2007 May 11	4x1800	192	69(36)	35(51)	12
265.0p00.9	2007 May 12	4x1800	180	74(41)	36(49)	12
275.1p00.6	2007 May 14	4x1800	193	69(36)	31(45)	14
285.0p00.3	2007 May 12	4x1800	185	72(39)	52(72)	12
295.0p00.0	2007 May 11	4x1800	221	75(34)	37(49)	12
305.0n00.2	2007 May 12,13	2x1800,4x2400	235	77(33)	53(69)	15
315.1n00.6[b]	2007 May 11	4x1800	322	87(27)	77(89)	12

[a] Field 060.0p00.6 was eventually removed from the data set because of problems with the spectroscopy.

[b] A repeat observation of field 315.1n00.6 taken on 2010 April 24 was eventually removed from the data set because of problems with the spectroscopy.

Table 3.2: IMACS Repeat Spectroscopic Observations

Field	UT Date	Exp. Time (s)	N_{Cands}	$N_{Targets}(\%)$	$N_{RVs}(\%)$	N_{Align}
000.0n01.4[a]	2007 Oct 5–6	4x1800	23583	117(0.5)	99(85)	17
000.0n01.6[a]	2007 Oct 5	4x1800	23583	117(0.5)	104(89)	16
000.0n01.6[a]	2010 Apr 23	4x1800	23583	117(0.5)	95(81)	16
000.1n01.5[a]	2007 May 11,14	4x1800	23583	118(0.5)	104(88)	11
359.9n01.5[a]	2007 May 14	4x1800	23583	123(0.5)	110(89)	10
359.9n01.5[a]	2008 May 30	3x1800	23583	123(0.5)	83(67)	10
359.9n01.5[a]	2010 Apr 22	4x1800	23583	123(0.5)	109(89)	10
010.1n03.2	2006 Sep 21	4x1800	1016	115(11)	110(96)	10
010.1n03.2	2010 Apr 25	4x1800	1016	115(11)	93(81)	10

[a] Sgr center fields.

the locations of the alignment boxes for future use. Also, during the afternoon and/or at the end of the night, a series of zero-second bias frames were usually taken. At the end of each observing run, all of the individual bias exposures (typically 100–300 in number) were combined into a single master bias frame to be used later during the data reduction process.

At night, after slewing the telescope to a field's center coordinates, a direct image is taken without the mask or reflection grating inserted. The IRAF task `ialign` is then run on this image. This task measures the centroid of the bright source nearest to the location of each alignment box, as recorded in the afternoon. The two-dimensional offset between each measured centroid and the center of the corresponding alignment box is then calculated. Each of these offset measurements is then used to calculate an offset solution in RA, DEC, and rotation angle. After these offsets are sent to the telescope and executed, the alignment stars should be very near to the centers of their boxes. The `ialign` task is run interactively to allow the observer to ensure

that the correct alignment stars are selected, and to reject any discrepant, possibly misidentified, alignment stars before the offset solution is calculated.

Next, the multi-slit mask is inserted and another direct image is taken, still without the reflection grating. The process of removing and reinserting a slit-mask has an inherent inaccuracy of up to several pixels. Therefore, it is likely that the locations of the alignment boxes in this new image are slightly shifted from their locations during the afternoon measurements. To correct for these shifts, the IRAF task `ifalign` is run on this image. This task uses the background sky counts to determine the borders of each alignment box, and also calculates the two dimensional centroids of the alignment objects. The offsets of these centroids from the centers of their alignment boxes are then used to determine an offset solution in RA, DEC, and position angle. After this final offset is sent to the telescope and executed, the alignment stars will finally be centered within their boxes, and thus the target objects should be centered within their slits. As with the previous IRAF task `ialign`, the `ifalign` task is run interactively to allow the observer the opportunity to reject discrepant alignment objects from the final offset solution.

Once the alignment of the multi-slit mask is complete, the reflection grating can be inserted (600 lines mm^{-1} with a central wavelength of 5180 Å, in our case), and the calibration and data images can be taken. The typical observing procedure we tried to follow began by first acquiring a spectroscopic flat field image followed by a comparison arc spectrum. Next, we acquired four consecutive target spectra, and then finished with another comparison arc spectrum and spectroscopic flat field image.

The spectroscopic flat field exposures and the comparison arc calibration spectra were both taken using the screen located at the pupil image generated by the Gregorian optical system of the Baade telescope. For the spectroscopic flat field images, a bright quartz-halogen lamp was used with an exposure time of ∼50 seconds. For comparison arc spectra, Helium, Neon, and Argon lamps were used with an exposure time of ∼30 seconds. Typically, four consecutive 1800 second (30 minute) exposures were acquired of our target stars (see tables 3.1 and 3.2). Figures 3.3 and 3.4 show a full-sized and close-up view of a typical single exposure of a Sgr field. Overall, the total time required to take the calibration and target images, as well the additional overheads, such as slewing, aligning the mask, and CCD readout times, adds up to about two hours and twenty minutes per field. Depending on the season, it was possible to complete the data collection for three to five fields in a single night.

3.1.3 Data Reduction

The reduction of IMACS data was performed with two software packages in series. First, the Carnegie Observatories System for Multi-Object Spectroscopy (COSMOS) data reduction package was used to extract two-dimensional, wavelength calibrated spectra from the object frames, and then combine them using a cosmic ray rejection algorithm. Then, standard IRAF procedures are used to collapse the spectra down to one dimension, and measure their radial velocities by cross-correlating them against a synthetic stellar spectrum. Since the COSMOS data reduction software (which is only used for the reduction of IMACS and LDSS3 data from the Magellan telescopes) is unfamiliar to most, a detailed description of the reduction process is provided below.

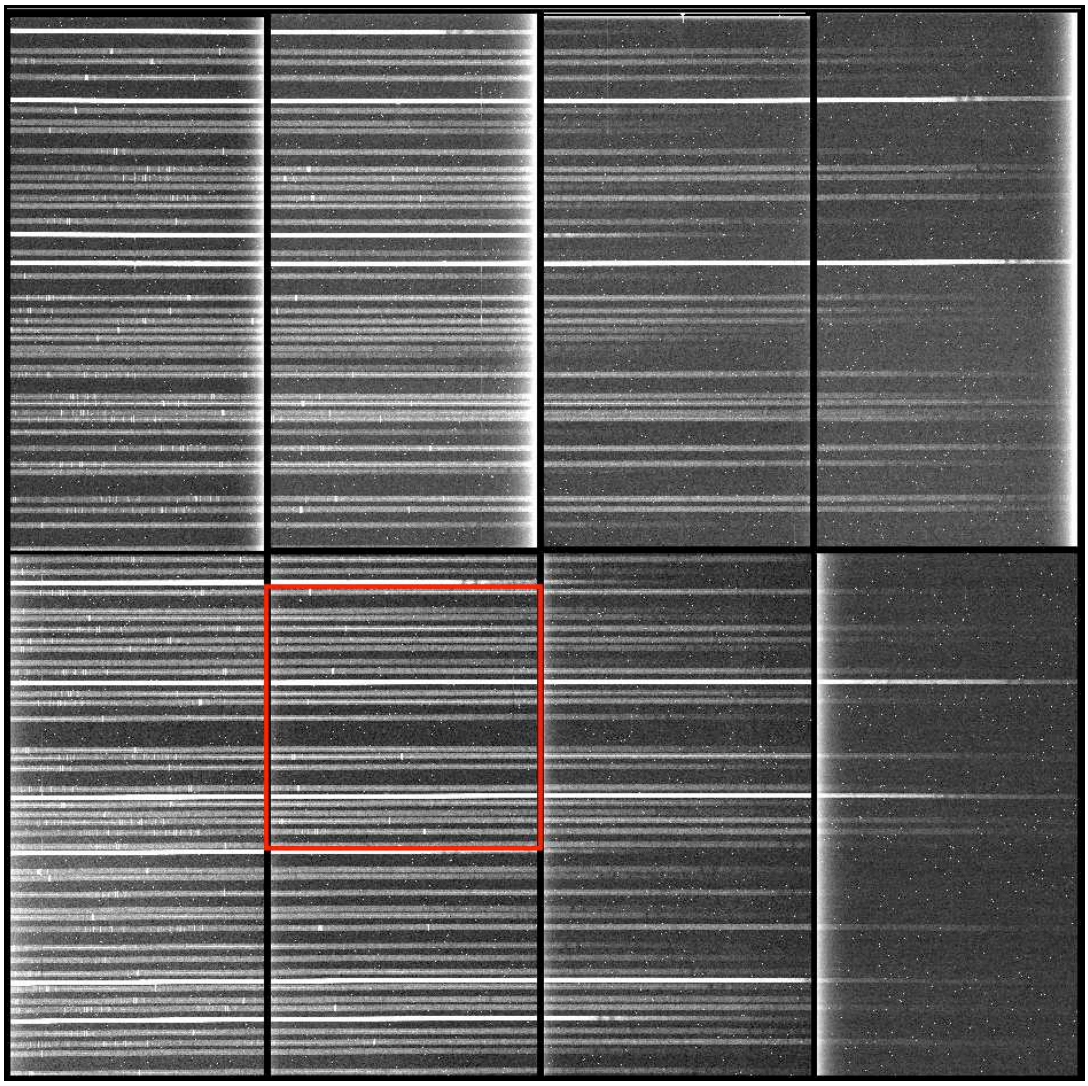

Figure 3.3: Unprocessed IMACS spectroscopic image. The eight chip CCD mosaic is shown for a single 1800 second spectroscopic exposure of the representative field 020.5p00.1. The vertical axis is the spatial direction, which covers 15′.4. Wavelengths increases from right to left. This field contained 76 target slits, 3 of which did not fall on the detector. It also contained ten alignment stars, which appear as the over-exposed spectra. A number of night sky emission lines are visible towards the red ends of the spectra. Many cosmic rays, which were later removed by co-adding multiple exposures, are visible throughout the image. The red box outlines a region for which a close-up is provided in Figure 3.4.

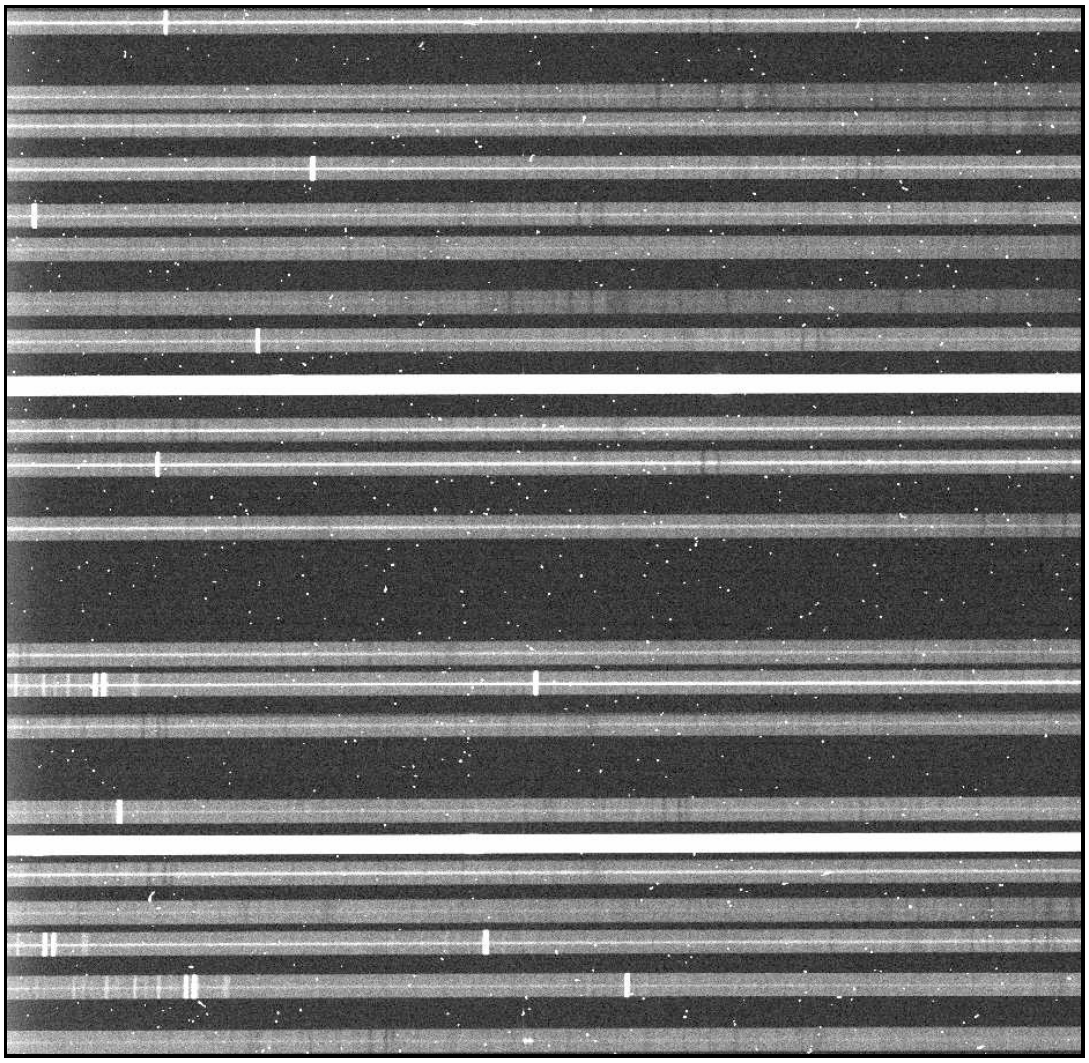

Figure 3.4: Close-up of unprocessed IMACS spectroscopic image. The two-dimensional spectra of twenty Sgr targets and two alignment stars are shown. The vertical axis is the spatial direction, which covers $\sim 4'$. The slits have a length of $5''$ (24 pixels) each. The spectra of the targets can be seen running through the centers of the slits, with background sky immediately above and below them. This close-up view is drawn from the highlighted region in Figure 3.4.

3.1.3.1 Reductions with COSMOS

Preparations

To begin spectroscopic data reductions of any particular field using the COSMOS software package a number of files are required. Obviously this includes all relevant data frames: object spectra, comparison arc spectra, spectroscopic flats, and bias frames. COSMOS also requires the mask definition file (".SMF" file) produced by the `maskgen` program while designing the multi-slit masks, and a default dewar offset file (".dewoff" file), available with any installation of the software. The default dewar offset file is a one line text file that provides a starting point approximation for the relative alignment between a generic slitmask and the CCD focal plane. While the provided dewar offset file is always available to be used, a better initial guess at the alignment is usually obtained by using the final dewar offset file created while reducing another field from the same observing run. The single line in a dewar offset file lists the default positional zero point offsets (focal plane scale, dewar rotation angle, and (x, y) positional offsets) for the instrumental setup being used. The details of the instrumental setup that are important for this purpose include the camera choice (the long, $f/4.3$ camera in our case), the choice of grating or grism (the 600 lines mm^{-1} grating with a central wavelength of 5180 Å, in our case), and the dewar mounting position (Nod & Shuffle in our case, though we did not observe in Nod & Shuffle mode). Finally, a long emission line list and an abbreviated line list specifying the wavelengths (in Angstroms) of emission lines relevant to the observer's choice of arc lamp and spectral range will be needed.

The first step in reducing IMACS spectroscopic data with COSMOS is to inform COSMOS of which directory to look in for the image files with the handy GUI application `setcosdir`.

Next, it is necessary to create a spectroscopic observation definition file (".obsdef"). This is accomplished with the GUI application `defineobs`. The user is asked to fill in information related to the observational setup, including: the instrument used (IMACS2, in our case), the mask name (ex. 119.9p00.0), the name of the default dewar offset file (LC600.5l_NS.dewoff), the camera used (Long $f/4$), the mode used (spectroscopic), the dispersing element (600 line), and the order (1) and angle (8.4964) of the grating. The spectroscopic observation definition file produced by `defineobs` is a text file that records these settings.

Slitmask Alignment

The next step is to determine the alignment of the slitmask relative to the CCD focal plane. This is a crucial step, because once the relative alignment is known, the COSMOS software is able to employ the precise optical model of the IMACS spectrograph that has been built in to it to accurately predict the locations of spectral features on the CCD mosaic. The four parameters that characterize the alignment of the slitmask relative to the CCD focal plane (focal plane scale, rotation angle, and (x, y) positional offsets) are all contained within the dewar offset file. Approximate values for these parameters are provided by the default dewar offset file. However, the process of continually inserting and removing the slitmasks and disperser elements into and out of the focal plane inevitably results in slight deviations in these parameters

from their default values. Therefore, the default values are to be used as a reasonably accurate starting point from which improvements will eventually be made.

The COSMOS task that makes these necessary improvements to the relative alignment between the slitmask and focal plane is known as `align-mask`. The `align-mask` task needs to first be supplied with the spectroscopic observation definition file so that it knows the details of the instrumental setup and the name of the mask definition file in which the slit locations can be found. The spectroscopic observation definition file also provides the name of the default dewar offset file to be used as a starting point for the focal plane scale, rotation angle, and (x, y) positional offsets. The task also needs to be provided with an abbreviated arc line list containing the wavelengths of just a few bright, isolated emission lines. We used a list of eight emission lines that spanned the full extent of our desired spectral range. All of this information can then be used in conjunction with the precise optical model of the IMACS spectrograph built in to the COSMOS software to be able to accurately predict the locations of the specified emission lines on the CCD mosaic.

When executed on any one particular comparison arc frame, `align-mask` searches for the specified emission lines produced by every slit within a user-defined neighborhood around their predicted locations. The program then calculates the (x, y) positional offsets between the predicted locations of the emission lines and their actual locations on the CCD mosaic. From this set of offsets the `align-mask` task determines new values for the focal plane scale, rotation angle, and (x, y) positional offsets that minimize the median errors. The output from `align-mask` is a new dewar offset

file containing improved values for the focal plane scale, rotation angle, and (x, y) positional offsets. To ensure that in the future COSMOS uses the newly created dewar offset file instead of the default one, the task `defineobs` is run again. This brings up the GUI application, in which the name of the dewar offset file can be changed from the default name to the name of the newly created file. This generates a new spectroscopic observation definition file which is then used as the input file for a second iteration of `align-mask`. The task can be iterated upon in this way several times until the changes to the focal plane scale, rotation angle, and (x, y) positional offsets converge to zero. Figures 3.5 and 3.6 show the offsets between the expected and the actual emission line locations for the first and second iterations of `align-mask`. The typical residuals from this emission line fitting procedure are a few pixels, and they are dominated by systematic errors due to distortions in the optics of IMACS that not reproduced by the COSMOS software. These small errors will be removed by a later task that relies on the final version of the dewar offset file produced by the final iteration of `align-mask`.

Creating the Spectral Map

The next step is to generate the spectral map (".map") file. The spectral map file, which forms the basis for the remaining spectral reduction procedures, specifies the mapping between the observed coordinate system on the CCD mosaic and the science coordinate system of slit position and wavelength. Once this mapping is known COSMOS can proceed with data reductions without the computational machinery required when using the optical model of the spectrograph. The COSMOS task that

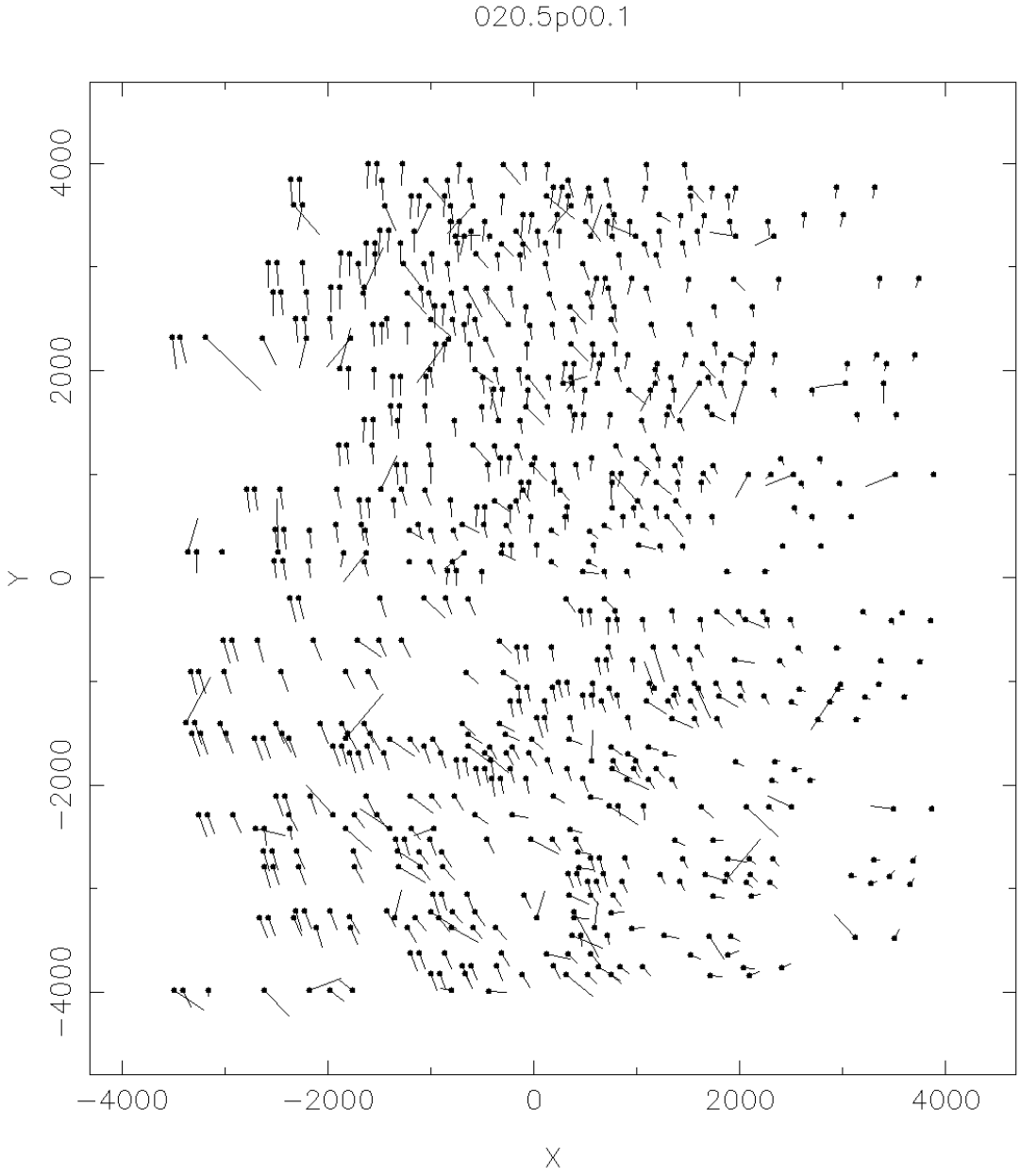

Figure 3.5: First iteration of `align-mask`. The expected locations of eight bright arc emission lines are plotted for every slit from the representative field 020.5p00.1. The vectors show the offsets to where the emission line centers were found after searching. The lengths of the vectors have been multiplied by 15 to enhance their visibility. The corrections made from this run of `align-mask` were: offsets of 2.7 and –8.5 pixels in the x and y directions, respectively, a rotation angle change of 0.072°, and a negligible scale change.

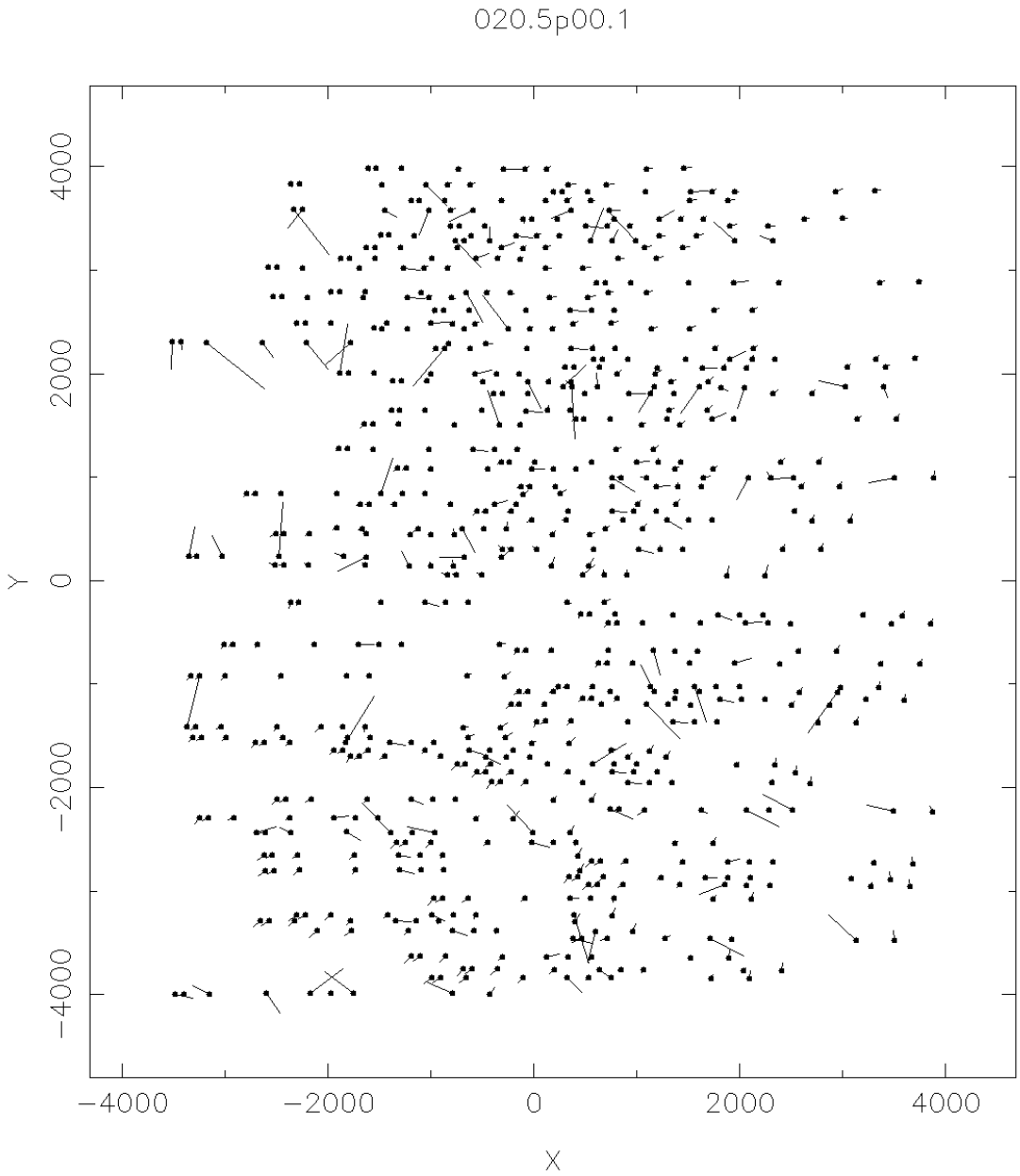

Figure 3.6: Second iteration of `align-mask`. The expected locations of eight bright arc emission lines are plotted for every slit from the representative field 020.5p00.1. The vectors show the offsets to where the emission line centers were found after searching. The lengths of the vectors have been multiplied by 15 to enhance their visibility. The corrections made from this run of `align-mask` were: offsets of 0.1 pixels in the x and y directions, respectively, a rotation angle change of 0.002°, and a negligible scale change. Subsequent iterations of `align-mask` yielded no improvements in the relative alignment.

generates an initial spectral map (which will later be improved upon) is known as `map-spectra`. The `map-spectra` task takes as its sole input the spectroscopic observation definition file. The spectroscopic observation definition file is required because it specifies the three things that `map-spectra` needs, along with the built-in optical model of the IMACS spectrograph, to determine the mapping: the name of the mask definition file containing the details of each slit on the mask, the name of the improved dewar offset file produced by `align-mask` in the previous step, and the details of the observational setup. Note that this task does not make use of a comparison arc frame in any way. That will be done in a later step to adjust and improve upon the approximate spectral map produced here by `map-spectra`. Like the previous step, `align-mask`, the typical residuals from `map-spectra` are a few pixels. The spectral map file generated by `map-spectra` is a text file that lists, for every slit on the mask, the polynomial coefficients of the mapping between the science coordinate system (of slit position and wavelength) and the observed coordinate system (for each chip of the CCD mosaic).

Included with the COSMOS software are several useful programs for visually checking and ensuring that the data reduction process is progressing as expected. For example, COSMOS provides an IRAF routine called `display8` which operates just like the familiar IRAF routine `display`, except that it displays the mosaiced image of all eight of the IMACS chip images in to a single image buffer with their proper orientation. It is useful for viewing the entire mosaic, but it has several limitations. The displayed mosaic is not astrometrically accurate. The eight chips

are simply placed immediately next to each other without properly taking in to account the small gaps between the chips or the tiny rotations of the chips relative to each other. The `display8` task also can not handle binned data, and since it is not a real image file other IRAF tasks (`imexam` for example) can not interact with it. There is, however, a solution for these last two issues. The COSMOS task `mosaic` combines the eight IMACS chips in to a newly created FITS image file with their proper orientation. This task can work with data like ours that has been binned, and because it is a real image file it can interact with other IRAF tasks. However, it still is not astrometrically accurate. Like `display8` it simply places the chips immediately next to each other without properly taking in to account the small gaps between the chips or the tiny rotations of the chips relative to each other.

The task `mosaic` along with the COSMOS task `spectral-map` provide the tools necessary to visually check the accuracy of the spectral map file. The `spectral-map` task takes as its input the spectral map file, the full emission line list, and the binning of the CCD data (2×2 in our case). Our full emission line list contains the wavelengths of 69 Helium, Neon, and Argon emission lines between the wavelengths of 3800–7000 Å. Twenty six of those lines fall within our intended spectral range of 3800–5300 Å. We found it helpful to extend the spectral range over which we performed the wavelength calibrations beyond our intended spectral range wherever possible. By extending out beyond 5300 Å we achieved a more robust wavelength solution. When executed, the `spectral-map` task uses the polynomial mapping function specified in the spectral map file to calculate the expected (x, y) locations on

the CCD mosaic of the spectral features listed in the emission line list. The output from the task is an aperture data file (".xy" file) containing these CCD coordinates for each emission line and for every slit. The accuracy of the spectral map can then be visually checked in IRAF with the task `tvmark`. After a mosaiced comparison arc spectrum has been created with the COSMOS task `mosaic` and displayed in IRAF with the `display` task, the `tvmark` task can then be used with the aperture data file as an input to overlay marks at the expected locations of the emission lines. Since the accuracy of the spectral map file is limited by the accuracy achieved by the previously performed `map-spectra` task, typical offsets between the marked positions and the corresponding emission lines are a few pixels. Figure 3.7 shows the slight offsets between the actual and expected emission line locations for a sample region of a representative field.

Improving the Spectral Map

To improve upon the approximate spectral map produced by `map-spectra` it is necessary to use the comparison arc spectra along with the COSMOS task `adjust-map`. This task works best with bias subtracted comparison arc frames. The first step in bias subtracting the comparison arc frames is to create a master bias frame. To do this we used the IRAF task `zerocombine`. Over the course of each IMACS observing run we took several hundred bias frames in roughly equal numbers each night. The `zerocombine` task is then used to average together all of the bias frames from a given observing run. We used the "minmax" rejection algorithm to remove roughly the highest 5% and lowest 5% of the pixel values before averaging. The master bias

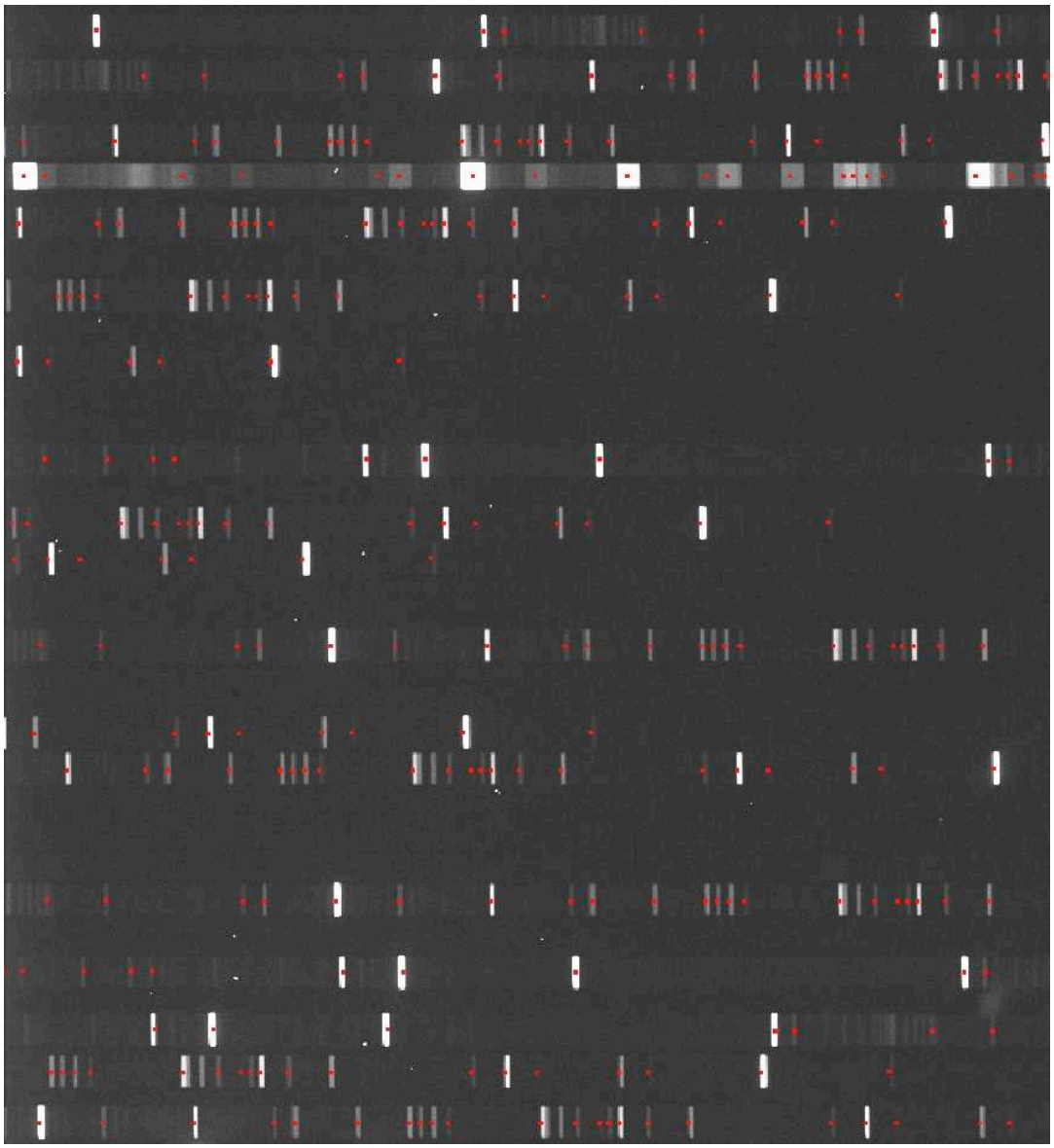

Figure 3.7: Accuracy of the initial spectral map file. The IRAF task `tvmark` was used to plot the expected locations of comparison arc emission lines as calculated using the COSMOS tasks `map-spectra` and `spectral-map`. This is a sample region from the representative field 020.5p00.1. Many of the marks appear to be a bit to the left of the emission lines. This will be improved upon by a subsequent step.

frame can then be used by the COSMOS task `biasflat` to bias subtract all of the comparison arc frames taken during that observing run. The `biasflat` task also performs an overscan correction and makes appropriate adjustments to correct for the relative gains of the eight chips in the CCD mosaic. The outputs from `biasflat` are new bias subtracted comparison arc frames, whose file names have had the suffix "_b" appended to indicate that the bias level has been subtracted.

The final wavelength solution for each slit is obtained by using the COMSOS task `adjust-map` to make small corrections to the approximate spectral map file originally produced by `map-spectra`. This task takes the bias subtracted comparison arc frames as inputs along with the current approximate spectral map file and the full emission line list. When executed, `adjust-map` uses the approximate spectral map file to predict, for every slit, the (x, y) pixel coordinates on the CCD mosaic of each of the emission lines specified in the line list. It then searches within a user defined area around the predicted locations of the emission lines for their true locations on the comparison arc image. Each of the offsets (between the predicted and actual emission line locations) is calculated and polynomial fits are performed along both the spatial axis and the dispersion axis for every slit. The orders of these can be set by the user. We found a fourth-order polynomial along the dispersion axis and a third-order polynomial along the spatial axis generally provided the best results. We chose to run several iterations of the task and exclude from future iterations the points that deviated from the fits by more than a few standard deviations. There are three outputs from `adjust-map`: a postscript file containing plots of both the dispersion and

spatial fits for each slit, a ".rms" text file listing the standard deviations of both the dispersion and spatial fits for each slit, and, most importantly, the new and improved spectral map file. Figure 3.8 shows the fits to the emission line locations in both the dispersion and spatial directions for four typical slits from a representative field.

One significant limitation to the `adjust-map` task is that all of the user specified parameters (such as the dimensions of the search area, the fit orders, and the standard deviation rejection limit) are universally applied to all of the slits on the comparison arc image. There are usually several slits per frame for which better fits can be achieved with different parameter choices. Unfortunately, COSMOS does not allow the user to make specific parameter choices that are tailored to the needs of each individual slit. However, there is a slightly cumbersome way of getting around this. The `adjust-map` task can be run multiple times on a given comparison arc image with different parameter choices each time. The output files from each execution of the task need to be renamed to prevent them from being overwritten by the next execution. In the end, these multiple results can be consolidated into a single, merged spectral map file by copying the coefficients representing the polynomial fits for each slit out of their tailor-made spectral map file (i.e. the one created with the specific parameter choices for those slits) and pasting that information into a final, merged spectral map file.

At this point, each comparison arc image now has its own finalized spectral map file specifying the mapping between the observed coordinate system on the CCD mosaic and the science coordinate system of slit position and wavelength. The ac-

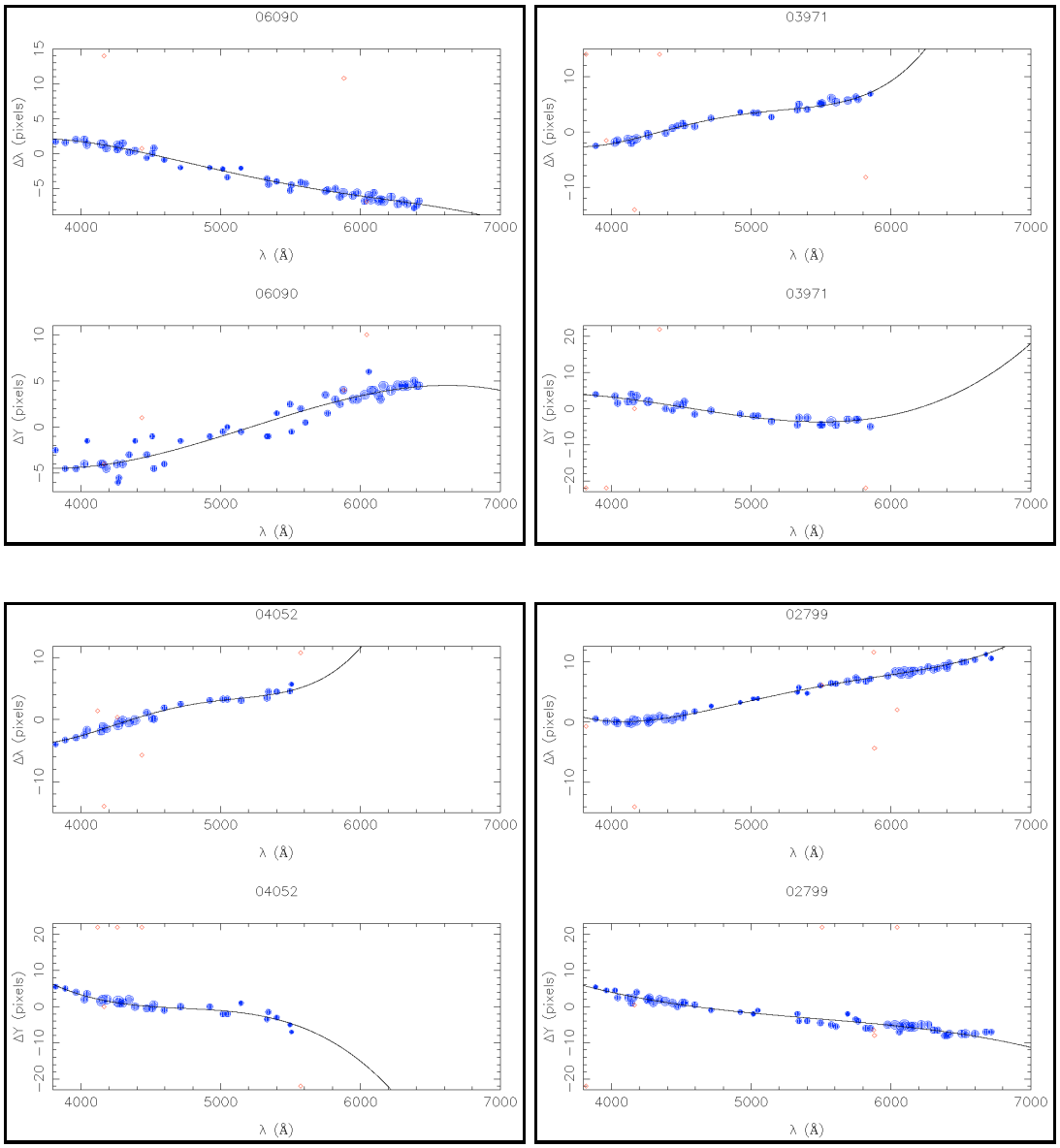

Figure 3.8: Sample fits from `adjust-map`. Fits are shown along both the dispersion (upper plot) and spatial (lower plot) axes for four sample slits from the representative field 020.5p00.1. The standard deviations of the fits to the (dispersion, spatial) axes are (clockwise from the top left): (0.54, 0.68) , (0.41, 0.98) , (0.52, 0.79) , (0.35, 0.89). Note the differing scales along the vertical axes.

curacy of these mappings can be visually checked, as they were before, by running the `spectral-map` task on the spectral map files to generate aperture data files containing the expected CCD coordinates for each emission line and for every slit. The IRAF task `tvmark` is then used with the aperture data files to overlay marks on top of the mosaiced comparison arc images at the expected locations of the emission lines. Since the final spectral map files produced by `adjust-map` have errors that are just a fraction of a pixel, the marked positions are now observed to be centered perfectly on the emission lines, to within the pixelization, as depicted in Figure 3.9. With the final spectral map files in hand, reductions of the science exposures can proceed.

Preparing the Images

The next step is to bias subtract and flat field the object images. To do this, the spectroscopic flat field images must first be properly prepared using the COMSOS task `sflats`. The `sflats` task takes as its inputs the name of the spectroscopic flat field image to be processed, the name of the spectral map file from the temporally nearest comparison arc image, and the name of the master bias frame. When executed, `sflats` first subtracts the bias level using the master bias frames. Next, `sflats` applies a polynomial fit to the continuum of every quartz-halogen lamp spectrum in the flat field image. A standard deviation clipping algorithm is implemented to reject cosmic rays while performing these fits. These fits are then used to normalize each spectrum to unity. The output from `sflats` is a new bias subtracted and normalized spectroscopic flat field image, whose file name has had the suffix "_flat" appended to indicate that it has been processed with `sflats`.

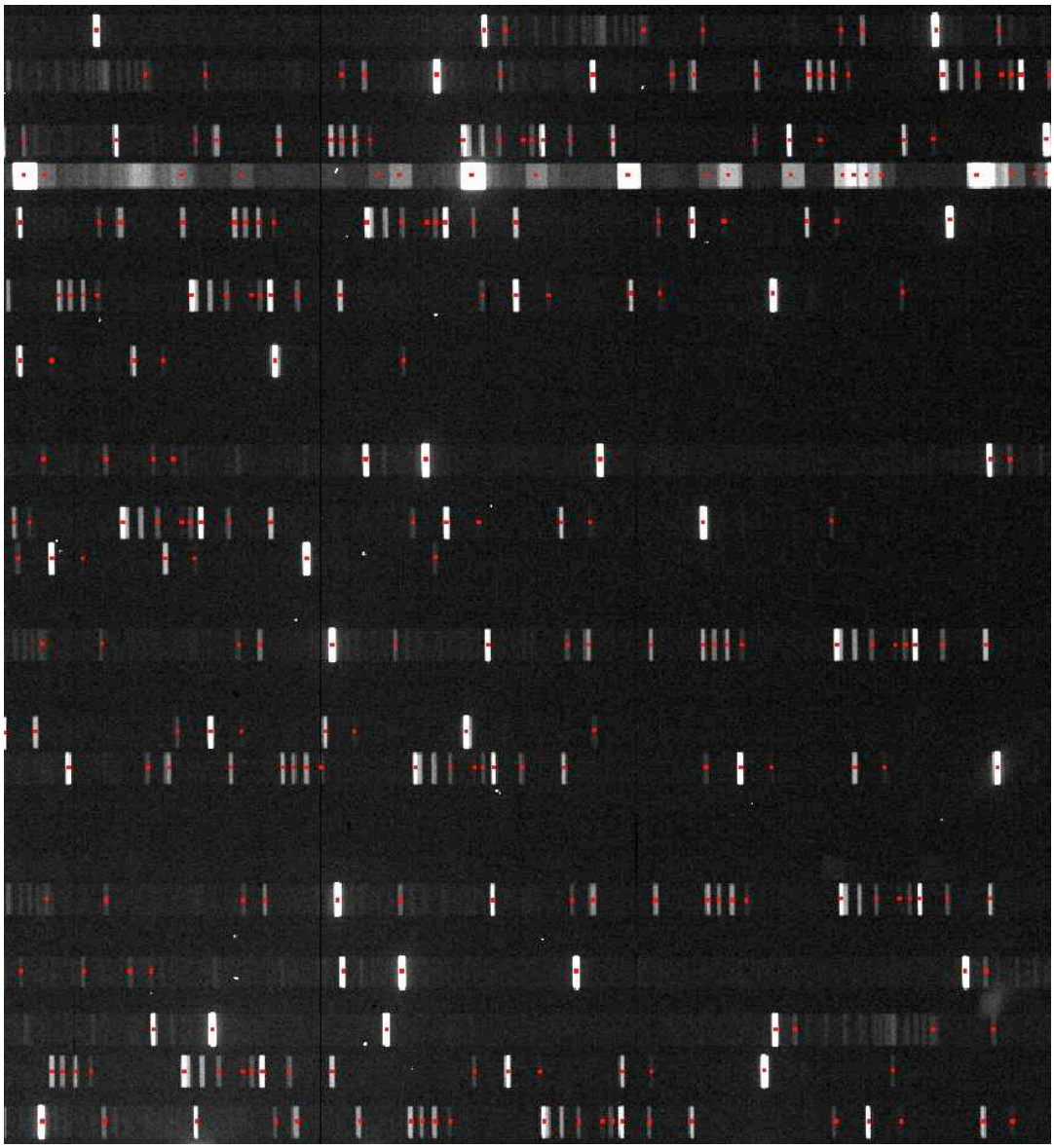

Figure 3.9: Accuracy of the final spectral map file. The IRAF task `tvmark` was used to plot the expected locations of comparison arc emission lines as calculated using the COSMOS tasks `adjust-map` and `spectral-map`. This is a sample region from the representative field 020.5p00.1. The marks in this final version of the spectral map file are now seen to be perfectly centered (to within the pixelation) on the comparison arc emission lines.

The object images can now be processed using `biasflat`. This time the inputs to `biasflat` are: the name of the object images to be processed, the name of the master bias frame, and the name of the newly prepared spectroscopic flat field image that is temporally closest to the object images being processed. When executed, `biasflat` will first subtract the master bias frame from the object images, and then perform an overscan correction on the object images. The task will also make appropriate adjustments to correct for the relative gains of the eight chips in the CCD mosaic. Finally, `biasflat` will flatten the object images by dividing them by the prepared spectroscopic flat field image. The outputs from this iteration of `biasflat` are the newly processed object images, which have had the suffix "_f" appended to indicate that they has been bias subtracted and flattened.

The object images are now ready for sky subtraction with the COSMOS task `subsky`. This task takes the newly processed object images as its inputs, along with the name of the spectral map file from the temporally nearest comparison arc image. It then performs an optimally sampled sky subtraction using the procedure of Kelson (2003). The `subsky` task fits a one-dimensional third-order B-spline to the sky spectrum of each slit. A user-defined strip around the object spectrum is excluded from the fit, and cosmic rays are rejected from the fit by the implementation of a standard deviation clipping algorithm. The median sky spectrum for each slit is then subtracted from its corresponding slit image. The outputs from `subsky` are the sky subtracted object images, which have had the suffix "_s" appended to indicate that they has been sky subtracted.

Extracting the Two-Dimensional Spectra

In order to work with the spectra of individual objects, those spectra first need to be extracted from their image files. The COSMOS task for doing this is called `extract-2dspec`. This task takes as its inputs the name of the object image from which to extract the individual spectra, and the name of the spectral map file from the temporally nearest comparison arc image. When executed, `extract-2dspec` uses the information in the specified spectral map file to determine the size, shape, location, and wavelength calibration of every spectrum in the object image.

Before performing the extraction `extract-2dspec` first employs an algorithm to correct for object offsets along the slit (i.e. in the spatial direction). There are several reasons why an object might be offset from the slit center, including: a slight misalignment of the multislit mask on the sky, errors in the astrometry that produced the object's coordinates, and the effects of atmospheric refraction. These offsets need to be corrected for before combining the multiple object exposures to ensure that they are properly aligned with each other.

As a preliminary step to determining the offsets, a correction is first made for the curvature of the spectra. The task first searches for the location of each spectrum within a user-defined distance above and below the expected location. Once found, the mean slit position as a function of wavelength (i.e. the trace) is determined by fitting a polynomial (fourth-order in our case) to each of the object spectra individually. The data and fit for each object are plotted to the screen, allowing the user to interactively reject from the mean trace calculation the spectra of faint objects,

whose trace could not be well established. This mean spectral curve is then used to correct the curvature of all object spectra. it is important to note that the correction curve that is applied is normalized to zero offset. Only the shapes are corrected by this preliminary step. The actual offsets along the slits are unaffected.

Once the curvature of the spectra has been corrected for, a subset of the objects can be used to determine the mean slit offset. The user can chose to use the alignment stars and/or a specified percentage of the brightest object spectra for this calculation. We chose to use the alignment stars and the brightest 25% of the object spectra. Using this subset of objects, the offset along each of their slits is determined, and the mean offset is calculated. We have found the mean offset to typically be 0–4 pixels. This mean offset is then applied to every object slit. Next, a rotation angle (which is always very small) is calculated and applied to the data. Finally, a scale factor (which is also always very small) is calculated and applied to the data.

Once the corrections for curvature and slit offset have been made, `extract-2dspec`, as the name implies, extracts each individual spectrum onto a two-dimensional array of wavelength and slit position. The data are rebinned such that each pixel represent $0\farcs20$ in the spatial direction and 0.75 Å in the dispersion direction. The total dimensions of each two-dimensional output spectrum is equal to the slit length ($\sim$22 pixels) along the spatial axis, and ranges from 3800–6000 Å ($\sim$ 2395 pixels) along the dispersion axis. All of our object spectra extend out to at least 5300 Å by design. For those whose spectral range does not reach 6000 Å, their spectra are padded with enough zero-intensity pixels as are necessary to get there. The output

file from `extract-2dspec` is a single multi-dimensional FITS image file containing one extension for every individual two-dimensional object spectrum. The output file has the suffix "_2dspec" appended to indicate that it has been processed by the `extract-2dspec` task.

The final COSMOS data reduction step is to sum together the multiple exposures of each of the individual object spectra. This is done with the COSMOS task `sumspec`. This task first scales the exposures by their exposure time. The task then executes a standard deviation clipping algorithm over several iterations to remove cosmic rays. Finally, the task sums together the scaled, cleaned spectra. The format of the single output FITS file is identical to the format of the multiple input FITS files.

3.1.3.2 Reductions with IRAF

Extracting the One-Dimensional Spectra

It is now necessary to extract each of the individual object spectra out from the multiple extensions embedded within the multispectrum FITS image file produced by the COSMOS task `sumspec`. The IRAF task `imcopy` can be used to perform this extraction, resulting in individual two-dimensional FITS image files for each object spectrum. Each of these spectra can then be stacked in to a single image by first using the IRAF task `imcreate` to create a blank image file, and then `imcopy` to paste each of the object spectra into this newly created blank image. Figures 3.10 and 3.11 show a full-sized and close-up view of the final two-dimensional spectra for a representative field.

Each of these individual two-dimensional object spectra need to be collapsed down

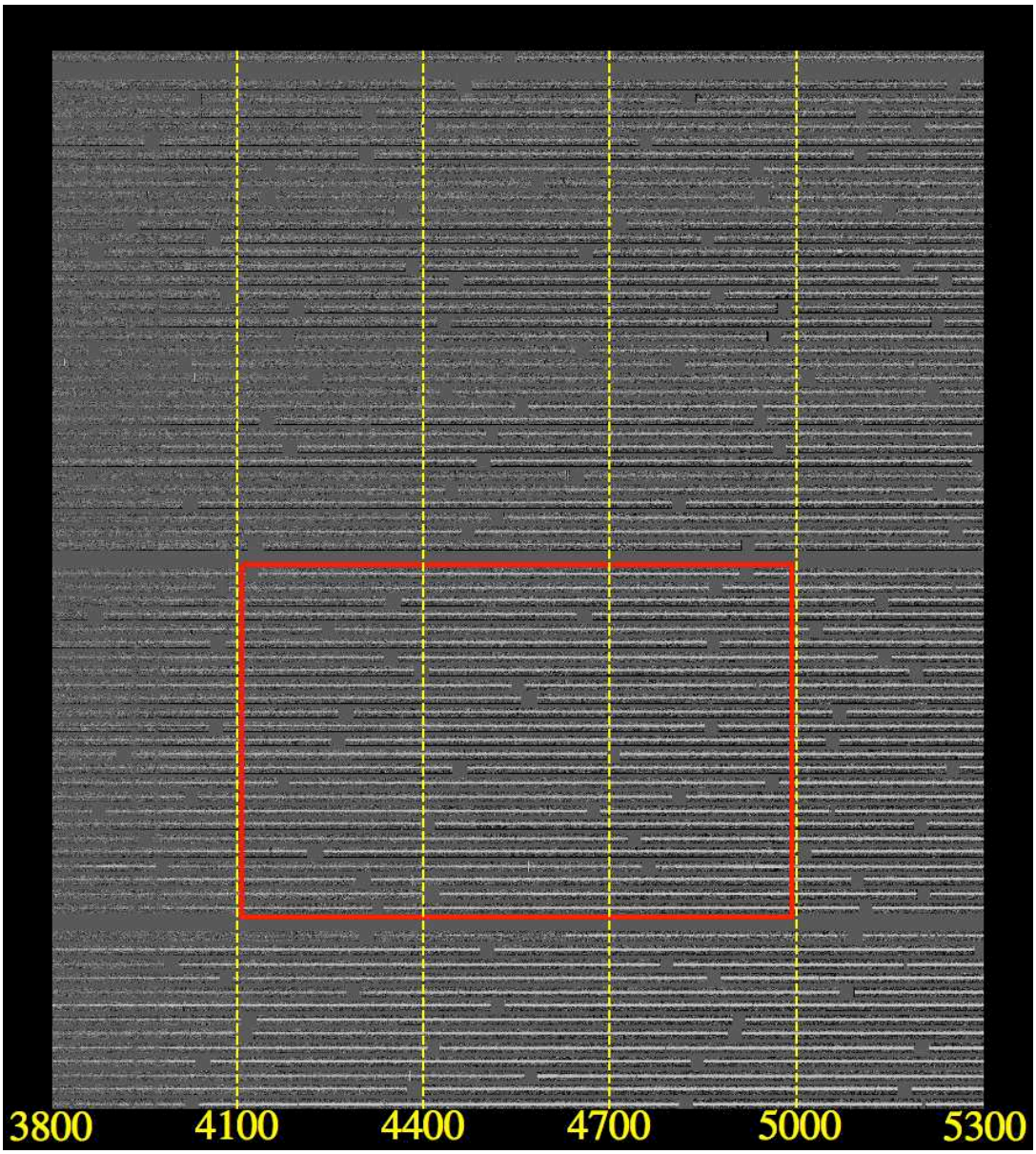

Figure 3.10: Final IMACS two-dimensional spectra. The spectra from each of the 76 slits of the representative field 020.5p00.1 are shown. Each one spans the wavelength range 3800–5300 Å from left to right. They are roughly in order of increasing brightness from top to bottom. The three blank spectra are place holders for slits that were lost off of the CCD detector. Each spectrum has (rarely) one or (usually) two gaps of approximately 30 pixels (23 Å) in length due to the gaps between neighboring chips in the CCD mosaic. Each slit is 24 pixels high, which corresponds to 5″ in length. In making this image the slits have been spaced 6 pixels apart. The actual object spectrum is the bright line running through the middle of each slit, with a width of approximately 4–6 pixels (depending of the object's brightness). The 9–10 pixels above and below each object spectrum are the background sky. The red box outlines a region for which a close-up image is shown in Figure 3.11.

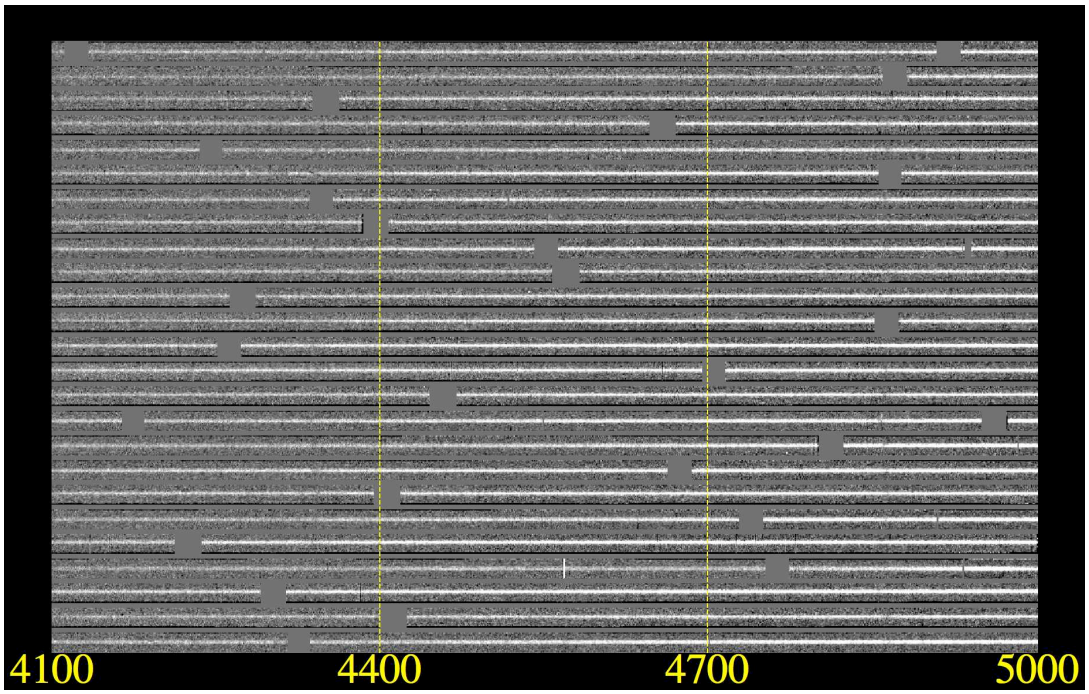

Figure 3.11: Close-up of final IMACS two-dimensional spectra. This close-up view of 25 IMACS two-dimenssional spectra from the representative field 020.5p00.1 is drawn from the highlighted region in Figure 3.10. Wavelengths are indicated along the bottom axis.

to one-dimensional spectra. The IRAF task to accomplish this is called `apall`. The `apall` task performs several different functions sequentially in the process of collapsing the two-dimensional spectra.

First, `apall` scans a specified image column perpendicular to the dispersion axis (and optionally performs a sum of the neighboring columns) for a peak in intensity that it automatically identifies as the object spectrum. The task then centers the extraction aperture on this location. The upper and lower bounds for the extraction window (specified in pixel units) are manually set by the user within the parameter file. The aperture's upper and lower bounds as well as its center can also be set interactively using IRAF's aperture editor display tool.

Next, `apall` performs a trace of the spectrum along the dispersion axis. There

are several reasons why the spectrum may not be perfectly parallel to the dispersion axis, including: distortions in the optics of the camera, a slight misalignment of the reflection grating, and differential atmospheric refraction which causes the blue end of the spectrum to be shifted along the spatial axis closer to the zenith than the red end. When the trace is performed `apall` essentially repeats the initial aperture identification procedure at user-defined intervals along the dispersion axis. At each location it finds the location of peak intensity using the previous location as a starting point. A number of neighboring columns can be summed together at each step to increase the signal-to-noise ratio. Once the full set of peak intensity locations as a function of dispersion axis position is determined a polynomial fit is then performed. We found the IMACS spectra to be surprisingly serpentine, and thus chose to fit the trace with a fifth-order Legendre polynomial. The fit is iterated upon several times, and a standard deviation clipping algorithm is used to reject highly discrepant points from the fit to the trace. An interactive curve fitting program can optionally be used to make adjustments to all aspects of the trace and the fit to it.

The final function performed by `apall` is to sum the data within the extraction aperture (which is centered at the fit locations) at every pixel along the dispersion axis. Since a background subtraction was already performed by the COSMOS task `subsky` we elected not to perform another background subtraction here with `apall`. Rather than simply performing a straight sum of the pixels within the extraction aperture, we elected to do a variance-wieghted "optimal" extraction (Horne, 1986). This algorithm utilizes the known characteristics of the CCD detector (readnoise,

gain, and saturation level) to mathematically assign weights to the extraction pixels that are inversely proportional to their statistical uncertainties. This has the effect of giving less weight to the pixels at the edges of the extraction apertures where the intensity of the light from the object spectra begin to approach the brightness of the background sky.

Once the optimal extraction has finished, the output from the `apall` task is a single one-dimensional, wavelength calibrated object spectrum for each input spectrum. We then used the IRAF task `imcopy` to trim the object spectra so that they all share the same spectral range of 3800–5300 Å.

Removing the Continuum

The penultimate step in the reduction of our IMACS data was to normalize each object spectrum by dividing it by a polynomial fit to its continuum. With IMACS spectra this task proved to be particularly difficult. Given the length of our trimmed object spectra (3800–5300 Å, or 2002 pixels), and the width of the chips in the IMACS CCD mosaic (1024 pixels each when binned 2×2), nearly all of the object spectra spanned three different CCD chips. A small fraction, whose slit locations were located at just the right locations along the dispersion axis, managed to barely fit on to two CCD chips. The fact that all of our trimmed spectra spanned multiple chips made fitting their continua challenging for several reasons. First, the different gain values of the chips resulted in abrupt, discontinuous jumps in the intensity at the chip boundaries (a problem that was improved, but not fully resolved, by the COSMOS task `biasflat`). Second, the varied curvature seen in the spectral segments

from different chips each required their own unique, independent fit. Finally, the presence of the gaps between the chips, whose long stretches of zero-intensity pixels was observed to have an undue influence on the fitting function. For these reasons the standard IRAF routine for producing continuum normalized spectra, `continuum`, was inadequate.

To the accomplish the necessary continuum normalization an IDL program was devised to perform a piecewise continuum fit to the object spectra. When executed, it first identifies the locations of the chip gaps by searching for strings of consecutive zero-intensity values. It then divides the spectra in to two or three segments at the midpoints of the chip gaps. The program then performs a polynomial fit (of typically second or third-order) to each spectral segment, ignoring all pixels with intensity less than or equal to zero and also those that are greater than several times the median intensity value of the segment. The fit to each segment is then divided in to the corresponding segment. To further cleanup the spectra, the zero-intensity pixels at the chip gaps and the pixels identified as being excessively deviant, both above and below the fit, are replaced with pixels that have an intensity value of one. The final output from the program is a one-dimensional spectrum that has been successfully normalized to unity. Figure 3.12 shows as an example the spectra of two typical target stars, the piecewise fit to their continua, and the final continuum-subtracted spectra.

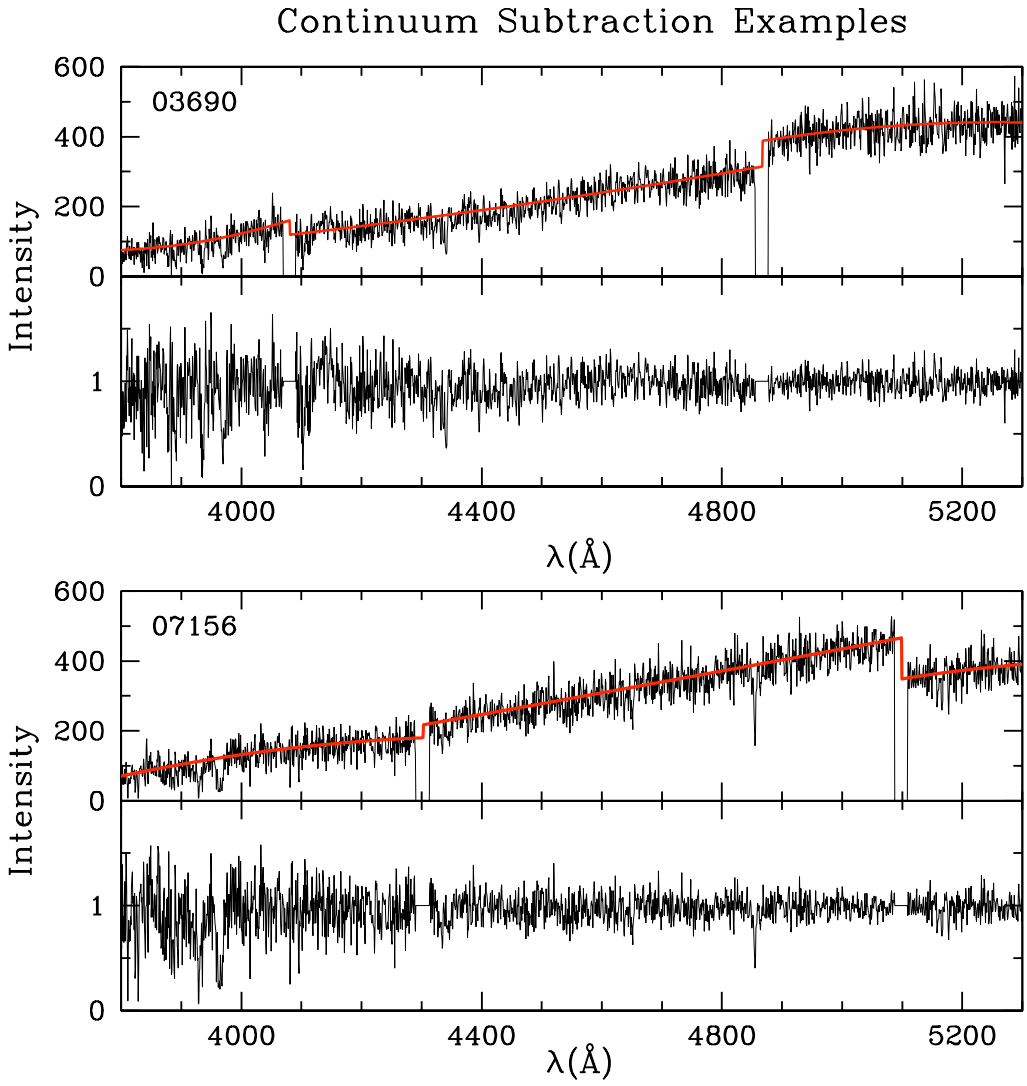

Figure 3.12: Continuum subtraction examples. The spectra of two typical targets (03690 and 07156) from the representative field 020.5p00.1 are presented in the upper panels along with the piecewise fit to their continua shown in red. The three segments of each spectra were independently fit by second-order polynomials using an IDL code written to account for the abrupt discontinuities that sometimes occur across the chip gaps. The two lower panels show the continuum-subtracted spectra for each target.

Measuring Velocities

The final step in the reduction of our IMACS spectroscopic data set was to measure the line-of-sight velocities of all of our object spectra. The observed wavelengths (λ) of a star's various spectral features will be Doppler shifted relative to their rest wavelengths (λ_0) by an amount that is proportional to the star's observed radial velocity ($V_{\rm obs}$). This relationship is summarized by the non-relativistic Doppler effect equation:

$$V_{\rm obs} = c\,\frac{\lambda - \lambda_0}{\lambda_0} = c\,\frac{\Delta\lambda}{\lambda_0} \tag{3.1}$$

where c is the speed of light. Stellar radial velocities can be determined by measuring the shifts in a star's spectral features relative to the rest wavelengths of those features. The IRAF task for doing this is known as `fxcor`. The `fxcor` task takes as its inputs an object spectrum of unknown radial velocity, and a radial velocity template spectrum. At the outset, both the object and template spectra are re-binned to the common log-linear wavelength dispersion of the object spectrum. The `fxcor` task then uses the method of Tonry & Davis (1979) to determine the cross-correlation function of the Fourier transforms of the object and template spectra. This method is particularly powerful because it measures the object's radial velocity not from the shift of a single spectral feature, but from the entire spectrum.

Before calculating the cross-correlation function, `fxcor` first filters the Fourier transforms of both the object and template spectra so as to ensure that the low frequency residuals that remain in the continuum (even after the efforts of the previous

step) and the high frequency pixel-to-pixel variations (due to either under-sampled features or spectral noise) do not contribute to the cross-correlation function. The task then determines the relative radial velocity ($V_{\rm rel}$) between the object and template spectra from the center of a Gaussian profile fit to the highest peak in the cross-correlation function. The `fxcor` task also computes a useful quantity known at the Tonry-Davis R value (R_{TD}; Tonry & Davis 1979). This quantity represents the ratio of the height of the tallest peak in the cross-correlation function to the height of the average peak. It therefore provides a quantitative way to assess the reliability of each velocity measurement, and will later be utilized to estimate the uncertainties in the measured velocities (Section 3.3.1).

While running `fxcor` the cross-correlation functions for every object were inspected by eye and fit interactively. This allowed for the removal of objects with poorly measured velocities from our data set. Objects for which the highest peak in the cross-correlation function corresponded to velocities too extreme to be local group stars were rejected. Objects for which the highest peak was not unambiguous were also rejected. Finally, objects whose peak profiles in the cross-correlation function were not sufficiently symmetric, so that their centers could be well determined by a Gaussian fit, were also rejected. Figures 3.13 and 3.14 show the spectra and cross-correlation functions of eight Sgr targets spanning a representative range of R_{TD} values.

The radial velocity template used for all of the cross-correlations was a high-resolution synthetic stellar spectrum taken from the library of Coelho et al. (2005).

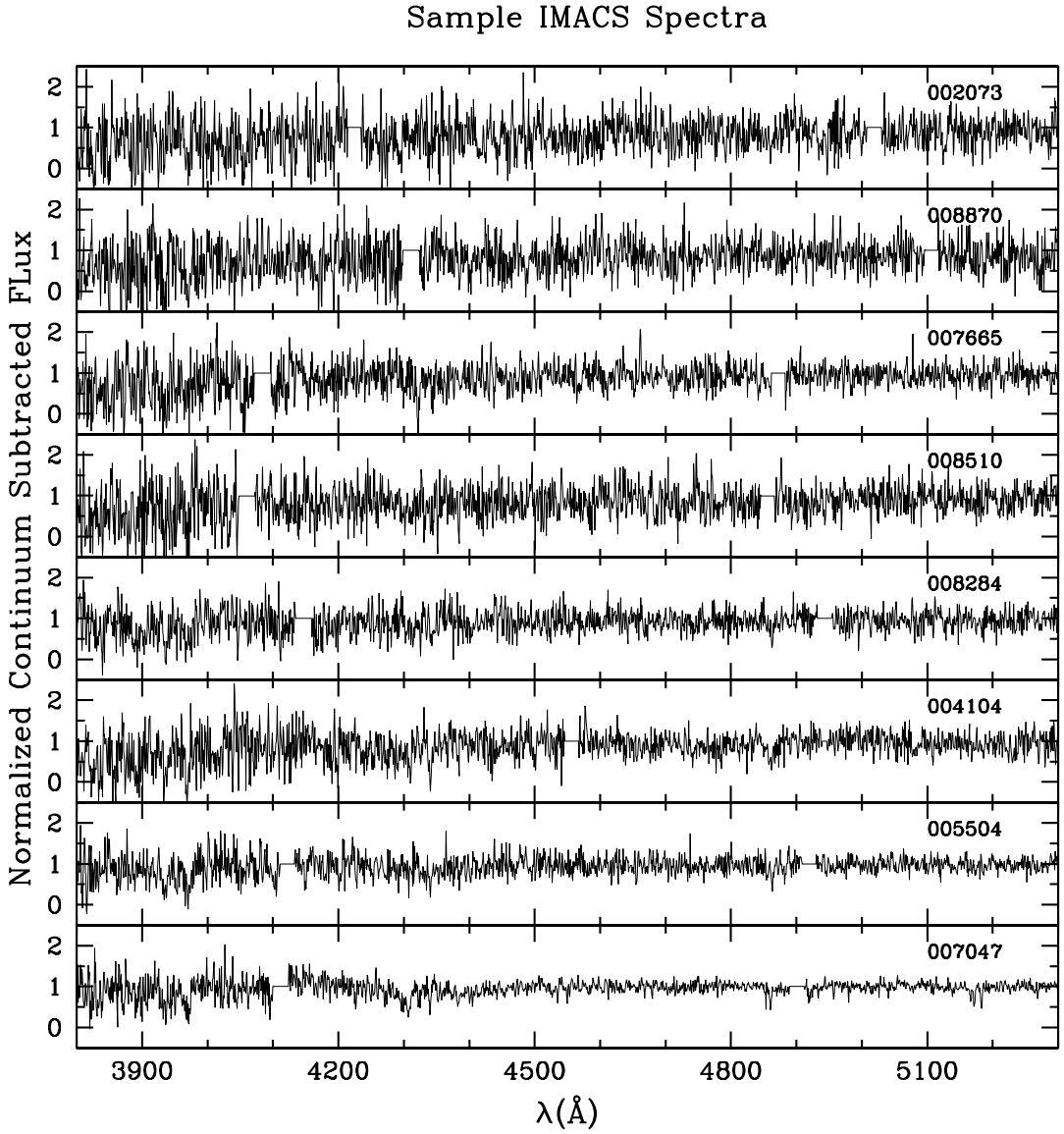

Figure 3.13: Sample IMACS spectra. The spectra of eight typical Sgr targets from the representative field 020.5p00.1 are presented in order of increasing R_{TD} from top to bottom. Their object identifiers are given in the upper right corner of each panel. Their corresponding cross-correlation results are presented in Figure 3.14.

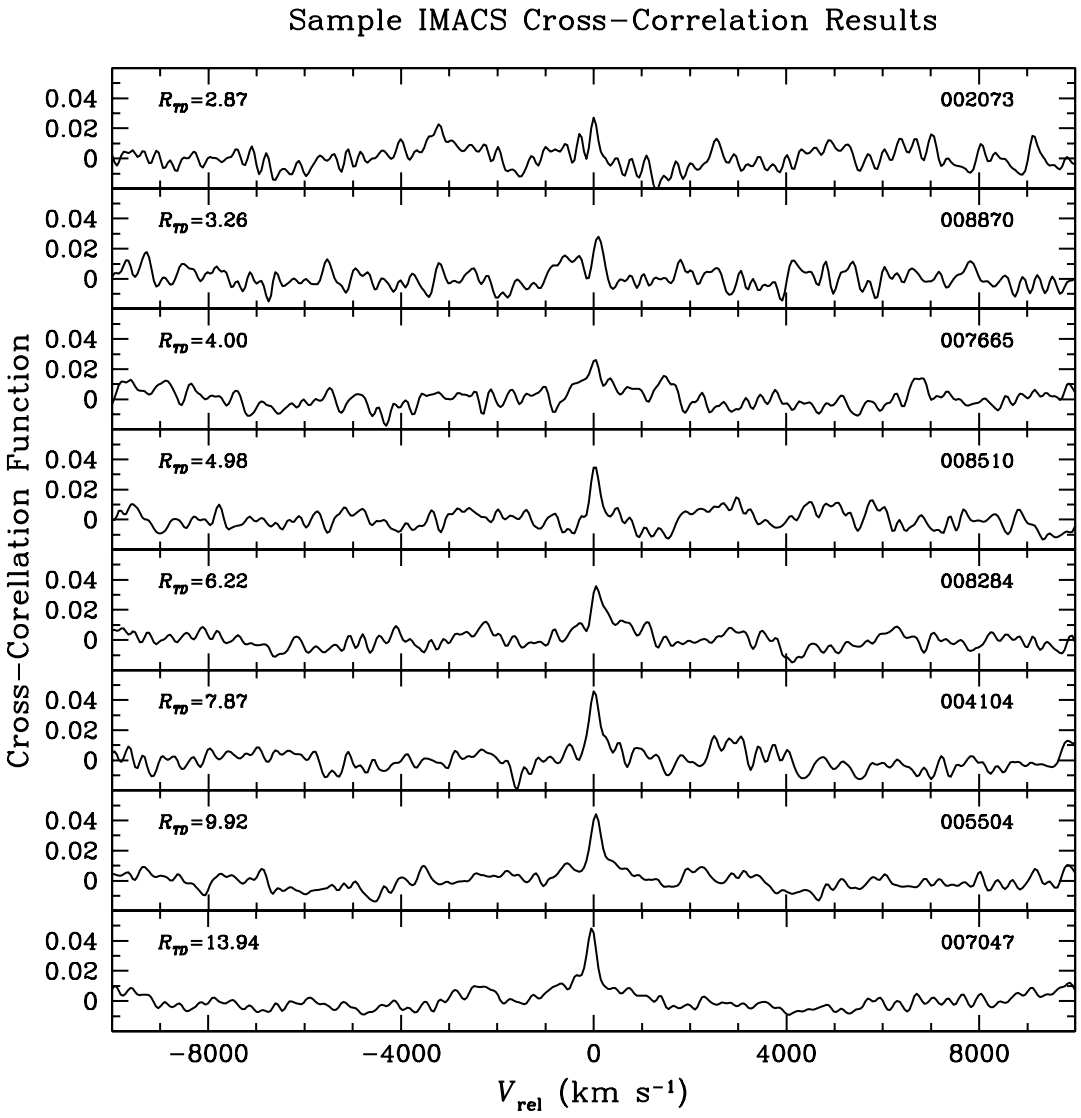

Figure 3.14: Sample IMACS cross-correlation results. The cross-correlation function for eight typical Sgr targets from the representative field 020.5p00.1 are presented in order of increasing R_{TD} from top to bottom. Their R_{TD} values are given in the upper left corner of each panel. Their object identifiers are given in the upper right corner of each panel. Their corresponding spectra are presented in Figure 3.13.

We tested a range of their synthetic stellar spectra, including stars modeled to be A6, F1, F5, G1, G5, and K0 main-sequence stars. Based on both the velocity measurement errors and the Tonry-Davis R values reported by `fxcor` we determined that the G1 spectrum was a slightly better match to our date set than the G5 spectrum, which was significantly better than the rest. We therefore chose to use the G1 spectrum, which was designed to have properties similar to those of a G1 dwarf, specifically: $T_{eff} = 6000$ K, $\log g = 4.5$, [Fe/H] = 0.0, and $[\alpha/\mathrm{Fe}] = 0.0$. The synthetic spectrum of the G1 dwarf is presented in Figure 3.15. Before performing the cross-correlation, the `fxcor` task automatically rebins the template from its inherently high linear wavelength dispersion of 0.02 Å pixel^{-1} down to the same log-linear dispersion as the object spectra (which have a linear dispersion of 0.75 Å pixel^{-1}). Keywords were added to the template's header (RA, DEC, EQUINOX, DATE-OBS, UTMID, and VHELIO) using the IRAF task `hedit` to ensure that its observed velocity ($V_{\mathrm{obs,t}}$), as measured from the Earth's rest frame, and its heliocentric velocity ($V_{\mathrm{helio,t}}$), as measured from the Sun's rest frame, were exactly zero.

The observed geocentric radial velocities (V_{obs}) have the unfortunate property of including velocity components due to the annual orbit of the Earth around the sun ($\sim$30 km s^{-1}) and the diurnal rotation of the Earth about its axis ($\sim$0.5 km s^{-1} at the equator). These motions introduce undesirable dependencies in to the radial velocity measurements. The observed radial velocity for a given target will periodically vary over the course of a year due to the orbital motion of the Earth. Likewise, the observed radial velocity for a given target will periodically vary over the course of a

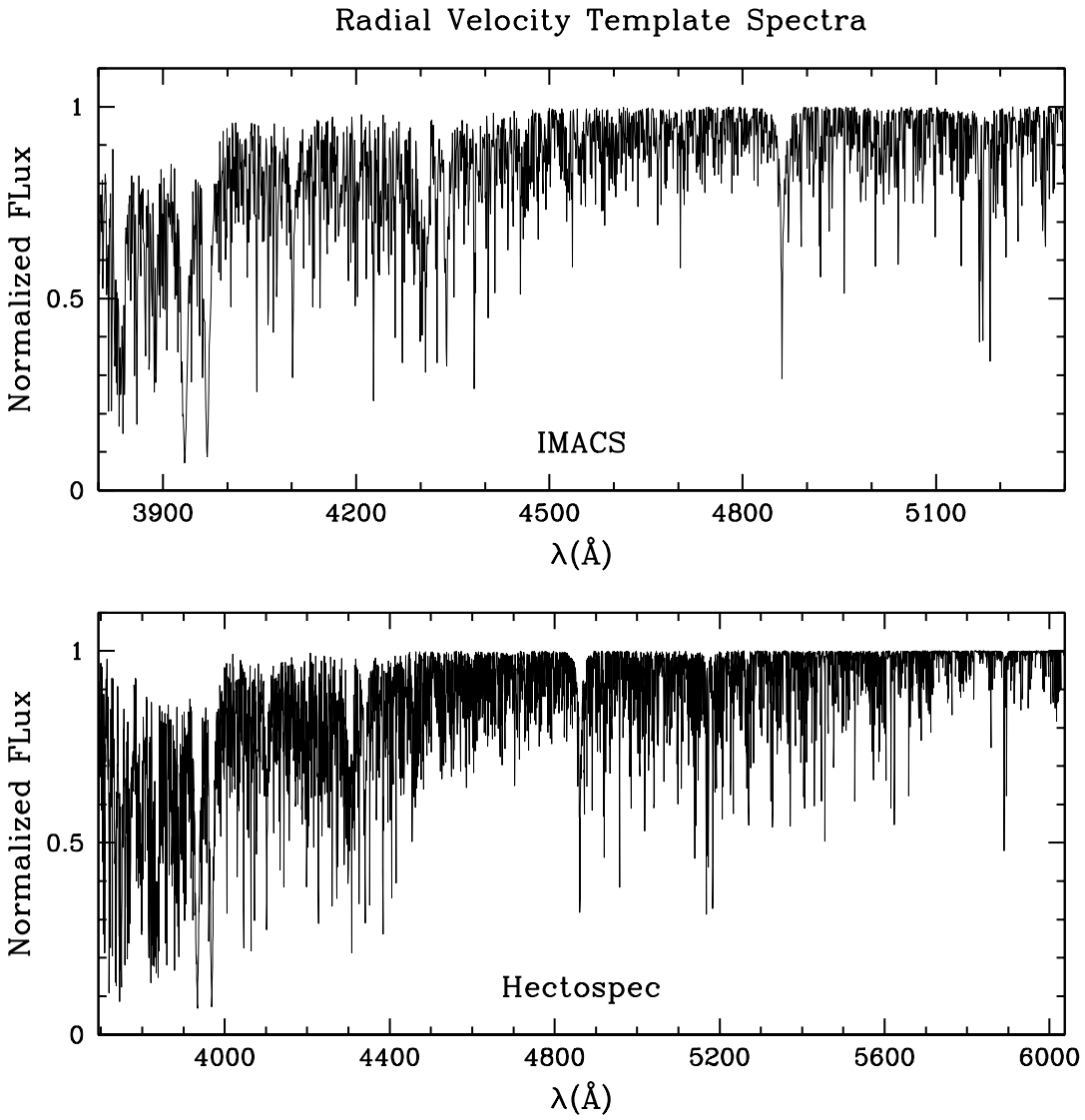

Figure 3.15: Radial velocity template spectrum. This synthetic stellar spectrum, taken from the library of Coelho et al. (2005), was used as the radial velocity template when measuring the velocities of target stars with the `fxcor` task. It was designed to have properties similar to those of a G1 main-sequence star. The upper panel shows the synthetic stellar spectrum with the same wavelength range (3800-5300 Å) and dispersion (0.75 Å pixel^{-1}) as the IMACS data. The lower panel shows the same spectrum but with the wavelength range (3694-6037 Å) and dispersion (0.55 Å pixel^{-1}) of the Hectospec data (see Section 3.2).

day, and depend on the latitude of the observatory, due to the rotational motion of the Earth. For these reasons, the geocentric reference frame is unsuitable for reporting the radial velocities of astronomical targets. Fortunately, the `fxcor` task removes these terrestrial velocity components from the observed radial velocity, effectively transforming from the geocentric to a heliocentric reference frame. Radial velocities in the heliocentric rest frame ($V_{\rm helio}$) are not subject to variations on such short timescales (components of the Sun's velocity vary on timescales $\gtrsim 10^7$ years) and are not observatory dependent.

The transformation from the geocentric observed radial velocity ($V_{\rm obs}$) to the heliocentric radial velocity ($V_{\rm helio}$) can be made by computing what is known as the heliocentric correction (HC). The `fxcor` task calculates the heliocentric correction for both the object ($HC_{\rm o}$) and the template ($HC_{\rm t}$) spectra using the aforementioned keywords in the image headers, and the known geographical information for the observatory specified in the task parameters.

There are several steps that the `fxcor` task must go through to calculate the heliocentric radial velocity of the object spectrum ($V_{\rm helio,o}$). First, from the information in the template spectrum's header, it reads the specified heliocentric radial velocity ($V_{\rm helio,t}$) and computes the heliocentric correction ($HC_{\rm t}$). From these it can easily calculate the template's observed radial velocity ($V_{\rm obs,t}$):

$$V_{\rm obs,t} = V_{\rm helio,t} - HC_{\rm t} \tag{3.2}$$

In our case, all three terms in the above equation are equal to zero by design.

Next, the observed radial velocity of the object ($V_{\rm obs,o}$) is calculated from the relative radial velocity between the object and template spectra ($V_{\rm rel}$). The relative radial velocity ($V_{\rm rel}$) is the quantity that is determined from the center of the Gaussian profile fit to the highest peak in the cross-correlation function.

$$\begin{aligned} V_{\rm obs,o} &= V_{\rm rel} + V_{\rm obs,t} \\ &= V_{\rm rel} + V_{\rm helio,t} - HC_{\rm t} \end{aligned} \tag{3.3}$$

In our case, since the last two terms in the above equation are equal to zero, this equation simplifies to: $V_{\rm obs,o} = V_{\rm rel}$.

Finally, from the information in the object spectrum's header, `fxcor` calculates its heliocentric correction ($HC_{\rm o}$), and then uses the correction to convert from the observed radial velocity ($V_{\rm obs,o}$) to the heliocentric radial velocity ($V_{\rm helio,o}$):

$$\begin{aligned} V_{\rm helio,o} &= V_{\rm obs,o} + HC_{\rm o} \\ &= V_{\rm rel} + HC_{\rm o} + V_{\rm obs,t} \\ &= V_{\rm rel} + HC_{\rm o} + V_{\rm helio,t} - HC_{\rm t} \end{aligned} \tag{3.4}$$

In our case, since the last two terms in the above equation are equal to zero, this equation simplifies to: $V_{\rm helio,o} = V_{\rm rel} + HC_{\rm o}$.

There is one significant drawback to reporting radial velocities in the solar rest frame. Consider two hypothetical target stars having very different galactic coordinates (l, b) in the halo of the Milky Way. Even if they are both approaching or

receding from the Sun with the same velocity, their heliocentric radial velocities will not be equal. This is because the component of the Sun's velocity along the line of sight to each star will be different. It is preferable to report radial velocities from the Galactic standard of rest frame ($V_{\rm gsr}$), which is defined to be instantaneously centered at the location of the Sun, but at rest with respect to the Galactic center. In this rest frame, stars throughout the halo that are approaching or receding from the solar location at the same rate will have the same $V_{\rm gsr}$.

To transform from the heliocentric radial velocity ($V_{\rm helio}$) to the Galactic standard of rest radial velocity ($V_{\rm gsr}$) requires removing the component of the sun's velocity along the line of sight to the target. Let Θ_0 represent the local-standard-of-rest (lsr) rotation velocity, and (u, v, w) represent the components of the Sun's peculiar motion relative to the lsr. By convention u is taken to be directed radially inward towards the Galactic center, v is directed forward into the direction of rotation, and w is directed upwards towards the north Galactic pole. Then, the Galactic standard of rest radial velocity for a star having galactic coordinates (l, b) can be calculated from its heliocentric velocity ($V_{\rm helio}$) as:

$$V_{\rm gsr} = V_{\rm helio} + u\cos(l)\cos(b) + (\Theta_0 + v)\sin(l)\cos(b) + w\sin(b) \qquad (3.5)$$

We adopt the International Astronomical Union's recommended value for the local-standard-of-rest rotation velocity, Θ_0, of 220 km s^{-1}. For the components of the Sun's peculiar velocity relative to the lsr we adopt the values of Dehnen & Binney (1998), who measured (u, v, w) = (–10.00, 5.25, 7.17) km s^{-1}. Given the small size

of our spectroscopic fields, when transforming radial velocities from the heliocentric rest frame to the Galactic standard of rest frame we adopt for all stars in the field the galactic coordinates (l, b) of the field center. The Galactic standard of rest radial velocities for each target star is listed in the tables at the end of this chapter.

3.2 Hectospec Spectroscopy

3.2.1 Planning Observations with Hectospec

The northernmost fields of the Sgr stream, having declinations $\delta \gtrsim 20^\circ$ (see Figure 2.1), are inaccessible from the Las Campanas Observatory, which is located at a latitude of $\sim$29° S. Therefore, IMACS could not be used to obtain spectroscopy in this portion of the stream. Instead, we used the Hectospec multi-fiber spectrograph (Fabricant et al., 2005), located at the MMT Observatory in southern Arizona, to acquire data in six fields having declinations $25^\circ < \delta < 31^\circ$. The Multiple Mirror Telescope (MMT), with its classical Cassegrain design, has a 6.5 m primary mirror and three interchangeable secondary mirrors.

The Hectospec instrument operates with the wide field $f/5$ secondary in place, and has a 1° diameter field of view. It features 300 1.″5 diameter fibers, which can be accurately positioned by a pair of six-axis robots in $\sim$300 seconds. Our desired wavelength range of 3800–5900 Å was chosen to include several of the hydrogen Balmer lines at the blue end and the Sodium I lines at 5890 and 5896 Å towards the red. By choosing the 600 lines mm^{-1} grating with a central wavelength of 4800 Å, we were able to achieve a wavelength range of 3694–6037 Å. The 600 line grating

has a dispersion of 0.55 Å pixel^{-1} and a spectral resolution of ∼2.2 Å, resulting in a spectral resolving power of $R \sim 2200$.

The Hectospec CCD detector includes two 4608 × 2048 chips arranged in a 4608 × 4096 array. The long axes of the chips correspond to the dispersion direction. With this orientation the individual spectra are fully contained on a single chip, and do not cross the gap between the two chips, which runs parallel to the spectra. In order to achieve a higher packing efficiency on the detector, the even and odd fibers are mounted such that their spectra are offset by ∼34 pixels (∼19 Å) along the dispersion direction.

In preparation for an observing run with Hectospec, configuration files that specify the assignments of fibers to targets must first be generated for each field. The software program that accomplishes this is known as `XFITFIBS`. This program takes as its input a catalog file containing the list of potential target and guide star candidates in the field. The catalog file lists the coordinates, identifier name, and priority rank for these stars. We assigned all target stars an equal priority to avoid the unnecessary introduction of a selection bias.

The guide stars are used to accurately establish the field alignment. It is therefore crucial to have excellent relative astrometry between the guide and target star candidates. There are significant constraints placed upon the positions and brightnesses of the guide star candidates. First, they must have brightnesses between ∼13–16 magnitudes, and they ones that are ultimately selected for use should not differ in brightness by more than two magnitudes. Second, to be accessible to the guide star

probes they must lie within three thin annular segments just beyond the 1° field of view of Hectospec. At least two, and ideally all three, probes need to be able to access a valid guide star in order to accurately align on the field. The `XFITFIBS` program runs a classification routine to eliminate galaxies, double stars, and stars with nearby neighbors from the list of candidate guide stars.

In addition to the catalog file, the `XFITFIBS` program also requires additional information for each field, including: the approximate date and time that the field will be observed, the desired number and length of exposures, the priority ranking for the configuration, and the choice of grating and central wavelength. Once this information is entered, a graphical user interface is used to choose a field center and rotation angle that ensures the stringent guide star requirements are met. With the field center and rotation angle set, the final step is to allow the software to optimize the fiber-to-target assignments so as to maximize the number of targets acquired. In this process, the `XFITFIBS` program also assigns fibers to (presumably) empty positions on the sky to be used later for sky subtraction when reducing the data. We specified a minimum of 10 and maximum of 100 fibers be allocated for background sky spectra. Ultimately, in the six fields in which we obtained data, a range of 86–96 fibers were assigned to the sky. The spatial distribution on the sky of assigned fibers and unassigned candidates for a representative Hectospec field is shown in Figure 3.16.

3.2.2 Data Acquisition

Observations with Hectospec are made in queue mode so as to distribute lost time due to weather, telescope and instrument malfunctions evenly amongst all observers.

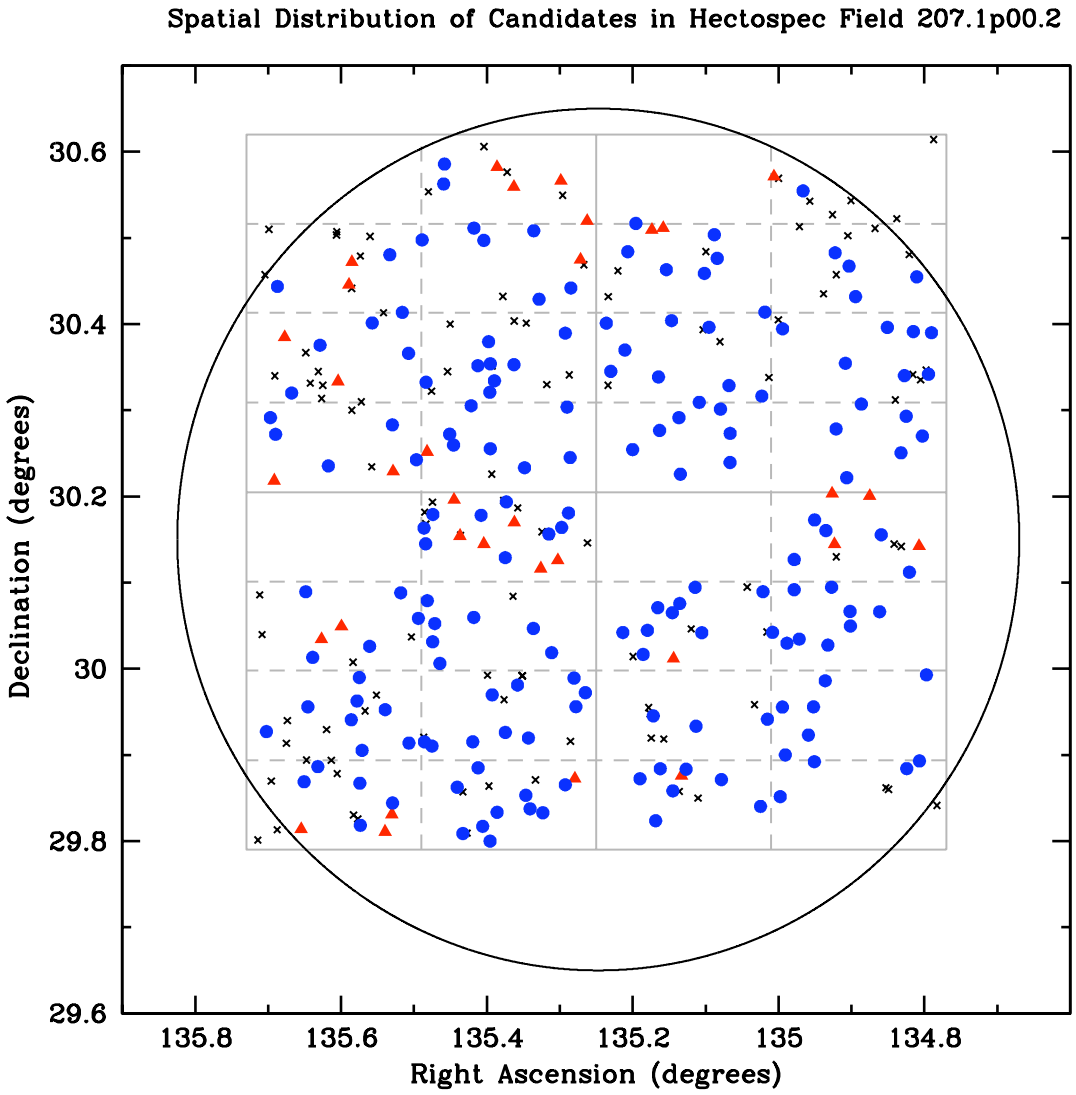

Figure 3.16: Spatial distribution of candidates in a representative Hectospec field. The total number of candidate stars in this field, 207.1p00.2, was 318. The unobserved stars (N=112) are depicted as black diagonal crosses. The stars with reliable radial velocity measurements (N=173) are shown as blue circles. Acquired stars that were rejected due to poor velocity measurements (N=33) are represented as red triangles. The large black circle represents the field of view of Hectospec. The four contiguous grey squares represent the four pointings used to acquire photometry with the 8K detector on the MDM 2.4 m telescope. The dashed lines denote the boundaries of the eight CCD chips in the 8K detector. The chip in the upper left corner of the detector was not functional, so there are no candidates in those areas.

Each principal investigator is assigned to observer with Hectospec for a number of nights equal to their allocated time. In our case we were assigned three consecutive nights in 2008 March. Unfortunately, the first two nights were lost due to problems with the robotic fiber positioners. On our third and final night, data was acquired in three of our fields. Given the significant amount of lost time during our allocated nights, the queue observing mode of Hectospec greatly benefitted our project. Four nights after the conclusion of our assigned observing run, another observer acquired data for us in two more of our fields. About a month after that, a sixth data field and a radial velocity standard field were observed for us in 2008 April.

In total, six Sgr fields were observed with Hectospec. One of these fields contained no stellar spectra, apparently due to inaccurate astrometry, and has been excluded from the data set. The remaining five Sgr fields contained a total of 902 target stars, with a range of 143–206 targets per field. One radial velocity standard field, SA 57, containing twelve targets was also observed. For each Sgr field, three to five total exposures of equal length were acquired. The total exposure times for the Sgr fields ranged from 7200–9000 seconds.

Basic information on all Hectospec observations is summarized in Table 3.3. The provided information includes the field name in the first column, the date of the observation in the second column, and the number of exposures and their exposure times in the third column. Also included for each mask is the total number of photometrically identified candidate stars in the field in the fourth column, the number of target stars (i.e. candidate stars with assigned fibers) and this number expressed

Table 3.3: Hectospec Spectroscopic Observations

Field	UT Date	Exp. Time (s)	N_{Cands}	$N_{Targets}$(%)	N_{RVs}(%)	N_{Sky}
177.4n02.7	2008 Mar 8	3x2700	612	199(33)	187(94)	90
197.4n00.9	2008 Mar 12	4x1800	262	172(66)	154(90)	93
207.1p00.2	2008 Mar 8	3x3000	318	206(65)	175(85)	86
215.1p00.8	2008 Apr 9	5x1800	289	182(63)	137(75)	95
224.9p01.1[a]	2008 Mar 12	4x1800	166	139(84)	0(00)	96
235.1p01.8	2008 Mar 8	3x2400	240	143(60)	110(77)	96
SA 57[b]	2008 Apr 9	3x120	143	12(08)	12(100)	49

[a] Field 224.9p01.1 contained no spectra due to inaccuracies in the astrometry.
[b] Field SA 57 is a radial velocity standard field.

as a percentage of the total number of candidate stars in the fifth column, and the number of sky fibers in the seventh column. The total number of target stars that ultimately resulted in reliable radial velocity measurements is provided in column six, along with this number expressed as a percentage of the total number of target stars.

The observing sequence begins with the verification by the robot operators that a minimum of two guide stars are available, and that the rotator demand angles will remain within their limits for the duration of the observations. If not, the position angle can usually be adjusted to correct either of these issues. The telescope is then slewed to the zenith, at which point the robots begin to position the 300 fibers, taking in to account the airmass and instrument rotator position at the expected observation midpoint. After about five minutes, the fibers are in place, and the guide star probes are then positioned. Before acquiring data, a wave front sensor probe is used to correct the collimation of the telescope and the shape of the primary mirror by adjusting the support forces. These corrections are made after slewing the telescope to the position of a bright star near the field to be observed. The telescope is then slewed to the field position and the instrument rotator tracking is enabled to maintain

the required position angle. The robot guide cameras are then deployed. Autoguiding software is used to adjust the telescope pointing and rotator angle until the guide stars are centered at their specified coordinates. The positions of the guide stars within the guide probes are then used to maintain the telescope guiding throughout the observations. This procedure ensures that the telescope pointing, rotator angle, and guiding are tied to the same astrometric system as the fiber positions. Finally, the robots are parked and data acquisition can begin.

In addition to obtaining spectroscopic data in the target fields, several other types of images are necessary to properly reduce and calibrate the target spectra. Typically, about ten zero-second bias frames were taken in the afternoon. These were later combined in to a single master bias frame to be used later during the data reduction process. Also, during each afternoon, a series of three comparison arc spectra were taken with exposure times of 600 or 900 seconds each. These were acquired by illuminating a screen mounted on to the MMT building shutters with Neon–Argon–Fe emission line lamps. Two types of spectroscopic flat field images were also taken. During the afternoon, a series of five to ten dome flat images, with exposure times of 20–25 seconds each, were taken. These images were also acquired by illuminating the dome-mounted screen with incandescent continuum lamps. Finally, a series of about five twilight sky flats, with exposure times increasing from about three to twenty seconds, were taken during the evening twilight.

3.2.3 Data Reduction

The reduction of the Hectospec data set was performed using standard, well-known IRAF procedures. For all images, the initial processing steps were accomplished using the `ccdproc` task. First, the overscan bias level was determined, then subtracted, and finally trimmed from all frames. Next, the `zerocombine` task was used to create two master bias images by separately averaging together the 20/22 individual zero-second exposures taken during the March/April observations. The `ccdproc` task was then used again to subtract these master bias frames from the concurrent data and calibration images.

As mentioned earlier, the Hectospec detector consists of two 4608 $\times$ 2048 CCDs, which we refer to as chips "A" and "B". Each CCD is read out through two amplifiers. Once the initial processing with `ccdproc` is complete, the data from both amplifiers are combined to form a single image for each CCD. From this point forward, the reductions of the A and B chips progressed in parallel.

The spectra display a noticeable curvature along the spatial axis of the detector due to anamorphic optical effects within the instrument. This can be seen in Figure 3.17, which shows the combined A and B chips for a single, unprocessed, 1800 second exposure of the representative field 215.1p00.8. Figure 3.18 shows an enlarged portion of the full image presented in Figure 3.17.

IRAF's `apextract` package was used in a multi-step process to trace the observed curvature, and ultimately extract one-dimensional spectra from the data frames and comparison arc frames. First, the well-exposed, feature-less dome flat images were

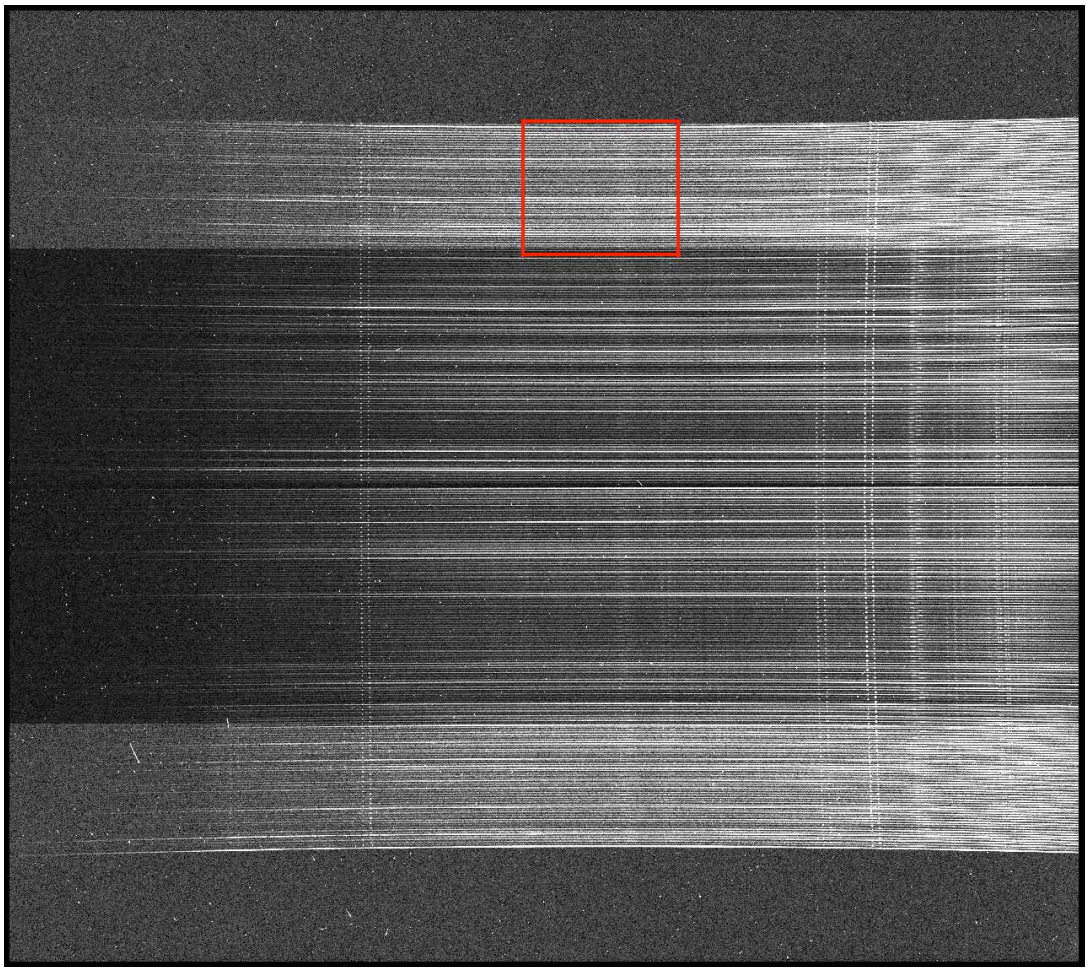

Figure 3.17: Unprocessed Hectospec image. A single 1800 second spectroscopic exposure of the representative field 215.1p00.8 is shown. The vertical axis represents the spatial direction. Wavelengths increases from ∼3700 Å on the left to ∼6000 Å on the right. This field contained 182 target fibers and 95 assigned to the background sky. A number of night sky emission lines are visible, mostly towards the red ends of the spectra. They also reveal the alternating offset pattern of consecutive fibers. Many cosmic rays, which were later removed by co-adding multiple exposures, are visible throughout the image. The relative brightness in the fibers at the very top and bottom is a consequence of a small difference in the gain settings for the two amps on each CCD chip. The red box outlines a region for which a close-up is provided in Figure 3.18.

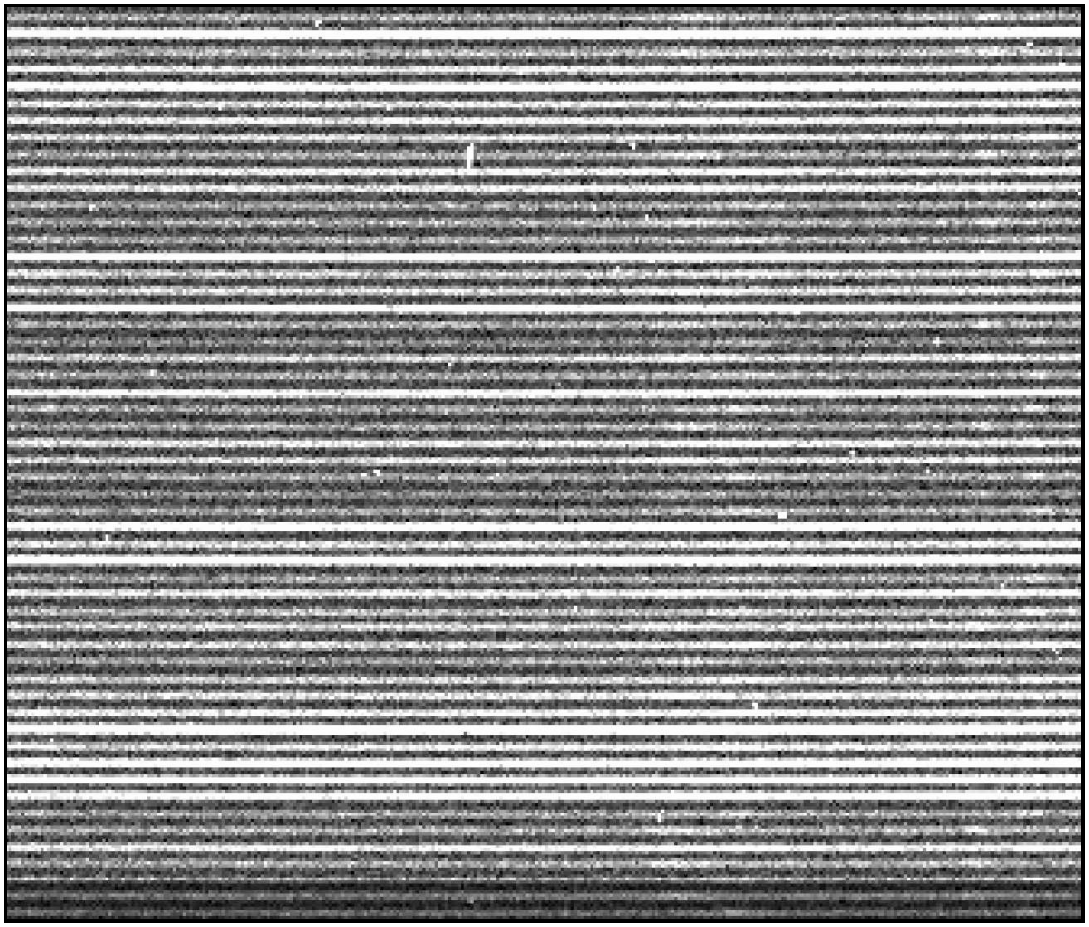

Figure 3.18: Close-up of unprocessed Hectospec image. The two-dimensional spectra from a sample of 54 fibers are shown. This close-up view is drawn from the highlighted region in Figure 3.17.

used to determine the locations of the individual apertures on the detectors, and to trace each one along the dispersion axis while accounting for its curvature along the spatial axis. These traces were then applied to the corresponding apertures in each individual data frame. To account for the possibility of small spatial offsets of the spectra between the images, a uniform spatial shift was applied to the full set of reference spectral traces to best match the target spectra. Once extracted, the spectral traces applied to the target frame apertures were then applied to the corresponding apertures in the temporally nearest comparison arc exposures. In this way, the `apall` task was used to extract one-dimensional spectra from all of the data frames, and, corresponding, identically-traced, one-dimensional spectra from the temporally nearest comparison arc exposures.

To correct for the differing relative throughputs of the fibers, twilight sky flat images were used (except for the data collected on the night of 2008 April 8 when only dome flats were taken). The median intensity values in the one-dimensional flat field spectra were used to determine appropriate scaling factors for the individual fibers. Normalized spectra were then created by dividing by the estimated fiber-dependent throughputs.

The next task was determine the wavelength solutions for the Neon–Argon–Fe comparison arc spectra. Due to the $\sim$34 pixel offset between even and odd numbered apertures, it was necessary to manually identify the arc emission lines of four individual spectra (one even and one odd numbered aperture from each CCD chip). Once the manual identifications were made using the IRAF task `identify`, the task

`reidentify` was used automatically find the same features in the remaining apertures and comparison arc images. We used a line list containing 88 known emission lines spanning the wavelength range 3720–6074 Å. The `reidentify` task typically found 70–80 emission lines in each aperture, which were then fit to a fifth-order Chebyshev polynomial. Emission lines with residuals exceeding $\pm 3\sigma$ were rejected over three iterations. The typical rms scatter from the polynomial fits had a range of $\sim$0.08–0.12 pixels, corresponding to $\sim$3–4 km s^{-1}.

To apply the wavelength solutions from the arc spectra to their corresponding target spectra, the header information of the target image files needed to be edited with the IRAF task `hedit` to include the "REFSPEC1" keyword. For each data image, this keyword was assigned the name of the corresponding comparison arc image whose wavelength solution was to be applied to it. The IRAF task `dispcor` was then executed, which applied the aperture-dependent dispersion solution from the temporally nearest comparison arc exposure. All apertures were rebinned by `dispcor` to have a uniform dispersion of 0.55 Å pixel^{-1}. For consistency when cross-corellating to measure radial velocities, we restricted the wavelength range of the output spectra to be the maximum range common to all spectra, 3551–6037 Å.

The corresponding apertures from the multiple exposures of each field were then averaged together using the IRAF task `scombine`. When averaging, a conservative sigma-clipping algorithm (`ccdclip`) was applied to exclude pixels that deviated significantly from the median value due to the presence of cosmic rays or bad pixels on the detector. It was necessary to apply scaling factors to the three exposures of field

235.1p01.8 due to an increasing amount of background counts from internal scattered light within the spectrograph chamber.

The final processing step before measuring the targets' radial velocities was to remove the background sky spectrum from each target spectrum. To do this we created two master sky spectra for each field by averaging together all of the background sky fiber spectra on each CCD chip using the IRAF task `scombine`. Our Sgr fields had 38–49 sky fibers per CCD chip, and the SA 57 radial velocity standard field and 24–25. We applied the `minmax` rejection algorithm to exclude the highest and lowest $\sim$10% of pixel values from the average. This was meant to eliminate the potential contamination of the master sky spectrum by sky fibers that may have been randomly positioned on to astronomical sources such as foreground stars or resolved background galaxies. The IRAF task `imarith` was then used to subtract each master sky spectrum from all other spectra from the same field and on the same CCD chip.

Before measuring radial velocities, the IRAF task `scopy` was used to restrict the wavelength range for all target spectra to 3694–6037 Å. This effectively trimmed off the the bluest portions of the spectra, which, due to the rapidly decreasing efficiency of the reflection grating and throughput of the instrument, lacked any discernible spectral signal from even our brightest targets.

To measure the radial velocities of the target stars in each field the IRAF task `fxcor` was used. This task determines the cross-correlation function of the Fourier transforms of each input object spectrum and a radial velocity template spectrum. After filtering out extreme high and low frequency contributions to the Fourier trans-

forms, the relative velocity of the object spectrum is measured by fitting a Gaussian profile to the highest peak in the cross-correlation function. Figures 3.19 and 3.20 show the spectra and cross-correlation functions of eight Sgr targets spanning a representative range of R_{TD} values. The radial velocity template used was a high-resolution synthetic stellar spectrum from the library of Coelho et al. (2005). It was designed to have properties similar to those of a G1 dwarf. The template spectrum is presented in Figure 3.15. The heliocentric velocities measured by `fxcor` were then converted to the Galactic standard of rest frame. For more information on the various velocity reference frames, the radial velocity template, and the `fxcor` task in general, see the detailed discussion in the "Measuring Velocities" subsection of Section 3.1.3.2.

3.3 Velocity Uncertainties and Errors

3.3.1 Velocity Measurement Uncertainties

There are many factors that contribute to the quality of an individual target's spectrum, and thus the reliability of its radial velocity measurement. Chief among these include the inherent brightness of the source, the atmospheric observing conditions, the characteristics of the telescope, instrument, and detector, and the data reduction process itself. To perform a proper analysis of the data it is critical to know the uncertainty associated with each radial velocity measurement. Unfortunately, it is impossible to directly determine the uncertainty in any individual velocity measurement since there is no way to know or estimate the object's true velocity. Individual measurement uncertainties can only be estimated indirectly. However, our data set

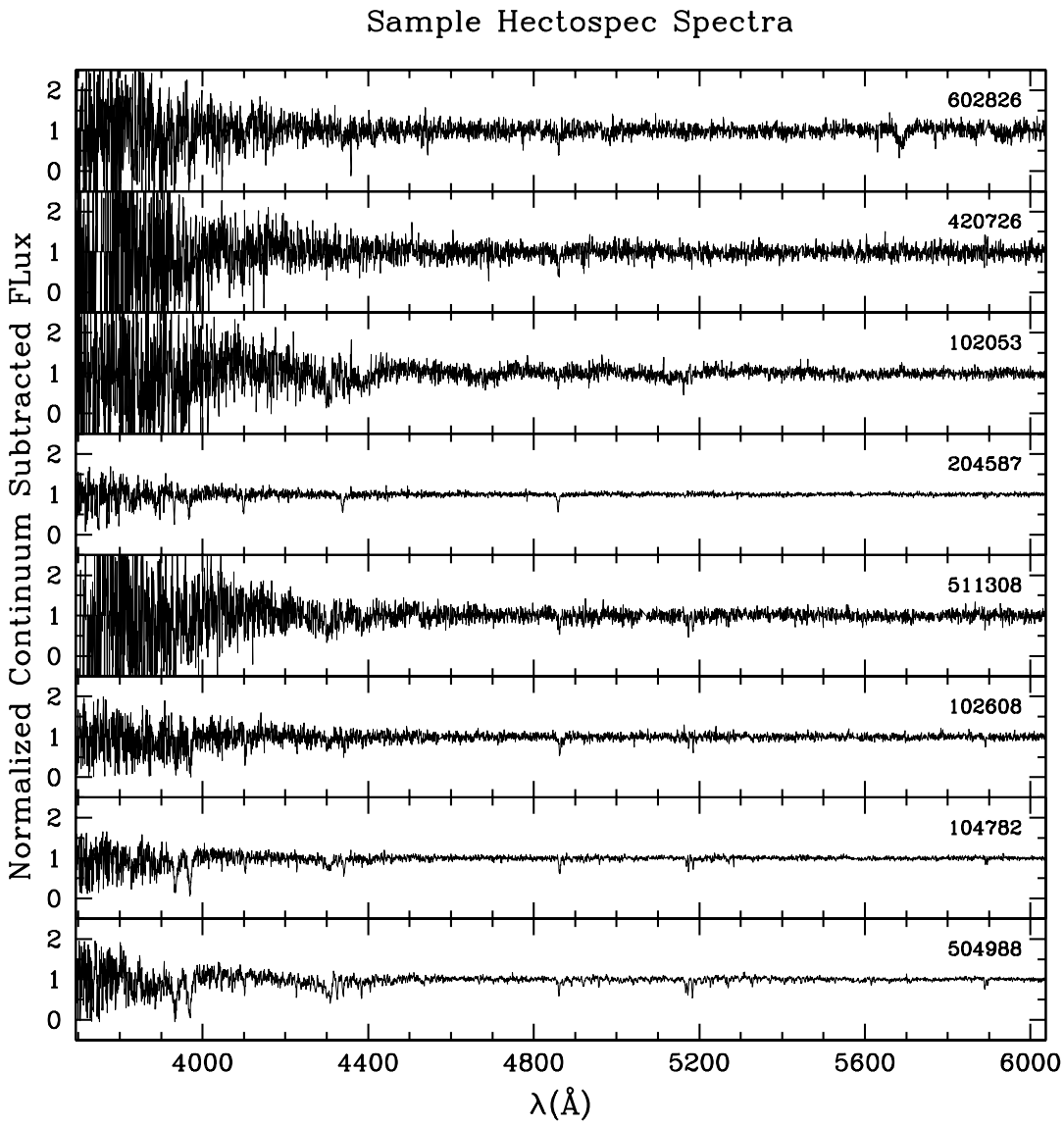

Figure 3.19: Sample Hectospec spectra. The spectra of eight typical Sgr targets from the representative field 215.1p00.8 are presented in order of increasing R_{TD} from top to bottom. Their object identifiers are given in the upper right corner of each panel. Their corresponding cross-correlation results are presented in Figure 3.20.

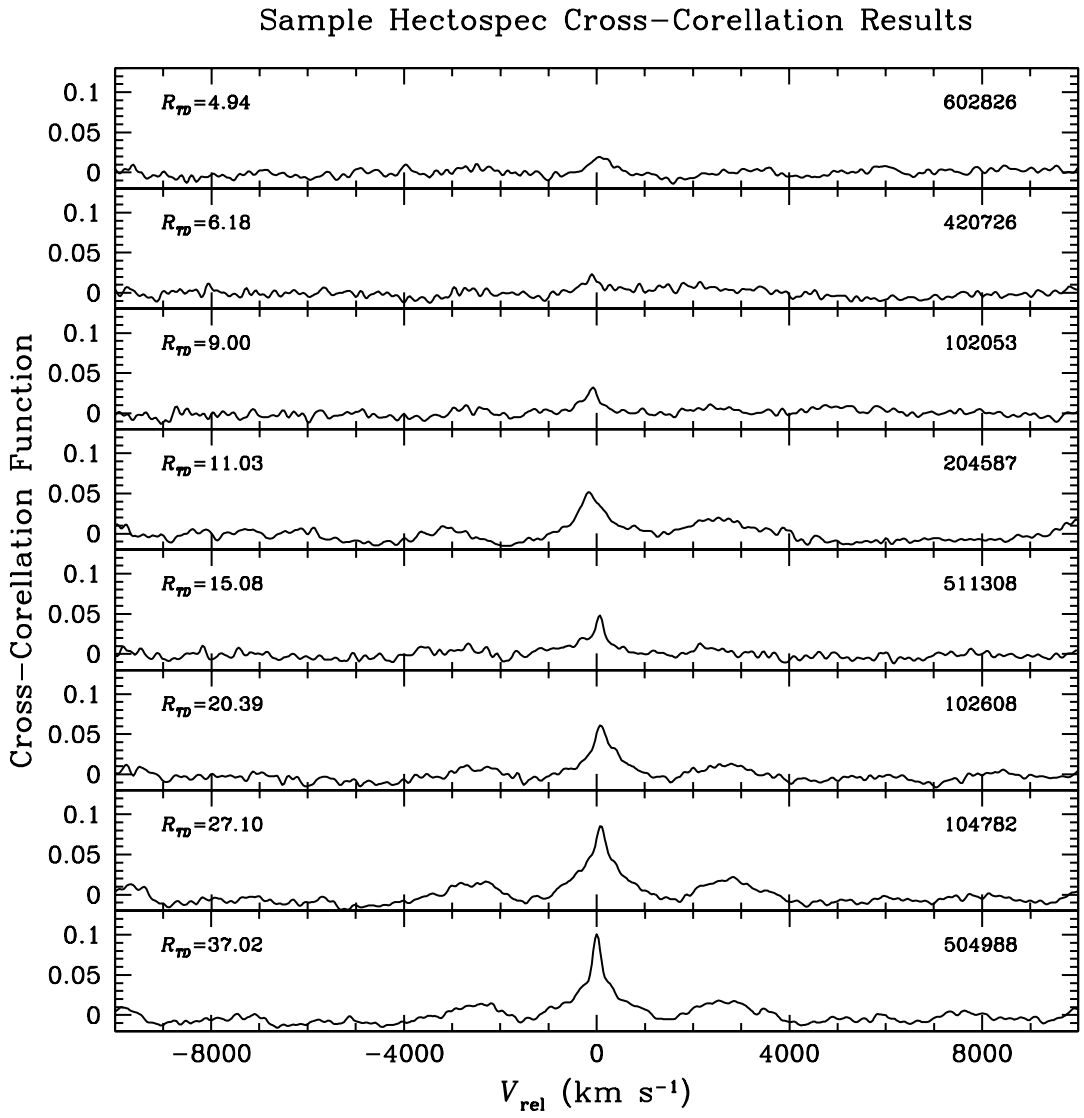

Figure 3.20: Sample Hectospec cross-correlation results. The cross-correlation function for eight typical Sgr targets from the representative field 215.1p00.8 are presented in order of increasing R_{TD} from top to bottom. Their R_{TD} values are given in the upper left corner of each panel. Their object identifiers are given in the upper right corner of each panel. Their corresponding spectra are presented in Figure 3.19.

contains some stars whose velocity uncertainties can be directly estimated: those with repeat measurements. For each star with multiple independent velocity measurements, the star's true velocity can be estimated as the weighted average of the individual measurements. The differences between each individual measurement and the estimate of the true velocity should correlate with the Tonry-Davis statistic, R_{TD} (Tonry & Davis, 1979). The R_{TD} value represents the ratio of the height of the tallest peak in the cross-correlation function to the height of the average peak. It provides a quantitative way to assess the reliability of each velocity measurement, and is therefore expected to correlate strongly with the velocity measurement uncertainty. We can therefore use the many cases of repeat observations to constrain a parameterized functional relationship between the R_{TD} statistic and the estimated velocity uncertainty. This relationship then provides an indirect way, using only their R_{TD} values, to estimate the uncertainties for objects with only a single velocity measurement.

The functional relationship between the R_{TD} statistic and the velocity measurement uncertainty due to noise in the cross-correlation function was first described by Tonry & Davis (1979) as $\sigma_{CCF} \propto (1 + R_{TD})^{-1}$. Walker et al. (2006), and later Walker et al. (2007), expanded upon this formalism. In the discussion that follows we summarize the methodology behind their approach to error analysis. For consistency we adopt their symbolic notation as well.

Suppose a data set consists of N stars, each of which has multiple independent velocity measurements. For the j^{th} star in the data set, let V_{ij} represent the the

velocity of the i^{th} of n_j measurements. The velocity measurement error for that star can be then be represented as:

$$V_{ij} - V_{*j} = \left(\sigma_{CCF,ij}^2 + \sigma_0^2\right)^{1/2} \epsilon_{ij}, \tag{3.6}$$

where V_{*j} represents the true velocity for the j^{th} star, and $\sigma_{CCF,ij}$ represents the uncertainty in the i^{th} measurement of the j^{th} star due to noise in the cross-correlation function, which is assumed to follow a Gaussian distribution with variance $\sigma_{CCF,ij}^2$. The σ_0 term represents the minimum achievable uncertainty for the specific telescope, instrumental configuration, and detector used. Even an ideal target (with negligible σ_{CCF}) observed under perfect atmospheric conditions would have a non-zero velocity uncertainty due to the finite spectral resolution of the instrument and detector. It is assumed to also follow a Gaussian distribution with variance σ_0^2. Finally, the ϵ_{ij} term represents the intrinsic uncertainty of measurement, and therefore follows the standard normal distribution, having a mean value of zero and variance of unity.

The relationship between $\sigma_{CCF,ij}$ and R_{TD} can be modeled as follows:

$$\sigma_{CCF,ij} = \frac{\alpha}{(1 + R_{TD,ij})^x}, \tag{3.7}$$

where α and x represent free parameters that are constrained by the velocity measurements of stars with multiple observations. Inserting Equation 3.7 into Equation 3.6 and taking the base-ten logarithm of the square of each side gives:

$$\log\left[(V_{ij}-V_{*j})^2\right] = \log\left[\frac{\alpha^2}{(1+R_{TD,ij})^{2x}}+\sigma_0^2\right] + \log\left[\epsilon_{ij}^2\right]. \tag{3.8}$$

Since ϵ_{ij} follows the standard normal distribution, ϵ_{ij}^2 follows the χ^2 distribution with one degree of freedom. Walker et al. (2006) use Monte Carlo simulations to determine that the term $\log\left[\epsilon_{ij}^2\right]$ has a mean value of $\left\langle \log\left[\epsilon_{ij}^2\right]\right\rangle = 0.55$. Using this information, the optimal values for the parameters α and x can be estimated by employing a non-linear regression algorithm to minimize the following sum:

$$\sum_{j=1}^{N}\sum_{i=1}^{n_j}\left(\log\left[(V_{ij}-V_{*j})^2\right] - \left[\log\left(\frac{\alpha^2}{(1+R_{TD,ij})^{2x}}+\sigma_0^2\right)-0.55\right]\right)^2. \tag{3.9}$$

The measured velocities, V_{ij}, and the $R_{TD,ij}$ values are calculated by the IRAF task `fxcor`. Before minimizing the sum in Expression 3.9 to solve for the free parameters α and x, the true velocities V_{*j} and the minimum instrumental uncertainty, σ_0, needed to be estimated. These two terms had to be estimated differently for the two spectrographs used, since one (Hectospec) lacked repeat observations.

3.3.1.1 IMACS Error Model

The IMACS data set contained several instances of multiply-observed IMACS spectroscopic masks (see Table 3.2). Field 359.9n01.5 contained 123 targets, and was observed three separate times, yielding (chronologically) 110, 89, and 109 reliable

Table 3.4: IMACS Error Analysis Data Set

Field	$N_{Observations}$	$N_{Targets}$	N_{RVs}	N_3[a]	N_2[a]	N_{Total}
000.0n01.6	2	117	104,95	0	89	178
010.1n03.2	2	115	110,93	0	90	180
359.9n01.5	3	123	110,83,109	73	32	283
Total	7	355	704	73	211	641

[a] N_3 and N_2 represent the number of targets with exactly three and two unique velocity measurements, respectively.

radial velocity measurements. Seventy-three of the targets had acceptable measurements from all three observations, and 32 had acceptable measurements from only two of the observations, providing a total of 283 individual velocity measurements with which to perform the error analysis. Fields 000.0n01.6 and 010.1n03.2 were each observed twice, and contained 117 and 115 targets respectively. The two observations of field 000.0n01.6 yielded 104 and 95 reliable radial velocity measurements, with an overlap of 89 reliably measured targets between the two observations. The two observations of field 010.1n03.2 yielded 110 and 93 reliable radial velocity measurements, with an overlap of 90 reliably measured targets between the two observations. Fields 000.0n01.6 and 010.1n03.2 therefore contributed an additional 178 and 180 individual velocity measurements, respectively, to the error analysis for IMACS, bringing the total to 641 unique observations of 284 different targets. These numbers are summarized in Table 3.4.

The true velocities of these multiply-observed stars, V_{*j}, were estimated as the weighted average, $\overline{V}_{*j}$, of the individual measurements. To calculate the weighted average we assigned to each measured velocity, V_{ij}, a weight, w_{ij}, which was calculated

as the sum in quadrature of the minimum instrumental uncertainty, σ_0, and the velocity error computed by `fxcor`, $\sigma_{FX,ij}$:

$$w_{ij} = (\sigma_{FX,ij}^2 + \sigma_0^2)^{-1}. \tag{3.10}$$

The $\sigma_{FX,ij}$ terms are, to first order, proportional to the $\sigma_{CCF,ij}$ terms of Equation 3.6. To estimate the true velocities, V_{*j}, the weighted averages, $\overline{V}_{*j}$, were then calculated as:

$$\begin{aligned} V_{*j} \simeq \overline{V}_{*j} &= \frac{\sum_{i=1}^{n_j} w_{ij} V_{ij}}{\sum_{i=1}^{n_j} w_{ij}} \\ &= \frac{\sum_{i=1}^{n_j} V_{ij} (\sigma_{FX,ij}^2 + \sigma_0^2)^{-1}}{\sum_{i=1}^{n_j} (\sigma_{FX,ij}^2 + \sigma_0^2)^{-1}} \qquad \text{for } j = 1, 2, ..., N. \end{aligned} \tag{3.11}$$

Before making these calculations, it was first necessary to estimate the minimum instrumental uncertainty, σ_0, for IMACS. To do this we considered the high R_{TD} regime, where the uncertainty due to noise in the cross-correlation function, $\sigma_{CCF,ij}$, is very low, such that $\sigma_0^2 \gg \sigma_{CCF,ij}^2$. When the minimum instrumental uncertainty is the dominant source of error, Equation 3.6 simplifies to $(V_{ij} - V_{*j}) \simeq \sigma_0$. We therefore estimated σ_0 for IMACS by calculating the standard deviation of the estimated errors $(V_{ij} - V_{*j})$ using just the 10% of repeat measurements with the highest R_{TD} values (N=64). Since the estimate of the true velocities, V_{*j}, depends on σ_0 (as per Equation 3.11) this had to be done iteratively. After several iterations, the calcula-

Table 3.5: Error Model Parameters

Instrument	$N_{Measurements}$	σ_0 (km s^{-1})	α (km s^{-1})	x
IMACS	641	11.6	945	1.85
Hectospec	1189	2.3	825	1.68

tion converged on a value of $\sigma_{0,\mathrm{IMACS}} = 11.6$ km s^{-1}. Using this value, the weights in Equation 3.11 were calculated, and the true velocity for every repeated object was estimated.

With all terms now known in the summation Expression 3.9, the free parameters $\{\alpha,x\}$ were estimated via a non-linear regression algorithm to be the values that minimized the sum. The IMACS repeat observations consisted of 641 unique measurements of 284 different objects. Using this data set, the best estimates of the values of $\{\alpha,x\}$ for IMACS were $\{945$ km s^{-1},1.85$\}$. This information is summarized in Table 3.5.

Figure 3.21 graphically depicts several key aspects of this velocity uncertainty estimation method for the IMACS data. The upper panel plots the data for the 641 repeated observation in the $\log[(V_{ij}-V_{*j})^2]$ versus R_{TD} plane (see Equation 3.8). The best-fit curve, determined from the optimal values of the free parameters $\{\alpha,x\}$, is overplotted. The middle panel shows the estimated errors, $V_{ij} - V_{*j}$, as a function of R_{TD}. As expected, it has a fan-shaped distribution that broadens at low R_{TD} values, where measurement uncertainties are dominated by the noise in the cross-correlation function, σ_{CCF}, and narrows at high R_{TD} values, where the measurement uncertainties are dominated by the minimum instrumental uncertainty, σ_0.

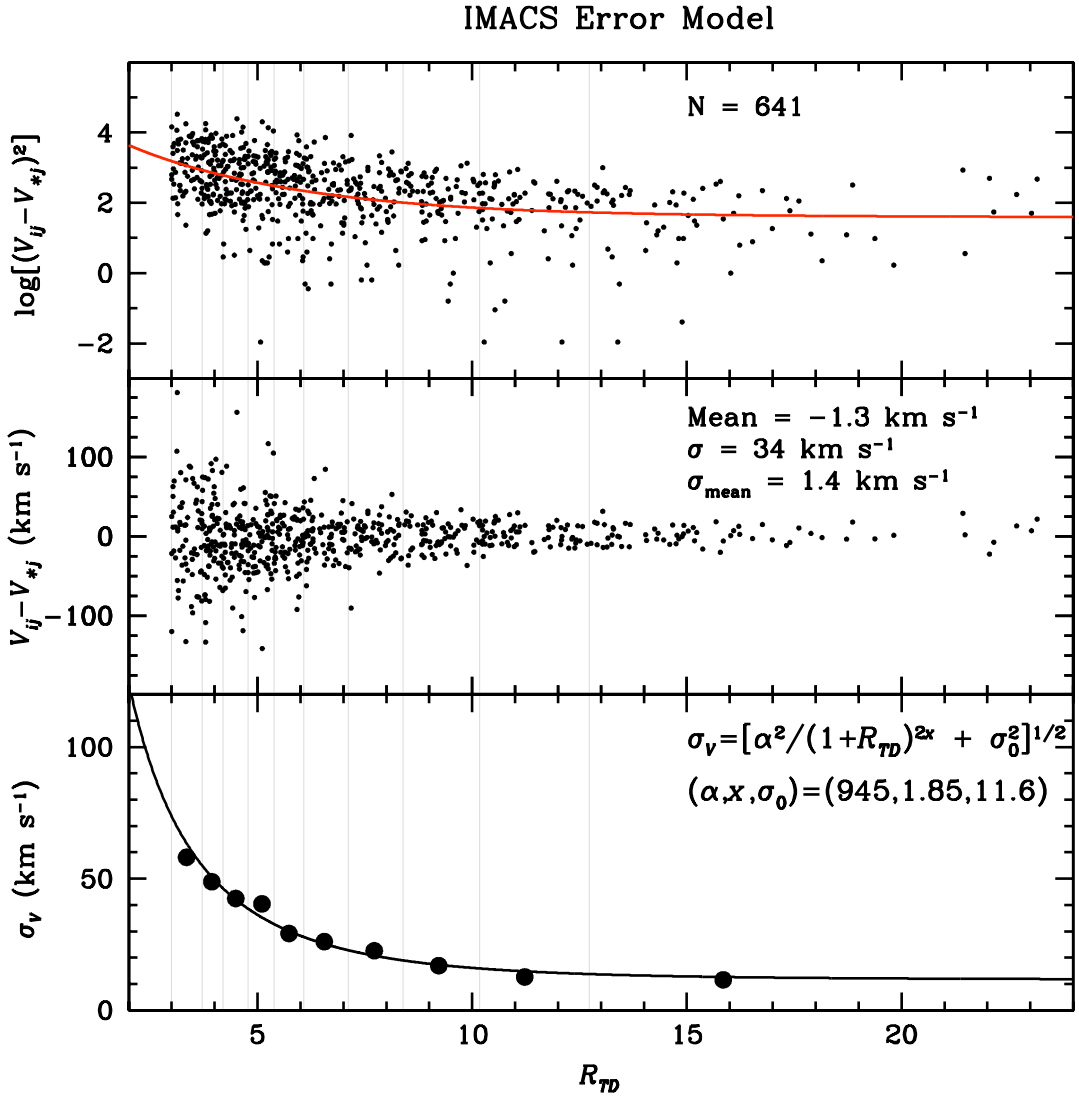

Figure 3.21: IMACS error model. The upper panel plots the data for the 641 repeated observation in the $\log[(V_{ij} - V_{*j})^2]$ versus R_{TD} plane (see Equation 3.8). The best-fit curve, determined from the optimal values of the free parameters $\{\alpha,x\}$, is overplotted. The middle panel shows the estimated errors, $V_{ij} - V_{*j}$, as a function of R_{TD}. Relevant statistics are also provided. The bottom panel shows the functional relationship between the estimated velocity uncertainty, σ_V, and the R_{TD} values. Spanning across all three panels are vertical lines that divide the 641 data points by their R_{TD} values in to ten bins of nearly equal number. In the bottom panel, a data point is placed in each bin that has as its coordinates the average R_{TD} value of all the data points within the bin (as seen in the upper panels), and the standard deviation of their $V_{ij} - V_{*j}$ values (as plotted in the middle panel). The data in the last bin, with $R_{TD} > 12.73$, represents the 10% of repeat measurements with the highest R_{TD} values, which were used to estimate the minimum instrumental uncertainty of IMACS, $\sigma_0 = 11.6$ km s^{-1}. A more thorough discussion of this figure is given in the text.

The bottom panel of Figure 3.21 shows the functional relationship between the estimated velocity uncertainty, σ_V, and the R_{TD} values. This relationship can be expressed mathematically as:

$$\sigma_V = \left[\left(\frac{\alpha}{(1 + R_{TD})^x} \right)^2 + \sigma_0^2 \right]^{1/2} . \tag{3.12}$$

Since α, x, and σ_0 are known, this equation allows for the estimation of the velocity measurement uncertainty of any IMACS spectrum given only its R_{TD} value as determined from its cross-correlation function. Spanning across all three panels in Figure 3.21 are vertical lines that divide the 641 data points by their R_{TD} values in to ten bins of nearly equal number. In the bottom panel, a data point is placed in each bin that has as its coordinates the average R_{TD} value of all the data points within the bin (as seen in the upper panels), and the standard deviation of their $V_{ij} - V_{*j}$ values (as plotted in the middle panel). The data in the last bin, with $R_{TD} > 12.73$, represents the 10% of repeat measurements with the highest R_{TD} values. This bin was used to estimate that the minimum instrumental uncertainty of IMACS, σ_0, had a value of 11.6 km s^{-1}. The fact that all ten points lie on, or near to, the $\sigma_V(R_{TD})$ curve provides further assurance of the accuracy of the adopted error model.

3.3.1.2 Hectospec Error Model

Unlike IMACS, the Hectospec data set lacked any repeat observations. Therefore, individual spectroscopic exposures were used to develop the error model for the Hectospec observations. As with IMACS, it was defined by assessing how multiple ve-

Table 3.6: Hectospec Error Analysis Data Set

Field	$N_{Exposures}$	$N_{Targets}$	N_{RVs}	N_5[a]	N_3[a]	N_{Total}
207.1p00.2	3	206	173	0	173	519
215.1p00.8	5	182	134	134	0	670
Total	8	388	307	134	173	1189

[a] N_5 and N_3 represent the number of targets with exactly five and three unique velocity measurements, respectively.

locity measurements of a single object differed from their estimated true velocities as a function of the R_{TD} value. Since the R_{TD} values for the spectra in a given field improve with increasing exposure time, we chose to perform the error analysis using two fields that spanned the maximum range of exposure times: field 207.1p00.2 had the longest exposure times (3×3000 s), and field 215.1p00.8 was one of the fields with the shortest exposure times (5×1800 s). This choice provided a sufficient number of data points at both high and low R_{TD} values to adequately calibrate the error model across the full range of R_{TD}.

Field 207.1p00.2 contained 206 targets, 173 of which produced reliable radial velocities (See Table 3.3). Since a total of three exposures were taken, field 207.1p00.2 provided 519 individual velocity measurements from its 173 unique targets that were used in this analysis. Field 215.1p00.8 contained 182 targets, 139 of which produced reliable radial velocities. However, an additional five of these 139 objects had to be rejected because their individual exposures yielded unacceptable velocity measurements. Since a total of five exposures were taken, field 215.1p00.8 provided 670 individual velocity measurements from its 134 different objects. Combined, these two fields provided 1189 unique velocity measurements from 307 different targets. These numbers are summarized in Table 3.6.

A few IRAF reduction steps were necessary to prepare the individual exposures to be cross-correlated with the `fxcor` task. First, the `imarith` task was used to subtract the averaged sky spectra (which were prepared as described in Section 3.2.3) from the wavelength-calibrated individual-exposure spectra. The spectra were then trimmed, as before, to have a common wavelength range of 3694–6037 Å. Finally, to remove cosmic rays from the individual-exposure spectra, they were first divided by their exposure-combined spectrum using the `imarith` task. Then, pixel values that deviated greatly from unity were replaced with a value of one using the `imreplace` task. The final step was to then multiply the individual-exposure spectra by their exposure-combined spectrum using the `imarith` task again. This three step procedure to remove the cosmic rays (i.e. divide by the combined spectrum, replace deviant pixels values with a value of one, then multiply by the combined spectrum) effectively replaced the cosmic rays in the individual-exposure spectra with the flux values (at those problem wavelengths) from the exposure-combined spectra. Once the cosmic rays were removed, the individual-exposure spectra were cross-correlated with `fxcor` as before.

The error model we applied to the Hectospec data is identical to the IMACS error model, with one small difference. Rather than using the weighted mean velocity, $\overline{V}_{*j}$, as the best estimate of an object's true velocity, V_{*j}, we instead adopted the velocity measured from each object's exposure-combined spectrum as its estimated true velocity. This velocity is more likely to provide the most accurate measure of an object's true velocity.

As with IMACS, we estimated the value of the minimum instrumental uncertainty, σ_0, of Hectospec by calculating the standard deviation of the estimated errors $(V_{ij} - V_{*j})$ using just the 10% of velocity measurements with the highest R_{TD} values (N=119). This calculation produced a value of $\sigma_{0,\mathrm{Hectospec}} = 2.3$ km s^{-1}.

With all terms now known in the summation Expression 3.9, the free parameters $\{\alpha,x\}$ were estimated via a non-linear regression algorithm to be the values that minimized the sum. In total, 1189 unique measurements of 307 different objects were used for the Hectospec error analysis. Using this data set, the best estimates of the values of $\{\alpha,x\}$ for Hectospec were $\{825$ km s^{-1},1.68$\}$. This information is summarized in Table 3.5.

Figure 3.22 graphically depicts several key aspects of this velocity uncertainty estimation method for the Hectospec data. The upper panel plots the data for the 1189 unique velocity measurements in the $\log[(V_{ij} - V_{*j})^2]$ versus R_{TD} plane (see Equation 3.8). The data points from fields 207.1p00.2 (N= 519) and 215.1p00.8 (N=670) are shown in different colors. The best-fit curves, determined from the optimal values of the free parameters $\{\alpha,x\}$, are overplotted in black for the combined data, and in matching colors for the two individual fields. The middle panel shows the estimated errors, $V_{ij} - V_{*j}$, as a function of R_{TD}. As expected, it has a fan-shaped distribution that broadens at low R_{TD} values, where measurement uncertainties are dominated by the noise in the cross-correlation function, σ_{CCF}, and narrows at high R_{TD} values, where the measurement uncertainties are dominated by the minimum instrumental uncertainty, σ_0. The data points from field 207.1p00.2 (shown in red)

are located preferentially at high R_{TD} values due to the long (3000 s) exposure times, while the data points from field 215.1p00.8 (shown in blue) are located preferentially at low R_{TD} values due to the relatively short (1800 s) exposure times.

The bottom panel of Figure 3.22 shows the functional relationship (as expressed in Equation 3.12) between the estimated velocity uncertainty, σ_V, and the R_{TD} values. In addition, the $\sigma_V(R_{TD})$ curve from the combined data set, and the curves from the two individual fields are shown for comparison purposes as well. Since α, x, and σ_0 are known, Equation 3.12 allows for the estimation of the velocity measurement uncertainty of any Hectospec spectrum given only its R_{TD} value as determined from its cross-correlation function. Spanning across all three panels in Figure 3.22 are vertical lines that divide the 1189 data points by their R_{TD} values in to ten bins of nearly equal number. In the bottom panel, a data point is placed in each bin that has as its coordinates the average R_{TD} value of all the data points within the bin (as seen in the upper panels), and the standard deviation of their $V_{ij} - V_{*j}$ values (as plotted in the middle panel). The data in the last bin, with $R_{TD} > 32.9$, represents the 10% of unique, individual-exposure, velocity measurements with the highest R_{TD} values. This bin was used to estimate that the minimum instrumental uncertainty of Hectospec, σ_0, had a value of 2.3 km s^{-1}. Due to a small number of measurements with unusually large $|V_{ij} - V_{*j}|$ values, some which fall beyond the [-200 km s^{-1},200 km s^{-1}] limits of the middle panel plot, we exclude the five most deviant of the 119 points in each bin from the standard deviation calculation. These ten data points are seen to be in very good agreement with the combined $\sigma_V(R_{TD})$ curve in the bottom

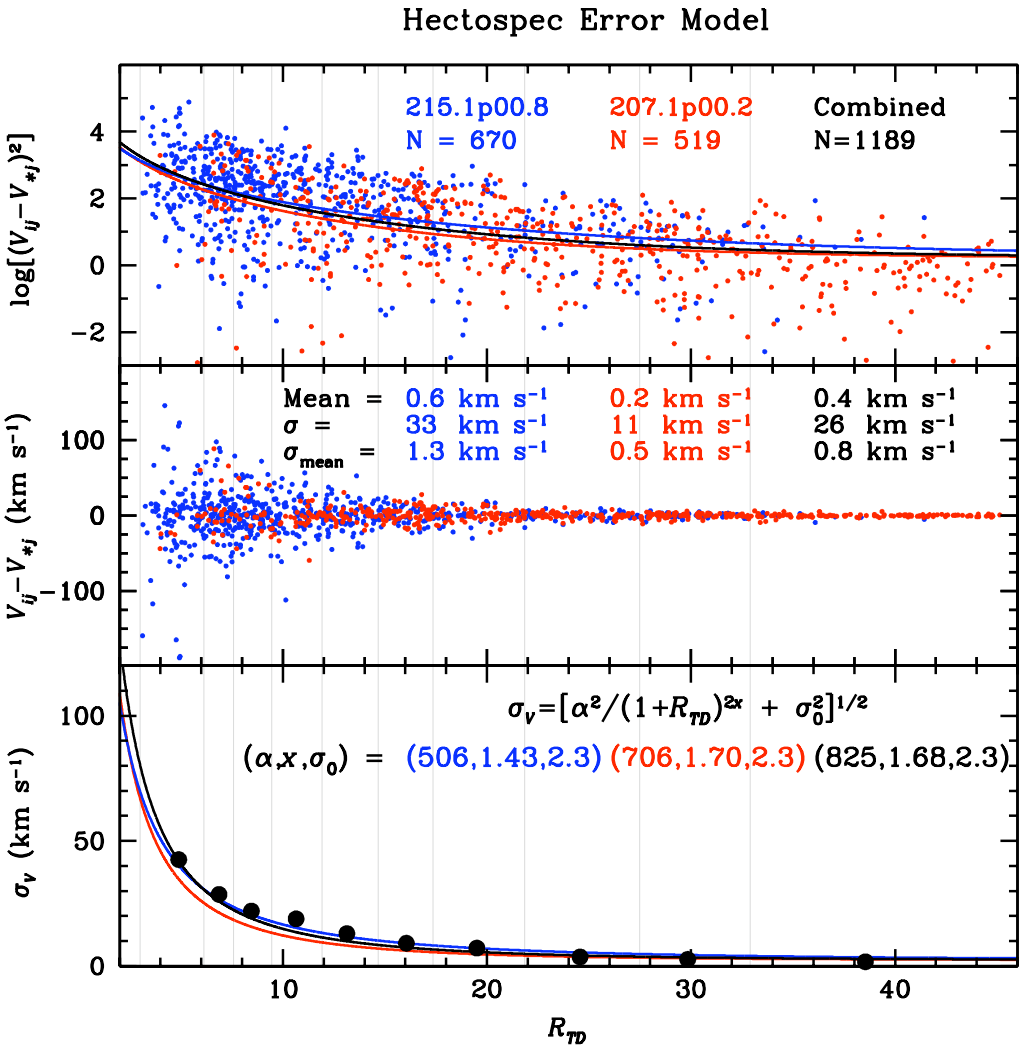

Figure 3.22: Hectospec error model. The upper panel plots the 1189 unique velocity measurements in the $\log[(V_{ij} - V_{*j})^2]$ versus R_{TD} plane (see Equation 3.8). The data points from fields 207.1p00.2 (N= 519) and 215.1p00.8 (N=670) are shown in red and blue, respectively. The best-fit curves, determined from the optimal values of the free parameters $\{\alpha,x\}$, are overplotted in matching colors for the three samples. The middle panel shows the estimated errors, $V_{ij} - V_{*j}$, as a function of R_{TD}. The long-expsoure 207.1p00.2 (red) data points and the short-expsoure 215.1p00.8 (blue) points are located preferentially at high and low R_{TD} values, respectively. Relevant statistics for each sample are provided. The bottom panel shows the functional relationship between the estimated velocity uncertainty, σ_V, and the R_{TD} values for the three samples. Vertical lines span across all three panels, dividing the 1189 data points by their R_{TD} values in to ten bins of nearly equal number. In the bottom panel, a black data point is placed in each bin that has as its coordinates the average R_{TD} value of all the data points within the bin (as seen in the upper panels), and the standard deviation of their $V_{ij} - V_{*j}$ values (as plotted in the middle panel). Due to a small number of measurements with unusually large $|V_{ij} - V_{*j}|$ values, we exclude the five most deviant of the 119 points in each bin from the standard deviation calculation. A more thorough discussion of this figure is given in the text.

panel. Fortunately, a small number of highly-discrepant velocity measurements are unable to exert a disproportionate influence on the parameterized error model, further bolstering our confidence in the accuracy and robustness of the adopted model.

3.3.2 Repeat Observations

Section 3.3.1 utilized the multiple velocity measurements of both IMACS and Hectospec targets to constrain the parameters of an error model that defines a functional relationship between the easily measured R_{TD} value of a spectrum, and its estimated velocity uncertainty. This analysis relied on velocity measurements from the many cases of repeat IMACS observations, and from individual Hectospec exposures. It is worth while to take a closer look at this data to gain a clearer picture of the reliability of our velocity measurements. Throughout this section we provide numerous plots and related statistics to aid in this effort.

All of the figures presented in this section take the form of $V_{ij} - V_{*j}$ histograms. The quantity $V_{ij} - V_{*j}$ measures the difference between each individual velocity measurement (from unique observations for IMACS, and individual exposures for Hectospec), V_{ij}, and the object's estimated true velocity, V_{*j}. As explained in Section 3.3, for the IMACS spectra, an object's true velocity is estimated as the weighted mean of the repeated individual measurements. For the Hectospec data, the true velocity is estimated as the velocity measured from each object's exposure-combined spectrum.

In Figures 3.23 (for IMACS) and 3.24 (for Hectospec), the $V_{ij} - V_{*j}$ distributions are shown for each instrument's entire set of multiply-measured object velocities. These two figures also contain five additional panels that show these parent

distributions separated in to five quintiles based on the R_{TD} values of their measurements. These same quintiles can also be seen in the instrumental error model plots of Section 3.3 (Figures 3.21 and 3.22, where technically deciles are shown). Standard statistics, including the number of objects, the mean, the standard deviation, and the standard deviation of the mean, are given in every panel, and are collated in Tables 3.7 (for IMACS) and 3.8 (for Hectospec). As expected, for both instruments, the standard deviations decrease rapidly from the first to the fifth quintile. While the standard deviations in the first quintiles are nearly the same for the two instruments (50.7 km s^{-1} for Hectospec compared to 53.5 km $s^{-1}$for IMACS), the Hectospec distributions are seen to have dramatically lower dispersions in every other quintile. This is because the Hectospec set contains many more high-R_{TD} value observations than the IMACS set, a fact which can also be seen in Figures 3.21 and 3.22.

In Figures 3.25 and 3.26 the same $V_{ij} - V_{*j}$ distributions are shown for each instrument's entire set of multiply-measured object velocities, but this time the additional panels are used to separate these parent distributions in to their individual, constituent fields. The IMACS repeat data set consists of three fields: 000.0n01.6 and 010.1n03.2, which were each observed twice, and 359.9n01.5 which was observed three times (see Table 3.4). The Hectospec set consists of three 3000-second exposures of field 207.1p00.2, and five 1800-second exposures of field 215.1p00.8 (see Table 3.6). Within the individual field panels, the $V_{ij} - V_{*j}$ distributions are also shown for the subset of stars that have R_{TD} values greater than the median R_{TD} value. As before, the same standard statistics are given for every distribution, and are collated

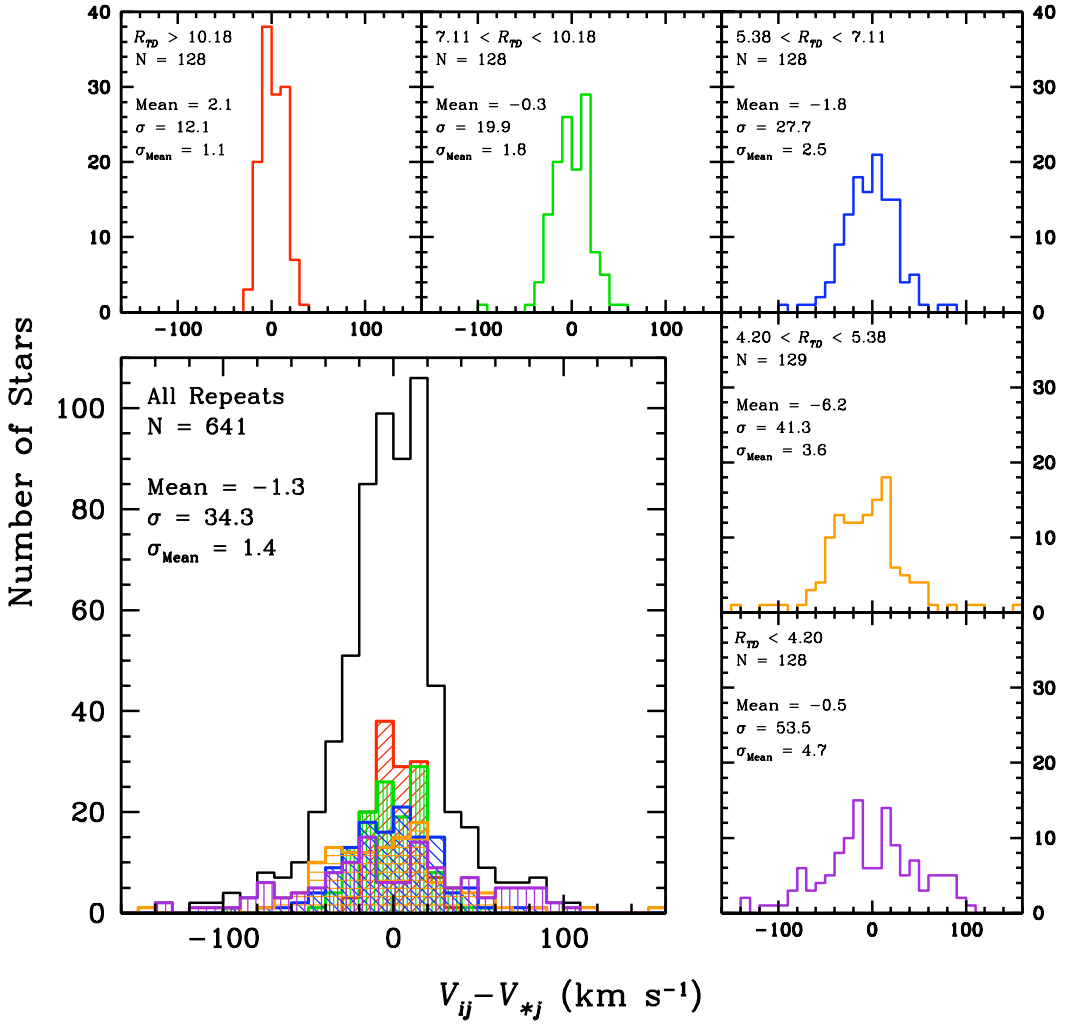

Figure 3.23: IMACS $V_{ij}-V_{*j}$ distributions: R_{TD} quintiles. The lower left panel shows the $V_{ij}-V_{*j}$ distribution of the entire set of IMACS objects with multiple independent velocity measurements. The five smaller panels show this parent distribution separated in to five quintiles based on the R_{TD} values of their measurements. These five distributions are also overplotted, in matching colors, in the lower left panel. Standard statistics, including the number of objects, the mean, the standard deviation, and the standard deviation of the mean, are given in every panel, and are collated in Table 3.7.

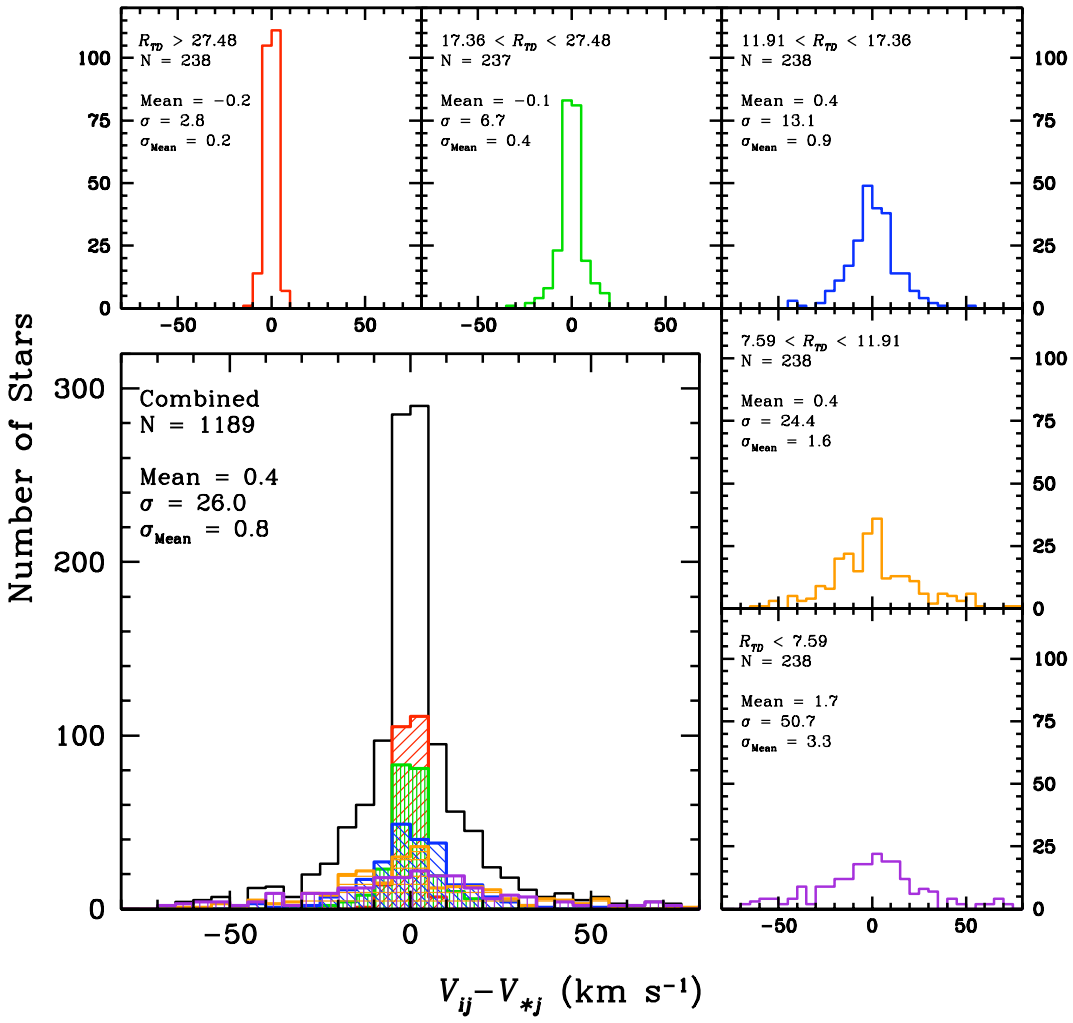

Figure 3.24: Hectospec $V_{ij} - V_{*j}$ distributions: R_{TD} quintiles. The lower left panel shows the $V_{ij} - V_{*j}$ distribution drawn from the full set of velocity measurements from individual Hectospec exposures. The five smaller panels show this parent distribution separated in to five quintiles based on the R_{TD} values of their measurements. These five distributions are also overplotted, in matching colors, in the lower left panel. Standard statistics, including the number of objects, the mean, the standard deviation, and the standard deviation of the mean, are given in every panel, and are collated in Table 3.8.

Table 3.7: IMACS Repeat Error Statistics

Field	Sample	Figure(s)	N	Mean (km s^{-1})	σ (km s^{-1})	σ_{Mean} (km s^{-1})
Combined	All	3.23,3.25	641	–1.3	34.3	1.4
Combined	R_{TD} – 1^{st} Quintile	3.23	128	–0.5	53.5	4.7
Combined	R_{TD} – 2^{nd} Quintile	3.23	129	–6.2	41.3	3.6
Combined	R_{TD} – 3^{rd} Quintile	3.23	128	–1.8	27.7	2.5
Combined	R_{TD} – 4^{th} Quintile	3.23	128	–0.3	19.9	1.8
Combined	R_{TD} – 5^{th} Quintile	3.23	128	2.1	12.1	1.1
000.0n01.6	All	3.25,3.29	178	1.6	25.9	1.9
000.0n01.6	$R_{TD,1/2}$	3.25	89	–0.9	15.5	1.6
000.0n01.6	2007 Oct – All	3.29	89	–10.2	19.3	2.0
000.0n01.6	2007 Oct – $R_{TD,1/2}$	3.29	44	–8.2	15.4	2.3
000.0n01.6	2010 Apr – All	3.29	89	13.5	26.3	2.8
000.0n01.6	2010 Apr – $R_{TD,1/2}$	3.29	44	9.3	10.8	1.6
010.1n03.2	All	3.25,3.30	180	–3.6	34.4	2.6
010.1n03.2	$R_{TD,1/2}$	3.25	90	2.6	18.2	1.9
010.1n03.2	2006 Sep – All	3.30	90	15.2	27.2	2.9
010.1n03.2	2006 Sep – $R_{TD,1/2}$	3.30	45	9.4	9.4	1.4
010.1n03.2	2010 Apr – All	3.30	90	–22.4	30.4	3.2
010.1n03.2	2010 Apr – $R_{TD,1/2}$	3.30	45	–15.5	16.3	2.4
359.9n01.5	All	3.25,3.31	283	–1.8	38.7	2.3
359.9n01.5	$R_{TD,1/2}$	3.25	141	1.3	21.0	1.8
359.9n01.5	2007 May – All	3.31	102	–7.1	29.2	2.9
359.9n01.5	2007 May – $R_{TD,1/2}$	3.31	51	–4.7	13.9	2.0
359.9n01.5	2008 May – All	3.31	80	–28.6	37.1	4.1
359.9n01.5	2008 May – $R_{TD,1/2}$	3.31	40	–25.8	29.8	4.7
359.9n01.5	2010 Apr – All	3.31	101	24.8	30.7	3.1
359.9n01.5	2010 Apr – $R_{TD,1/2}$	3.31	50	19.2	14.3	2.0

Note: $R_{TD,1/2}$ refers to the set of objects whose R_{TD} values are greater than the median R_{TD} value.

Table 3.8: Hectospec Repeat Error Statistics

Field	Sample	Figure(s)	N	Mean (km s^{-1})	σ (km s^{-1})	σ_{Mean} (km s^{-1})
Combined	All	3.24,3.26	1189	0.4	26.0	0.8
Combined	R_{TD} – 1^{st} Quintile	3.24	238	1.7	50.7	3.3
Combined	R_{TD} – 2^{nd} Quintile	3.24	238	0.4	24.4	1.6
Combined	R_{TD} – 3^{rd} Quintile	3.24	238	0.4	13.1	0.9
Combined	R_{TD} – 4^{th} Quintile	3.24	237	–0.1	6.7	0.4
Combined	R_{TD} – 5^{th} Quintile	3.24	238	–0.2	2.8	0.2
207.1p00.2	All	3.26,3.27	519	0.2	11.0	0.5
207.1p00.2	$R_{TD,1/2}$	3.26	259	–0.1	2.9	0.2
207.1p00.2	Exposure 1 – All	3.27	173	0.3	11.4	0.9
207.1p00.2	Exposure 1 – $R_{TD,1/2}$	3.27	86	–0.1	3.1	0.3
207.1p00.2	Exposure 2 – All	3.27	173	1.4	11.3	0.9
207.1p00.2	Exposure 2 – $R_{TD,1/2}$	3.27	86	–0.1	2.7	0.3
207.1p00.2	Exposure 3 – All	3.27	173	–1.3	10.3	0.8
207.1p00.2	Exposure 3 – $R_{TD,1/2}$	3.27	86	–0.2	3.0	0.3
215.1p00.8	All	3.26,3.28	670	0.6	33.3	1.3
215.1p00.8	$R_{TD,1/2}$	3.26	335	–0.3	15.2	0.8
215.1p00.8	Exposure 1 – All	3.28	134	–4.0	19.7	1.7
215.1p00.8	Exposure 1 – $R_{TD,1/2}$	3.28	67	–4.8	10.9	1.3
215.1p00.8	Exposure 2 – All	3.28	134	2.9	29.2	2.5
215.1p00.8	Exposure 2 – $R_{TD,1/2}$	3.28	67	–2.6	13.3	1.6
215.1p00.8	Exposure 3 – All	3.28	134	1.8	33.5	2.9
215.1p00.8	Exposure 3 – $R_{TD,1/2}$	3.28	67	0.0	15.6	1.9
215.1p00.8	Exposure 4 – All	3.28	134	2.9	39.6	3.4
215.1p00.8	Exposure 4 – $R_{TD,1/2}$	3.28	67	2.5	15.0	1.8
215.1p00.8	Exposure 5 – All	3.28	134	–0.3	39.9	3.5
215.1p00.8	Exposure 5 – $R_{TD,1/2}$	3.28	67	3.2	21.6	2.6

Note: $R_{TD,1/2}$ refers to the set of objects whose R_{TD} values are greater than the median R_{TD} value.

in Tables 3.7 (for IMACS) and 3.8 (for Hectospec). The distributions of two of the IMACS fields (010.1n03.2 and 359.9n01.5) appear to show a dual-peak structure that hints at the possibility of a velocity offset between the multiple observations of the fields. The significance of this is fully explored in the following paragraph and in the next set of figures. The two Hectospec fields are seen to have standard deviations that differ greatly (by a factor of three if calculated from all measurements, and a factor of five if calculated only from those with R_{TD} values greater than the median). This is because of the large difference in exposure times for these fields (1800 seconds versus 3000 seconds). These two fields were chosen to perform the error analysis with specifically because their individual exposure times represented the two extremes for our data set.

Finally, we present a figure for each of the five aforementioned Sgr fields showing their $V_{ij}-V_{*j}$ distributions along with the distributions of their individual, constituent observations (exposures for Hectospec). For the Hectospec observations, Figures 3.27 and 3.28 show these plots for fields 207.1p00.2 and 215.1p00.8, respectively. For the IMACS observations, Figures 3.29, 3.30, and 3.31, show these plots for fields 000.0n01.6, 010.1n03.2, and 359.9n01.5, respectively. Within the individual observation/expsoure panels, the $V_{ij} - V_{*j}$ distributions are also shown for the subset of stars that have R_{TD} values greater than the median R_{TD} value. As before, the same standard statistics are given for every distribution, and are collated in Tables 3.7 (for IMACS) and 3.8 (for Hectospec).

The $V_{ij} - V_{*j}$ distributions of the three individual, long (3000 s) exposures of

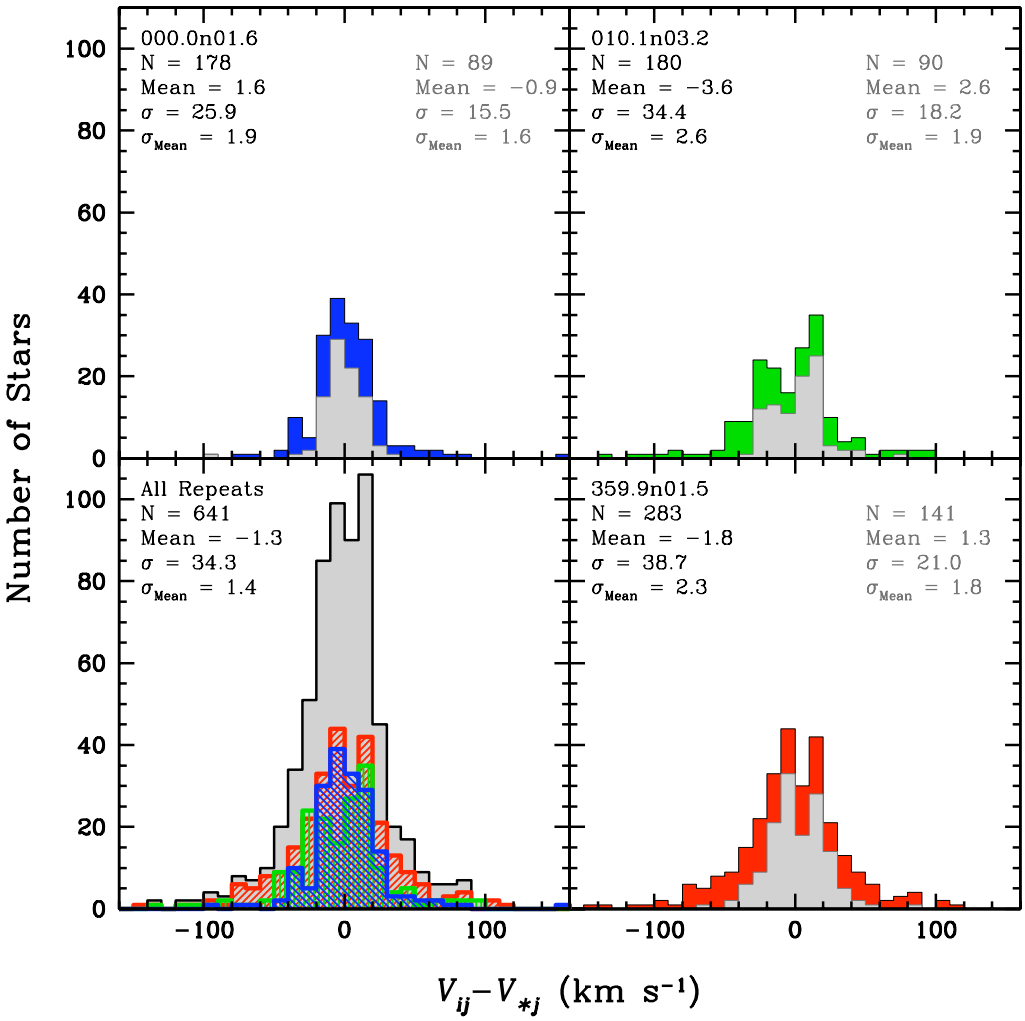

Figure 3.25: IMACS $V_{ij} - V_{*j}$ distributions: Individual Fields. The lower left panel shows the $V_{ij} - V_{*j}$ distribution of the entire set of IMACS objects with multiple independent velocity measurements. Also overplotted in this panel (in red, blue, and green) are the distributions of the three mutliply-observed IMACS fields. The other three panels show the distributions of these three individual fields (in matching colors) separately. Also shown in the three field panels (as grey histograms) are the distributions of the subset of stars that have R_{TD} values greater than the median R_{TD} value. Standard statistics, including the number of objects, the mean, the standard deviation, and the standard deviation of the mean, are provided for all distributions, and are collated in Table 3.7.

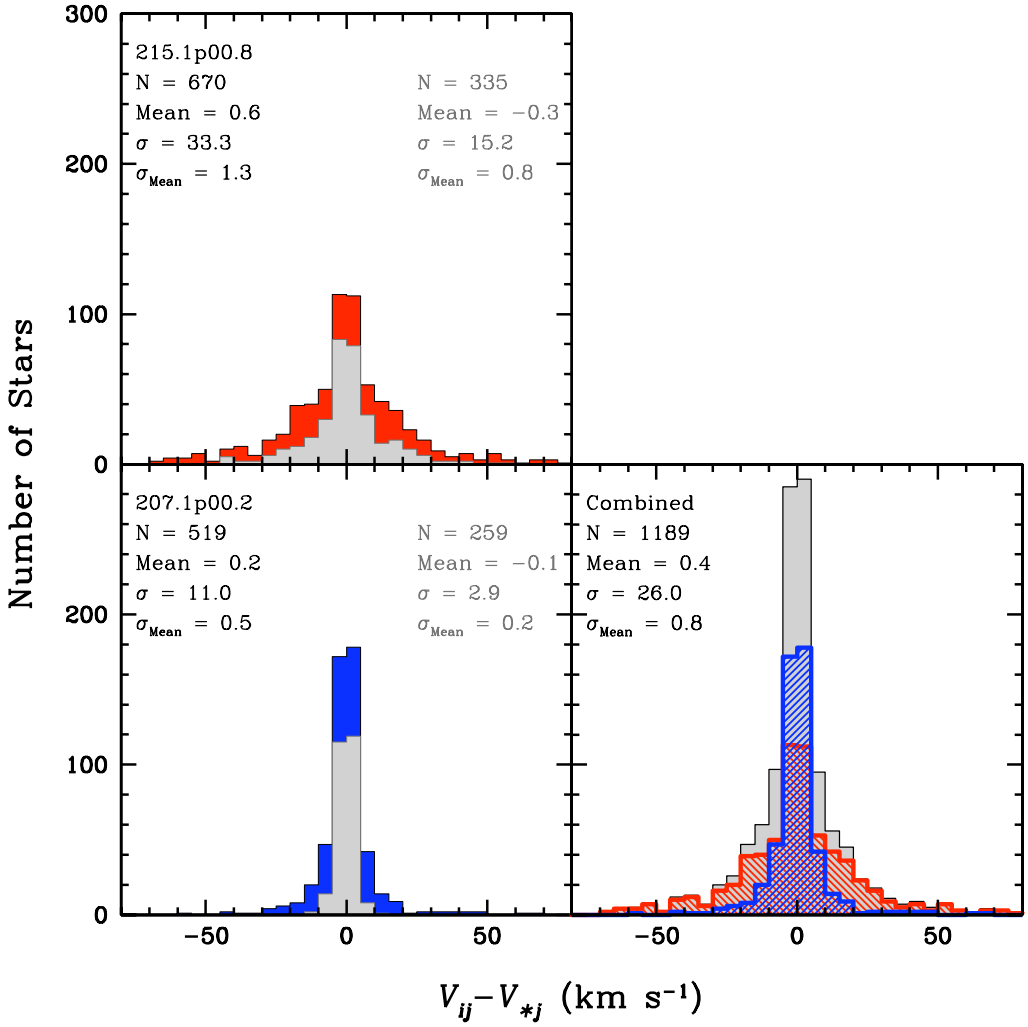

Figure 3.26: Hectospec $V_{ij} - V_{*j}$ distributions: Individual Fields. The lower right panel shows the $V_{ij} - V_{*j}$ distribution drawn from the full set of velocity measurements from individual Hectospec exposures. Also overplotted in this panel (in red and blue) are the distributions of the two individual fields. The other two panels show the distributions of these two individual fields (in matching colors) separately. Also shown in the two field panels (as grey histograms) are the distributions of the subset of stars that have R_{TD} values greater than the median R_{TD} value. Standard statistics, including the number of objects, the mean, the standard deviation, and the standard deviation of the mean, are provided for all distributions, and are collated in Table 3.8.

Hectospec field 207.1p00.2 (Figure 3.27) have remarkably consistent mean values and standard deviations. The distributions of the five individual, short (1800 s) exposures of Hectospec field 215.1p00.8 (Figure 3.28) also have fairly consistent mean values, indicating that no significant velocity offsets exist between the exposures. However, the standard deviations of the distributions generally increase from one exposure to the next. The reason for this is unknown. It may be due to worsening atmospheric observing conditions, but since these observations were obtained by other observers in the Hectospec queue, we can not be sure. Even at its worst, the distribution seen in exposure 5, though inflated by a small number of objects with highly discrepant $V_{ij} - V_{*j}$ values, still has a fairly reasonable standard deviation of $\sim$40 km s^{-1}.

Each of the three IMACS fields, however, show clear signs of velocity offsets between their individual observations, as alluded to earlier. First consider field 000.0n01.6 (Figure 3.29), which is the best of the three. The two observations of this field have $V_{ij} - V_{*j}$ distributions with mean values of –8.2 and 9.3 km s^{-1} (calculated using the more accurate high-R_{TD} subset). Likewise, the two observations of field 010.1n03.2 (Figure 3.30) have $V_{ij} - V_{*j}$ distributions with mean values of 9.4 and –15.5 km s^{-1}. Finally, the three observations of field 359.9n01.5 (Figure 3.31) have $V_{ij} - V_{*j}$ distributions with mean values of –4.7, –25.8, and 19.2 km s^{-1}. It is worth noting that the middle of these three observations, which is clearly the worst of the three, was limited to only three fourths of the total exposure time as all other repeated IMACS fields (see Table 3.2). If this one observation was excluded, the other two observations of field 359.9n01.5, which have nearly identical dispersions, would

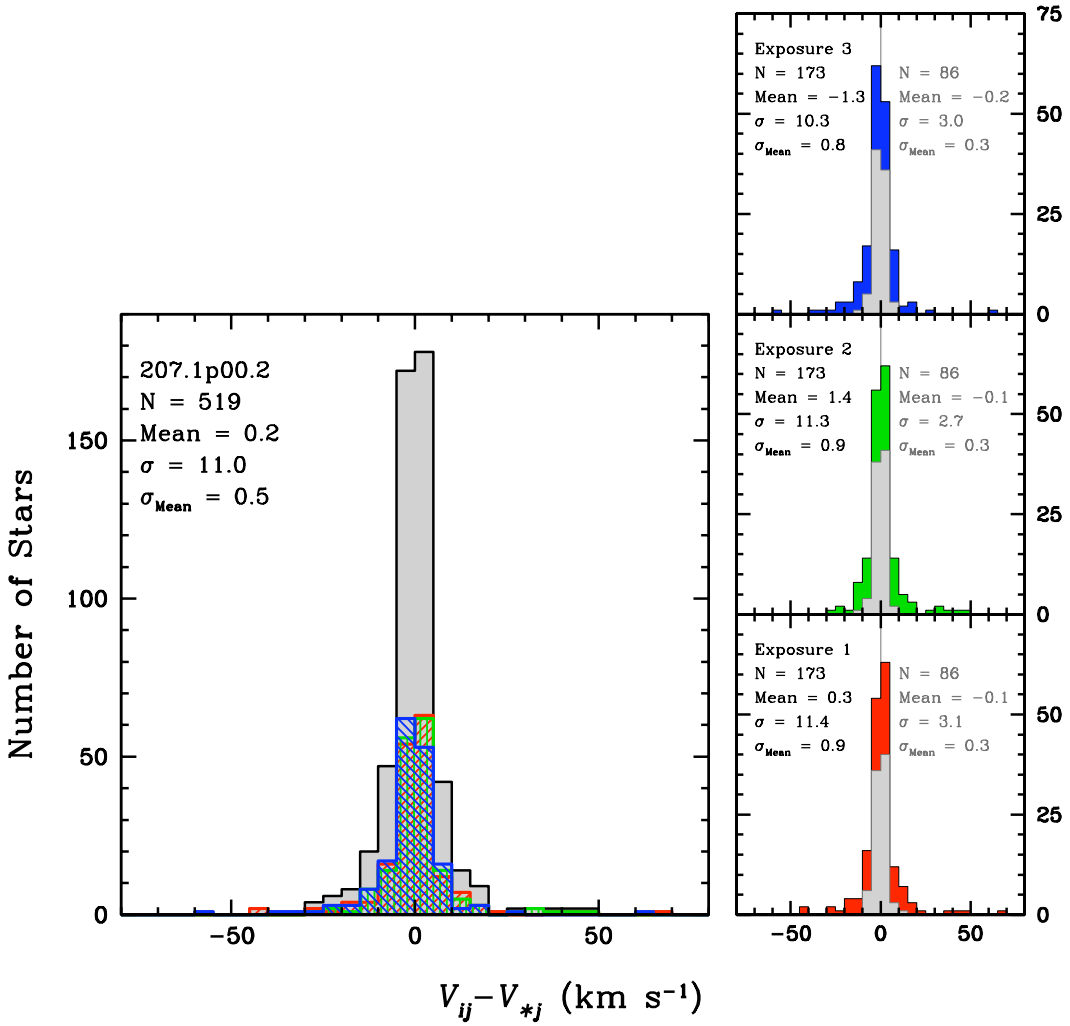

Figure 3.27: Hectospec $V_{ij} - V_{*j}$ distributions: Field 207.1p00.2. The left panel shows the combined $V_{ij} - V_{*j}$ distribution of all velocity measurements from the three individual exposures of field 207.1p00.2. Also overplotted in this panel (in red, blue, and green) are the distributions of those three individual exposures. The three smaller panels show, in matching colors, the distributions of those three individual exposures separately. The integrations times for these individual exposures (3000 s) were the longest of any in our Hectospec data set (see Table 3.3). Also shown in the three individual exposure panels (as grey histograms) are the distributions of the subset of stars that have R_{TD} values greater than the median R_{TD} value. Standard statistics, including the number of objects, the mean, the standard deviation, and the standard deviation of the mean, are provided for all distributions, and are collated in Table 3.8.

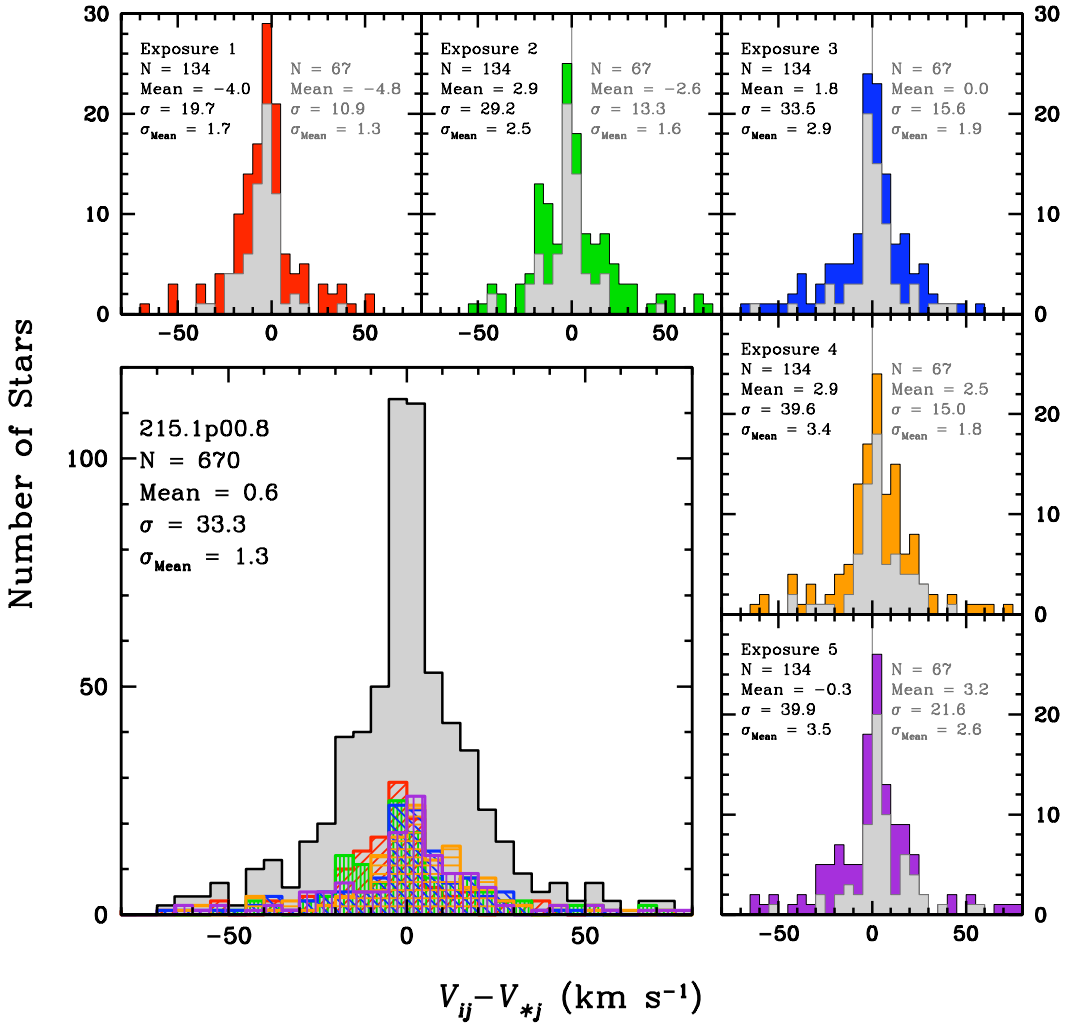

Figure 3.28: Hectospec $V_{ij} - V_{*j}$ distributions: Field 215.1p00.8. The lower left panel shows the combined $V_{ij} - V_{*j}$ distribution of all velocity measurements from the five individual exposures of field 207.1p00.2. Also, overplotted in this panel (in various colors) are the distributions of those five individual exposures. The five smaller panels show, in matching colors, the distributions of those five individual exposures separately. The integrations times for these individual exposures (1800 s) were equal to the shortest of any in our Hectospec data set (see Table 3.3). Also shown in the five individual exposure panels (as grey histograms) are the distributions of the subset of stars that have R_{TD} values greater than the median R_{TD} value. Standard statistics, including the number of objects, the mean, the standard deviation, and the standard deviation of the mean, are provided for all distributions, and are collated in Table 3.8.

show offsets of –13.1 and 12.3 km s^{-1}. From this, we can conclude that the velocity distributions resulting from any individual IMACS observation are likely to suffer from a zero-point offset relative to the object's true velocities of $\sim 8 - 16$ km s^{-1}.

To some extent, the added velocity measurement uncertainty resulting from the presence of these zero-point offsets is taken in to account by the adopted IMACS error model, discussed in Section 3.3.1. Since these offsets are present in the data used to calibrate the error model, they had the effect of artificially increasing in magnitude the values of $V_{ij} - V_{*j}$ (as plotted in the top and middle panels of Figure 3.21). This then, as a consequence, had the effect of inflating the functional relationship between R_{TD} and σ_V (as plotted in the bottom panel of Figure 3.21), so that, for a give R_{TD} value, the corresponding velocity measurement uncertainty, σ_V, is necessarily higher.

A great deal of effort was spent trying to determine the source of these zero-point offsets, so that they could be corrected for. No errors could be found with the Fourier cross-correlation method used to measured the velocities (such as incorrect header information for the object or template spectra, for example).

We also attempted to use sky features to correct for the offsets. The IMACS reduction process previously executed (see Section 3.1.3) subtracted the background sky from each spectrum, and then discarded it. Since the background sky spectra would be needed to assess the offsets, it was necessary to reduce the spectroscopic images from the repeated fields again. This required skipping over the COSMOS task `subsky`, which, as the name implies, performs a background subtraction of each slit. After that, the `extract-2dspec` task was executed, as before, to extract each

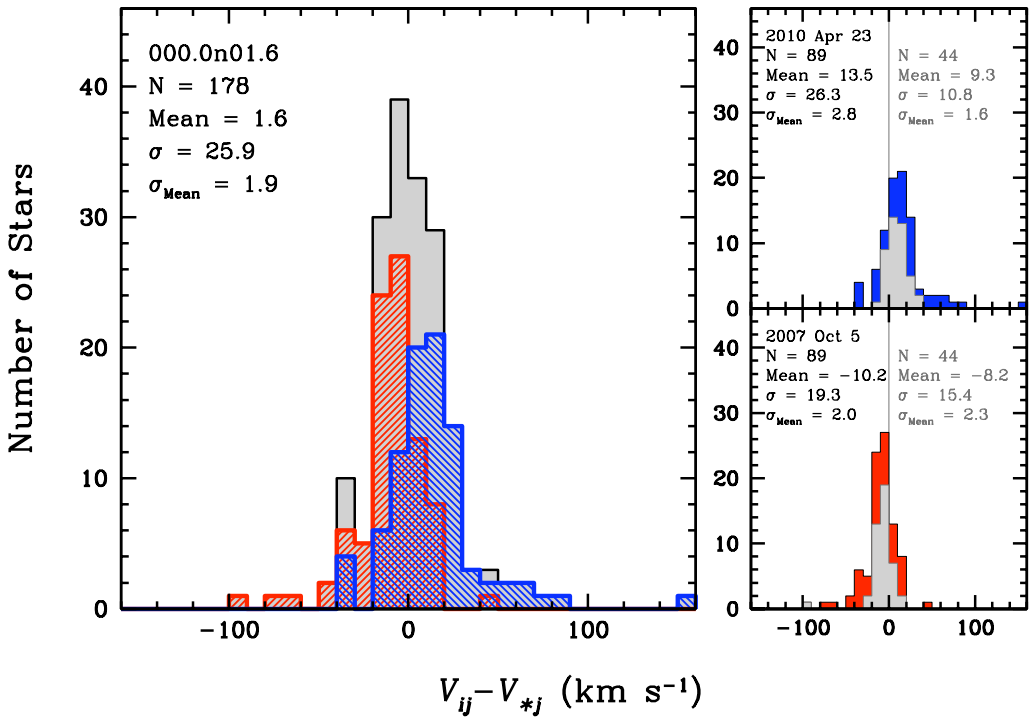

Figure 3.29: IMACS $V_{ij} - V_{*j}$ distributions: Field 000.0n01.6. The left panel shows the $V_{ij} - V_{*j}$ distribution (in grey) of the combined velocity measurements from both independent observations of field 000.0n01.6. Also overplotted in this panel (in red and blue) are the distributions of those two independent observations. The two smaller panels on the right also show the distributions of the two independent observations, in matching colors, along with the distributions (in grey) of the subset of stars that have R_{TD} values greater than the median R_{TD} value. Standard statistics, including the number of objects, the mean, the standard deviation, and the standard deviation of the mean, are provided for all distributions, and are collated in Table 3.7.

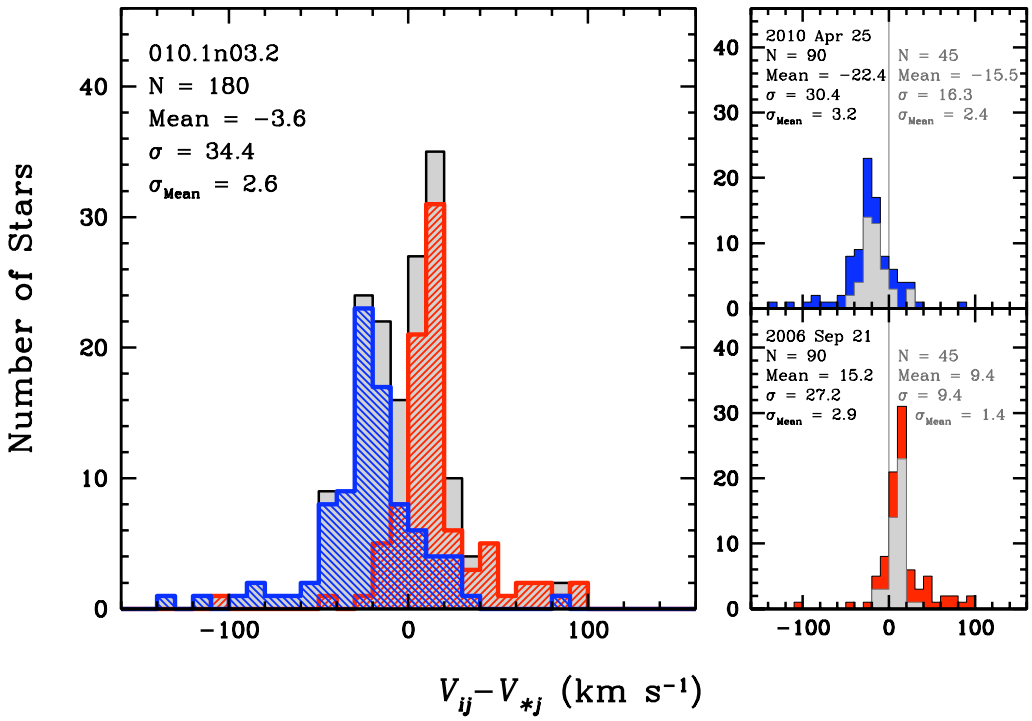

Figure 3.30: IMACS $V_{ij} - V_{*j}$ distributions: Field 010.1n03.2. The left panel shows the $V_{ij} - V_{*j}$ distribution (in grey) of the combined velocity measurements from both independent observations of field 010.1n03.2. Also overplotted in this panel (in red and blue) are the distributions of those two independent observations. The two smaller panels on the right also show the distributions of the two independent observations, in matching colors, along with the distributions (in grey) of the subset of stars that have R_{TD} values greater than the median R_{TD} value. Standard statistics, including the number of objects, the mean, the standard deviation, and the standard deviation of the mean, are provided for all distributions, and are collated in Table 3.7.

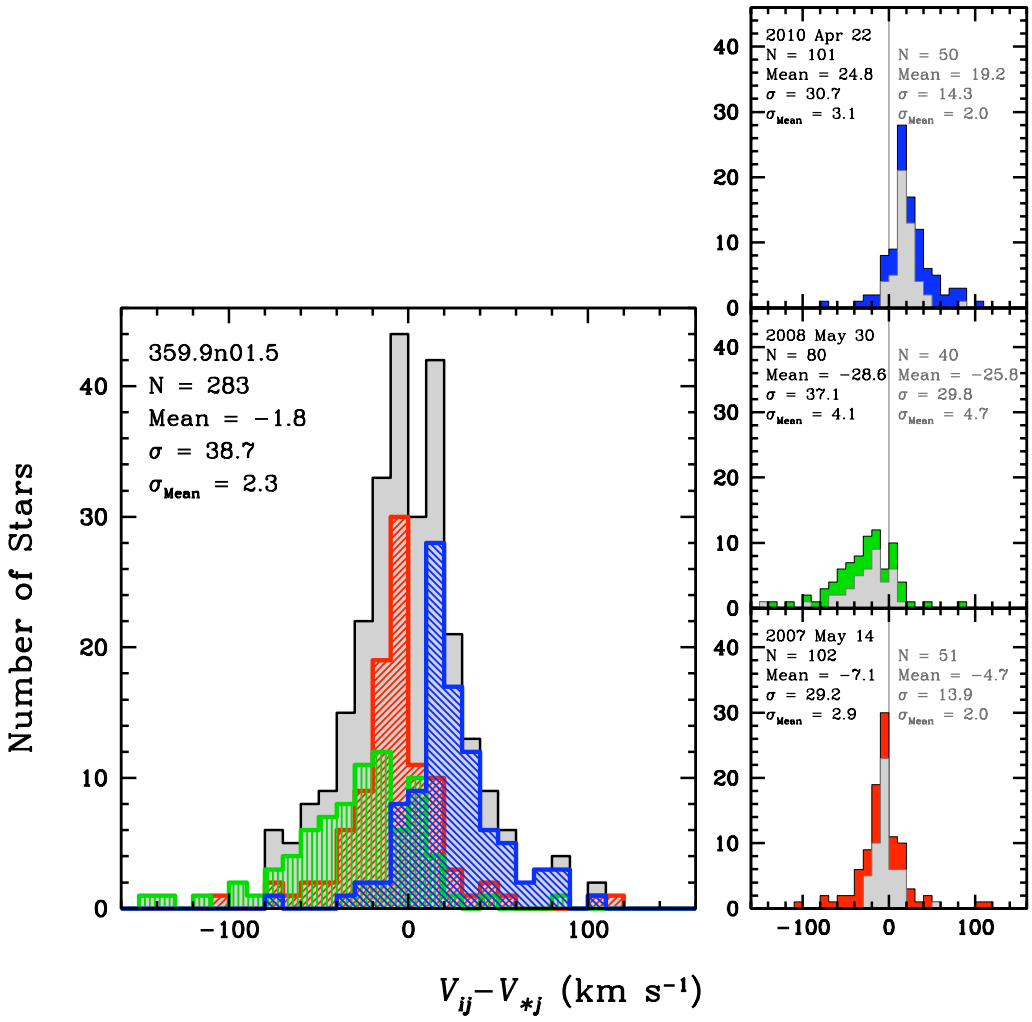

Figure 3.31: IMACS $V_{ij} - V_{*j}$ distributions: Field 359.9n01.5. The left panel shows the $V_{ij} - V_{*j}$ distribution (in grey) of the combined velocity measurements from the three independent observations of field 359.9n01.5. Also overplotted in this panel (in red, blue, and green) are the distributions of those three independent observations. The three smaller panels on the right also show the distributions of the three independent observations, in matching colors, along with the distributions (in grey) of the subset of stars that have R_{TD} values greater than the median R_{TD} value. It is worth noting that the middle of these three observations (shown in green), which is clearly the worst of the three, was limited to only three fourths of the total exposure time as all other repeated IMACS fields (see Table 3.2). Standard statistics, including the number of objects, the mean, the standard deviation, and the standard deviation of the mean, are provided for all distributions, and are collated in Table 3.7.

individual spectrum onto a two-dimensional array of wavelength and slit position. The COSMOS task `sumspec` was then skipped over, as it requires background subtracted spectra to function optimally. Instead, the IRAF task `scombine` was used to average the individual exposures for each spectrum using the `ccdclip` algorithm for cosmic ray rejection. Next, the IRAF task `apall` was used to produce one-dimensional, wavelength-calibrated sky and object spectra from each input spectrum. Finally, the `scombine` task was used once more to sum all of the individual sky spectra in to a single sky spectrum for each field.

We first tried to use the night sky emission line due to OI at 5577.35 Å to assess the velocity offsets. If a uniform velocity zero-point error is affecting all of the objects from a given field, one would expect the observed wavelength of this bright night sky emission line to be offset by an equal amount from its expected wavelength. The IRAF task `splot` was used to measure the observed wavelength of the OI line as the center of a Gaussian fit to the line's profile. Unfortunately, in all but one case, the shift between the observed wavelength of the emission line and the expected wavelength could only account for a small fraction of the observed velocity offsets.

We next attempted to look at the night sky absorption spectrum due to scattered sunlight. We measured the radial velocities of the night sky spectrum from each field using the IRAF task `fxcor`. We tested three versions of the night sky spectra: one that had been normalized, one that had been normalized and had cosmic rays removed, and one that had been normalized, had cosmic rays removed, and had wavelengths above 5300 Å trimmed. As with the emission line analysis, if a uniform

velocity zero-point error is affecting all of the objects from a given field, one would expect the measured velocity of the field's night sky absorption spectrum to be offset by an equal amount. Unfortunately, as before, in all but one case, the offsets determined by measuring the velocities of the night sky absorption spectra were only able to account for a small fraction of the observed velocity offsets.

The final potential source of the observed velocity offsets are slit errors due to a misaligned mask. If a multi-slit mask is offset from it's intended alignment along the spatial axis, the target stars would still be centered along the widths of their slits, and no velocity offset would be observed. If the mask is offset along the dispersion axis, the target stars would also be offset along the widths of their slits, and the result would be velocity offsets similar to the ones observed. Unfortunately, there is no way to test if this has occurred. So even if a slit error of this variety was occurring frequently with IMACS multi-slit masks, there would be no way to determine the magnitude of the effect on the majority of our fields that have only one observation. A final case to consider is the possibility of a rotational offset of the mask. If this was occurring, one would expect to see the targets whose slits are furthest from the center of the mask along the spatial direction exhibit the largest velocity offsets. This is easy to check for. Figure 3.32 plots, for all seven of the repeated observations, the velocity difference, $V_{ij} - V_{*j}$, between the individual measured velocity and the weighted mean velocity for each target, against the slit position along the spatial axis. If a rotational offset was the source of the velocity offsets the data points would be seen to lie along a diagonal line, such that the points nearest to the top and bottom of each panel

would have the highest $V_{ij} - V_{*j}$ values in magnitude. However, after inspecting the plots in Figure 3.32, there appears to be no correlation between $V_{ij} - V_{*j}$ and the slit position on the spatial axis.

The source of the velocity offsets observed in our repeated IMACS observations therefore remains, unsatisfyingly, unknown and uncorrected for. Although, as mentioned earlier, since these velocity offsets were present in the multiply-observed fields used to calibrate the IMACS error model, the possibility that similar offsets occurred in our other IMACS fields is accounted for by an increase in the velocity measurement uncertainty, σ_V, for all IMACS targets.

3.3.3 Comparisons to Previous Work

3.3.3.1 Comparisons to SDSS Data

As a consistency check, we looked to directly compare our radial velocity measurements to other kinematic studies of Sgr candidate stars. However, with one exception, no published data sets could be found that targeted main-sequence Sgr stream stars. The only study that offered a means of comparison was the Sloan Digital Sky Survey (SDSS).

To search the SDSS database for stars in common with our data set we used the online "CrossID" tool with Data Release 10 (Ahn et al., 2013). This tool allowed us to upload a file containing the coordinates of our candidate stars, and search their database for the nearest objects within a radius we specified to be $1.8''$. In total, 18 matches were found in the SDSS database to our IMACS spectroscopic data set, and 25 matches were found to our Hectospec data set. The 43 matches had an average

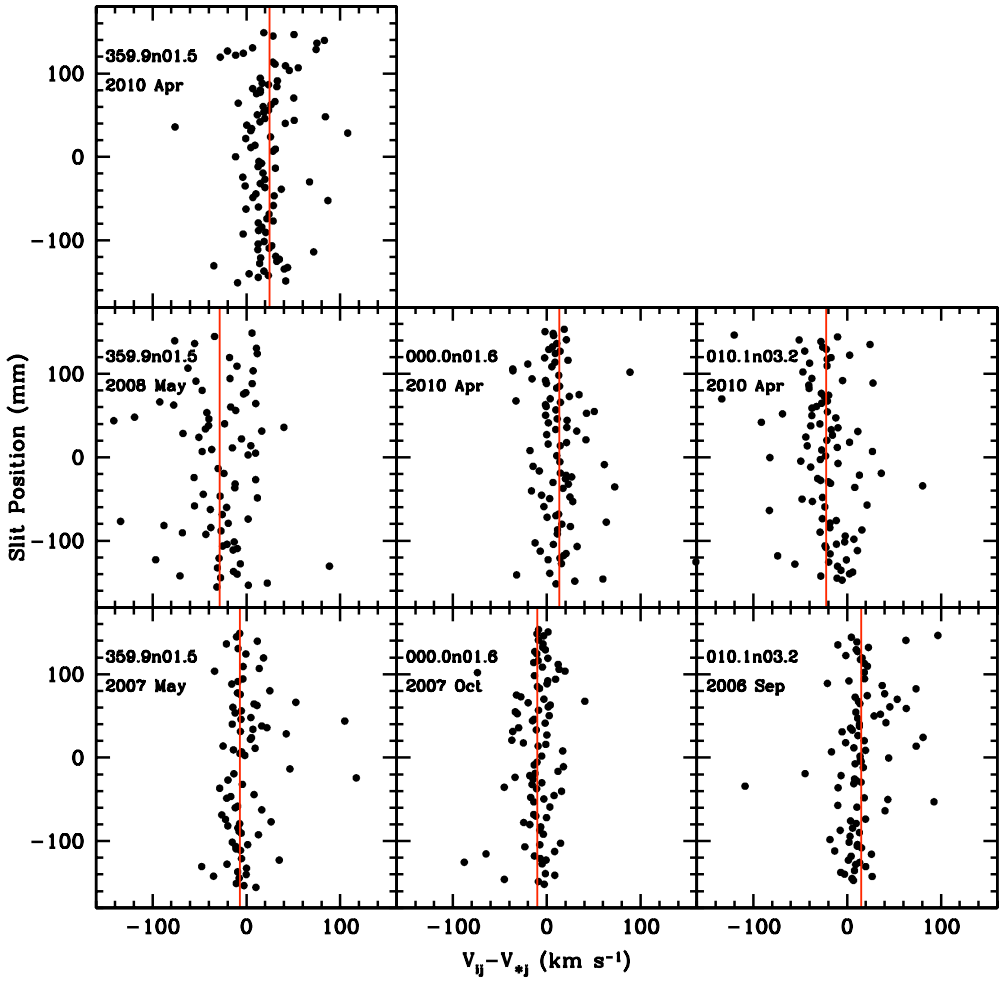

Figure 3.32: Velocity offsets as a function of slit position. For each of the seven repeated IMACS observations, the velocity difference, $V_{ij} - V_{*j}$, between the individual measured velocity and the weighted mean velocity for each target, is plotted against the slit position along the spatial axis. The red vertical lines are drawn at the average $V_{ij} - V_{*j}$ value for each field.

Table 3.9: Comparisons to Previous Work

Sample	N_{Stars}	$\langle \Delta V \rangle$ (km s^{-1})	$\sigma_{\Delta V}$ (km s^{-1})	$\sigma_{\langle \Delta V \rangle}$ (km s^{-1})	$\langle \Delta V \rangle_{bw}$ (km s^{-1})	$\sigma_{\Delta V,bw}$ (km s^{-1})	$\sigma_{\langle \Delta V \rangle,bw}$ (km s^{-1})
IMACS–SDSS	18	20.0	60.6	14.3	16.9	55.4	13.1
IMACS–SDSS[a]	14	20.8	47.1	12.6	9.9	26.5	7.1
Hectospec–SDSS	25	4.5	26.3	5.3	5.1	22.2	4.4
Hectospec–SA 57	12	–3.7	1.1	0.3	–3.7	1.1	0.3

Note: The "bw" subscripts on the final three column labels refer to the biweight estimates of these statistics, as discussed in the text.
[a] The second IMACS-SDSS sample listed uses only the fourteen brightest stars in the sample, and excludes the four faintest, as discussed in the text.

coordinate offset of just $0.3''$, and the largest individual coordinate offset for any match was $1.1''$.

Figures 3.33 and 3.34 plot the velocity differences defined as $\Delta V_{H-S} = V_{Hectospec} - V_{SDSS}$ and $\Delta V_{I-S} = V_{IMACS} - V_{SDSS}$, respectively, against I_0, the dereddened I magnitude. The error bars on each data point are calculated as the sum in quadrature of our velocity measurement uncertainty and the uncertainty reported by the SDSS: $\sigma_V = (\sigma^2_{IMACS/Hectospec} + \sigma^2_{SDSS})^{1/2}$. Also provided on each figure are the statistics of the ΔV distributions, including the mean ($\langle \Delta V \rangle$), standard deviation ($\sigma_{\Delta V}$), and standard deviation of the mean ($\sigma_{\langle \Delta V \rangle}$). Since these statistics are highly sensitive to the presence of even one significant outlier, their biweight estimates (Beers et al., 1990) are also given. For an adequately sized data set ($N \gtrsim 10$), the biweight estimates provide a more robust method for estimating these statistics in the presence of outliers. All of these statistics are summarized in Table 3.9.

The Hectospec and SDSS matches are in very good agreement. The mean value, $\langle \Delta V_{H-S} \rangle = 4.5 \pm 5.3$ km s^{-1}, is consistent with zero. The standard deviation,

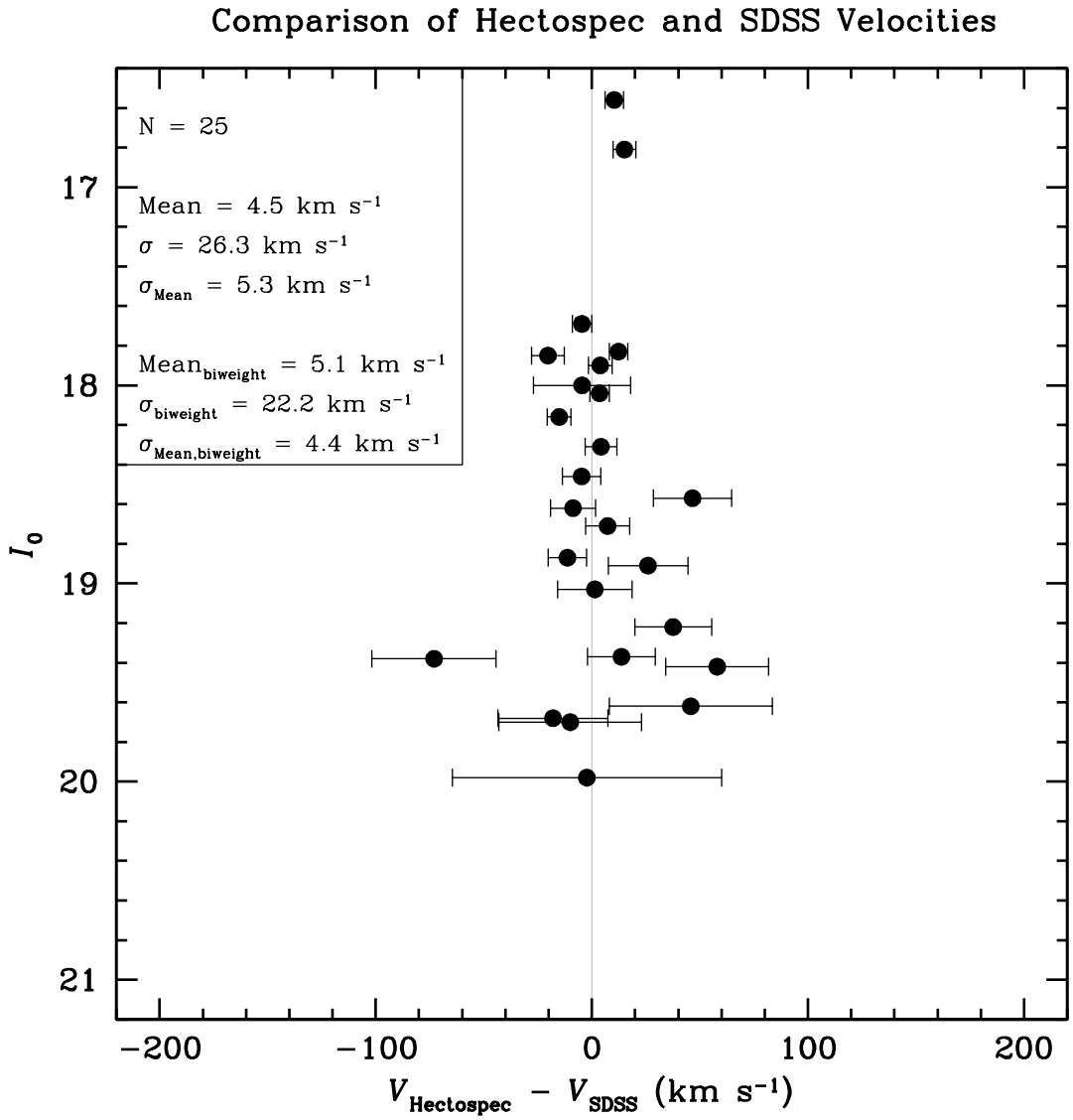

Figure 3.33: Comparison of Hectospec and SDSS velocities. The velocity differences, defined as $\Delta V_{\mathrm{H-S}} = V_{\mathrm{Hectospec}} - V_{\mathrm{SDSS}}$, for the 25 stars in common between our Hectospec data set and the SDSS spectroscopic data set, are plotted against I_0, the dereddened I magnitude. The error bars are calculated as the sum in quadrature of our velocity measurement uncertainty and the uncertainty reported by SDSS: $\sigma_V = (\sigma^2_{\mathrm{Hectospec}} + \sigma^2_{\mathrm{SDSS}})^{1/2}$. The statistics of the $\Delta V_{\mathrm{H-S}}$ distribution, including the mean, standard deviation, and standard deviation of the mean are listed. The biweight estimates, which provide a more robust method for estimating these statistics in the presence of outliers, are also provided.

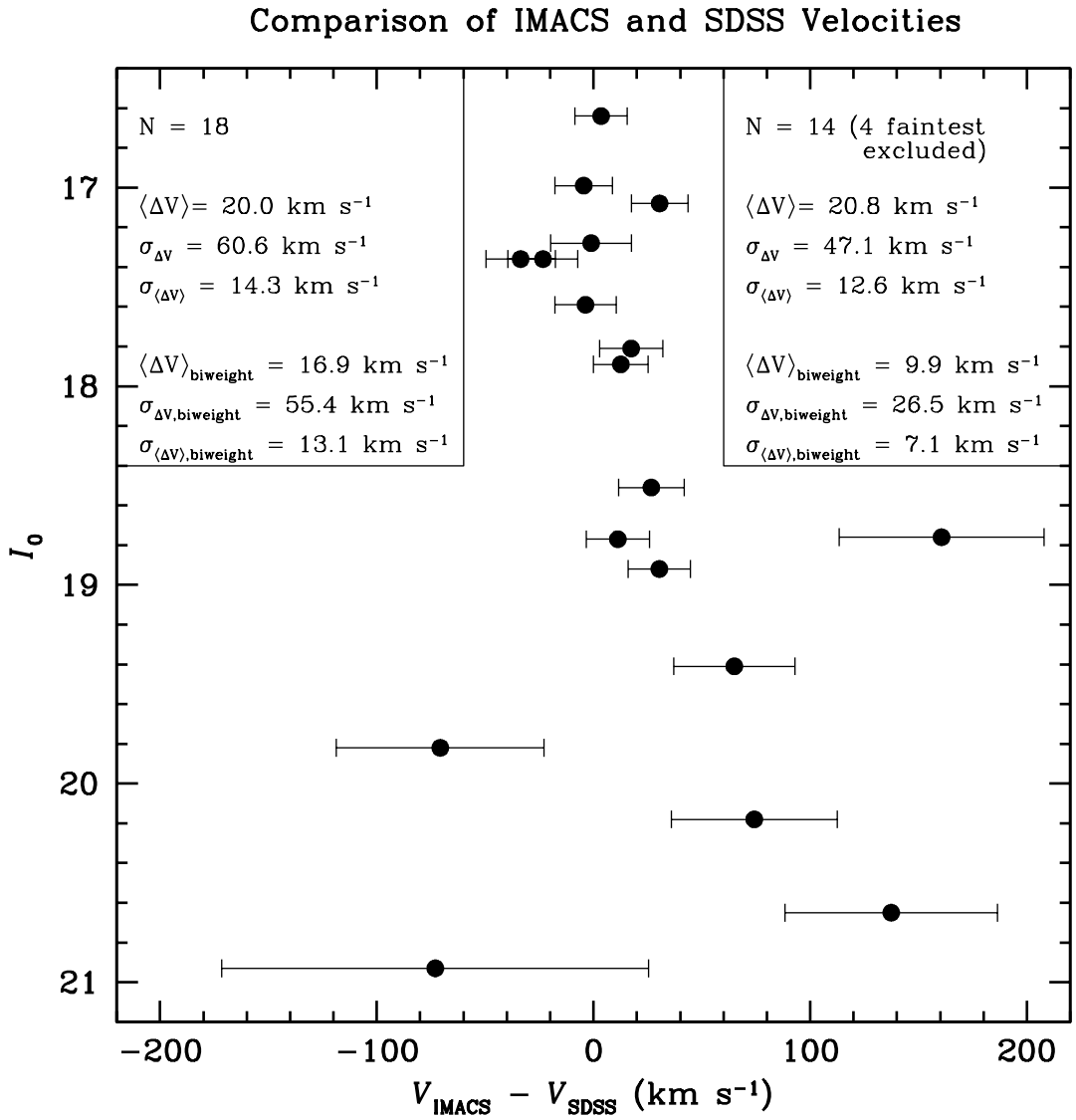

Figure 3.34: Comparison of IMACS and SDSS velocities. The velocity differences, defined as $\Delta V_{\mathrm{I-S}} = V_{\mathrm{IMACS}} - V_{\mathrm{SDSS}}$, for the 18 stars in common between our IMACS spectroscopic data set and the SDSS spectroscopic data set, are plotted against I_0, the dereddened I magnitude. The error bars are calculated as the sum in quadrature of our velocity measurement uncertainty and the uncertainty reported by SDSS: $\sigma_V = (\sigma^2_{\mathrm{IMACS}} + \sigma^2_{\mathrm{SDSS}})^{1/2}$. The statistics of the $\Delta V_{\mathrm{I-S}}$ distribution, including the mean, standard deviation, and standard deviation of the mean are listed. The biweight estimates, which provide a more robust method for estimating these statistics in the presence of outliers, are also provided. Additionally, the same statistics are listed for the subsample of 14 stars that excludes the four faintest stars, as discussed in the text.

$\sigma_{\Delta V_{\mathrm{H-S}}} = 26.3$ km s^{-1}, is reasonable in comparison with the typical measurement uncertainties, as depicted by the error bars (which are, on average, 16.3 km s^{-1}).

The IMACS and SDSS matches, however, show some disagreement, particularly for the faintest stars ($I_0 \gtrsim 20$). Overall, there appears to be a slight offset ($\langle \Delta V_{\mathrm{I-S}} \rangle_{\mathrm{biweight}} = 16.9 \pm 13.1$ km s^{-1}), though it is not much larger than the standard deviation of the mean. However, the standard deviation, $(\sigma_{\Delta V_{\mathrm{I-S}}})_{\mathrm{biweight}} = 55.4$ km s^{-1}, is large in comparison to the typical measurement uncertainties, as depicted by the error bars (which are, on average, 26.9 km s^{-1}). Not surprisingly, the faintest stars are most responsible for inflating these statistics. The set of Hectospec–SDSS matches shown in Figure 3.33 contains no stars with $I_0 > 20$, so the degree of agreement between those two data sets remains unknown for the faintest stars. However, four of the 18 matches in the IMACS–SDSS set have $I_0 > 19.8$. If these four stars are excluded, the biweight statistics become much closer to those of the Hectospec–SDSS set: $(\sigma_{\Delta V_{\mathrm{I-S}}})_{\mathrm{biweight}} = 26.5$ km s^{-1}, $(\sigma_{\Delta V_{\mathrm{H-S}}})_{\mathrm{biweight}} = 22.2$ km s^{-1}.

Section 3.3.1 describes the error models adopted for our data sets as being the sums of two independent Gaussian error components. However, there are also several sources of non-Gaussian errors that can result in large discrepancies between our measured velocities and those of the SDSS. We consider the likelihood of misidentified matches to be slim, given that none of the 43 matches had an astrometric offset between our coordinates and those of the SDSS in excess of 1.1″. It is possible, if not likely, that this set of matches contains a small number of binary stars observed at different orbital phases. This could be a potential explanation for some of the most

discrepant velocity measurements. However, the most likely source of the discrepancies is noise in the cross-correlation function. A noisy cross-correlation function can result in the misidentification of the correct peak, or a very poorly fit Gaussian to the peak. Both errors can result in large velocity measurement discrepancies, and would preferentially affect the faintest stars, as seen in Figures 3.34 and 3.33. It should be noted that these sources of non-Gaussian errors are equally likely to affect our measurements as they are those of the SDSS.

3.3.3.2 Radial Velocity Standard Field SA57

Despite our limited time with Hectospec, we were able to obtain spectra of twelve bright ($9.6 < V < 12.3$) stars in the radial velocity standard field SA 57 using a single fiber setup. In Figure 3.35 we compare our measured velocities for these stars to those published by Stefanik et al. (2006). The figure shows the velocity differences, defined as $\Delta V_{\rm SA\,57} = V_{\rm Hectospec} - V_{\rm Stefanik}$, plotted against the V magnitude of the stars. The error bars on each data point are calculated as the sum in quadrature of our velocity measurement uncertainty and the uncertainty reported by Stefanik et al. (2006): $\sigma_V = (\sigma^2_{\rm Hectospec} + \sigma^2_{\rm Stefanik})^{1/2}$. Also provided on the figure are the statistics of the $\Delta V_{\rm SA\,57}$ distribution, including the mean, standard deviation, and standard deviation of the mean. Their biweight estimates are also given. Since there are no outliers present, the biweight estimates are equal to the standard statistical values. All of these statistics are summarized in Table 3.9.

Overall, there appears to be very good agreement between our velocity measurements and those by Stefanik et al. (2006). The individual $\Delta V_{\rm SA\,57}$ values range from

$|\Delta V_{\mathrm{SA\,57}}|_{\mathrm{Min}} = 2.2$ km s^{-1} to $|\Delta V_{\mathrm{SA\,57}}|_{\mathrm{Max}} = 5.8$ km s^{-1}. There appears to be a rather small, but statistically significant, zero-point offset, $\langle \Delta V_{\mathrm{SA\,57}} \rangle = 3.7 \pm 0.3$ km s^{-1}, between our velocity measurements and those published by Stefanik et al. (2006). Given the uncertain nature of the offset (unfortunately it was not possible to attempt to replicate it), and how small the offset is in comparison with the typical velocity measurement uncertainties of the stars in our data set, we deem the potential adoption of a velocity zero-point correction superfluous.

3.3.4 Sample Selection

In order to ensure the quality of the final data set used for analysis, multiple steps were taken to reject unreliable radial velocity measurements from the sample. The first step was to visually inspect the final two-dimensional spectra (as shown in Figures 3.10 and 3.11, for example) to eliminate the objects whose spectra contained conspicuous emission lines. These objects are background galaxies that, despite our best efforts at candidate selection, made it through in to the final candidate lists. Although none of the spectra in the referenced figures contain obvious emission lines, an example of such emission lines can be seen near the middle of the bottom spectrum in the unprocessed IMACS image presented in Figure 3.4.

The second quality control step took place during the cross-correlation process with the IRAF task `fxcor`, and was briefly discussed in the "Measuring Velocities" subsection of Section 3.1.3.2. The Fourier cross-correlation of every object spectrum was performed interactively. This allowed for the visual inspection of each object's cross-correlation function and the manual fitting of the Gaussian profile to

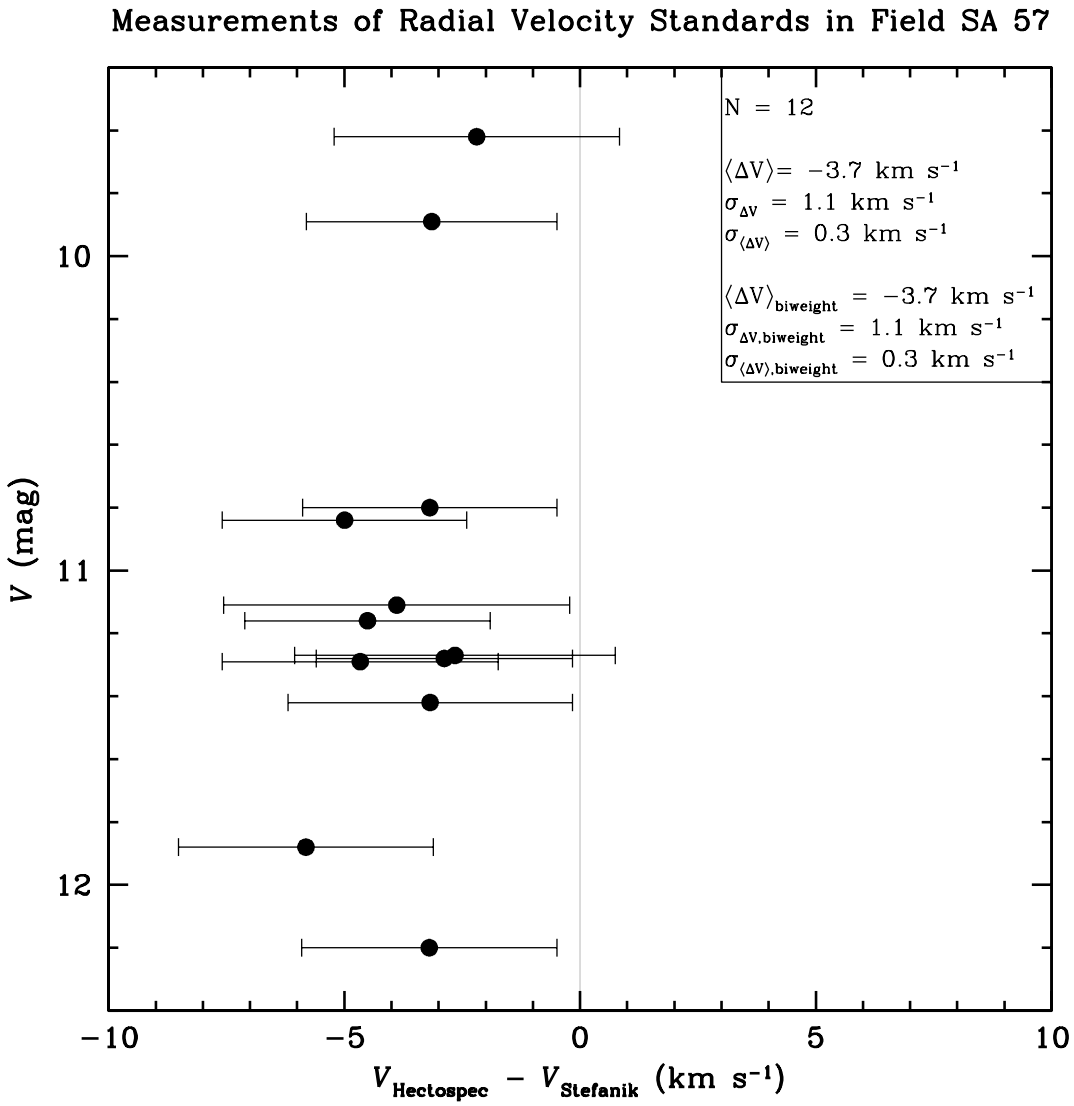

Figure 3.35: Measurements of radial velocity standards in field SA 57. The velocity differences, defined as $\Delta V_{\mathrm{SA\,57}} = V_{\mathrm{Hectospec}} - V_{\mathrm{Stefanik}}$, for twelve radial velocity standard stars from the field SA 57, are plotted against the V magnitude of the stars. The error bars are calculated as the sum in quadrature of our velocity measurement uncertainty and the uncertainty reported by Stefanik et al. (2006): $\sigma_V = (\sigma^2_{\mathrm{Hectospec}} + \sigma^2_{\mathrm{Stefanik}})^{1/2}$. The statistics of the $\Delta V_{\mathrm{SA\,57}}$ distribution, including the mean, standard deviation, and standard deviation of the mean are listed. The biweight estimates, which provide a more robust method for estimating these statistics in the presence of outliers, are also provided. However, since no outliers are present, the biweight estimates are equal to the standard statistical values.

the function's peak. Each spectrum needed to satisfy several conditions in order to merit inclusion in the final data set. First, objects whose highest peak in the cross-correlation function corresponded to velocities too extreme to be local group stars were immediately rejected. Second, objects for which the highest peak was not unambiguous were also rejected. Finally, objects whose peak profiles in the cross-correlation function were not sufficiently symmetric, so that their centers could be well determined by a Gaussian fit, were also rejected. Figures 3.14 (for IMACS) and 3.20 (for Hectospec) show the cross-correlation functions of eight Sgr targets spanning a representative range of R_{TD} values. The top panels in each figure are representative of the minimally acceptable cross-correlation profiles for each instrument.

The final sample selection filter was to define a cutoff value for the Tonry-Davis R statistic, $R_{TD,c}$, below which all spectra would be removed from the data set. To do this we consider two sets of spectra: those that failed either one of the qualitative criteria described above (hereafter referred to unsatisfactory spectra), and those those passed both criteria (hereafter referred to satisfactory spectra). Figures 3.36 (for IMACS) and 3.37 (for Hectospec) present, for both the satisfactory and unsatisfactory spectra, their distributions in R_{TD}, σ_V, and I_0. The lower left panels of each figure plot the cumulative distribution functions (*cdfs*) of R_{TD} for the unsatisfactory spectra, along with the complementary cumulative distribution functions (*ccdfs*, defined as $ccdf = 1 - ccf$) for the satisfactory spectra. We define the R_{TD} cutoff value for each instrument, $R_{TD,c}$, to be the the R_{TD} value at the intersection of these two functions. At this intersection, the percentage of satisfactory spectra with R_{TD} values greater

than $R_{TD,c}$ is equal to the percentage of unsatisfactory spectra with R_{TD} values less than $R_{TD,c}$. For IMACS, the value of $R_{TD,c}$ was found to be 2.80, and for Hectospec the value of $R_{TD,c}$ was found to be 5.07. These R_{TD} values correspond to velocity measurement uncertainties, σ_V, of 80.8 and 39.9 km s^{-1} for IMACS and Hectospec, respectively. The lower right panels of Figures 3.36 and 3.37 plot the *cdfs* of σ_V for the satisfactory spectra and the *ccdfs* for the unsatisfactory spectra. Dashed lines span across the panels marking the values of $R_{TD,c}$ and the corresponding values of $\sigma_{V,c}$, for each instrument. Histograms of R_{TD} and σ_V for the satisfactory and unsatisfactory spectra are provided in the middle panels. The upper panels show the dereddened I magnitude, I_0, plotted as a function of R_{TD} and σ_V for both the satisfactory and unsatisfactory spectra. The upper right panel shows the histograms and *cdfs* of I_0 for both the satisfactory and unsatisfactory spectra.

Objects whose cross-corellation functions had R_{TD} values less than $R_{TD,c}$ have been removed from the final sample used for analysis. The application of this third, quantitative, selection filter resulted in the removal of 70 of the 1997 satisfactory IMACS spectra (3.5%), and 14 of the 763 satisfactory Hectospec spectra (1.8%). The excluded IMACS spectra had R_{TD} values ranging from 2.40 to 2.79, while the excluded Hectospec spectra had R_{TD} values ranging from 4.13 to 5.06. The remaining spectra, comprising the final sample, had median and average R_{TD} values of 5.59 and 6.66 for IMACS, and 19.35 and 19.13 for Hectospec. The median and average σ_V values were 31.1 and 35.1 km s^{-1} for IMACS, and 5.7 and 8.6 km s^{-1} for Hectospec.

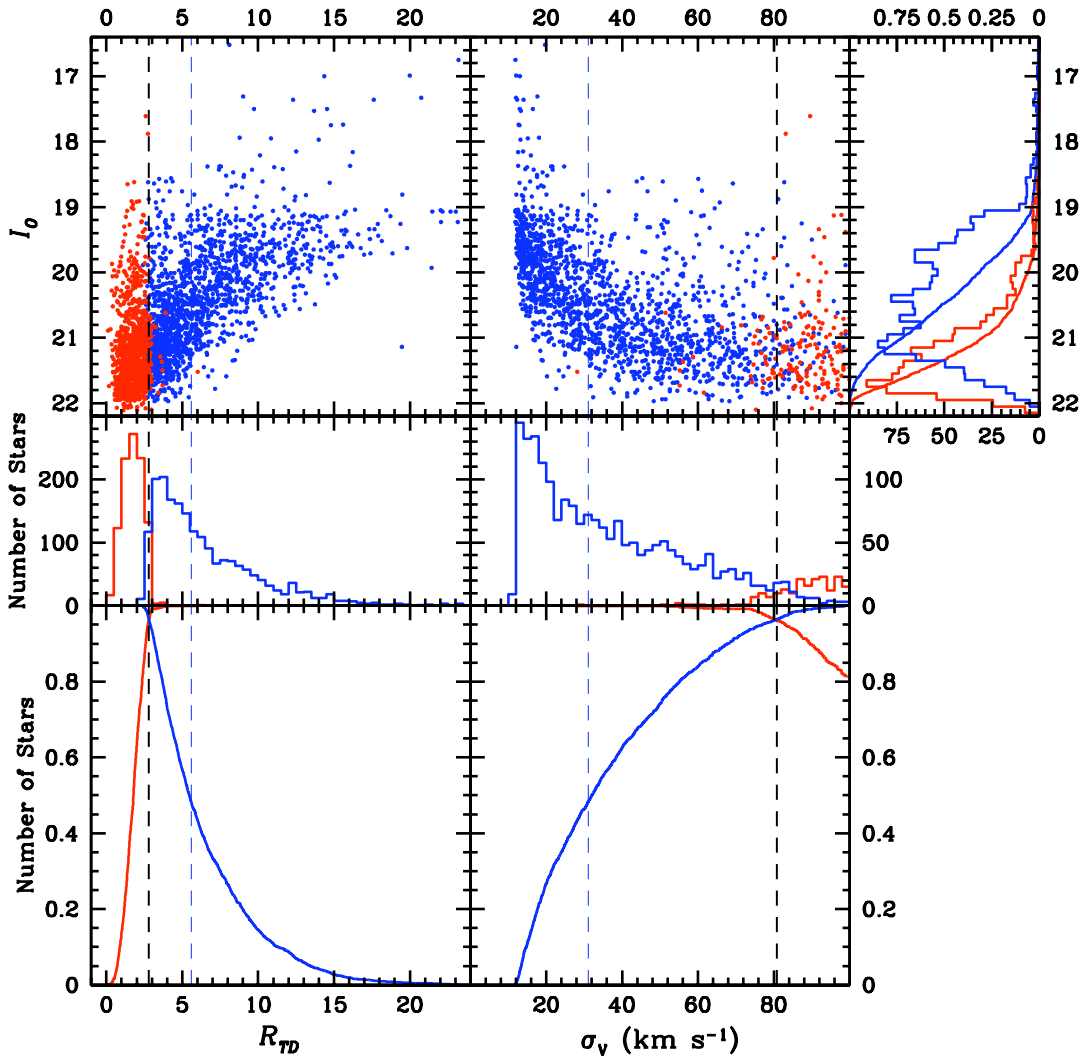

Figure 3.36: IMACS R_{TD}, σ_V, and I_0 Distributions. Blue (red) points, histograms, and curves correspond to measurements made from the satisfactory (unsatisfactory) set of IMACS spectra, as described in the text. N = 1997 (1020). The lower left panel plots the *ccdf* (*cdf*) of R_{TD} for the satisfactory (unsatisfactory) spectra. The lower right panel plots the *cdf* (*ccdf*) of σ_V for the satisfactory (unsatisfactory) spectra. The two middle panels plot histograms of R_{TD} and σ_V for the satisfactory and unsatisfactory spectra. The upper panels show the dereddened I magnitude, I_0, plotted as a function of R_{TD} and σ_V for both the satisfactory and unsatisfactory spectra. The upper right panel shows the histograms and *cdfs* of I_0 for both the satisfactory and unsatisfactory spectra. Spanning across the panels are dashed lines indicating the values of $R_{TD,c}$ and $\sigma_{V,c}$ (in black) and the median R_{TD} and σ_V values of the final IMACS sample (in blue).

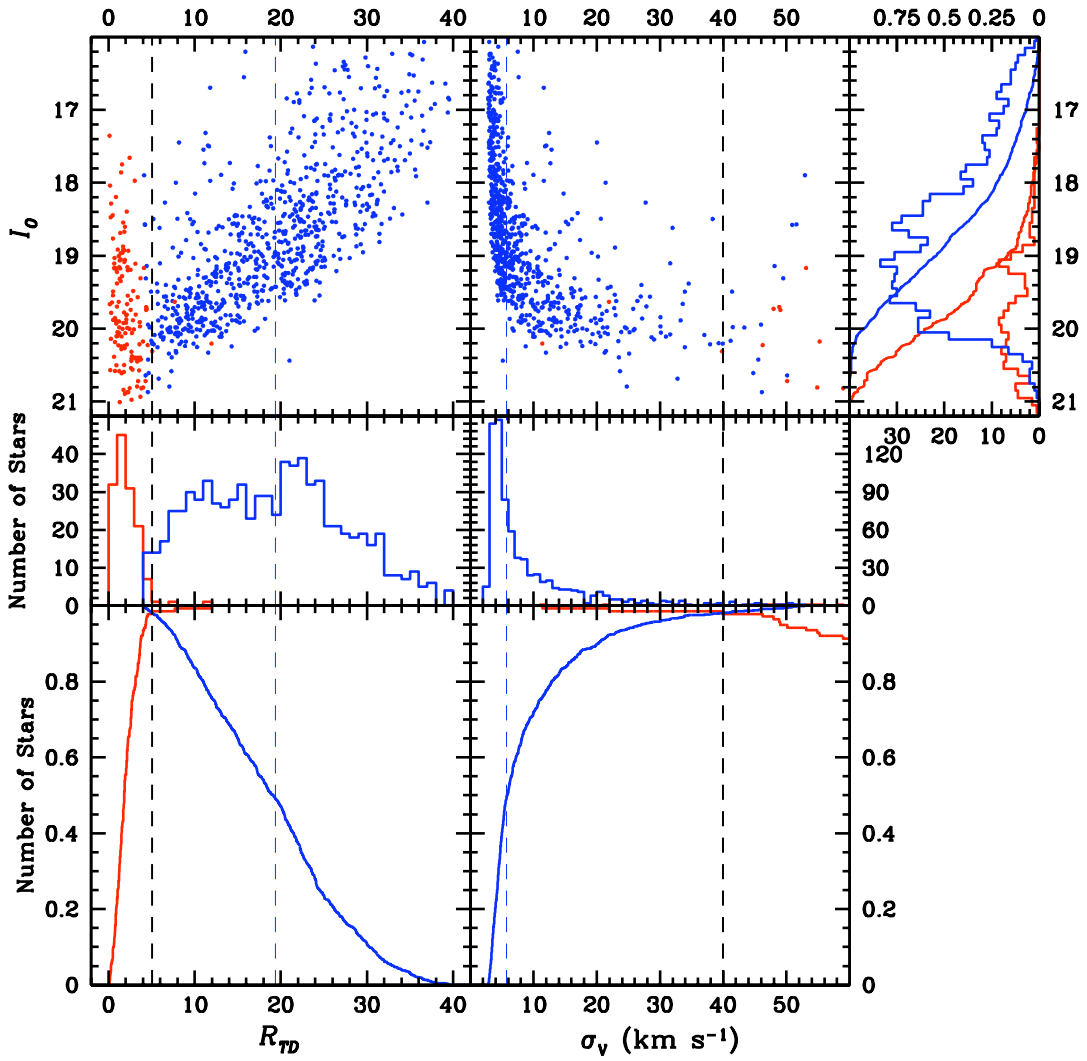

Figure 3.37: Hectospec R_{TD}, σ_V, and I_0 Distributions. Blue (red) points, histograms, and curves correspond to measurements made from the satisfactory (unsatisfactory) set of Hectospec spectra, as described in the text. N = 763 (139). The lower left panel plots the *ccdf* (*cdf*) of R_{TD} for the satisfactory (unsatisfactory) spectra. The lower right panel plots the *cdf* (*ccdf*) of σ_V for the satisfactory (unsatisfactory) spectra. The two middle panels plot histograms of R_{TD} and σ_V for the satisfactory and unsatisfactory spectra. The upper panels show the dereddened I magnitude, I_0, plotted as a function of R_{TD} and σ_V for both the satisfactory and unsatisfactory spectra. The upper right panel shows the histograms and *cdfs* of I_0 for both the satisfactory and unsatisfactory spectra. Spanning across the panels are dashed lines indicating the values of $R_{TD,c}$ and $\sigma_{V,c}$ (in black) and the median R_{TD} and σ_V values of the final Hectospec sample (in blue).

These median values for R_{TD} and σ_V are marked on Figures 3.36 and 3.37 with a blue dashed line.

At the end of this chapter, a table is provided for every field (Tables 3.10 to 3.47) listing each target's identifier (ID), equatorial coordinates (α, δ), dereddened magnitude and color $(I_0, (V-I)_0)$, heliocentric and Galactic standard of rest radial velocities $(V_{\rm helio}, V_{\rm gsr})$, velocity measurement uncertainty (σ_V), and Tonry-Davis R value (R_{TD}). Note that objects excluded from further analysis due to the $R_{TD,c}$ cut described above are included in the field tables for reference.

The tables for the two fields (000.1n01.5 and 010.1n03.2) that were observed multiple times, Tables 3.10 and 3.11, have a slightly different format than the other field tables. These tables include an additional column labeled "Obs.", with format N.M, indicating which observation (M) of which mask (N) is the source of the kinematic information listed on that particular row. See the note at the end of each table for details on how this shorthand notation corresponds to the specific observations listed in Table 3.2.

For the stars with multiple observations, their kinematic information is presented on multiple rows. There is one row for each independent observation (identified by the aforementioned "Obs." column), preceded by a row summarizing the positional and photometric information. Also listed on this initial summary row is the weighted averages of the velocities, $V_{\rm helio}$ and $V_{\rm gsr}$, and their corresponding velocity measurement uncertainty, σ_V. The weighted average velocities are calculated in a similar fashion as described earlier in Equations 3.10 and 3.11. Specifically, the weighted averages of

the heliocentric and Galactic standard of rest radial velocities can be calculated from each of the individual velocity measurements as:

$$\overline{V}_{*j} = \frac{\sum_{i=1}^{n_j} V_{ij}\sigma_{ij}^{-2}}{\sum_{i=1}^{n_j} \sigma_{ij}^{-2}}. \tag{3.13}$$

The estimated uncertainty in the weighted average velocities can then be calculated as:

$$\sigma_{V_{*j}} = \frac{1}{\sqrt{\sum_{i=1}^{n_j} \sigma_{ij}^{-2}}}. \tag{3.14}$$

While stars with R_{TD} values less than $R_{TD,c}$ are listed in the field tables below for reference, such stars were excluded from the weighted average calculations made for stars with multiple observations.

Table 3.10: Spectroscopic and Photometric Data for Objects in Field 000.1n01.5

ID	$\alpha_{J2000.0}$	$\delta_{J2000.0}$	$I_{\rm Inst}$	$(V-I)_{\rm Inst}$	Obs.	$V_{\rm helio}$ (km s^{-1})	$V_{\rm gsr}$ (km s^{-1})	σ_V (km s^{-1})	R_{TD}
000051	18 55 26.60	–30 35 56.2	20.49	0.47	···	59.5	88.5	34.5	···
···	···	···	···	···	3.1	–36.0	–7.0	53.8	3.77
···	···	···	···	···	3.2	126.5	155.5	45.0	4.28
000061	18 55 27.47	–30 35 55.9	20.46	0.49	···	134.9	163.9	25.6	···
···	···	···	···	···	3.1	162.7	191.7	38.7	4.77
···	···	···	···	···	3.2	113.4	142.4	34.1	5.23
000077	18 54 56.52	–30 35 56.6	20.96	0.79	···	122.8	151.8	37.4	···
···	···	···	···	···	3.1	99.7	128.7	58.9	3.53
···	···	···	···	···	3.2	138.4	167.4	48.5	4.06
000130	18 55 39.19	–30 35 53.9	20.44	0.72	1.1	52.4	81.8	41.5	4.54
000177	18 55 01.77	–30 35 54.7	21.01	0.49	···	133.9	162.9	28.3	···
···	···	···	···	···	3.1	96.1	125.1	40.2	4.64
···	···	···	···	···	3.2	170.9	199.9	39.9	4.67
000232	18 55 26.99	–30 35 52.5	20.67	0.66	···	142.0	171.0	31.6	···
···	···	···	···	···	3.1	179.3	208.3	55.2	3.70
···	···	···	···	···	3.2	123.8	152.8	38.6	4.78
000338	18 54 59.49	–30 35 51.6	19.87	0.43	···	152.8	181.8	9.3	···
···	···	···	···	···	3.1	138.9	167.9	13.4	13.48
···	···	···	···	···	3.2	165.8	194.8	13.0	14.67
000340	18 55 04.67	–30 35 51.3	21.41	0.54	3.1	155.3	184.3	71.4	3.07
000486	18 55 11.20	–30 35 48.5	20.70	0.51	···	140.4	169.4	24.5	···
···	···	···	···	···	3.1	128.1	157.1	38.7	4.77
···	···	···	···	···	3.2	148.7	177.7	31.7	5.52
000503	18 55 39.10	–30 35 47.0	20.88	0.45	1.1	43.1	72.5	46.4	4.19
000613	18 55 11.77	–30 35 46.2	20.22	0.77	···	109.1	138.1	18.6	···
···	···	···	···	···	3.1	88.5	117.5	24.0	6.82
···	···	···	···	···	3.2	139.9	168.9	29.3	5.84
000683	18 55 05.53	–30 35 45.1	20.81	0.43	···	80.3	109.3	15.8	···
···	···	···	···	···	3.1	95.0	124.0	20.8	7.71
···	···	···	···	···	3.2	60.2	89.2	24.2	6.77
000714	18 54 44.96	–30 35 45.2	20.08	0.38	···	135.4	164.5	10.8	···
···	···	···	···	···	2.1	147.7	176.8	12.8	15.15
···	···	···	···	···	2.2	106.1	135.2	19.8	8.05
000824	18 55 28.08	–30 35 41.6	19.33	0.64	···	223.1	252.1	10.3	···
···	···	···	···	···	3.1	218.3	247.3	14.2	12.08
···	···	···	···	···	3.2	228.5	257.5	15.0	11.03
000930	18 55 08.43	–30 35 40.6	21.39	0.52	···	49.5	78.5	31.5	···
···	···	···	···	···	3.1	–0.4	28.6	52.0	3.86
···	···	···	···	···	3.2	78.5	107.5	39.6	4.69
001036	18 55 22.85	–30 35 38.3	19.91	0.49	···	–69.5	–40.5	13.5	···
···	···	···	···	···	3.1	–78.8	–49.8	17.3	9.24
···	···	···	···	···	3.2	–55.2	–26.1	21.5	7.49
001062	18 54 40.62	–30 35 39.2	20.99	0.57	···	146.3	175.4	25.0	···
···	···	···	···	···	2.1	144.3	173.4	33.0	5.35
···	···	···	···	···	2.2	148.9	178.1	38.1	4.82
001122	18 55 23.58	–30 35 36.9	19.87	0.36	···	162.8	191.8	11.4	···
···	···	···	···	···	3.1	163.1	192.1	15.5	10.53
···	···	···	···	···	3.2	162.5	191.5	16.9	9.44
001178	18 55 07.30	–30 35 36.5	20.36	0.46	···	133.0	162.0	14.4	···
···	···	···	···	···	3.1	132.4	161.4	16.7	9.56
···	···	···	···	···	3.2	134.8	163.9	28.0	6.05
001215	18 54 55.77	–30 35 36.0	20.94	0.55	···	90.9	119.9	31.0	···
···	···	···	···	···	3.1	49.3	78.3	38.6	4.78
···	···	···	···	···	3.2	167.0	196.0	52.2	3.85
001241	18 55 20.09	–30 35 34.6	19.88	0.25	···	145.3	174.3	23.1	···
···	···	···	···	···	3.1	117.7	146.7	33.9	5.25
···	···	···	···	···	3.2	169.3	198.3	31.6	5.53
001244	18 55 02.94	–30 35 35.2	20.22	0.47	3.2	148.7	177.7	14.0	12.38
001387	18 55 18.50	–30 35 32.0	20.29	0.46	···	150.6	179.6	14.4	···
···	···	···	···	···	3.1	130.7	159.7	22.2	7.28

Continued on Next Page...

Table 3.10 – 000.1n01.5 (Continued)

ID	$\alpha_{J2000.0}$	$\delta_{J2000.0}$	$I_{\rm Inst}$	$(V-I)_{\rm Inst}$	Obs.	$V_{\rm helio}$ (km s^{-1})	$V_{\rm gsr}$ (km s^{-1})	σ_V (km s^{-1})	R_{TD}
···	···	···	···	···	3.2	165.0	194.0	18.9	8.43
001429	18 55 12.34	–30 35 31.4	21.33	0.56	3.1	71.9	100.9	54.4	3.74
001439	18 55 36.57	–30 35 30.2	19.97	0.47	1.1	94.4	123.8	27.8	6.08
001449	18 54 39.57	–30 35 32.0	21.09	0.44	···	109.0	138.1	26.5	···
···	···	···	···	···	2.1	98.3	127.5	48.3	4.07
···	···	···	···	···	2.2	131.3	160.5	47.8	4.10
···	···	···	···	···	2.3	99.6	128.8	42.2	4.48
001496	18 54 37.30	–30 35 31.4	20.32	0.42	···	154.8	183.8	10.3	···
···	···	···	···	···	3.1	141.8	170.8	13.6	13.14
···	···	···	···	···	3.2	172.8	201.8	16.0	10.13
001762	18 55 39.22	–30 35 24.7	20.58	0.49	1.1	155.9	185.3	53.2	3.80
001818	18 54 34.11	–30 35 25.9	21.52	0.69	···	131.0	160.2	30.8	···
···	···	···	···	···	2.1	92.0	121.2	44.6	4.31
···	···	···	···	···	2.3	166.4	195.6	42.5	4.46
001963	18 54 37.85	–30 35 23.3	20.96	0.51	···	137.7	166.7	26.7	···
···	···	···	···	···	3.1	79.3	108.3	47.5	4.12
···	···	···	···	···	3.2	164.6	193.6	32.2	5.45
002054	18 55 15.55	–30 35 20.5	21.36	0.62	···	128.3	157.3	34.5	···
···	···	···	···	···	3.1	108.2	137.2	40.5	4.62
···	···	···	···	···	3.2	181.9	210.9	66.0	3.25
002065	18 55 10.77	–30 35 20.4	20.85	0.64	···	90.1	119.1	20.1	···
···	···	···	···	···	3.1	65.3	94.3	25.2	6.56
···	···	···	···	···	3.2	133.5	162.5	33.4	5.31
002278	18 55 29.29	–30 35 15.5	20.80	0.41	···	135.0	164.1	22.3	···
···	···	···	···	···	1.1	86.9	116.3	50.7	3.93
···	···	···	···	···	3.1	131.2	160.2	43.5	4.39
···	···	···	···	···	3.2	153.9	182.9	30.2	5.72
002343	18 54 47.60	–30 35 15.2	19.54	0.61	···	63.0	92.0	9.9	···
···	···	···	···	···	3.1	62.7	91.7	12.9	14.89
···	···	···	···	···	3.2	63.4	92.4	15.2	10.76
002441	18 54 40.99	–30 35 13.3	20.60	0.52	···	160.6	189.8	11.9	···
···	···	···	···	···	2.1	154.8	183.9	17.3	9.20
···	···	···	···	···	2.2	134.9	164.1	34.0	5.24
···	···	···	···	···	2.3	175.1	204.2	18.6	8.55
002611	18 55 28.79	–30 35 08.2	20.65	0.69	···	–75.7	–46.7	18.2	···
···	···	···	···	···	1.1	19.3	48.7	68.3	3.17
···	···	···	···	···	3.1	–71.3	–42.3	23.7	6.90
···	···	···	···	···	3.2	–103.7	–74.7	31.5	5.54
002676	18 55 16.48	–30 35 07.4	21.27	0.37	···	139.4	168.5	33.6	···
···	···	···	···	···	3.1	135.1	164.1	38.5	4.79
···	···	···	···	···	3.2	153.6	182.6	69.2	3.14
002710	18 54 52.62	–30 35 07.6	19.60	0.77	···	139.7	168.7	9.1	···
···	···	···	···	···	3.1	136.6	165.6	12.9	14.81
···	···	···	···	···	3.2	142.8	171.8	12.9	14.92
002771	18 54 41.59	–30 35 06.7	20.95	0.50	···	163.1	192.3	15.5	···
···	···	···	···	···	2.1	132.7	161.9	32.7	5.39
···	···	···	···	···	2.2	97.0	126.1	39.2	4.73
···	···	···	···	···	2.3	191.1	220.2	19.8	8.07
002893	18 55 37.87	–30 35 02.0	20.09	0.50	1.1	159.7	189.1	20.5	7.80
003020	18 54 53.54	–30 35 01.1	20.61	0.78	···	77.0	106.0	22.3	···
···	···	···	···	···	3.1	81.2	110.2	26.8	6.25
···	···	···	···	···	3.2	67.8	96.8	40.0	4.66
003031	18 55 04.15	–30 35 00.5	19.12	0.30	···	124.2	153.2	23.7	···
···	···	···	···	···	3.1	119.5	148.5	28.2	6.02
···	···	···	···	···	3.2	135.5	164.5	43.7	4.37
003038	18 54 48.63	–30 35 00.8	20.61	0.47	···	135.6	164.8	11.5	···
···	···	···	···	···	2.1	135.0	164.1	15.8	10.28
···	···	···	···	···	2.2	125.4	154.5	46.9	4.16
···	···	···	···	···	2.3	138.0	167.2	18.0	8.83
003039	18 55 20.57	–30 34 59.7	21.04	0.63	···	121.1	150.1	19.9	···
···	···	···	···	···	3.1	89.6	118.7	27.4	6.15
···	···	···	···	···	3.2	156.3	185.3	29.0	5.89

Continued on Next Page...

Table 3.10 – 000.1n01.5 (Continued)

ID	$\alpha_{J2000.0}$	$\delta_{J2000.0}$	$I_{\rm Inst}$	$(V-I)_{\rm Inst}$	Obs.	$V_{\rm helio}$ (km s^{-1})	$V_{\rm gsr}$ (km s^{-1})	σ_V (km s^{-1})	R_{TD}
003255	18 55 35.35	–30 34 55.1	19.54	0.53	1.1	103.8	133.2	20.7	7.74
003302	18 55 13.00	–30 34 55.1	20.88	0.42	···	149.3	178.3	23.9	···
···	···	···	···	···	3.1	148.3	177.4	27.9	6.06
···	···	···	···	···	3.2	151.8	180.8	46.2	4.20
003317	18 55 02.51	–30 34 55.3	19.13	0.83	···	65.4	94.4	10.3	···
···	···	···	···	···	3.1	55.0	84.0	13.7	12.91
···	···	···	···	···	3.2	79.3	108.3	15.8	10.24
003478	18 54 50.95	–30 34 52.6	21.41	0.59	3.1	97.3	126.3	41.6	4.53
003543	18 54 40.43	–30 34 51.7	21.03	0.74	···	120.5	149.6	17.5	···
···	···	···	···	···	2.1	115.7	144.8	20.8	7.71
···	···	···	···	···	2.2	111.3	140.5	55.4	3.69
···	···	···	···	···	2.3	143.7	172.8	40.6	4.61
003566	18 55 01.29	–30 34 50.7	20.88	0.87	···	185.1	214.1	33.1	···
···	···	···	···	···	3.1	209.7	238.8	67.7	3.19
···	···	···	···	···	3.2	177.4	206.4	37.9	4.84
003591	18 55 07.69	–30 34 50.0	21.22	0.53	···	100.3	129.3	29.1	···
···	···	···	···	···	3.1	72.2	101.2	46.7	4.17
···	···	···	···	···	3.2	118.2	147.2	37.3	4.90
003675	18 54 36.61	–30 34 49.3	21.05	0.50	···	60.9	89.9	39.2	···
···	···	···	···	···	3.1	53.1	82.1	49.3	4.01
···	···	···	···	···	3.2	74.2	103.2	64.7	3.30
003739	18 54 54.69	–30 34 47.8	21.08	0.58	···	113.0	142.0	22.2	···
···	···	···	···	···	3.1	130.5	159.5	33.0	5.35
···	···	···	···	···	3.2	98.5	127.5	30.0	5.75
003910	18 55 13.59	–30 34 44.2	20.95	0.45	1.1	57.8	87.2	48.0	4.09
003959	18 54 35.23	–30 34 44.5	20.94	0.69	···	111.9	141.0	16.6	···
···	···	···	···	···	2.1	95.9	125.1	19.1	8.35
···	···	···	···	···	2.2	23.1	52.2	98.9	2.40
···	···	···	···	···	2.3	163.2	192.3	34.2	5.22
003996	18 55 06.84	–30 34 43.0	19.71	0.85	···	–48.6	–19.6	11.5	···
···	···	···	···	···	3.1	–58.8	–29.8	15.3	10.69
···	···	···	···	···	3.2	–35.2	–6.2	17.5	9.08
004168	18 55 22.35	–30 34 38.9	19.91	0.52	···	144.8	173.8	10.9	···
···	···	···	···	···	3.1	136.7	165.7	14.7	11.39
···	···	···	···	···	3.2	154.8	183.8	16.4	9.82
004187	18 55 30.27	–30 34 38.2	21.21	0.52	1.1	89.1	118.5	88.2	2.62
004202	18 55 05.07	–30 34 39.1	21.12	0.64	3.1	112.9	141.9	48.3	4.07
004234	18 54 35.66	–30 34 39.2	21.38	0.81	···	140.0	169.1	25.6	···
···	···	···	···	···	2.1	138.7	167.8	35.6	5.07
···	···	···	···	···	2.2	107.7	136.9	49.9	3.98
···	···	···	···	···	2.3	182.4	211.6	55.0	3.71
004319	18 55 21.18	–30 34 35.9	21.71	0.68	3.2	206.5	235.5	66.6	3.23
004436	18 55 16.05	–30 34 33.9	21.47	0.57	···	73.4	102.4	39.5	···
···	···	···	···	···	3.1	48.5	77.5	47.0	4.15
···	···	···	···	···	3.2	132.7	161.7	72.7	3.03
004437	18 55 16.95	–30 34 33.8	21.63	0.23	3.2	19.8	48.8	43.3	4.40
004504	18 54 44.24	–30 34 33.2	20.67	0.57	···	197.7	226.9	24.0	···
···	···	···	···	···	2.1	175.4	204.5	28.5	5.97
···	···	···	···	···	2.2	311.5	340.7	61.8	3.41
···	···	···	···	···	2.3	188.4	217.5	63.9	3.33
004540	18 55 39.20	–30 34 30.4	20.23	0.42	1.1	92.8	122.2	24.1	6.80
004548	18 55 24.39	–30 34 31.0	19.55	0.38	···	148.2	177.2	9.4	···
···	···	···	···	···	3.1	149.2	178.2	12.6	16.02
···	···	···	···	···	3.2	146.8	175.8	14.0	12.34
004554	18 55 09.82	–30 34 31.4	19.74	0.47	···	150.1	179.1	9.8	···
···	···	···	···	···	3.1	150.2	179.2	13.5	13.39
···	···	···	···	···	3.2	150.0	179.0	14.2	12.09
004601	18 54 54.04	–30 34 30.8	21.38	0.50	3.1	118.2	147.2	55.4	3.69
004716	18 54 56.97	–30 34 28.6	20.40	0.46	···	128.5	157.5	13.2	···
···	···	···	···	···	3.1	123.1	152.1	17.9	8.87
···	···	···	···	···	3.2	134.9	163.9	19.5	8.17
004724	18 55 14.07	–30 34 27.9	21.50	0.43	···	24.3	53.4	37.6	···

Continued on Next Page...

Table 3.10 – 000.1n01.5 (Continued)

ID	$\alpha_{J2000.0}$	$\delta_{J2000.0}$	$I_{\rm Inst}$	$(V-I)_{\rm Inst}$	Obs.	$V_{\rm helio}$ (km s^{-1})	$V_{\rm gsr}$ (km s^{-1})	σ_V (km s^{-1})	R_{TD}
···	···	···	···	···	3.1	13.7	42.7	50.0	3.97
···	···	···	···	···	3.2	38.2	67.2	57.1	3.61
004759	18 54 43.13	–30 34 27.8	20.50	0.58	···	130.5	159.5	11.9	···
···	···	···	···	···	3.1	125.6	154.6	14.4	11.68
···	···	···	···	···	3.2	140.6	169.6	20.8	7.69
004771	18 54 29.72	–30 34 27.9	20.34	0.71	···	–23.7	5.3	13.5	···
···	···	···	···	···	3.1	–28.4	0.6	17.1	9.36
···	···	···	···	···	3.2	–15.8	13.2	22.0	7.35
004819	18 55 35.31	–30 34 24.6	20.04	0.36	1.1	134.6	164.0	19.6	8.12
004882	18 54 47.87	–30 34 25.0	19.63	0.67	···	131.5	160.6	8.1	···
···	···	···	···	···	2.1	112.9	142.1	14.6	11.43
···	···	···	···	···	2.2	127.1	156.3	15.8	10.24
···	···	···	···	···	2.3	147.7	176.8	12.5	16.76
004945	18 55 15.02	–30 34 23.2	20.70	0.46	···	166.2	195.2	16.1	···
···	···	···	···	···	3.1	168.4	197.4	24.5	6.72
···	···	···	···	···	3.2	164.5	193.5	21.3	7.55
005088	18 54 55.37	–30 34 20.9	19.34	0.64	···	107.3	136.3	9.2	···
···	···	···	···	···	3.1	94.7	123.7	12.4	17.32
···	···	···	···	···	3.2	122.8	151.8	13.7	12.91
005117	18 55 38.03	–30 34 18.6	19.63	0.66	1.1	132.3	161.7	18.1	8.81
005244	18 55 34.30	–30 34 16.3	21.48	0.68	···	109.1	138.1	36.8	···
···	···	···	···	···	3.1	101.7	130.7	52.4	3.84
···	···	···	···	···	3.2	116.3	145.3	51.7	3.88
005269	18 54 40.39	–30 34 17.8	21.61	0.47	···	103.6	132.7	43.6	···
···	···	···	···	···	2.1	74.4	103.6	67.7	3.19
···	···	···	···	···	2.3	124.2	153.3	56.9	3.62
005608	18 54 31.50	–30 34 11.0	21.20	0.46	···	136.8	165.9	26.7	···
···	···	···	···	···	2.1	162.8	192.0	51.3	3.90
···	···	···	···	···	2.2	31.2	60.3	59.9	3.49
···	···	···	···	···	2.3	163.0	192.2	36.7	4.96
005618	18 54 48.03	–30 34 10.5	21.07	0.59	···	151.2	180.2	23.6	···
···	···	···	···	···	3.1	143.8	172.8	29.1	5.87
···	···	···	···	···	3.2	165.3	194.3	40.3	4.63
005759	18 54 58.45	–30 34 07.2	21.16	0.56	···	87.4	116.5	24.9	···
···	···	···	···	···	3.1	72.7	101.7	28.7	5.94
···	···	···	···	···	3.2	133.0	162.0	50.4	3.95
005848	18 54 48.44	–30 34 05.6	21.06	0.55	···	130.9	160.0	11.9	···
···	···	···	···	···	2.1	123.4	152.5	20.6	7.76
···	···	···	···	···	2.2	99.4	128.6	60.1	3.48
···	···	···	···	···	2.3	143.7	172.9	23.6	6.93
···	···	···	···	···	3.1	115.2	144.2	32.4	5.43
···	···	···	···	···	3.2	141.7	170.7	24.4	6.74
005981	18 54 53.05	–30 34 02.8	20.91	0.59	···	153.4	182.4	19.9	···
···	···	···	···	···	3.1	133.9	162.9	27.3	6.17
···	···	···	···	···	3.2	175.7	204.7	29.2	5.86
006037	18 55 33.69	–30 34 00.3	19.95	0.60	1.1	98.6	128.0	29.4	5.83
006116	18 54 49.67	–30 34 00.3	20.97	0.55	···	191.9	221.0	18.4	···
···	···	···	···	···	2.1	134.4	163.5	28.6	5.96
···	···	···	···	···	2.3	242.6	271.7	27.3	6.17
···	···	···	···	···	3.2	198.0	227.0	50.7	3.93
006272	18 55 24.82	–30 33 56.2	20.31	0.71	···	–119.0	–90.0	23.1	···
···	···	···	···	···	3.1	–114.1	–85.1	25.8	6.45
···	···	···	···	···	3.2	–139.2	–110.2	52.4	3.84
006310	18 55 32.23	–30 33 55.1	19.83	0.64	···	34.5	63.6	9.7	···
···	···	···	···	···	1.1	15.3	44.7	20.2	7.90
···	···	···	···	···	3.1	28.0	57.0	15.0	10.98
···	···	···	···	···	3.2	54.9	83.9	16.4	9.76
006547	18 55 17.37	–30 33 51.4	20.70	0.38	···	175.1	204.1	21.7	···
···	···	···	···	···	3.1	176.4	205.4	35.2	5.11
···	···	···	···	···	3.2	174.2	203.2	27.6	6.11
006619	18 54 28.71	–30 33 51.7	19.60	0.53	3.1	133.1	162.1	12.8	15.26
006742	18 55 13.66	–30 33 48.4	20.80	0.53	···	121.2	150.2	18.4	···

Continued on Next Page...

Table 3.10 – 000.1n01.5 (Continued)

ID	$\alpha_{J2000.0}$	$\delta_{J2000.0}$	$I_{\rm Inst}$	$(V-I)_{\rm Inst}$	Obs.	$V_{\rm helio}$ (km s^{-1})	$V_{\rm gsr}$ (km s^{-1})	σ_V (km s^{-1})	R_{TD}
···	···	···	···	···	1.1	58.3	87.7	56.7	3.63
···	···	···	···	···	3.1	111.8	140.8	26.4	6.33
···	···	···	···	···	3.2	148.6	177.6	28.8	5.92
007010	18 54 47.17	–30 33 45.0	21.41	0.77	···	169.5	198.6	43.8	···
···	···	···	···	···	2.1	113.4	142.5	60.1	3.48
···	···	···	···	···	2.3	232.8	262.0	63.9	3.33
007350	18 54 58.89	–30 33 39.0	21.11	0.54	···	103.0	132.0	17.5	···
···	···	···	···	···	3.1	88.6	117.6	22.1	7.32
···	···	···	···	···	3.2	127.4	156.4	28.8	5.92
007503	18 54 48.07	–30 33 37.1	19.61	0.74	···	151.2	180.4	8.0	···
···	···	···	···	···	2.1	145.4	174.5	12.7	15.85
···	···	···	···	···	2.2	137.6	166.7	17.6	9.02
···	···	···	···	···	2.3	163.9	193.0	12.6	16.21
007660	18 55 31.94	–30 33 32.8	19.92	0.58	1.1	79.9	109.3	18.9	8.42
007802	18 54 49.11	–30 33 32.0	21.23	0.50	···	94.0	123.1	16.4	···
···	···	···	···	···	2.1	89.3	118.5	37.2	4.91
···	···	···	···	···	2.2	90.6	119.8	50.9	3.92
···	···	···	···	···	2.3	124.5	153.6	31.7	5.52
···	···	···	···	···	3.1	78.0	107.0	25.0	6.61
008078	18 55 35.79	–30 33 26.0	20.34	0.60	1.1	126.7	156.1	24.9	6.63
008125	18 55 00.05	–30 33 26.7	20.24	0.50	···	128.6	157.6	15.8	···
···	···	···	···	···	3.1	140.4	169.4	24.7	6.66
···	···	···	···	···	3.2	120.4	149.4	20.5	7.79
008356	18 54 42.00	–30 33 23.6	20.25	0.49	···	167.1	196.2	9.6	···
···	···	···	···	···	2.1	155.0	184.2	16.1	10.04
···	···	···	···	···	2.2	141.1	170.2	19.5	8.16
···	···	···	···	···	2.3	193.4	222.6	15.1	10.87
008393	18 54 35.63	–30 33 23.2	20.46	0.78	···	–15.9	13.1	19.9	···
···	···	···	···	···	3.1	–71.7	–42.7	22.6	7.18
···	···	···	···	···	3.2	175.0	204.1	41.7	4.52
008521	18 55 09.04	–30 33 20.5	21.22	0.36	3.1	11.1	40.1	48.0	4.09
008528	18 55 26.13	–30 33 19.8	20.78	0.48	1.1	28.1	57.5	44.2	4.34
008703	18 54 57.94	–30 33 17.9	20.75	0.30	···	108.2	137.2	15.2	···
···	···	···	···	···	3.1	97.1	126.1	18.5	8.61
···	···	···	···	···	3.2	131.6	160.6	26.7	6.27
008710	18 54 36.21	–30 33 18.3	21.59	0.36	···	106.6	135.6	19.9	···
···	···	···	···	···	3.1	105.8	134.9	24.5	6.71
···	···	···	···	···	3.2	108.0	137.0	34.1	5.23
008752	18 54 40.32	–30 33 17.4	19.07	0.61	···	–67.4	–38.3	5.4	···
···	···	···	···	···	2.1	–57.5	–28.3	12.0	21.48
···	···	···	···	···	2.2	–79.5	–50.4	12.7	15.78
···	···	···	···	···	2.3	–46.3	–17.1	11.9	22.68
···	···	···	···	···	3.1	–84.7	–55.7	11.9	22.15
···	···	···	···	···	3.2	–70.3	–41.3	11.9	23.03
008820	18 54 50.47	–30 33 16.3	20.53	0.48	···	110.5	139.5	17.1	···
···	···	···	···	···	3.1	113.1	142.1	22.2	7.27
···	···	···	···	···	3.2	106.7	135.7	26.6	6.29
008877	18 55 18.89	–30 33 14.1	21.16	0.67	···	59.1	88.2	26.1	···
···	···	···	···	···	1.1	63.7	93.1	68.0	3.18
···	···	···	···	···	3.1	106.7	135.7	48.3	4.07
···	···	···	···	···	3.2	33.3	62.3	34.8	5.15
009214	18 55 30.44	–30 33 08.1	19.63	0.50	···	145.6	174.6	9.0	···
···	···	···	···	···	3.1	147.2	176.2	12.1	19.82
···	···	···	···	···	3.2	143.7	172.7	13.6	13.16
009258	18 54 33.88	–30 33 09.1	20.60	0.54	···	134.2	163.3	11.8	···
···	···	···	···	···	2.1	114.8	143.9	22.8	7.13
···	···	···	···	···	2.2	116.8	146.0	28.4	5.98
···	···	···	···	···	2.3	148.8	177.9	15.7	10.31
009336	18 55 31.63	–30 33 05.8	19.83	0.62	···	137.5	166.6	8.3	···
···	···	···	···	···	1.1	116.2	145.6	15.6	10.45
···	···	···	···	···	3.1	135.6	164.6	14.2	12.06
···	···	···	···	···	3.2	155.2	184.2	13.5	13.29

Continued on Next Page...

Table 3.10 – 000.1n01.5 (Continued)

ID	$\alpha_{J2000.0}$	$\delta_{J2000.0}$	$I_{\rm Inst}$	$(V-I)_{\rm Inst}$	Obs.	$V_{\rm helio}$ (km s^{-1})	$V_{\rm gsr}$ (km s^{-1})	σ_V (km s^{-1})	R_{TD}
009415	18 55 37.49	–30 33 04.3	19.68	0.58	···	297.0	326.0	9.8	···
···	···	···	···	···	3.1	298.3	327.4	12.9	14.77
···	···	···	···	···	3.2	295.1	324.1	15.1	10.91
009529	18 54 38.51	–30 33 04.5	21.22	0.60	···	95.8	124.8	31.1	···
···	···	···	···	···	3.1	101.6	130.6	39.4	4.71
···	···	···	···	···	3.2	86.3	115.3	50.6	3.94
009665	18 55 31.52	–30 33 00.2	19.42	0.61	1.1	102.1	131.4	16.3	9.84
009710	18 54 43.61	–30 33 01.1	21.46	0.64	···	88.3	117.3	33.1	···
···	···	···	···	···	2.3	171.4	200.5	89.6	2.59
···	···	···	···	···	3.1	88.3	117.3	33.1	5.34
009790	18 55 35.31	–30 32 58.2	21.52	0.46	···	60.6	89.6	34.3	···
···	···	···	···	···	3.1	49.5	78.5	43.3	4.40
···	···	···	···	···	3.2	79.3	108.3	56.0	3.66
010533	18 54 40.73	–30 32 48.3	20.89	0.49	···	180.0	209.0	26.8	···
···	···	···	···	···	2.3	267.3	296.5	63.6	3.34
···	···	···	···	···	3.1	171.7	200.7	37.8	4.85
···	···	···	···	···	3.2	144.6	173.6	47.3	4.13
010558	18 55 19.46	–30 32 46.7	19.26	0.61	···	129.8	158.9	7.3	···
···	···	···	···	···	1.1	141.3	170.6	13.7	12.88
···	···	···	···	···	3.1	121.9	150.9	12.1	19.38
···	···	···	···	···	3.2	128.7	157.7	12.3	17.89
010871	18 54 43.42	–30 32 43.0	20.87	0.56	···	140.0	169.2	19.9	···
···	···	···	···	···	2.1	153.6	182.7	30.9	5.62
···	···	···	···	···	2.2	97.6	126.7	62.8	3.37
···	···	···	···	···	2.3	137.2	166.4	28.7	5.94
010885	18 55 24.32	–30 32 41.4	21.09	0.58	1.1	54.9	84.2	67.7	3.19
011240	18 54 48.89	–30 32 37.4	20.35	0.48	···	154.8	183.9	10.8	···
···	···	···	···	···	2.1	149.3	178.5	16.0	10.10
···	···	···	···	···	2.2	86.7	115.8	34.1	5.23
···	···	···	···	···	2.3	175.5	204.6	16.1	10.02
011383	18 55 29.58	–30 32 34.1	19.73	0.52	1.1	131.1	160.5	18.7	8.51
011727	18 54 46.02	–30 32 30.9	20.56	0.52	···	134.0	163.1	10.3	···
···	···	···	···	···	2.1	124.8	153.9	15.9	10.16
···	···	···	···	···	2.2	105.7	134.9	37.2	4.91
···	···	···	···	···	2.3	145.7	174.9	14.4	11.78
011842	18 55 35.73	–30 32 27.3	19.56	0.54	1.1	112.4	141.8	23.8	6.87
012172	18 55 33.49	–30 32 21.7	21.04	0.51	1.1	84.8	114.2	56.7	3.63
012472	18 54 39.52	–30 32 19.4	19.71	0.53	···	140.2	169.4	7.7	···
···	···	···	···	···	2.1	136.5	165.6	12.4	17.40
···	···	···	···	···	2.2	107.6	136.8	16.3	9.88
···	···	···	···	···	2.3	162.1	191.2	12.2	18.86
012891	18 55 32.70	–30 32 11.9	19.52	0.44	···	129.4	158.5	8.0	···
···	···	···	···	···	1.1	127.8	157.1	17.9	8.91
···	···	···	···	···	3.1	128.2	157.2	12.3	18.15
···	···	···	···	···	3.2	131.8	160.8	13.2	14.04
013001	18 54 46.80	–30 32 12.2	21.22	0.47	···	143.0	172.1	28.7	···
···	···	···	···	···	2.1	123.8	153.0	37.0	4.93
···	···	···	···	···	2.2	55.8	84.9	60.6	3.46
···	···	···	···	···	2.3	325.4	354.5	69.5	3.13
013137	18 55 00.49	–30 32 09.9	21.37	0.50	3.1	28.4	57.4	49.9	3.98
013324	18 55 33.37	–30 32 05.5	20.05	0.47	···	119.9	149.0	9.1	···
···	···	···	···	···	1.1	112.7	142.1	22.0	7.34
···	···	···	···	···	3.1	117.2	146.2	13.0	14.46
···	···	···	···	···	3.2	127.5	156.5	15.6	10.47
013551	18 54 32.57	–30 32 04.6	19.50	0.87	···	138.6	167.7	7.6	···
···	···	···	···	···	2.1	135.3	164.5	17.7	9.01
···	···	···	···	···	2.2	123.2	152.4	24.2	6.77
···	···	···	···	···	2.3	155.2	184.3	15.0	10.98
···	···	···	···	···	3.1	132.1	161.1	14.4	11.77
···	···	···	···	···	3.2	136.8	165.8	17.9	8.90
014016	18 54 41.56	–30 31 58.0	20.61	0.48	···	206.2	235.4	18.2	···
···	···	···	···	···	2.1	223.5	252.6	34.0	5.24

Continued on Next Page...

Table 3.10 – 000.1n01.5 (Continued)

ID	$\alpha_{J2000.0}$	$\delta_{J2000.0}$	$I_{\rm Inst}$	$(V-I)_{\rm Inst}$	Obs.	$V_{\rm helio}$ (km s^{-1})	$V_{\rm gsr}$ (km s^{-1})	σ_V (km s^{-1})	R_{TD}
···	···	···	···	···	2.2	63.1	92.3	53.4	3.79
···	···	···	···	···	2.3	225.7	254.8	23.5	6.95
014017	18 55 33.89	–30 31 56.2	19.05	0.74	1.1	–2.2	27.2	14.2	12.00
014335	18 54 32.14	–30 31 53.6	20.34	0.55	···	142.6	171.6	17.6	···
···	···	···	···	···	3.1	150.6	179.6	19.7	8.10
···	···	···	···	···	3.2	110.0	139.0	39.7	4.68
014530	18 54 51.85	–30 31 50.8	20.34	0.48	···	85.7	114.7	11.5	···
···	···	···	···	···	3.1	72.5	101.5	14.0	12.39
···	···	···	···	···	3.2	114.0	143.0	20.4	7.84
014610	18 54 46.95	–30 31 49.8	19.23	0.49	···	149.9	179.0	7.1	···
···	···	···	···	···	2.1	127.2	156.4	11.9	22.05
···	···	···	···	···	2.2	151.2	180.4	13.5	13.26
···	···	···	···	···	2.3	171.2	200.4	11.9	23.16
014773	18 55 30.72	–30 31 46.4	21.00	0.62	1.1	86.3	115.7	56.9	3.62
015505	18 55 35.23	–30 31 36.4	21.34	0.56	1.1	226.1	255.5	61.6	3.42
015540	18 54 46.30	–30 31 37.6	20.81	0.50	···	51.8	80.8	35.4	···
···	···	···	···	···	3.1	31.0	60.0	40.5	4.62
···	···	···	···	···	3.2	119.0	148.0	72.7	3.03
015632	18 55 25.76	–30 31 35.1	21.27	0.48	···	13.2	42.2	27.0	···
···	···	···	···	···	3.1	6.7	35.7	31.2	5.58
···	···	···	···	···	3.2	32.6	61.6	54.0	3.76
015791	18 55 17.88	–30 31 33.1	20.72	0.46	···	114.6	143.6	21.6	···
···	···	···	···	···	3.1	116.6	145.6	27.5	6.13
···	···	···	···	···	3.2	111.4	140.4	34.7	5.16
015800	18 54 39.14	–30 31 34.1	20.39	0.44	···	148.4	177.6	10.4	···
···	···	···	···	···	2.1	125.6	154.7	15.8	10.26
···	···	···	···	···	2.2	126.0	155.2	31.1	5.59
···	···	···	···	···	2.3	175.9	205.1	15.5	10.54
015950	18 55 36.99	–30 31 30.1	19.57	0.46	···	155.4	184.5	8.3	···
···	···	···	···	···	1.1	143.8	173.2	19.2	8.27
···	···	···	···	···	3.1	148.9	177.9	13.5	13.25
···	···	···	···	···	3.2	166.1	195.1	12.6	16.09
016109	18 54 44.24	–30 31 29.4	20.44	0.51	···	112.5	141.5	17.4	···
···	···	···	···	···	3.1	108.0	137.0	19.9	8.00
···	···	···	···	···	3.2	126.8	155.8	35.8	5.05
016534	18 54 39.38	–30 31 23.3	21.54	0.87	···	110.0	139.2	37.9	···
···	···	···	···	···	2.2	69.1	98.3	59.2	3.52
···	···	···	···	···	2.3	138.5	167.6	49.3	4.01
016939	18 55 28.97	–30 31 16.4	20.97	0.73	1.1	42.1	71.5	55.0	3.71
017067	18 54 29.24	–30 31 16.7	20.01	0.57	···	123.8	152.9	8.1	···
···	···	···	···	···	2.1	145.7	174.8	15.5	10.51
···	···	···	···	···	2.2	90.9	120.1	23.1	7.05
···	···	···	···	···	2.3	128.9	158.0	15.3	10.74
···	···	···	···	···	3.1	113.6	142.6	14.1	12.11
017348	18 55 36.85	–30 31 11.0	20.43	0.45	1.1	62.8	92.2	51.8	3.87
017662	18 54 35.13	–30 31 09.5	20.22	0.51	···	125.7	154.8	10.7	···
···	···	···	···	···	2.1	111.4	140.5	17.4	9.16
···	···	···	···	···	2.2	102.1	131.3	60.6	3.46
···	···	···	···	···	2.3	136.1	165.2	13.9	12.46
017767	18 55 36.43	–30 31 05.9	19.79	0.55	···	123.6	152.8	8.6	···
···	···	···	···	···	1.1	132.3	161.7	15.7	10.31
···	···	···	···	···	3.1	115.9	144.9	13.1	14.30
···	···	···	···	···	3.2	126.5	155.5	16.6	9.67
018045	18 54 30.26	–30 31 04.2	20.54	0.50	···	138.5	167.6	10.8	···
···	···	···	···	···	2.1	122.2	151.4	17.2	9.28
···	···	···	···	···	2.2	76.3	105.4	38.4	4.80
···	···	···	···	···	2.3	160.3	189.4	15.0	11.06
018141	18 55 36.65	–30 31 00.7	20.59	0.53	1.1	120.8	150.2	45.0	4.28
018620	18 55 32.02	–30 30 55.0	19.86	0.62	1.1	67.1	96.4	32.7	5.39
018677	18 54 46.87	–30 30 55.8	21.14	0.52	···	49.9	79.0	31.5	···
···	···	···	···	···	2.3	110.2	139.3	44.3	4.33
···	···	···	···	···	3.1	–11.5	17.5	44.7	4.30

Continued on Next Page...

Table 3.10 – 000.1n01.5 (Continued)

ID	$\alpha_{J2000.0}$	$\delta_{J2000.0}$	$I_{\rm Inst}$	$(V-I)_{\rm Inst}$	Obs.	$V_{\rm helio}$ (km s^{-1})	$V_{\rm gsr}$ (km s^{-1})	σ_V (km s^{-1})	R_{TD}
019139	18 55 39.18	–30 30 48.7	21.06	0.76	···	50.3	79.4	34.0	···
···	···	···	···	···	1.1	66.5	95.9	49.9	3.98
···	···	···	···	···	3.2	36.2	65.2	46.4	4.19
019443	18 54 41.57	–30 30 47.0	21.04	0.58	···	91.3	120.4	33.7	···
···	···	···	···	···	2.1	34.1	63.3	40.3	4.63
···	···	···	···	···	2.2	55.6	84.8	88.2	2.62
···	···	···	···	···	2.3	222.3	251.4	61.1	3.44
020248	18 54 47.07	–30 30 36.3	21.14	0.50	···	110.9	140.0	21.5	···
···	···	···	···	···	2.1	89.9	119.0	42.0	4.50
···	···	···	···	···	2.2	122.5	151.7	70.7	3.09
···	···	···	···	···	2.3	117.7	146.9	26.7	6.28
020260	18 55 38.55	–30 30 34.3	20.35	0.58	1.1	86.2	115.6	36.7	4.96
020653	18 54 39.77	–30 30 30.4	19.60	0.69	···	–203.4	–174.3	9.2	···
···	···	···	···	···	2.1	–198.3	–169.2	22.6	7.18
···	···	···	···	···	2.2	–209.6	–180.5	27.2	6.19
···	···	···	···	···	2.3	–152.1	–123.0	17.4	9.17
···	···	···	···	···	3.1	–259.0	–229.9	18.0	8.83
···	···	···	···	···	3.2	–203.3	–174.3	21.2	7.57
020781	18 55 38.93	–30 30 26.4	21.04	0.44	1.1	51.8	81.2	63.1	3.36
020942	18 54 42.63	–30 30 26.0	20.65	0.51	3.1	–2.0	27.0	35.9	5.04
021112	18 54 35.19	–30 30 23.8	20.40	0.56	···	109.9	139.0	10.4	···
···	···	···	···	···	2.1	130.8	160.0	21.8	7.40
···	···	···	···	···	2.2	76.7	105.8	39.4	4.71
···	···	···	···	···	2.3	132.8	161.9	17.2	9.30
···	···	···	···	···	3.1	73.9	102.9	19.8	8.04
···	···	···	···	···	3.2	94.6	123.6	41.9	4.51
021346	18 55 37.20	–30 30 18.0	21.15	0.48	1.1	71.0	100.4	42.8	4.44
021438	18 54 33.96	–30 30 18.7	21.14	0.56	···	–10.2	18.9	42.8	···
···	···	···	···	···	2.1	–23.4	5.8	66.6	3.23
···	···	···	···	···	2.2	126.1	155.2	98.4	2.41
···	···	···	···	···	3.1	–0.9	28.1	55.8	3.67
022082	18 54 31.05	–30 30 07.6	21.20	0.57	···	12.8	41.9	22.1	···
···	···	···	···	···	2.1	46.3	75.5	45.8	4.23
···	···	···	···	···	2.3	92.9	122.1	67.7	3.19
···	···	···	···	···	3.1	–59.1	–30.1	36.7	4.96
···	···	···	···	···	3.2	45.9	74.9	40.6	4.61
022106	18 55 38.66	–30 30 05.0	19.65	0.61	···	133.7	162.8	14.1	···
···	···	···	···	···	1.1	129.8	159.1	21.2	7.56
···	···	···	···	···	3.2	136.7	165.7	18.8	8.45
022431	18 54 30.48	–30 30 01.7	20.17	0.49	···	105.2	134.3	7.8	···
···	···	···	···	···	2.1	93.9	123.0	17.4	9.13
···	···	···	···	···	2.2	110.0	139.2	36.1	5.02
···	···	···	···	···	2.3	142.1	171.3	15.4	10.61
···	···	···	···	···	3.1	79.6	108.6	13.0	14.60
···	···	···	···	···	3.2	118.3	147.4	21.2	7.57
022449	18 55 36.16	–30 29 59.3	19.93	0.40	1.1	151.4	180.8	21.0	7.63
022793	18 54 40.01	–30 29 56.4	20.84	0.52	···	146.8	176.0	26.2	···
···	···	···	···	···	2.1	155.8	185.0	40.1	4.65
···	···	···	···	···	2.3	140.1	169.3	34.5	5.18
023336	18 54 40.58	–30 29 48.1	19.73	0.55	···	128.5	157.6	8.1	···
···	···	···	···	···	2.1	123.6	152.7	12.4	16.99
···	···	···	···	···	2.2	115.8	145.0	16.8	9.50
···	···	···	···	···	2.3	142.6	171.8	13.6	13.08
023541	18 55 33.51	–30 29 42.9	19.17	0.67	1.1	122.7	152.1	20.4	7.85
023739	18 54 33.01	–30 29 42.2	21.61	0.66	···	71.2	100.3	39.3	···
···	···	···	···	···	2.1	18.9	48.1	52.6	3.83
···	···	···	···	···	2.3	137.3	166.4	59.2	3.52
023921	18 55 31.80	–30 29 37.4	20.41	0.46	1.1	108.8	138.2	29.1	5.88
024303	18 54 45.76	–30 29 33.1	20.42	0.58	···	135.0	164.1	10.9	···
···	···	···	···	···	2.1	125.3	154.4	16.1	10.04
···	···	···	···	···	2.2	154.8	184.0	55.0	3.71
···	···	···	···	···	2.3	164.7	193.9	18.8	8.47

Continued on Next Page...

Table 3.10 – 000.1n01.5 (Continued)

ID	$\alpha_{J2000.0}$	$\delta_{J2000.0}$	$I_{\rm Inst}$	$(V-I)_{\rm Inst}$	Obs.	$V_{\rm helio}$ (km s^{-1})	$V_{\rm gsr}$ (km s^{-1})	σ_V (km s^{-1})	R_{TD}
···	···	···	···	···	3.1	79.3	108.3	38.6	4.78
···	···	···	···	···	3.2	113.4	142.4	36.7	4.96
024572	18 55 39.09	–30 29 26.7	19.54	0.76	1.1	–170.0	–140.6	25.3	6.55
024757	18 55 34.79	–30 29 24.2	20.93	0.49	···	221.2	250.2	79.7	···
···	···	···	···	···	3.1	164.2	193.2	90.5	2.57
···	···	···	···	···	3.2	221.2	250.2	79.7	2.83
024789	18 54 42.00	–30 29 25.7	20.93	0.58	···	109.7	138.8	22.6	···
···	···	···	···	···	2.1	170.9	200.1	33.9	5.25
···	···	···	···	···	2.2	–1.9	27.2	65.5	3.27
···	···	···	···	···	2.3	50.0	79.1	39.2	4.73
···	···	···	···	···	3.1	166.3	195.3	69.5	3.13
025334	18 55 32.29	–30 29 15.8	21.48	0.46	1.1	43.7	73.1	63.9	3.33
025758	18 54 41.85	–30 29 11.4	19.65	0.64	···	153.1	182.3	9.4	···
···	···	···	···	···	2.1	139.0	168.1	13.3	13.66
···	···	···	···	···	2.2	128.3	157.4	51.5	3.89
···	···	···	···	···	2.3	169.9	199.0	13.7	12.85
025791	18 55 28.44	–30 29 09.2	19.62	0.47	1.1	111.1	140.5	14.9	11.08
025960	18 54 45.13	–30 29 07.5	20.95	0.50	···	57.9	86.9	25.0	···
···	···	···	···	···	3.1	54.2	83.2	26.6	6.29
···	···	···	···	···	3.2	85.9	114.9	73.6	3.00
026060	18 54 37.30	–30 29 05.7	21.64	0.71	2.1	99.4	128.5	84.0	2.72
026359	18 54 30.46	–30 29 00.1	21.69	0.79	2.1	73.8	102.9	70.4	3.10
026643	18 54 31.40	–30 28 54.6	21.36	0.79	···	56.6	85.7	25.2	···
···	···	···	···	···	2.1	99.7	128.8	57.8	3.58
···	···	···	···	···	2.2	23.1	52.3	35.7	5.06
···	···	···	···	···	2.3	84.1	113.3	45.3	4.26
026843	18 55 35.15	–30 28 49.3	19.91	0.31	1.1	163.3	192.6	32.0	5.48
026930	18 54 46.05	–30 28 49.2	21.29	0.62	···	117.2	146.3	32.3	···
···	···	···	···	···	2.1	85.7	114.9	70.7	3.09
···	···	···	···	···	2.3	125.4	154.6	36.3	5.00
027195	18 55 29.76	–30 28 42.8	19.94	0.67	···	71.1	100.2	10.9	···
···	···	···	···	···	1.1	83.3	112.7	29.3	5.84
···	···	···	···	···	3.1	60.4	89.4	13.8	12.68
···	···	···	···	···	3.2	92.2	121.2	22.3	7.24
027504	18 54 41.88	–30 28 37.7	20.79	0.46	···	97.3	126.5	21.4	···
···	···	···	···	···	2.1	94.2	123.3	23.2	7.01
···	···	···	···	···	2.3	115.0	144.2	55.0	3.71
027680	18 55 38.06	–30 28 31.0	19.57	0.53	···	100.6	129.6	9.2	···
···	···	···	···	···	1.1	108.0	137.4	24.1	6.80
···	···	···	···	···	3.1	88.1	117.1	13.0	14.75
···	···	···	···	···	3.2	115.4	144.4	15.5	10.52
027754	18 54 41.18	–30 28 31.4	20.94	0.72	···	166.1	195.3	32.1	···
···	···	···	···	···	2.1	153.7	182.8	45.6	4.24
···	···	···	···	···	2.2	117.4	146.6	91.9	2.54
···	···	···	···	···	2.3	178.2	207.4	45.0	4.28
028018	18 54 48.07	–30 28 24.7	20.62	0.46	···	132.2	161.3	29.2	···
···	···	···	···	···	2.2	24.3	53.5	96.8	2.44
···	···	···	···	···	2.3	132.2	161.3	29.2	5.86
028282	18 55 38.73	–30 28 14.0	20.21	0.60	1.1	41.3	70.6	38.6	4.78
028370	18 54 33.47	–30 28 14.9	21.08	0.62	···	107.2	136.4	28.7	···
···	···	···	···	···	2.1	112.6	141.8	33.9	5.25
···	···	···	···	···	2.3	93.6	122.7	54.0	3.76
028638	18 55 39.18	–30 28 08.7	19.87	0.49	1.1	55.2	84.6	35.3	5.10
028875	18 54 30.32	–30 28 07.4	20.77	0.51	···	32.2	61.3	26.4	···
···	···	···	···	···	2.1	30.8	60.0	33.7	5.27
···	···	···	···	···	2.2	34.3	63.5	42.5	4.46
029008	18 55 29.00	–30 28 02.5	21.31	0.58	1.1	50.1	79.4	73.0	3.02
029173	18 54 33.44	–30 28 01.1	20.14	0.44	···	118.6	147.8	14.0	···
···	···	···	···	···	2.1	112.9	142.1	17.3	9.21
···	···	···	···	···	2.2	129.6	158.8	24.0	6.83
029274	18 55 38.95	–30 27 56.9	21.45	0.54	1.1	49.1	78.5	50.2	3.96
029474	18 54 42.59	–30 27 55.4	19.93	0.51	···	140.4	169.5	8.3	···

Continued on Next Page...

Table 3.10 – 000.1n01.5 (Continued)

ID	$\alpha_{J2000.0}$	$\delta_{J2000.0}$	$I_{\rm Inst}$	$(V-I)_{\rm Inst}$	Obs.	$V_{\rm helio}$ (km s^{-1})	$V_{\rm gsr}$ (km s^{-1})	σ_V (km s^{-1})	R_{TD}
···	···	···	···	···	2.1	131.3	160.5	13.9	12.42
···	···	···	···	···	2.2	89.2	118.4	20.4	7.84
···	···	···	···	···	2.3	164.7	193.8	12.0	21.43
029606	18 55 30.43	–30 27 51.1	20.99	0.43	1.1	85.4	114.7	64.7	3.30
029883	18 54 47.15	–30 27 48.3	19.59	0.45	···	148.0	177.1	8.7	···
···	···	···	···	···	2.1	134.7	163.8	14.3	11.82
···	···	···	···	···	2.2	111.5	140.6	18.7	8.51
···	···	···	···	···	2.3	179.3	208.5	13.6	13.04
030178	18 54 29.52	–30 27 42.8	19.16	0.45	···	128.8	157.9	7.7	···
···	···	···	···	···	2.1	137.6	166.8	13.1	14.25
···	···	···	···	···	2.2	113.4	142.5	14.1	12.25
···	···	···	···	···	2.3	133.1	162.3	12.8	15.23
030496	18 55 29.08	–30 27 33.8	19.19	0.71	4.1	137.8	167.4	16.3	9.84
030508	18 54 43.55	–30 27 35.1	19.76	0.55	···	169.9	199.0	10.5	···
···	···	···	···	···	2.1	147.5	176.7	18.7	8.52
···	···	···	···	···	2.2	177.1	206.2	23.4	6.96
···	···	···	···	···	2.3	181.5	210.6	15.1	10.95
030842	18 55 22.22	–30 27 27.6	19.80	0.87	···	131.2	160.8	18.3	···
···	···	···	···	···	1.1	65.3	94.6	33.8	5.26
···	···	···	···	···	4.1	158.8	188.4	21.8	7.38
031223	18 55 33.34	–30 27 21.4	21.59	0.54	1.1	63.9	93.3	20.2	7.90
031378	18 55 15.38	–30 27 19.6	19.72	0.39	4.1	154.4	184.0	16.3	9.83
031539	18 55 36.61	–30 27 15.6	20.87	0.52	1.1	60.0	89.4	57.6	3.59
031885	18 54 43.04	–30 27 11.6	19.27	0.77	···	–62.9	–33.7	10.1	···
···	···	···	···	···	2.1	–59.0	–29.8	15.7	10.34
···	···	···	···	···	2.2	–68.5	–39.3	21.7	7.43
···	···	···	···	···	2.3	–64.0	–34.8	16.8	9.49
031919	18 54 37.67	–30 27 11.3	21.12	0.45	4.1	176.2	205.8	37.0	4.93
032018	18 54 38.81	–30 27 09.3	20.21	0.55	4.1	184.8	214.4	36.9	4.94
032170	18 54 39.15	–30 27 05.9	20.09	0.51	···	131.6	160.8	10.8	···
···	···	···	···	···	2.1	132.6	161.7	14.9	11.09
···	···	···	···	···	2.2	76.5	105.7	28.9	5.91
···	···	···	···	···	2.3	152.8	182.0	18.5	8.58
032271	18 55 35.05	–30 27 01.6	20.08	0.52	1.1	63.6	93.0	31.8	5.50
032502	18 54 46.16	–30 26 59.5	21.15	0.48	···	59.5	88.6	36.5	···
···	···	···	···	···	2.2	9.8	39.0	49.0	4.03
···	···	···	···	···	2.3	121.6	150.7	54.8	3.72
032667	18 55 38.17	–30 26 55.3	20.20	0.44	1.1	43.4	72.8	35.1	5.12
032731	18 54 50.39	–30 26 56.0	19.04	0.67	4.1	25.8	55.4	12.6	16.39
032874	18 54 33.41	–30 26 54.2	19.19	0.66	4.1	–85.6	–56.0	14.7	11.33
032971	18 54 47.45	–30 26 52.6	21.23	0.49	···	73.7	102.9	32.2	···
···	···	···	···	···	2.1	112.8	141.9	58.2	3.56
···	···	···	···	···	2.2	2.8	31.9	46.4	4.19
···	···	···	···	···	2.3	178.3	207.4	69.8	3.12
033163	18 54 34.91	–30 26 50.1	20.39	0.57	4.1	171.8	201.4	19.6	8.14
033265	18 55 37.33	–30 26 46.6	21.07	0.48	1.1	57.4	86.8	69.8	3.12
033590	18 54 42.36	–30 26 44.4	20.69	0.46	···	162.6	191.8	16.9	···
···	···	···	···	···	2.1	157.4	186.5	20.9	7.66
···	···	···	···	···	2.2	180.1	209.3	48.5	4.06
···	···	···	···	···	2.3	168.4	197.6	36.0	5.03
033705	18 55 25.23	–30 26 41.5	21.12	0.45	1.1	79.6	108.9	58.5	3.55
033736	18 54 32.79	–30 26 42.7	19.65	0.72	4.1	–113.5	–83.9	16.1	10.01
034042	18 55 31.22	–30 26 36.2	21.69	0.48	1.1	27.1	56.5	53.4	3.79
034106	18 54 48.96	–30 26 36.9	20.60	0.52	···	126.0	155.2	19.7	···
···	···	···	···	···	2.1	132.8	162.0	27.3	6.17
···	···	···	···	···	2.2	82.3	111.4	55.4	3.69
···	···	···	···	···	2.3	131.6	160.7	33.0	5.35
034167	18 55 34.04	–30 26 34.3	20.51	0.46	4.1	252.9	282.5	55.2	3.70
034535	18 55 37.51	–30 26 29.7	19.74	0.47	···	133.9	163.4	14.3	···
···	···	···	···	···	1.1	102.3	131.7	19.5	8.16
···	···	···	···	···	4.1	170.5	200.1	21.0	7.63
034576	18 54 39.44	–30 26 31.3	21.33	0.68	···	203.8	232.9	28.0	···

Continued on Next Page...

Table 3.10 – 000.1n01.5 (Continued)

ID	$\alpha_{J2000.0}$	$\delta_{J2000.0}$	$I_{\rm Inst}$	$(V-I)_{\rm Inst}$	Obs.	$V_{\rm helio}$ (km s^{-1})	$V_{\rm gsr}$ (km s^{-1})	σ_V (km s^{-1})	R_{TD}
···	···	···	···	···	2.1	221.4	250.6	41.6	4.53
···	···	···	···	···	2.2	239.6	268.7	50.6	3.94
···	···	···	···	···	2.3	123.5	152.6	57.6	3.59
035088	18 54 39.53	–30 26 25.2	20.90	0.53	···	125.7	154.9	18.8	···
···	···	···	···	···	2.1	142.6	171.8	31.2	5.58
···	···	···	···	···	2.2	86.0	115.1	46.2	4.20
···	···	···	···	···	2.3	126.6	155.8	27.2	6.18
035350	18 54 31.19	–30 26 21.4	20.77	0.59	4.1	108.6	138.2	49.5	4.00
035524	18 54 40.36	–30 26 19.0	19.86	0.34	···	49.0	78.2	12.5	···
···	···	···	···	···	2.1	32.3	61.4	22.6	7.17
···	···	···	···	···	2.2	24.2	53.3	28.4	5.98
···	···	···	···	···	2.3	88.7	117.9	22.5	7.20
···	···	···	···	···	4.1	36.1	65.7	29.1	5.88
035584	18 55 37.07	–30 26 16.4	20.57	0.51	···	80.1	109.6	29.2	···
···	···	···	···	···	1.1	38.9	68.3	36.4	4.99
···	···	···	···	···	4.1	154.9	184.5	49.0	4.03
035966	18 54 47.56	–30 26 13.6	21.08	0.58	···	109.1	138.2	45.8	···
···	···	···	···	···	2.1	95.2	124.3	65.8	3.26
···	···	···	···	···	2.3	122.2	151.3	63.9	3.33
036088	18 55 23.41	–30 26 10.8	21.39	0.63	4.1	137.9	167.5	87.4	2.64
036298	18 55 28.27	–30 26 07.4	19.27	0.56	···	127.3	156.8	9.9	···
···	···	···	···	···	1.1	107.1	136.5	14.4	11.70
···	···	···	···	···	4.1	145.5	175.1	13.7	12.91
036349	18 54 32.59	–30 26 08.4	21.22	0.61	···	123.7	152.8	19.5	···
···	···	···	···	···	2.1	217.7	246.9	32.9	5.37
···	···	···	···	···	2.2	–28.3	0.8	35.2	5.11
···	···	···	···	···	2.3	163.9	193.0	33.5	5.29
036774	18 54 37.58	–30 26 02.2	19.77	0.44	···	153.6	182.7	8.9	···
···	···	···	···	···	2.1	148.9	178.0	13.2	14.06
···	···	···	···	···	2.2	114.7	143.8	22.8	7.13
···	···	···	···	···	2.3	174.2	203.4	14.2	11.97
036824	18 55 27.47	–30 25 59.8	19.83	0.43	1.1	31.7	61.1	24.7	6.66
037077	18 54 50.88	–30 25 57.4	20.35	0.48	4.1	–29.3	0.3	47.3	4.13
037170	18 54 40.77	–30 25 56.1	20.40	0.51	···	140.8	170.1	13.3	···
···	···	···	···	···	2.1	143.0	172.2	23.2	7.01
···	···	···	···	···	2.2	19.1	48.2	40.0	4.66
···	···	···	···	···	2.3	222.4	251.6	25.1	6.58
···	···	···	···	···	4.1	104.1	133.8	25.3	6.55
037173	18 55 34.67	–30 25 54.1	20.48	0.49	1.1	46.4	75.8	35.4	5.09
037566	18 55 06.20	–30 25 49.6	20.73	0.61	4.1	167.2	196.8	34.4	5.19
037651	18 54 38.38	–30 25 49.2	21.02	0.47	···	160.2	189.4	27.5	···
···	···	···	···	···	2.1	151.5	180.6	33.1	5.34
···	···	···	···	···	2.3	172.5	201.6	72.7	3.03
···	···	···	···	···	4.1	185.5	215.1	67.2	3.21
037991	18 55 21.98	–30 25 42.8	20.04	0.51	1.1	93.5	122.9	18.3	8.67
038136	18 54 54.09	–30 25 41.7	20.51	0.40	4.1	262.5	292.1	67.5	3.20
038263	18 54 35.44	–30 25 40.3	20.10	0.49	···	139.0	168.2	10.3	···
···	···	···	···	···	2.1	130.4	159.5	15.6	10.41
···	···	···	···	···	2.2	100.2	129.4	27.5	6.14
···	···	···	···	···	2.3	160.9	190.1	15.9	10.18
038420	18 55 23.86	–30 25 36.3	21.41	0.67	4.1	–35.6	–6.0	46.9	4.16
038426	18 55 35.52	–30 25 35.7	19.87	0.49	···	98.7	128.2	12.0	···
···	···	···	···	···	1.1	73.4	102.8	16.3	9.85
···	···	···	···	···	4.1	128.6	158.2	17.7	8.98
038480	18 55 19.33	–30 25 35.7	21.06	0.38	4.1	64.7	94.4	76.4	2.92
038492	18 54 44.50	–30 25 36.5	21.15	0.57	4.1	21.0	50.7	50.4	3.95
038546	18 54 51.54	–30 25 35.4	20.18	0.57	4.1	167.0	196.6	16.7	9.60
038723	18 54 33.92	–30 25 32.9	19.71	0.74	···	46.5	75.8	8.6	···
···	···	···	···	···	2.1	37.4	66.6	13.9	12.51
···	···	···	···	···	2.2	31.5	60.7	20.0	7.98
···	···	···	···	···	2.3	66.5	95.7	17.8	8.92
···	···	···	···	···	4.1	54.6	84.3	19.3	8.24

Continued on Next Page...

Table 3.10 – 000.1n01.5 (Continued)

ID	$\alpha_{J2000.0}$	$\delta_{J2000.0}$	$I_{\rm Inst}$	$(V-I)_{\rm Inst}$	Obs.	$V_{\rm helio}$ (km s^{-1})	$V_{\rm gsr}$ (km s^{-1})	σ_V (km s^{-1})	R_{TD}
038871	18 55 13.40	–30 25 29.2	20.75	0.39	4.1	189.1	218.7	63.1	3.36
038975	18 55 35.91	–30 25 26.2	19.06	0.56	1.1	148.2	177.6	15.0	10.98
039274	18 55 36.08	–30 25 21.0	19.71	0.41	1.1	98.9	128.3	19.8	8.04
039408	18 54 42.00	–30 25 20.6	19.11	0.70	···	11.0	40.1	8.5	···
···	···	···	···	···	2.1	–3.3	25.8	13.6	13.05
···	···	···	···	···	2.2	–5.5	23.6	21.8	7.38
···	···	···	···	···	2.3	29.0	58.1	12.7	15.68
039635	18 55 00.10	–30 25 16.9	21.21	0.43	4.1	–37.3	–7.7	94.3	2.49
039695	18 55 32.12	–30 25 14.8	21.10	0.60	4.1	13.9	43.5	60.1	3.48
039818	18 55 36.58	–30 25 12.7	21.17	0.51	1.1	62.9	92.3	43.0	4.42
039855	18 54 44.82	–30 25 14.1	20.02	0.39	···	157.4	186.5	12.2	···
···	···	···	···	···	2.1	163.6	192.7	14.9	11.11
···	···	···	···	···	2.2	74.8	103.9	37.0	4.93
···	···	···	···	···	2.3	178.5	207.6	25.6	6.49
040150	18 55 36.75	–30 25 06.9	21.12	0.82	1.1	40.9	70.3	48.0	4.09
040165	18 54 34.52	–30 25 08.8	20.20	0.41	···	171.0	200.2	9.0	···
···	···	···	···	···	2.1	180.3	209.5	15.8	10.24
···	···	···	···	···	2.2	182.1	211.2	29.9	5.76
···	···	···	···	···	2.3	163.4	192.6	13.8	12.77
···	···	···	···	···	4.1	166.1	195.8	22.6	7.16
040180	18 55 32.77	–30 25 06.4	20.00	0.54	4.1	172.0	201.6	25.6	6.49
040376	18 54 45.03	–30 25 04.6	20.73	0.51	4.1	130.0	159.6	64.1	3.32
040469	18 54 35.56	–30 25 03.1	20.46	0.45	···	132.7	162.0	10.4	···
···	···	···	···	···	2.1	169.5	198.7	19.6	8.13
···	···	···	···	···	2.2	24.6	53.7	28.8	5.92
···	···	···	···	···	2.3	147.3	176.4	18.8	8.46
···	···	···	···	···	4.1	130.2	159.8	19.4	8.22
040519	18 55 39.16	–30 24 59.9	19.27	0.58	1.1	–80.7	–51.3	16.9	9.46
040605	18 55 01.83	–30 25 00.1	20.34	0.64	4.1	196.1	225.7	46.9	4.16
040962	18 55 37.26	–30 24 52.9	20.84	0.46	1.1	48.9	78.3	45.9	4.22
041257	18 54 41.64	–30 24 50.9	20.96	0.46	···	156.5	185.6	25.9	···
···	···	···	···	···	2.1	104.2	133.3	41.1	4.57
···	···	···	···	···	2.3	190.8	219.9	33.3	5.32
041375	18 55 04.99	–30 24 48.6	20.08	0.49	4.1	139.6	169.2	28.4	5.99
041441	18 55 25.83	–30 24 46.8	21.25	0.57	···	38.0	67.6	40.0	···
···	···	···	···	···	1.1	91.0	120.4	71.1	3.08
···	···	···	···	···	4.1	13.5	43.2	48.3	4.07
041739	18 54 58.69	–30 24 43.2	19.44	0.79	4.1	89.0	118.6	19.3	8.24
041837	18 54 48.88	–30 24 42.0	21.08	0.54	···	164.2	193.4	27.1	···
···	···	···	···	···	2.1	164.2	193.4	27.1	6.20
···	···	···	···	···	2.2	104.7	133.8	95.8	2.46
041886	18 55 33.60	–30 24 39.8	20.99	0.60	1.1	96.1	125.4	38.6	4.78
042261	18 54 48.41	–30 24 35.7	20.43	0.18	···	–24.9	4.2	12.4	···
···	···	···	···	···	2.1	–31.0	–1.9	17.2	9.29
···	···	···	···	···	2.2	–27.5	1.7	30.2	5.72
···	···	···	···	···	2.3	–13.6	15.5	22.0	7.33
042293	18 55 01.07	–30 24 34.8	21.02	0.56	4.1	154.5	184.1	31.3	5.57
042350	18 54 53.45	–30 24 33.9	20.92	0.66	4.1	103.1	132.7	25.2	6.57
042521	18 55 14.79	–30 24 30.2	20.15	0.48	1.1	126.9	156.3	17.0	9.37
042554	18 54 40.63	–30 24 30.8	20.03	0.43	···	176.8	205.9	10.7	···
···	···	···	···	···	2.1	167.7	196.8	15.8	10.24
···	···	···	···	···	2.2	176.5	205.7	20.9	7.66
···	···	···	···	···	2.3	191.9	221.1	20.2	7.89
043043	18 55 32.99	–30 24 21.6	21.51	0.53	1.1	34.4	63.8	73.3	3.01
043054	18 54 47.35	–30 24 23.2	21.25	0.60	···	95.8	125.0	23.8	···
···	···	···	···	···	2.1	167.0	196.2	50.6	3.94
···	···	···	···	···	2.2	95.0	124.1	33.4	5.31
···	···	···	···	···	2.3	156.8	185.9	67.5	3.20
···	···	···	···	···	4.1	–65.7	–36.1	63.1	3.36
043173	18 54 39.35	–30 24 21.1	20.14	0.50	4.1	179.0	208.6	34.9	5.14
043258	18 54 58.02	–30 24 19.3	19.95	0.45	···	156.1	185.7	17.8	···
···	···	···	···	···	4.1	166.0	195.6	19.7	8.08

Continued on Next Page...

Table 3.10 – 000.1n01.5 (Continued)

ID	$\alpha_{J2000.0}$	$\delta_{J2000.0}$	$I_{\rm Inst}$	$(V-I)_{\rm Inst}$	Obs.	$V_{\rm helio}$ (km s^{-1})	$V_{\rm gsr}$ (km s^{-1})	σ_V (km s^{-1})	R_{TD}
···	···	···	···	···	4.1	113.2	142.8	41.0	4.58
043386	18 54 43.09	–30 24 18.2	20.39	0.47	···	151.0	180.3	18.3	···
···	···	···	···	···	2.1	148.7	177.8	24.7	6.68
···	···	···	···	···	2.2	264.8	294.0	82.4	2.76
···	···	···	···	···	2.3	165.3	194.4	69.2	3.14
···	···	···	···	···	4.1	151.7	181.3	29.7	5.79
043425	18 55 38.42	–30 24 15.8	19.68	0.71	1.1	119.9	149.3	18.5	8.59
043609	18 54 28.64	–30 24 15.6	19.57	0.68	4.1	–31.8	–2.2	14.7	11.33
043794	18 55 29.99	–30 24 10.9	20.12	0.85	4.1	11.5	41.1	17.3	9.23
043847	18 54 48.66	–30 24 11.6	20.72	0.50	···	119.8	148.9	24.2	···
···	···	···	···	···	2.1	49.5	78.6	45.5	4.25
···	···	···	···	···	2.3	147.5	176.7	28.6	5.96
043874	18 55 31.69	–30 24 09.7	19.99	0.50	1.1	108.2	137.6	27.6	6.12
043956	18 54 28.21	–30 24 10.5	21.30	0.59	4.1	115.6	145.2	93.3	2.51
044116	18 55 19.82	–30 24 06.7	20.09	0.47	4.1	133.4	163.0	19.8	8.04
044185	18 55 18.75	–30 24 05.5	20.61	0.51	4.1	138.2	167.8	27.3	6.16
044290	18 54 43.02	–30 24 04.8	20.43	0.44	···	156.4	185.5	32.1	···
···	···	···	···	···	2.1	140.1	169.3	37.3	4.90
···	···	···	···	···	2.3	202.5	231.6	62.8	3.37
044326	18 55 28.06	–30 24 02.8	20.42	0.47	1.1	67.0	96.4	17.8	8.95
044331	18 54 54.97	–30 24 04.0	21.65	0.58	4.1	105.6	135.2	63.1	3.36
044485	18 55 05.53	–30 24 00.9	19.53	0.70	4.1	46.8	76.4	15.2	10.80
044487	18 55 18.29	–30 24 00.4	20.59	0.44	4.1	66.5	96.1	34.3	5.21
044543	18 54 43.54	–30 24 00.5	19.79	0.34	4.1	147.6	177.2	14.2	11.98
044591	18 54 30.23	–30 23 59.8	19.76	0.65	···	144.8	174.0	8.4	···
···	···	···	···	···	2.1	128.2	157.4	12.8	15.37
···	···	···	···	···	2.2	150.0	179.2	19.9	8.03
···	···	···	···	···	2.3	160.7	189.8	13.4	13.57
044610	18 54 59.13	–30 23 58.9	20.81	0.50	4.1	134.6	164.3	72.3	3.04
044660	18 55 39.04	–30 23 56.4	20.83	0.49	1.1	75.3	104.7	35.3	5.10
044719	18 55 07.34	–30 23 56.6	21.17	0.54	4.1	133.7	163.3	27.1	6.21
044753	18 55 09.85	–30 23 55.7	20.47	0.46	4.1	70.0	99.6	17.2	9.25
044936	18 55 37.41	–30 23 50.4	20.14	0.54	1.1	81.2	110.6	41.3	4.55
044939	18 55 16.75	–30 23 51.3	21.35	0.51	4.1	170.8	200.5	45.9	4.22
044990	18 55 17.17	–30 23 50.2	19.34	0.50	4.1	127.9	157.5	12.3	17.67
045014	18 54 31.81	–30 23 51.1	20.43	0.44	···	151.4	180.7	9.0	···
···	···	···	···	···	2.1	144.6	173.7	14.0	12.41
···	···	···	···	···	2.2	99.8	128.9	30.2	5.72
···	···	···	···	···	2.3	186.6	215.7	16.5	9.74
···	···	···	···	···	4.1	136.1	165.7	20.2	7.90
045350	18 55 39.21	–30 23 41.9	19.83	0.41	1.1	74.6	104.0	27.0	6.22
045463	18 54 48.45	–30 23 42.1	19.14	0.72	···	16.6	45.8	6.9	···
···	···	···	···	···	2.1	11.1	40.2	12.2	18.72
···	···	···	···	···	2.2	–2.7	26.5	18.6	8.57
···	···	···	···	···	2.3	29.5	58.7	13.3	13.68
···	···	···	···	···	4.1	19.9	49.5	13.0	14.52
045507	18 55 11.17	–30 23 40.5	21.12	0.63	4.1	131.2	160.9	39.2	4.73
045657	18 55 36.72	–30 23 36.7	19.48	0.54	1.1	129.1	158.5	17.3	9.24
045952	18 55 34.41	–30 23 32.1	20.51	0.43	4.1	192.8	222.4	21.2	7.58
045978	18 55 34.81	–30 23 31.6	21.12	0.49	4.1	94.9	124.5	40.2	4.64
046121	18 55 13.96	–30 23 30.3	19.22	0.75	4.1	136.7	166.3	13.5	13.33
046153	18 54 57.27	–30 23 30.4	19.95	0.50	4.1	150.6	180.2	18.8	8.45
046164	18 55 20.88	–30 23 29.4	20.85	0.75	1.1	37.4	66.8	42.8	4.44
046226	18 54 48.20	–30 23 29.3	21.49	0.48	2.2	18.5	47.7	56.7	3.63
046266	18 54 41.84	–30 23 28.9	21.32	0.51	4.1	174.9	204.5	56.5	3.64
046456	18 55 16.27	–30 23 24.2	19.44	0.76	···	124.6	154.1	10.0	···
···	···	···	···	···	1.1	108.1	137.5	15.7	10.33
···	···	···	···	···	4.1	136.0	165.6	13.0	14.48
046592	18 54 32.42	–30 23 22.9	21.46	0.60	4.1	77.3	106.9	40.0	4.66
046613	18 54 42.48	–30 23 22.4	20.68	0.64	2.1	78.9	108.0	43.9	4.36
046819	18 55 37.35	–30 23 16.5	19.54	0.73	1.1	133.5	162.9	18.8	8.44
046984	18 54 46.30	–30 23 15.3	20.45	0.55	···	169.1	198.2	16.8	···

Continued on Next Page...

Table 3.10 – 000.1n01.5 (Continued)

ID	$\alpha_{J2000.0}$	$\delta_{J2000.0}$	$I_{\rm Inst}$	$(V-I)_{\rm Inst}$	Obs.	$V_{\rm helio}$ (km s^{-1})	$V_{\rm gsr}$ (km s^{-1})	σ_V (km s^{-1})	R_{TD}
···	···	···	···	···	2.1	133.7	162.8	23.7	6.90
···	···	···	···	···	2.2	174.7	203.9	51.7	3.88
···	···	···	···	···	2.3	213.3	242.4	26.9	6.24
047057	18 55 11.85	–30 23 13.1	21.46	0.78	4.1	143.7	173.3	45.8	4.23
047126	18 55 12.95	–30 23 11.8	21.16	0.44	4.1	89.9	119.5	38.9	4.75
047280	18 55 06.71	–30 23 09.1	21.55	0.69	4.1	220.2	249.8	62.6	3.38
047301	18 54 55.66	–30 23 09.2	19.37	0.68	4.1	18.9	48.5	12.7	15.83
047387	18 54 45.76	–30 23 07.9	20.91	0.47	4.1	139.9	169.5	50.9	3.92
047486	18 54 47.74	–30 23 05.9	20.49	0.43	···	98.8	128.0	14.3	···
···	···	···	···	···	2.1	112.4	141.5	19.2	8.29
···	···	···	···	···	2.2	36.3	65.5	27.5	6.14
···	···	···	···	···	2.3	153.9	183.0	34.5	5.18
047688	18 55 12.41	–30 23 01.8	19.58	0.62	4.1	38.2	67.8	12.9	14.89
047690	18 55 36.58	–30 23 00.8	19.88	0.42	1.1	133.7	163.0	23.9	6.85
047805	18 55 07.87	–30 23 00.2	21.40	0.51	4.1	203.6	233.2	65.8	3.26
047883	18 54 37.30	–30 22 59.8	19.16	0.63	4.1	96.5	126.2	13.3	13.83
047913	18 54 48.06	–30 22 59.1	20.49	0.52	···	114.9	144.1	18.0	···
···	···	···	···	···	2.1	106.8	136.0	23.4	6.98
···	···	···	···	···	2.2	100.3	129.5	40.3	4.63
···	···	···	···	···	2.3	152.0	181.1	39.4	4.71
048124	18 55 29.59	–30 22 54.2	20.71	0.59	1.1	58.6	87.9	56.3	3.65
048242	18 54 48.40	–30 22 53.5	21.32	0.48	···	38.2	67.4	42.3	···
···	···	···	···	···	2.1	23.6	52.7	52.2	3.85
···	···	···	···	···	2.3	66.2	95.4	72.3	3.04
048508	18 55 37.91	–30 22 46.6	20.56	0.52	···	109.5	139.1	22.2	···
···	···	···	···	···	1.1	9.7	39.1	43.0	4.42
···	···	···	···	···	4.1	145.6	175.2	25.9	6.43
048549	18 55 14.80	–30 22 46.6	20.46	0.75	4.1	–204.6	–175.0	31.6	5.53
048581	18 55 36.42	–30 22 45.1	20.28	0.48	4.1	152.8	182.4	19.8	8.06
048607	18 54 32.61	–30 22 46.6	21.18	0.70	···	206.1	235.2	38.4	···
···	···	···	···	···	2.1	153.8	183.0	53.4	3.79
···	···	···	···	···	2.3	262.0	291.1	55.2	3.70
049005	18 54 52.31	–30 22 39.3	20.40	0.49	4.1	204.9	234.5	39.9	4.67
049075	18 54 39.32	–30 22 38.5	20.85	0.59	2.1	18.1	47.2	36.7	4.96
049119	18 55 08.32	–30 22 36.9	20.58	0.49	4.1	139.5	169.1	40.1	4.65
049217	18 55 15.18	–30 22 34.9	19.42	0.41	1.1	154.1	183.5	13.8	12.64
049578	18 54 48.00	–30 22 29.2	19.20	0.50	···	253.0	282.3	12.3	···
···	···	···	···	···	2.1	275.5	304.7	18.7	8.52
···	···	···	···	···	2.2	239.3	268.4	33.1	5.34
···	···	···	···	···	2.3	229.4	258.5	30.8	5.63
···	···	···	···	···	4.1	237.5	267.1	23.9	6.86
049593	18 55 20.44	–30 22 27.8	20.24	0.70	4.1	22.5	52.2	22.4	7.22
049649	18 55 37.81	–30 22 26.0	20.29	0.44	1.1	60.4	89.8	27.5	6.14
049864	18 54 30.03	–30 22 24.1	20.86	0.62	4.1	119.5	149.1	37.3	4.90
049945	18 54 46.81	–30 22 22.3	20.63	0.52	···	136.2	165.4	15.8	···
···	···	···	···	···	2.1	149.5	178.6	22.0	7.34
···	···	···	···	···	2.3	124.7	153.9	28.0	6.05
···	···	···	···	···	4.1	117.1	146.7	38.3	4.81
050135	18 55 21.61	–30 22 17.6	19.42	0.45	···	120.9	150.4	8.9	···
···	···	···	···	···	1.1	128.4	157.7	12.7	15.68
···	···	···	···	···	4.1	113.8	143.4	12.5	16.59
050153	18 54 49.87	–30 22 18.3	21.03	0.60	4.1	104.9	134.5	43.3	4.40
050158	18 55 14.38	–30 22 17.5	20.85	0.45	4.1	56.2	85.8	28.8	5.93
050318	18 54 38.29	–30 22 15.6	19.14	0.52	···	176.5	205.6	9.3	···
···	···	···	···	···	2.1	176.6	205.8	13.4	13.43
···	···	···	···	···	2.2	188.7	217.9	31.9	5.49
···	···	···	···	···	2.3	173.9	203.1	14.0	12.32
050439	18 55 04.47	–30 22 12.4	20.50	0.52	4.1	66.9	96.5	21.2	7.57
050577	18 54 49.48	–30 22 10.3	21.32	0.49	4.1	–42.6	–13.0	66.0	3.25
050633	18 55 30.78	–30 22 07.8	20.80	0.61	1.1	65.1	94.5	80.8	2.80
050724	18 54 47.89	–30 22 08.0	20.71	0.51	···	197.0	226.2	34.6	···
···	···	···	···	···	2.1	210.8	239.9	53.2	3.80

Continued on Next Page...

Table 3.10 – 000.1n01.5 (Continued)

ID	$\alpha_{J2000.0}$	$\delta_{J2000.0}$	$I_{\rm Inst}$	$(V-I)_{\rm Inst}$	Obs.	$V_{\rm helio}$ (km s^{-1})	$V_{\rm gsr}$ (km s^{-1})	σ_V (km s^{-1})	R_{TD}
···	···	···	···	···	2.3	187.0	216.2	45.5	4.25
050936	18 54 56.86	–30 22 04.0	20.15	0.49	4.1	112.9	142.5	19.5	8.17
050996	18 55 35.94	–30 22 01.5	19.94	0.52	···	130.7	160.2	12.3	···
···	···	···	···	···	1.1	66.9	96.3	25.0	6.60
···	···	···	···	···	4.1	150.8	180.4	14.1	12.22
051040	18 54 44.79	–30 22 02.6	20.35	0.38	···	152.5	181.6	41.7	···
···	···	···	···	···	2.1	85.8	115.0	66.3	3.24
···	···	···	···	···	2.3	196.0	225.2	53.6	3.78
051336	18 54 44.03	–30 21 56.9	19.20	0.62	···	–31.2	–1.8	9.4	···
···	···	···	···	···	2.1	–5.3	23.8	18.0	8.84
···	···	···	···	···	2.2	14.2	43.4	51.1	3.91
···	···	···	···	···	2.3	10.1	39.2	21.6	7.46
···	···	···	···	···	4.1	–63.6	–34.0	13.2	14.02
051344	18 55 16.14	–30 21 55.7	19.81	0.43	1.1	155.2	184.6	14.0	12.33
051451	18 54 56.34	–30 21 54.5	20.80	0.55	4.1	136.9	166.5	33.4	5.31
051645	18 55 20.95	–30 21 50.0	20.49	0.52	···	102.9	132.4	15.1	···
···	···	···	···	···	1.1	82.1	111.5	24.4	6.73
···	···	···	···	···	4.1	115.6	145.2	19.1	8.32
051885	18 54 44.68	–30 21 47.1	21.18	0.45	···	30.9	60.1	72.7	···
···	···	···	···	···	2.1	30.9	60.1	72.7	3.03
···	···	···	···	···	2.3	102.1	131.2	84.0	2.72
052179	18 55 36.09	–30 21 40.6	20.48	0.77	1.1	3.2	32.5	50.0	3.97
052290	18 54 49.08	–30 21 40.7	21.00	0.46	···	80.4	109.6	23.6	···
···	···	···	···	···	2.1	65.8	94.9	30.2	5.71
···	···	···	···	···	2.2	31.9	61.0	69.5	3.13
···	···	···	···	···	2.3	162.2	191.3	54.8	3.72
···	···	···	···	···	4.1	72.6	102.3	80.4	2.81
052457	18 54 36.41	–30 21 38.1	19.45	0.65	4.1	125.5	155.1	16.4	9.78
052893	18 54 39.88	–30 21 31.2	20.33	0.47	···	136.1	165.5	15.6	···
···	···	···	···	···	2.1	165.1	194.3	25.3	6.55
···	···	···	···	···	2.2	77.0	106.2	56.7	3.63
···	···	···	···	···	2.3	236.6	265.7	50.4	3.95
···	···	···	···	···	4.1	100.3	129.9	23.2	7.02
053742	18 54 48.92	–30 21 16.1	20.74	0.44	···	101.5	130.6	20.3	···
···	···	···	···	···	2.1	84.0	113.1	39.4	4.71
···	···	···	···	···	2.2	60.5	89.7	48.0	4.09
···	···	···	···	···	2.3	122.8	152.0	27.1	6.20
054021	18 54 40.06	–30 21 11.1	19.93	0.43	···	194.8	223.9	23.2	···
···	···	···	···	···	2.1	141.1	170.3	33.2	5.33
···	···	···	···	···	2.3	245.8	274.9	32.4	5.43
054274	18 55 33.35	–30 21 03.9	20.66	0.46	···	121.7	151.2	17.9	···
···	···	···	···	···	1.1	119.5	148.9	26.3	6.35
···	···	···	···	···	4.1	123.7	153.3	24.6	6.70
054307	18 55 29.42	–30 21 03.4	20.55	0.46	4.1	108.3	137.9	25.4	6.52
054328	18 54 46.08	–30 21 04.5	19.55	0.77	···	118.1	147.2	12.0	···
···	···	···	···	···	2.1	110.1	139.2	15.2	10.82
···	···	···	···	···	2.2	123.2	152.4	32.0	5.47
···	···	···	···	···	2.3	135.8	164.9	24.4	6.74
054748	18 55 02.37	–30 20 55.8	19.97	0.46	4.1	117.9	147.5	38.6	4.78
055085	18 54 37.52	–30 20 49.1	19.89	0.47	···	148.1	177.2	56.5	···
···	···	···	···	···	2.1	83.4	112.5	98.9	2.40
···	···	···	···	···	2.3	148.1	177.2	56.5	3.64
055190	18 55 25.26	–30 20 45.4	19.57	0.76	4.1	131.1	160.7	13.5	13.20
055278	18 54 41.42	–30 20 44.9	21.23	0.77	4.1	38.4	68.1	81.6	2.78
055315	18 54 36.85	–30 20 43.0	19.69	0.69	···	109.6	139.1	16.9	···
···	···	···	···	···	2.2	49.5	78.6	68.9	3.15
···	···	···	···	···	2.3	196.9	226.0	71.7	3.06
···	···	···	···	···	4.1	108.2	137.8	18.0	8.83

Note: For the objects with multiple observations, each measurement's kinematic data is given on its own line, preceded by a line listing the object's identification number, equatorial coordinates, I and $(V-I)$ magnitudes, and kinematic data (calculated as weighted averages). The "Obs." column, with format N.M, indicates which observation (M) of which mask (N) is the source of the listed kinematics. Obs. 1.1 and 4.1 refer to the only observations of masks 000.1n01.5 and 000.0n01.4. Obs. 2.1, 2.2, and 2.3 refer to the 2007 May, 2008 May, and 2010 Apr observations of mask 359.9n01.5. Obs. 3.1 and 3.2 refer to the 2007 Oct and 2010 Apr observations of mask 000.0n01.6.

Table 3.11: Spectroscopic and Photometric Data for Objects in Field 010.1n03.2

ID	$\alpha_{J2000.0}$	$\delta_{J2000.0}$	$I_{\rm Inst}$	$(V-I)_{\rm Inst}$	Obs.	$V_{\rm helio}$ (km s^{-1})	$V_{\rm gsr}$ (km s^{-1})	σ_V (km s^{-1})	R_{TD}
000041	19 41 04.14	–33 31 04.4	12.24	0.07	···	136.7	165.5	9.1	···
···	···	···	···	···	1.1	142.8	171.6	12.9	15.03
···	···	···	···	···	1.2	130.7	159.5	12.8	15.18
000063	19 41 20.37	–33 30 58.1	12.23	0.10	···	207.7	236.6	14.0	···
···	···	···	···	···	1.1	213.0	241.8	17.0	9.38
···	···	···	···	···	1.2	197.0	225.8	24.4	6.73
000165	19 41 11.46	–33 30 50.7	13.50	0.04	···	78.0	106.8	22.6	···
···	···	···	···	···	1.1	104.6	133.5	31.6	5.53
···	···	···	···	···	1.2	49.8	78.7	32.5	5.42
000176	19 41 39.50	–33 30 42.6	12.19	0.07	···	132.9	161.7	8.9	···
···	···	···	···	···	1.1	130.3	159.1	12.5	16.53
···	···	···	···	···	1.2	135.6	164.4	12.6	16.23
000316	19 41 35.50	–33 30 30.4	13.76	0.07	···	135.9	164.7	30.4	···
···	···	···	···	···	1.1	144.3	173.2	47.3	4.13
···	···	···	···	···	1.2	130.0	158.8	39.6	4.69
000332	19 40 56.99	–33 30 36.8	13.83	–0.14	···	142.7	171.6	22.4	···
···	···	···	···	···	1.1	137.6	166.4	29.0	5.89
···	···	···	···	···	1.2	150.3	179.1	35.1	5.12
000365	19 41 35.95	–33 30 25.0	14.09	–0.06	1.1	251.1	280.0	60.3	3.47
000509	19 41 37.12	–33 30 09.1	13.46	–0.05	···	169.5	198.4	22.8	···
···	···	···	···	···	1.1	187.0	215.8	26.6	6.29
···	···	···	···	···	1.2	122.2	151.0	43.9	4.36
000520	19 40 57.31	–33 30 16.5	12.88	0.04	···	125.6	154.4	18.9	···
···	···	···	···	···	1.1	142.2	171.1	28.3	6.00
···	···	···	···	···	1.2	112.2	141.0	25.4	6.52
000646	19 41 05.84	–33 30 02.2	12.31	0.05	···	130.5	159.3	9.7	···
···	···	···	···	···	1.1	144.9	173.7	12.9	14.93
···	···	···	···	···	1.2	112.0	140.9	14.6	11.46
000754	19 40 57.36	–33 29 54.3	13.22	–0.05	···	133.9	162.7	14.4	···
···	···	···	···	···	1.1	134.8	163.6	19.2	8.29
···	···	···	···	···	1.2	132.7	161.5	21.7	7.42
000817	19 41 32.64	–33 29 40.6	13.55	–0.03	···	169.1	197.9	23.2	···
···	···	···	···	···	1.1	183.7	212.5	25.7	6.47
···	···	···	···	···	1.2	105.4	134.2	53.6	3.78
000897	19 41 26.52	–33 29 33.7	14.08	0.04	···	166.0	194.9	35.5	···
···	···	···	···	···	1.1	176.7	205.6	40.8	4.59
···	···	···	···	···	1.2	132.7	161.5	72.0	3.05
000942	19 41 25.84	–33 29 28.5	14.05	0.04	···	169.1	197.9	37.3	···
···	···	···	···	···	1.1	209.2	238.0	43.3	4.40
···	···	···	···	···	1.2	54.3	83.1	73.3	3.01
001027	19 41 22.99	–33 29 22.4	13.32	0.02	···	131.7	160.6	28.0	···
···	···	···	···	···	1.1	122.4	151.3	35.7	5.06
···	···	···	···	···	1.2	146.6	175.4	45.0	4.28
001156	19 41 09.08	–33 29 11.6	12.98	0.07	···	127.8	156.6	12.0	···
···	···	···	···	···	1.1	146.6	175.5	16.9	9.44
···	···	···	···	···	1.2	108.7	137.6	17.0	9.39
001211	19 41 15.86	–33 29 05.9	12.55	–0.11	···	137.9	166.7	11.1	···
···	···	···	···	···	1.1	151.6	180.4	14.3	11.88
···	···	···	···	···	1.2	117.2	146.1	17.6	9.07
001270	19 41 11.53	–33 29 00.1	12.41	0.16	···	134.6	163.4	10.3	···
···	···	···	···	···	1.1	145.1	173.9	14.2	12.07
···	···	···	···	···	1.2	122.6	151.5	15.2	10.85
001391	19 40 56.54	–33 28 52.1	13.13	0.06	···	147.0	175.8	16.9	···
···	···	···	···	···	1.1	149.9	178.7	27.4	6.15
···	···	···	···	···	1.2	145.2	174.0	21.4	7.51
001410	19 41 36.14	–33 28 42.8	14.08	–0.06	···	34.2	63.0	33.2	···
···	···	···	···	···	1.1	18.7	47.5	53.0	3.81
···	···	···	···	···	1.2	44.1	73.0	42.5	4.46
001590	19 40 57.52	–33 28 31.7	12.83	–0.08	···	181.0	209.9	12.6	···
···	···	···	···	···	1.1	183.2	212.1	16.7	9.61

Continued on Next Page...

Table 3.11 – 010.1n03.2 (Continued)

ID	$\alpha_{J2000.0}$	$\delta_{J2000.0}$	$I_{\rm Inst}$	$(V-I)_{\rm Inst}$	Obs.	$V_{\rm helio}$ (km s^{-1})	$V_{\rm gsr}$ (km s^{-1})	σ_V (km s^{-1})	R_{TD}
···	···	···	···	···	1.2	178.1	206.9	19.4	8.22
001652	19 41 15.86	–33 28 26.1	13.93	0.03	1.2	69.0	97.8	67.7	3.19
001737	19 41 28.53	–33 28 18.5	12.48	0.05	···	–233.2	–204.4	11.7	···
···	···	···	···	···	1.1	–217.5	–188.6	14.8	11.23
···	···	···	···	···	1.2	–259.4	–230.5	19.1	8.34
001957	19 41 05.90	–33 28 10.9	13.37	–0.15	···	167.2	196.1	23.8	···
···	···	···	···	···	1.1	160.8	189.7	27.9	6.06
···	···	···	···	···	1.2	184.0	212.8	45.2	4.27
002000	19 41 29.99	–33 28 03.1	13.63	–0.04	···	189.5	218.4	20.9	···
···	···	···	···	···	1.1	193.9	222.8	23.1	7.03
···	···	···	···	···	1.2	169.7	198.6	49.0	4.03
002159	19 41 18.11	–33 27 54.6	13.83	0.12	1.1	219.7	248.6	37.5	4.88
002330	19 41 05.13	–33 27 46.8	13.15	–0.08	···	96.6	125.5	31.3	···
···	···	···	···	···	1.1	107.1	135.9	39.5	4.70
···	···	···	···	···	1.2	79.1	108.0	51.3	3.90
002473	19 41 17.80	–33 27 38.2	12.32	0.12	···	141.6	170.4	10.0	···
···	···	···	···	···	1.1	147.9	176.7	13.1	14.33
···	···	···	···	···	1.2	132.6	161.5	15.6	10.46
002515	19 41 29.51	–33 27 31.8	13.62	–0.14	···	146.3	175.2	25.7	···
···	···	···	···	···	1.1	163.1	191.9	32.2	5.45
···	···	···	···	···	1.2	117.1	146.0	42.5	4.46
002633	19 41 32.15	–33 27 21.4	13.82	0.10	1.2	86.9	115.8	68.9	3.15
002716	19 41 28.15	–33 27 14.6	13.91	0.16	1.1	211.2	240.0	85.2	2.69
002798	19 41 15.17	–33 27 08.4	13.74	–0.08	1.1	196.1	224.9	56.9	3.62
002864	19 41 11.17	–33 27 03.1	13.65	–0.14	···	135.0	163.9	27.6	···
···	···	···	···	···	1.1	170.3	199.1	32.7	5.39
···	···	···	···	···	1.2	47.0	75.9	51.7	3.88
002974	19 41 06.25	–33 26 50.6	12.84	–0.03	···	169.9	198.7	13.5	···
···	···	···	···	···	1.1	182.9	211.7	17.1	9.33
···	···	···	···	···	1.2	148.7	177.5	21.8	7.39
003006	19 41 20.25	–33 26 44.4	13.13	0.03	···	190.2	219.0	18.1	···
···	···	···	···	···	1.1	186.0	214.8	19.5	8.18
···	···	···	···	···	1.2	217.2	246.0	49.5	4.00
003066	19 41 39.08	–33 26 31.7	13.77	–0.01	···	176.2	205.0	36.3	···
···	···	···	···	···	1.1	239.8	268.6	50.9	3.92
···	···	···	···	···	1.2	110.2	139.1	51.8	3.87
003196	19 41 15.18	–33 26 24.0	13.75	–0.06	···	185.4	214.2	24.7	···
···	···	···	···	···	1.1	204.5	233.3	27.8	6.09
···	···	···	···	···	1.2	113.1	142.0	54.0	3.76
003265	19 40 58.98	–33 26 17.9	13.02	–0.10	···	131.3	160.2	18.7	···
···	···	···	···	···	1.1	146.1	174.9	22.9	7.09
···	···	···	···	···	1.2	101.6	130.5	32.5	5.41
003369	19 40 56.24	–33 26 06.9	13.96	0.14	1.1	138.7	167.6	34.5	5.18
003465	19 41 20.18	–33 25 54.6	13.63	0.06	···	116.2	145.0	32.5	···
···	···	···	···	···	1.1	116.2	145.0	32.5	5.42
···	···	···	···	···	1.2	87.9	116.7	96.8	2.44
003604	19 41 03.94	–33 25 43.1	13.14	–0.05	···	125.1	153.9	16.9	···
···	···	···	···	···	1.1	114.3	143.2	27.0	6.23
···	···	···	···	···	1.2	132.1	160.9	21.7	7.42
003624	19 41 24.98	–33 25 37.6	13.71	–0.09	···	11.4	40.3	35.1	···
···	···	···	···	···	1.1	–95.7	–66.9	53.4	3.79
···	···	···	···	···	1.2	93.5	122.3	46.7	4.17
003719	19 41 05.92	–33 25 29.0	13.20	–0.02	···	–84.0	–55.1	15.3	···
···	···	···	···	···	1.1	–77.1	–48.2	18.0	8.83
···	···	···	···	···	1.2	–101.9	–73.0	29.1	5.88
003755	19 41 38.18	–33 25 18.6	12.75	–0.04	···	152.5	181.4	11.1	···
···	···	···	···	···	1.1	164.7	193.6	13.5	13.28
···	···	···	···	···	1.2	126.6	155.4	19.7	8.10
003767	19 41 01.18	–33 25 23.7	12.99	0.00	···	140.9	169.7	18.8	···
···	···	···	···	···	1.1	153.9	182.7	23.8	6.87
···	···	···	···	···	1.2	119.2	148.0	30.7	5.64
003860	19 41 16.21	–33 25 12.4	12.64	–0.11	···	149.0	177.9	12.6	···

Continued on Next Page...

Table 3.11 – 010.1n03.2 (Continued)

ID	$\alpha_{J2000.0}$	$\delta_{J2000.0}$	$I_{\rm Inst}$	$(V-I)_{\rm Inst}$	Obs.	$V_{\rm helio}$ (km s^{-1})	$V_{\rm gsr}$ (km s^{-1})	σ_V (km s^{-1})	R_{TD}
···	···	···	···	···	1.1	156.9	185.8	14.1	12.17
···	···	···	···	···	1.2	117.6	146.4	28.2	6.02
004062	19 41 07.06	–33 25 00.8	13.33	0.03	···	132.6	161.5	28.8	···
···	···	···	···	···	1.1	126.2	155.0	35.3	5.10
···	···	···	···	···	1.2	145.7	174.5	50.0	3.97
004138	19 41 18.22	–33 24 54.1	13.63	–0.09	···	180.3	209.1	27.6	···
···	···	···	···	···	1.1	166.5	195.3	30.3	5.70
···	···	···	···	···	1.2	247.7	276.5	66.9	3.22
004226	19 41 15.48	–33 24 46.1	13.99	–0.11	1.1	153.6	182.5	62.6	3.38
004291	19 41 20.79	–33 24 40.4	13.84	0.15	1.1	184.0	212.9	81.6	2.78
004404	19 41 32.65	–33 24 32.6	13.13	0.03	···	160.4	189.2	16.6	···
···	···	···	···	···	1.1	167.5	196.4	17.7	8.98
···	···	···	···	···	1.2	111.4	140.2	46.5	4.18
004568	19 41 07.65	–33 24 26.1	13.98	–0.05	1.1	160.1	188.9	48.5	4.06
004643	19 41 09.29	–33 24 19.8	12.45	0.06	···	147.1	175.9	10.6	···
···	···	···	···	···	1.1	155.3	184.2	14.4	11.79
···	···	···	···	···	1.2	137.1	166.0	15.7	10.30
004706	19 41 18.04	–33 24 12.0	13.44	–0.03	···	200.2	229.0	17.7	···
···	···	···	···	···	1.1	209.9	238.7	19.2	8.30
···	···	···	···	···	1.2	145.4	174.3	45.5	4.25
004758	19 41 12.64	–33 24 06.3	13.20	0.03	···	142.3	171.1	15.7	···
···	···	···	···	···	1.1	152.2	181.0	18.0	8.86
···	···	···	···	···	1.2	109.5	138.4	32.6	5.40
004791	19 41 25.63	–33 23 59.6	12.63	0.02	···	151.0	179.9	21.5	···
···	···	···	···	···	1.1	170.2	199.0	23.3	6.99
···	···	···	···	···	1.2	43.6	72.5	55.2	3.70
004887	19 41 08.91	–33 23 53.7	13.28	–0.11	···	104.2	133.0	35.0	···
···	···	···	···	···	1.1	117.8	146.6	44.2	4.34
···	···	···	···	···	1.2	81.0	109.9	57.6	3.59
005086	19 41 07.39	–33 23 38.3	12.29	0.02	···	–6.5	22.4	14.7	···
···	···	···	···	···	1.1	–16.2	12.6	16.6	9.63
···	···	···	···	···	1.2	27.4	56.3	31.0	5.61
005141	19 41 12.56	–33 23 33.2	13.50	–0.10	···	116.3	145.1	30.4	···
···	···	···	···	···	1.1	126.7	155.5	34.4	5.19
···	···	···	···	···	1.2	80.0	108.8	64.4	3.31
005284	19 41 02.83	–33 23 24.4	12.46	–0.04	···	158.5	187.4	11.6	···
···	···	···	···	···	1.1	165.8	194.7	15.1	10.90
···	···	···	···	···	1.2	148.1	177.0	18.0	8.82
005332	19 41 09.79	–33 23 18.8	13.42	–0.05	···	123.2	152.0	20.5	···
···	···	···	···	···	1.1	169.5	198.3	26.5	6.32
···	···	···	···	···	1.2	53.4	82.3	32.5	5.42
005366	19 41 34.71	–33 23 12.9	13.60	–0.21	1.1	216.4	245.2	35.2	5.11
005425	19 41 37.75	–33 23 06.4	13.50	0.03	···	107.3	136.1	21.7	···
···	···	···	···	···	1.1	106.4	135.2	24.7	6.68
···	···	···	···	···	1.2	110.5	139.4	46.1	4.21
005562	19 41 01.94	–33 22 59.6	13.32	–0.04	···	–5.8	23.1	35.2	···
···	···	···	···	···	1.1	3.3	32.2	40.1	4.65
···	···	···	···	···	1.2	–36.5	–7.6	73.6	3.00
005564	19 41 37.94	–33 22 54.1	13.29	0.04	···	155.3	184.1	32.4	···
···	···	···	···	···	1.1	146.6	175.4	36.0	5.03
···	···	···	···	···	1.2	193.0	221.9	75.0	2.96
005679	19 41 18.94	–33 22 48.1	13.59	0.02	···	102.1	130.9	31.8	···
···	···	···	···	···	1.1	198.9	227.8	67.2	3.21
···	···	···	···	···	1.2	74.0	102.8	36.2	5.01
005714	19 41 38.39	–33 22 41.7	12.24	0.05	···	–354.2	–325.4	16.2	···
···	···	···	···	···	1.1	–342.6	–313.8	21.4	7.51
···	···	···	···	···	1.2	–369.7	–340.9	24.7	6.66
005800	19 41 32.90	–33 22 35.9	13.80	–0.12	1.1	–128.7	–99.9	64.7	3.30
005875	19 41 30.81	–33 22 28.7	12.61	0.01	···	174.5	203.4	16.3	···
···	···	···	···	···	1.1	171.9	200.7	17.8	8.93
···	···	···	···	···	1.2	188.6	217.5	41.0	4.58
005966	19 41 13.20	–33 22 22.9	13.67	–0.08	···	100.8	129.7	18.6	···

Continued on Next Page...

Table 3.11 – 010.1n03.2 (Continued)

ID	$\alpha_{J2000.0}$	$\delta_{J2000.0}$	$I_{\rm Inst}$	$(V-I)_{\rm Inst}$	Obs.	$V_{\rm helio}$ (km s^{-1})	$V_{\rm gsr}$ (km s^{-1})	σ_V (km s^{-1})	R_{TD}
···	···	···	···	···	1.1	103.6	132.5	19.9	8.03
···	···	···	···	···	1.2	81.2	110.0	52.8	3.82
006062	19 40 56.92	–33 22 15.9	12.89	0.08	···	–35.8	–7.0	16.4	···
···	···	···	···	···	1.1	–31.2	–2.4	20.2	7.89
···	···	···	···	···	1.2	–44.6	–15.8	28.0	6.05
006105	19 41 20.62	–33 22 09.5	12.89	–0.05	···	155.6	184.5	14.1	···
···	···	···	···	···	1.1	166.6	195.4	15.9	10.17
···	···	···	···	···	1.2	114.8	143.6	30.7	5.65
006160	19 41 37.11	–33 22 02.6	12.93	–0.08	···	149.4	178.2	13.7	···
···	···	···	···	···	1.1	162.0	190.8	16.3	9.84
···	···	···	···	···	1.2	119.9	148.8	24.9	6.62
006231	19 41 37.17	–33 21 57.0	13.61	0.06	···	85.5	114.4	25.0	···
···	···	···	···	···	1.1	130.3	159.2	30.7	5.64
···	···	···	···	···	1.2	–2.3	26.5	43.0	4.42
006370	19 41 00.75	–33 21 48.9	13.67	0.01	1.1	105.7	134.5	28.7	5.94
006437	19 41 11.84	–33 21 41.5	12.74	0.00	···	120.5	149.4	13.4	···
···	···	···	···	···	1.1	129.0	157.9	16.8	9.50
···	···	···	···	···	1.2	105.8	134.6	22.1	7.30
006523	19 41 26.51	–33 21 33.7	13.21	0.05	···	136.0	164.9	23.9	···
···	···	···	···	···	1.1	168.1	196.9	33.2	5.33
···	···	···	···	···	1.2	101.8	130.6	34.3	5.20
006620	19 41 06.31	–33 21 27.7	13.86	–0.08	···	138.2	167.1	25.9	···
···	···	···	···	···	1.1	153.1	181.9	27.9	6.06
···	···	···	···	···	1.2	48.8	77.6	68.6	3.16
006704	19 40 58.08	–33 21 20.6	13.33	–0.12	···	129.4	158.2	14.1	···
···	···	···	···	···	1.1	140.8	169.7	17.8	8.93
···	···	···	···	···	1.2	110.5	139.4	22.9	7.09
006775	19 41 13.96	–33 21 15.3	13.97	0.12	···	230.2	259.0	40.3	···
···	···	···	···	···	1.1	230.2	259.0	40.3	4.63
···	···	···	···	···	1.2	64.3	93.2	82.0	2.77
006837	19 41 36.32	–33 21 07.8	13.76	0.10	···	97.8	126.7	29.6	···
···	···	···	···	···	1.1	162.7	191.5	49.7	3.99
···	···	···	···	···	1.2	62.3	91.1	36.8	4.95
006941	19 41 06.85	–33 21 02.1	13.78	0.03	···	115.7	144.6	27.3	···
···	···	···	···	···	1.1	144.8	173.7	34.4	5.19
···	···	···	···	···	1.2	66.6	95.5	44.7	4.30
007028	19 41 17.38	–33 20 50.8	12.71	–0.07	···	151.6	180.4	11.1	···
···	···	···	···	···	1.1	167.2	196.0	14.1	12.22
···	···	···	···	···	1.2	126.3	155.2	17.9	8.88
007137	19 40 56.94	–33 20 43.3	13.05	–0.15	···	157.2	186.0	11.3	···
···	···	···	···	···	1.1	168.4	197.2	13.9	12.57
···	···	···	···	···	1.2	135.3	164.1	19.4	8.22
007167	19 41 38.72	–33 20 35.9	13.80	–0.06	···	140.6	169.5	39.3	···
···	···	···	···	···	1.1	211.4	240.2	49.9	3.98
···	···	···	···	···	1.2	24.5	53.3	63.9	3.33
007260	19 41 19.84	–33 20 28.4	13.38	0.03	···	139.3	168.1	18.3	···
···	···	···	···	···	1.1	145.8	174.6	20.4	7.84
···	···	···	···	···	1.2	113.1	141.9	41.0	4.58
007359	19 41 03.98	–33 20 23.0	13.38	0.15	···	24.8	53.6	16.6	···
···	···	···	···	···	1.1	35.5	64.3	19.3	8.26
···	···	···	···	···	1.2	–5.7	23.1	32.5	5.41
007425	19 41 03.19	–33 20 16.6	14.00	–0.18	···	98.1	126.9	32.4	···
···	···	···	···	···	1.1	127.0	155.8	42.9	4.43
···	···	···	···	···	1.2	59.6	88.4	49.5	4.00
007513	19 41 18.43	–33 20 07.7	13.81	0.14	1.1	–162.3	–133.5	26.8	6.26
007577	19 41 22.72	–33 19 59.3	13.86	0.00	···	94.1	122.9	33.8	···
···	···	···	···	···	1.1	171.7	200.5	59.9	3.49
···	···	···	···	···	1.2	57.8	86.6	41.0	4.58
007628	19 41 31.81	–33 19 53.0	13.73	0.02	1.1	212.3	241.1	49.0	4.03
007712	19 41 11.38	–33 19 47.9	12.94	–0.11	···	163.1	192.0	17.4	···
···	···	···	···	···	1.1	183.7	212.6	20.2	7.89
···	···	···	···	···	1.2	105.4	134.3	33.9	5.25

Continued on Next Page...

Table 3.11 – 010.1n03.2 (Continued)

ID	$\alpha_{J2000.0}$	$\delta_{J2000.0}$	$I_{\rm Inst}$	$(V-I)_{\rm Inst}$	Obs.	$V_{\rm helio}$ (km s^{-1})	$V_{\rm gsr}$ (km s^{-1})	σ_V (km s^{-1})	R_{TD}
007817	19 40 57.85	–33 19 40.7	13.30	0.14	···	124.8	153.6	20.3	···
···	···	···	···	···	1.1	107.5	136.4	25.2	6.56
···	···	···	···	···	1.2	156.1	184.9	34.0	5.24
007897	19 41 03.99	–33 19 32.2	13.71	0.12	···	145.3	174.2	27.4	···
···	···	···	···	···	1.1	146.6	175.4	30.3	5.70
···	···	···	···	···	1.2	139.8	168.6	63.9	3.33
007942	19 41 36.26	–33 19 24.8	12.36	–0.01	···	153.7	182.5	13.1	···
···	···	···	···	···	1.1	169.9	198.8	15.5	10.52
···	···	···	···	···	1.2	113.9	142.7	24.2	6.77
008130	19 41 27.19	–33 19 09.4	13.52	–0.11	1.1	133.4	162.3	32.2	5.45
008223	19 41 12.96	–33 19 02.3	13.22	–0.08	···	124.8	153.7	15.9	···
···	···	···	···	···	1.1	136.8	165.7	17.6	9.05
···	···	···	···	···	1.2	71.3	100.1	37.2	4.91
008348	19 41 31.69	–33 18 48.1	13.14	–0.06	···	167.6	196.5	42.2	···
···	···	···	···	···	1.1	181.9	210.8	50.6	3.94
···	···	···	···	···	1.2	134.6	163.5	76.7	2.91
008450	19 41 13.51	–33 18 41.0	12.76	–0.09	···	254.6	283.4	23.4	···
···	···	···	···	···	1.1	267.2	296.0	27.9	6.07
···	···	···	···	···	1.2	224.2	253.0	43.3	4.40
008515	19 41 35.09	–33 18 31.8	13.02	0.00	···	158.9	187.8	19.5	···
···	···	···	···	···	1.1	170.6	199.4	21.8	7.40
···	···	···	···	···	1.2	112.1	141.0	43.7	4.37
008711	19 41 19.38	–33 18 18.0	13.02	–0.02	···	135.1	163.9	15.0	···
···	···	···	···	···	1.1	146.6	175.4	18.2	8.73
···	···	···	···	···	1.2	111.2	140.1	26.2	6.36
008807	19 41 04.73	–33 18 12.5	12.15	–0.22	···	141.4	170.2	14.4	···
···	···	···	···	···	1.1	158.0	186.9	20.4	7.82
···	···	···	···	···	1.2	124.9	153.8	20.3	7.86
008855	19 41 20.08	–33 18 04.0	12.78	–0.01	···	185.4	214.2	14.0	···
···	···	···	···	···	1.1	184.6	213.4	15.6	10.42
···	···	···	···	···	1.2	188.6	217.4	31.7	5.51
009041	19 41 17.27	–33 17 50.0	13.93	–0.11	···	197.8	226.6	29.1	···
···	···	···	···	···	1.1	213.1	241.9	34.1	5.23
···	···	···	···	···	1.2	156.7	185.6	55.8	3.67
009104	19 41 12.42	–33 17 43.8	12.19	0.10	···	–185.2	–156.4	9.9	···
···	···	···	···	···	1.1	–173.9	–145.1	12.3	17.61
···	···	···	···	···	1.2	–205.7	–176.9	16.6	9.65
009189	19 40 58.43	–33 17 36.0	13.77	–0.08	···	94.4	123.2	23.2	···
···	···	···	···	···	1.1	112.9	141.8	29.5	5.81
···	···	···	···	···	1.2	64.3	93.1	37.6	4.87
009290	19 40 57.64	–33 17 27.1	13.00	–0.06	···	178.3	207.1	13.1	···
···	···	···	···	···	1.1	170.0	198.9	15.0	11.03
···	···	···	···	···	1.2	204.3	233.2	26.6	6.29
009388	19 41 01.86	–33 17 17.0	13.52	0.04	···	169.7	198.6	20.7	···
···	···	···	···	···	1.1	177.5	206.3	23.2	7.02
···	···	···	···	···	1.2	139.1	168.0	46.1	4.21
009428	19 41 12.12	–33 17 11.4	13.94	0.05	···	139.0	167.8	34.5	···
···	···	···	···	···	1.1	211.5	240.4	57.3	3.60
···	···	···	···	···	1.2	97.8	126.7	43.2	4.41
009544	19 40 57.19	–33 17 00.8	12.91	–0.06	···	165.1	193.9	13.3	···
···	···	···	···	···	1.1	168.7	197.5	15.3	10.73
···	···	···	···	···	1.2	153.9	182.8	26.9	6.24
009578	19 41 33.93	–33 16 54.4	13.96	–0.01	···	–68.4	–39.6	40.8	···
···	···	···	···	···	1.1	–1.8	27.0	49.0	4.03
···	···	···	···	···	1.2	–218.8	–190.0	73.6	3.00
009660	19 41 33.09	–33 16 48.7	13.10	–0.10	1.1	160.5	189.3	27.6	6.11

Note: For the objects with multiple observations three lines are used to summarize their acquired data. The first line provides the object's identification number, equatorial coordinates, I and $(V-I)$ instrumental magnitudes, heliocentric and Galactic standard of rest velocities (calculated as weighted averages), and velocity uncertainty. The second and third lines list the kinematic information, including the R_{TD} values, from the individual observations. Observation 1.1 refers to the first observation of field 010.1n03.2 on 2006 Sep 21. Observation 1.2 refers to the second observation of field 010.1n03.2 on 2010 Apr 25.

Table 3.12: Spectroscopic and Photometric Data for Objects in Field 020.1n06.1

ID	$\alpha_{J2000.0}$	$\delta_{J2000.0}$	$I_{\rm Inst}$	$(V-I)_{\rm Inst}$	$V_{\rm helio}$ (km s^{-1})	$V_{\rm gsr}$ (km s^{-1})	σ_V (km s^{-1})	R_{TD}
000781	20 29 01.90	–36 25 14.4	12.42	0.00	–69.3	–46.9	26.5	6.31
000865	20 29 02.41	–36 27 39.2	12.58	0.00	124.7	147.1	24.8	6.64
000960	20 29 03.03	–36 31 00.4	13.33	0.22	110.4	132.8	66.9	3.22
001201	20 29 04.29	–36 28 58.6	12.16	–0.04	–239.0	–216.5	28.2	6.01
001681	20 29 08.17	–36 26 51.1	12.68	0.05	68.9	91.3	27.8	6.09
001940	20 29 09.93	–36 26 04.0	12.82	0.08	39.4	61.8	37.7	4.86
002159	20 29 11.10	–36 26 04.0	12.37	0.17	153.5	176.0	17.7	8.99
002417	20 29 12.41	–36 27 46.2	12.98	0.13	–240.4	–218.0	80.8	2.80
002495	20 29 12.91	–36 28 49.4	12.57	–0.06	106.6	129.1	24.8	6.65
002764	20 29 14.39	–36 32 51.2	12.28	0.02	–141.5	–119.0	35.8	5.05
002824	20 29 14.91	–36 25 32.2	11.68	0.03	86.0	108.5	14.4	11.73
003000	20 29 15.89	–36 27 38.0	11.94	–0.04	96.4	118.8	18.8	8.46
003088	20 29 16.45	–36 29 00.1	11.90	0.10	44.0	66.4	40.6	4.61
003289	20 29 17.88	–36 29 12.9	13.22	0.18	62.9	85.3	39.9	4.67
003539	20 29 19.72	–36 25 09.5	11.36	0.03	158.6	181.0	14.3	11.81
003658	20 29 20.53	–36 27 43.7	13.14	0.17	89.0	111.5	37.9	4.84
004092	20 29 23.53	–36 26 49.0	13.15	0.28	47.6	70.1	59.6	3.50
004309	20 29 25.08	–36 25 13.3	11.64	0.05	104.3	126.8	13.0	14.56
004399	20 29 25.79	–36 26 07.9	12.30	0.18	–214.8	–192.4	32.2	5.45
004503	20 29 26.65	–36 27 12.6	11.44	0.16	–5.3	17.1	13.9	12.55
004574	20 29 27.09	–36 33 08.9	12.72	0.12	99.1	121.5	35.5	5.08
004665	20 29 27.55	–36 31 01.3	13.19	0.10	55.4	77.8	82.4	2.76
004799	20 29 28.30	–36 30 42.5	13.10	–0.03	120.2	142.6	54.8	3.72
004921	20 29 29.13	–36 26 44.0	12.07	0.12	42.0	64.4	15.7	10.32
004998	20 29 29.64	–36 26 00.2	12.39	0.05	76.7	99.1	23.1	7.05
005126	20 29 30.50	–36 28 59.1	12.15	0.05	–101.4	–79.0	30.9	5.62
005374	20 29 31.91	–36 24 55.2	13.05	0.23	89.2	111.7	43.2	4.41
005485	20 29 32.80	–36 29 09.0	13.28	0.18	80.8	103.3	63.1	3.36
005564	20 29 33.46	–36 27 31.4	12.05	0.02	89.1	111.5	13.7	12.96
005927	20 29 34.93	–36 28 18.0	13.25	0.22	75.5	97.9	33.3	5.32
006032	20 29 35.53	–36 26 46.5	12.90	0.07	80.8	103.3	46.5	4.18
006153	20 29 36.22	–36 26 49.4	12.17	0.03	–218.5	–196.0	29.0	5.89
006273	20 29 36.85	–36 31 03.6	12.89	0.10	87.4	109.8	24.9	6.63
006460	20 29 37.85	–36 30 32.9	12.93	0.04	86.1	108.5	36.3	5.00
006517	20 29 38.35	–36 28 44.2	11.52	0.14	–58.6	–36.1	18.4	8.63
006932	20 29 40.50	–36 26 04.5	11.92	0.05	70.2	92.7	25.0	6.61
007131	20 29 41.59	–36 30 58.4	12.74	0.15	100.7	123.1	42.6	4.45
007254	20 29 42.41	–36 27 18.2	13.32	0.19	71.5	93.9	28.7	5.94
007407	20 29 43.31	–36 28 53.8	11.68	0.18	311.6	334.0	20.3	7.87
007493	20 29 43.85	–36 32 15.7	12.41	0.05	125.2	147.6	22.8	7.12
007656	20 29 44.88	–36 28 14.7	12.88	0.16	76.7	99.2	25.6	6.48
007742	20 29 45.53	–36 30 33.8	12.30	0.08	93.5	116.0	15.4	10.65
007837	20 29 46.11	–36 31 32.0	12.44	0.28	–10.0	12.4	21.8	7.40
007957	20 29 46.93	–36 26 02.5	12.42	0.06	81.4	103.8	36.1	5.02
008110	20 29 47.68	–36 32 29.8	11.87	0.28	–113.4	–90.9	20.2	7.92
008307	20 29 48.94	–36 30 49.7	11.45	0.02	123.2	145.7	12.9	14.82
008399	20 29 49.70	–36 25 04.6	12.55	0.16	94.6	117.0	17.7	8.99

Continued on Next Page...

Table 3.12 – 020.1n06.1 (Continued)

ID	$\alpha_{J2000.0}$	$\delta_{J2000.0}$	$I_{\rm Inst}$	$(V-I)_{\rm Inst}$	$V_{\rm helio}$ (km s^{-1})	$V_{\rm gsr}$ (km s^{-1})	σ_V (km s^{-1})	R_{TD}
008505	20 29 50.28	–36 26 26.8	11.49	0.14	–312.7	–290.2	16.6	9.62
008572	20 29 50.81	–36 24 54.3	12.44	0.06	84.2	106.6	25.7	6.47
008927	20 29 52.96	–36 25 26.4	12.21	0.03	98.4	120.8	22.0	7.35
009023	20 29 53.50	–36 29 39.1	12.50	0.06	52.9	75.4	20.2	7.90
009276	20 29 55.02	–36 27 56.0	12.46	0.11	87.9	110.3	19.0	8.37
009390	20 29 55.69	–36 29 16.8	13.25	0.22	59.6	82.0	30.6	5.66
009496	20 29 56.33	–36 30 04.5	12.01	0.04	251.5	273.9	18.6	8.53
009566	20 29 56.92	–36 26 40.5	13.34	0.11	85.5	107.9	39.0	4.74
009840	20 29 58.48	–36 30 01.5	13.20	–0.06	85.4	107.8	36.7	4.96
009915	20 29 59.09	–36 25 12.1	11.87	0.18	–181.4	–158.9	16.0	10.09
010006	20 29 59.60	–36 30 04.5	12.07	0.25	65.1	87.6	65.8	3.26
010231	20 30 00.96	–36 25 24.5	12.57	0.11	–237.3	–214.9	63.9	3.33
010308	20 30 01.56	–36 28 56.3	12.74	0.15	144.8	167.2	22.7	7.15
010638	20 30 03.96	–36 25 40.5	12.52	0.06	80.8	103.3	23.7	6.90
010757	20 30 04.81	–36 29 04.2	11.72	0.15	48.7	71.1	12.5	16.74
010823	20 30 05.39	–36 29 35.4	12.26	0.15	172.0	194.4	18.1	8.80
010904	20 30 06.03	–36 25 14.1	12.51	–0.01	80.2	102.6	17.0	9.41
011109	20 30 07.24	–36 30 18.4	11.50	0.18	38.4	60.8	13.6	13.11
011164	20 30 07.72	–36 26 19.2	11.73	0.05	105.1	127.5	14.9	11.09
011404	20 30 09.56	–36 33 17.1	12.84	0.17	105.7	128.2	25.7	6.46
011589	20 30 10.86	–36 30 47.0	13.27	0.04	12.5	34.9	61.1	3.44
011677	20 30 11.50	–36 25 36.0	13.10	0.11	93.6	116.1	42.2	4.48
011757	20 30 12.13	–36 28 29.7	12.83	0.18	64.2	86.7	28.9	5.90
012070	20 30 14.66	–36 29 22.5	12.47	0.11	120.4	142.9	15.0	11.02
012159	20 30 15.26	–36 30 44.0	12.54	0.02	173.0	195.5	38.4	4.80

Table 3.13: Spectroscopic and Photometric Data for Objects in Field 020.5p00.1

ID	$\alpha_{J2000.0}$	$\delta_{J2000.0}$	$I_{\rm Inst}$	$(V-I)_{\rm Inst}$	$V_{\rm helio}$ (km s^{-1})	$V_{\rm gsr}$ (km s^{-1})	σ_V (km s^{-1})	R_{TD}
001539	20 30 03.81	–30 20 41.2	12.70	0.04	28.3	74.7	40.0	4.66
002073	20 30 07.68	–30 18 19.9	12.86	0.15	22.0	68.4	78.2	2.87
002183	20 30 08.49	–30 17 10.8	12.95	0.07	49.2	95.6	74.6	2.97
002278	20 30 08.99	–30 17 54.8	13.16	0.09	28.5	74.9	47.0	4.15
002511	20 30 10.38	–30 20 41.9	13.00	0.03	15.8	62.1	61.3	3.43
002718	20 30 11.49	–30 23 53.3	12.98	0.03	51.2	97.5	23.2	7.01
002799	20 30 12.09	–30 23 29.1	13.14	0.11	3.9	50.2	38.8	4.76
002831	20 30 12.67	–30 17 15.1	13.28	0.14	57.2	103.5	39.0	4.74
002954	20 30 13.39	–30 23 56.3	12.62	0.11	–4.4	41.9	29.4	5.83
002987	20 30 13.92	–30 17 13.1	11.31	–0.02	–270.1	–223.8	14.1	12.10
003126	20 30 14.96	–30 19 54.5	12.62	0.04	–193.5	–147.2	64.7	3.30
003341	20 30 16.97	–30 15 54.8	13.22	0.04	28.9	75.2	61.3	3.43
003512	20 30 18.51	–30 17 27.6	12.36	0.10	31.2	77.5	38.4	4.80
003690	20 30 19.97	–30 21 50.4	11.81	0.06	38.6	84.9	26.3	6.34
003805	20 30 20.82	–30 21 31.6	11.93	0.08	–59.9	–13.6	24.6	6.69
003858	20 30 21.49	–30 21 06.8	11.92	0.08	22.4	68.8	15.4	10.63
003927	20 30 22.07	–30 18 56.2	12.28	0.02	22.2	68.5	27.2	6.19
003971	20 30 22.61	–30 18 36.0	11.62	0.21	–85.6	–39.3	15.2	10.83
004052	20 30 23.22	–30 17 00.8	11.79	0.10	–33.0	13.3	25.6	6.48
004104	20 30 23.65	–30 15 44.8	12.72	0.21	29.8	76.1	20.3	7.87
004204	20 30 24.49	–30 15 38.1	13.30	0.22	16.9	63.3	36.6	4.97
004334	20 30 25.00	–30 22 45.3	12.51	–0.10	29.1	75.5	28.8	5.92
004505	20 30 26.41	–30 22 12.6	13.13	0.17	19.9	66.3	46.1	4.21
004583	20 30 26.88	–30 23 43.0	11.66	0.00	62.9	109.3	13.5	13.35
004662	20 30 27.50	–30 22 22.4	13.05	0.01	52.9	99.2	34.3	5.20
004727	20 30 27.89	–30 23 12.2	11.71	0.22	250.3	296.7	15.5	10.51
004809	20 30 28.73	–30 15 42.3	12.14	0.11	5.5	51.8	27.8	6.08
004982	20 30 29.83	–30 24 01.6	12.53	0.08	76.3	122.6	16.2	9.91
005095	20 30 30.86	–30 22 20.3	12.11	–0.03	–286.5	–240.1	22.0	7.34
005119	20 30 31.33	–30 16 21.4	11.92	0.08	48.8	95.2	15.4	10.64
005344	20 30 33.16	–30 24 14.4	12.68	0.12	141.7	188.0	30.7	5.65
005504	20 30 34.83	–30 17 41.2	12.50	0.03	63.4	109.7	16.2	9.92
005775	20 30 37.12	–30 20 53.8	12.18	–0.01	51.1	97.4	18.5	8.61
005877	20 30 37.87	–30 17 22.8	12.16	0.05	84.8	131.2	20.1	7.94
006090	20 30 39.27	–30 22 01.8	11.79	–0.02	88.1	134.4	16.2	9.93
006197	20 30 40.45	–30 17 23.7	12.16	0.14	58.3	104.7	29.8	5.78
006241	20 30 40.93	–30 18 27.0	12.17	0.03	–258.5	–212.2	33.0	5.35
006391	20 30 41.66	–30 22 37.7	11.95	0.01	–256.1	–209.8	23.8	6.88
006507	20 30 42.42	–30 21 29.7	12.65	0.06	223.7	270.0	38.6	4.78
006596	20 30 42.95	–30 19 06.5	12.94	0.20	–12.6	33.8	25.0	6.61
006774	20 30 43.82	–30 16 48.9	13.18	0.17	63.9	110.3	34.3	5.21
006870	20 30 44.47	–30 22 24.4	12.57	0.21	–3.7	42.6	19.4	8.19
006973	20 30 45.90	–30 19 51.9	11.75	0.05	79.8	126.1	19.7	8.11
007047	20 30 46.47	–30 21 59.9	11.47	0.21	–23.4	22.9	13.2	13.94
007156	20 30 47.49	–30 18 40.6	11.81	0.13	–360.5	–314.1	16.5	9.69
007375	20 30 49.55	–30 19 11.8	12.04	0.22	221.4	267.7	16.1	10.05
007436	20 30 50.08	–30 23 33.4	11.42	0.09	–35.9	10.4	20.1	7.93

Continued on Next Page...

Table 3.13 – 020.5p00.1 (Continued)

ID	$\alpha_{J2000.0}$	$\delta_{J2000.0}$	$I_{\rm Inst}$	$(V-I)_{\rm Inst}$	$V_{\rm helio}$ (km s^{-1})	$V_{\rm gsr}$ (km s^{-1})	σ_V (km s^{-1})	R_{TD}
007489	20 30 50.72	–30 19 45.0	12.64	0.10	–4.2	42.2	19.4	8.19
007665	20 30 52.13	–30 21 51.1	12.98	0.17	45.6	92.0	49.5	4.00
007764	20 30 53.13	–30 19 46.8	11.89	0.00	80.9	127.2	18.0	8.85
007864	20 30 53.75	–30 18 42.8	13.22	0.13	34.1	80.4	41.2	4.56
007956	20 30 54.32	–30 23 21.6	12.36	0.07	78.3	124.6	25.0	6.61
008030	20 30 55.04	–30 23 56.8	13.14	0.01	51.2	97.5	33.6	5.28
008108	20 30 55.87	–30 20 40.5	13.03	0.17	49.4	95.7	38.7	4.77
008245	20 30 57.47	–30 19 24.5	12.80	0.27	62.2	108.5	44.3	4.33
008284	20 30 57.91	–30 17 50.8	12.68	0.18	71.6	117.9	27.0	6.22
008393	20 30 59.01	–30 20 40.1	12.35	0.07	144.6	190.9	30.7	5.64
008510	20 31 00.04	–30 17 22.9	13.06	0.14	42.6	89.0	36.5	4.98
008554	20 31 00.49	–30 18 33.0	12.10	0.11	–325.3	–278.9	19.5	8.18
008660	20 31 01.35	–30 24 02.5	13.28	0.23	102.3	148.7	60.6	3.46
008773	20 31 02.47	–30 17 17.8	11.52	0.05	158.6	205.0	15.3	10.66
008870	20 31 03.28	–30 18 45.8	13.22	0.16	110.7	157.1	65.8	3.26
008974	20 31 04.18	–30 19 17.3	11.98	0.02	95.5	141.9	19.2	8.29
009092	20 31 05.19	–30 19 34.8	12.09	0.04	3.5	49.8	18.9	8.40
009190	20 31 06.01	–30 21 00.7	13.04	0.21	73.2	119.5	72.0	3.05
009454	20 31 08.09	–30 20 12.9	12.19	0.02	183.0	229.3	39.2	4.73
009557	20 31 09.38	–30 17 47.1	12.43	0.14	61.4	107.8	28.2	6.01
009734	20 31 10.71	–30 19 21.1	11.82	0.12	138.2	184.5	30.4	5.69

Table 3.14: Spectroscopic and Photometric Data for Objects in Field 060.1n01.3

ID	$\alpha_{J2000.0}$	$\delta_{J2000.0}$	I_0	$(V-I)_0$	$V_{\rm helio}$ (km s^{-1})	$V_{\rm gsr}$ (km s^{-1})	σ_V (km s^{-1})	R_{TD}
000598	23 26 04.98	–23 06 09.8	20.78	0.88	–77.7	–32.7	18.0	8.84
000603	23 25 51.32	–23 06 06.1	21.13	0.78	–21.8	23.2	25.9	6.43
000629	23 26 15.77	–23 05 41.7	20.79	0.60	–71.8	–26.8	25.4	6.52
000634	23 25 13.76	–23 05 41.4	19.95	1.01	–111.6	–66.6	16.5	9.75
000647	23 25 41.70	–23 05 37.4	21.81	0.96	–37.1	7.9	54.6	3.73
000665	23 25 49.25	–23 05 31.2	21.88	0.93	35.3	80.4	63.9	3.33
000752	23 26 05.99	–23 04 24.8	19.80	1.01	–172.3	–127.3	15.9	10.15
000753	23 25 17.61	–23 04 23.9	20.88	0.57	–126.4	–81.4	51.8	3.87
000755	23 25 42.85	–23 04 23.3	20.78	0.73	–122.5	–77.4	24.7	6.66
000764	23 26 09.05	–23 04 12.4	21.02	0.65	–278.2	–233.2	44.6	4.31
000767	23 25 49.62	–23 04 10.8	19.76	0.57	–82.5	–37.5	15.4	10.63
000784	23 25 23.56	–23 03 54.3	20.31	0.56	–235.3	–190.2	40.3	4.63
000804	23 26 03.18	–23 03 35.9	21.58	0.84	–139.8	–94.8	38.9	4.75
000810	23 25 53.93	–23 03 28.1	20.11	0.53	–82.0	–37.0	18.1	8.77
000812	23 26 11.95	–23 03 24.5	20.52	0.55	–118.8	–73.8	15.9	10.18
000828	23 25 44.98	–23 03 14.0	21.21	0.56	–87.7	–42.7	75.3	2.95
000851	23 26 10.54	–23 02 59.8	21.41	0.74	–96.6	–51.6	53.2	3.80
000876	23 26 13.63	–23 02 41.0	19.93	0.50	–82.6	–37.6	18.5	8.58
000878	23 25 43.69	–23 02 40.5	19.88	0.64	–156.6	–111.6	14.0	12.41
000897	23 26 07.00	–23 02 30.3	21.84	0.55	–197.6	–152.6	43.5	4.39
000910	23 25 14.39	–23 02 21.3	20.13	0.94	–131.1	–86.1	22.1	7.30
000933	23 26 16.36	–23 01 56.2	20.06	0.49	–72.6	–27.6	14.8	11.19
000950	23 25 21.26	–23 01 46.6	21.78	0.64	–81.7	–36.6	22.6	7.16
001014	23 25 50.92	–23 00 59.8	21.94	0.94	–126.0	–80.9	51.5	3.89
001016	23 26 14.69	–23 00 57.4	21.87	0.82	–104.7	–59.7	62.3	3.39
001044	23 25 37.80	–23 00 42.1	21.23	1.02	–217.8	–172.8	71.7	3.06
001055	23 25 33.13	–23 00 33.2	20.36	0.48	–149.1	–104.1	16.5	9.69
001069	23 25 39.65	–23 00 19.7	21.74	0.58	–46.9	–1.9	31.7	5.51
001073	23 25 43.29	–23 00 16.2	21.40	0.87	–200.0	–155.0	31.9	5.49
001074	23 25 23.00	–23 00 14.3	21.91	0.37	–20.5	24.5	32.4	5.43
001082	23 25 27.70	–23 00 09.2	20.44	0.44	–91.5	–46.5	23.3	7.00
001096	23 26 01.35	–23 00 02.7	21.50	0.43	–158.2	–113.1	35.4	5.09
001111	23 26 10.09	–22 59 52.6	19.34	0.55	101.9	146.9	13.3	13.66
001130	23 25 55.88	–22 59 44.5	20.97	0.61	–99.8	–54.8	17.3	9.20
001213	23 25 45.74	–22 59 04.0	21.78	0.98	–28.4	16.6	37.2	4.91
001216	23 25 46.77	–22 59 02.4	19.49	0.61	–95.3	–50.3	12.4	17.37
001257	23 25 38.94	–22 58 29.3	20.87	0.52	–50.0	–4.9	16.3	9.83
001303	23 25 19.91	–22 58 04.4	21.65	0.74	–93.9	–48.9	39.2	4.73
001319	23 26 17.33	–22 57 55.9	21.18	0.67	–89.3	–44.3	31.4	5.55
001328	23 25 53.35	–22 57 53.0	20.04	0.52	–88.5	–43.5	12.9	15.05
001329	23 25 38.56	–22 57 51.7	21.97	0.69	–53.2	–8.1	48.3	4.07
001334	23 25 26.27	–22 57 49.1	21.19	0.58	–247.7	–202.6	32.0	5.48
001335	23 25 18.65	–22 57 49.0	19.48	1.00	–51.2	–6.1	18.5	8.58
001353	23 25 40.11	–22 57 31.9	19.76	1.02	–151.7	–106.7	25.3	6.54
001359	23 25 27.17	–22 57 25.3	21.85	0.61	–20.9	24.2	41.3	4.55

Table 3.15: Spectroscopic and Photometric Data for Objects in Field 075.0p00.9

ID	$\alpha_{J2000.0}$	$\delta_{J2000.0}$	I_0	$(V-I)_0$	$V_{\rm helio}$ (km s^{-1})	$V_{\rm gsr}$ (km s^{-1})	σ_V (km s^{-1})	R_{TD}
000018	0 19 32.59	–14 56 39.1	21.21	0.65	–166.3	–117.4	68.9	3.15
000036	0 19 27.60	–14 56 26.8	21.61	0.79	–15.1	33.8	82.4	2.76
000105	0 19 15.67	–14 55 42.2	21.16	0.58	–93.7	–44.8	33.8	5.26
000115	0 19 37.85	–14 55 35.1	19.39	0.72	–109.1	–60.3	13.8	12.70
000145	0 19 31.43	–14 55 11.1	21.77	0.84	–19.4	29.4	91.9	2.54
000158	0 18 59.50	–14 54 58.9	20.78	0.62	145.1	193.9	24.1	6.80
000160	0 19 22.55	–14 54 56.3	19.35	0.63	–24.3	24.6	12.7	15.74
000161	0 19 11.94	–14 54 56.0	21.03	0.60	–82.3	–33.4	27.9	6.06
000164	0 19 44.71	–14 54 50.1	20.13	0.62	–155.2	–106.4	22.3	7.25
000174	0 19 21.29	–14 54 45.8	21.02	0.64	–121.3	–72.4	51.8	3.87
000204	0 19 58.60	–14 54 21.9	21.00	0.67	176.7	225.6	65.8	3.26
000248	0 19 47.18	–14 53 43.0	21.40	0.95	–103.6	–54.7	87.4	2.64
000252	0 19 07.86	–14 53 41.6	21.96	0.63	147.8	196.6	66.3	3.24
000266	0 19 28.58	–14 53 34.9	20.22	0.54	–92.1	–43.2	66.6	3.23
000279	0 19 03.63	–14 53 30.0	21.31	0.91	18.3	67.1	77.8	2.88
000293	0 19 24.01	–14 53 22.9	21.97	0.67	–78.3	–29.4	68.3	3.17
000299	0 19 37.34	–14 53 18.7	20.78	0.91	60.8	109.7	40.2	4.64
000382	0 19 31.81	–14 52 28.1	19.66	0.67	–110.0	–61.2	13.2	14.14
000447	0 19 01.78	–14 51 41.5	20.02	0.81	20.0	68.8	21.5	7.48
000482	0 19 34.56	–14 51 11.2	20.77	0.55	–77.6	–28.8	27.0	6.22
000483	0 19 05.88	–14 51 11.5	19.72	0.54	–73.8	–25.0	17.7	8.98
000544	0 19 04.06	–14 50 26.8	21.41	0.65	–56.5	–7.7	57.6	3.59
000545	0 19 40.22	–14 50 25.3	20.16	0.79	–28.0	20.9	17.7	9.00
000547	0 19 47.96	–14 50 21.1	21.69	0.76	–88.7	–39.8	77.4	2.89
000548	0 18 58.52	–14 50 22.6	20.17	0.58	–86.1	–37.3	27.6	6.11
000625	0 19 13.33	–14 49 19.9	20.95	0.66	–89.3	–40.5	49.0	4.03
000627	0 19 53.06	–14 49 16.3	21.58	0.82	–65.0	–16.1	62.8	3.37
000654	0 19 31.07	–14 49 01.5	20.39	0.51	–112.8	–64.0	29.9	5.76
000671	0 19 42.19	–14 48 47.3	20.76	0.58	–181.5	–132.6	50.6	3.94
000681	0 19 00.79	–14 48 42.6	20.29	0.59	–144.1	–95.2	31.3	5.57
000742	0 19 02.19	–14 47 59.6	21.14	0.66	–7.9	40.9	58.2	3.56
000769	0 19 24.86	–14 47 39.2	20.21	0.79	–104.8	–55.9	41.7	4.52

Table 3.16: Spectroscopic and Photometric Data for Objects in Field 075.1n01.1

ID	$\alpha_{J2000.0}$	$\delta_{J2000.0}$	I_0	$(V-I)_0$	$V_{\rm helio}$ (km s^{-1})	$V_{\rm gsr}$ (km s^{-1})	σ_V (km s^{-1})	R_{TD}
000488	0 23 00.67	–16 37 28.4	21.41	0.70	–24.4	17.0	63.3	3.35
000504	0 23 47.52	–16 37 17.8	21.03	0.61	–40.4	1.1	16.6	9.62
000552	0 23 10.30	–16 36 42.6	20.69	0.61	–12.2	29.2	26.5	6.32
000553	0 23 25.26	–16 36 40.8	20.56	0.53	–18.9	22.5	37.7	4.86
000566	0 23 39.36	–16 36 28.4	20.21	0.55	–23.1	18.3	13.7	12.95
000605	0 23 21.81	–16 36 00.5	20.67	0.96	–24.9	16.5	62.8	3.37
000648	0 22 55.64	–16 35 26.7	21.01	0.88	–71.5	–30.0	21.5	7.49
000653	0 22 52.03	–16 35 24.8	21.20	0.65	–57.5	–16.1	18.4	8.62
000671	0 23 23.37	–16 35 11.6	21.90	0.68	–96.4	–55.0	71.4	3.07
000672	0 23 18.23	–16 35 11.5	21.52	0.70	–117.1	–75.7	40.3	4.63
000691	0 23 11.69	–16 34 59.8	21.62	0.72	–7.1	34.4	38.6	4.78
000726	0 22 57.44	–16 34 40.9	20.80	0.58	–89.8	–48.4	17.0	9.38
000749	0 23 24.60	–16 34 15.6	20.66	0.57	–98.7	–57.3	14.7	11.36
000762	0 23 30.40	–16 34 09.8	21.45	0.85	–93.0	–51.5	25.9	6.43
000814	0 23 28.07	–16 33 24.0	21.82	0.73	–111.6	–70.2	52.6	3.83
000832	0 23 30.84	–16 33 15.1	21.19	0.64	24.0	65.4	71.1	3.08
000872	0 23 16.53	–16 32 52.6	21.04	0.56	–106.5	–65.1	17.0	9.39
000892	0 23 41.63	–16 32 37.4	21.38	0.70	–85.5	–44.1	65.5	3.27
000952	0 23 51.97	–16 32 07.6	21.81	0.85	39.7	81.1	70.4	3.10
001012	0 23 21.01	–16 31 25.8	21.10	0.62	–116.6	–75.2	25.8	6.44
001096	0 23 36.03	–16 30 19.2	20.77	0.66	–18.1	23.3	17.0	9.39
001105	0 23 20.34	–16 30 16.5	20.67	0.47	211.8	253.3	15.5	10.48
001124	0 23 12.06	–16 29 59.6	20.80	0.46	–29.2	12.2	19.2	8.28
001127	0 23 51.47	–16 29 56.7	20.67	0.72	119.7	161.2	30.6	5.66
001150	0 23 10.92	–16 29 42.3	21.91	0.53	–28.6	12.9	71.1	3.08
001152	0 23 33.04	–16 29 41.1	20.60	0.58	–56.8	–15.4	14.8	11.18
001153	0 22 56.23	–16 29 40.6	19.36	0.90	–177.9	–136.5	29.4	5.83
001157	0 23 44.31	–16 29 37.7	21.34	0.62	–81.1	–39.7	18.8	8.47
001179	0 23 29.65	–16 29 22.5	20.42	0.51	–51.9	–10.5	20.7	7.74
001200	0 23 09.27	–16 29 13.2	21.55	0.45	–58.4	–16.9	44.0	4.35
001212	0 23 31.53	–16 29 06.4	21.01	0.73	93.8	135.2	21.3	7.53
001216	0 23 34.03	–16 29 03.6	20.99	0.83	56.8	98.2	17.9	8.90
001226	0 23 08.33	–16 28 56.7	19.99	0.44	–45.6	–4.2	13.4	13.44
001238	0 23 35.41	–16 28 46.3	21.17	1.01	–18.6	22.8	62.6	3.38
001243	0 23 37.96	–16 28 44.3	21.67	0.61	131.4	172.8	60.6	3.46

Table 3.17: Spectroscopic and Photometric Data for Objects in Field 090.0n00.7

ID	$\alpha_{J2000.0}$	$\delta_{J2000.0}$	I_0	$(V-I)_0$	$V_{\rm helio}$ (km s^{-1})	$V_{\rm gsr}$ (km s^{-1})	σ_V (km s^{-1})	R_{TD}
000180	1 17 01.46	–9 15 51.7	21.53	0.68	–33.0	1.9	47.0	4.15
000207	1 16 54.91	–9 15 08.7	21.64	0.67	172.1	207.0	49.7	3.99
000219	1 16 56.90	–9 14 58.1	20.91	0.59	–92.0	–57.1	20.6	7.77
000221	1 16 55.85	–9 14 56.7	20.91	0.63	–138.8	–103.9	24.2	6.78
000249	1 16 48.64	–9 14 30.0	20.90	0.46	–108.5	–73.5	76.4	2.92
000287	1 17 21.40	–9 13 40.9	21.34	0.57	–95.0	–60.0	55.2	3.70
000291	1 17 13.48	–9 13 38.9	21.36	1.03	–136.0	–101.1	48.3	4.07
000297	1 16 54.17	–9 13 36.2	21.12	0.65	–19.2	15.7	37.1	4.92
000304	1 16 31.56	–9 13 34.6	20.59	0.74	–67.5	–32.6	19.3	8.25
000324	1 16 30.85	–9 13 14.3	21.50	0.52	–30.1	4.8	23.4	6.98
000335	1 17 14.57	–9 13 05.1	20.18	0.58	–107.8	–72.9	16.0	10.12
000336	1 16 37.06	–9 13 05.9	20.87	0.65	–0.2	34.7	36.5	4.98
000391	1 16 58.21	–9 12 04.1	21.48	0.65	–49.1	–14.2	34.0	5.24
000397	1 17 12.05	–9 11 59.6	21.60	0.72	–31.8	3.1	56.9	3.62
000399	1 17 15.39	–9 11 56.2	20.94	0.55	–123.9	–89.0	20.0	7.98
000408	1 17 06.39	–9 11 41.0	21.43	0.54	–71.6	–36.7	31.5	5.54
000448	1 16 48.11	–9 10 57.6	21.26	0.67	–70.8	–35.9	75.3	2.95
000489	1 16 24.30	–9 10 06.5	21.24	0.96	–56.7	–21.8	50.4	3.95
000492	1 17 10.36	–9 10 01.8	21.00	1.05	–75.2	–40.3	44.0	4.35
000499	1 16 29.29	–9 09 54.4	19.43	0.72	–227.8	–192.9	21.9	7.37
000511	1 16 32.27	–9 09 34.0	21.94	0.94	–30.5	4.4	62.8	3.37
000515	1 16 46.09	–9 09 28.5	20.24	0.56	–63.9	–29.0	41.2	4.56
000525	1 16 43.45	–9 09 20.9	20.49	1.03	–230.6	–195.7	26.8	6.26
000530	1 16 39.62	–9 09 18.0	20.35	0.66	–226.2	–191.3	35.5	5.08
000544	1 16 30.29	–9 09 02.8	21.13	0.72	–124.7	–89.8	43.5	4.39
000549	1 17 07.80	–9 08 59.8	21.52	0.48	–114.7	–79.8	50.9	3.92
000559	1 16 44.37	–9 08 43.9	20.49	0.90	–186.0	–151.1	28.4	5.99
000616	1 16 40.71	–9 07 52.1	21.47	0.76	–20.7	14.2	54.0	3.76

Table 3.18: Spectroscopic and Photometric Data for Objects in Field 090.0p01.3

ID	$\alpha_{J2000.0}$	$\delta_{J2000.0}$	I_0	$(V-I)_0$	$V_{\rm helio}$ (km s^{-1})	$V_{\rm gsr}$ (km s^{-1})	σ_V (km s^{-1})	R_{TD}
000116	1 13 00.20	–7 29 51.8	21.45	0.76	–93.9	–51.2	80.0	2.82
000120	1 12 59.27	–7 29 43.8	20.48	0.66	–247.2	–204.4	80.0	2.82
000151	1 12 46.65	–7 28 26.1	19.61	0.67	6.8	49.6	73.3	3.01
000167	1 12 17.15	–7 28 01.2	20.65	0.41	–58.3	–15.5	30.4	5.69
000171	1 12 18.98	–7 27 56.2	20.98	0.55	–192.0	–149.2	80.0	2.82
000200	1 13 12.09	–7 27 08.0	20.05	0.50	–167.5	–124.7	34.0	5.24
000262	1 12 49.69	–7 25 49.8	20.26	0.68	–153.7	–110.9	23.6	6.93
000277	1 12 52.00	–7 25 28.4	20.19	0.50	–30.6	12.1	54.6	3.73
000284	1 12 26.61	–7 25 21.4	21.39	0.68	–181.8	–139.0	63.9	3.33
000289	1 12 34.32	–7 25 12.4	21.29	0.67	–110.0	–67.2	42.6	4.45
000293	1 12 58.00	–7 25 06.3	20.90	0.82	142.5	185.3	47.7	4.11
000302	1 12 32.42	–7 24 55.9	21.15	0.51	–200.0	–157.3	39.9	4.67
000330	1 12 41.66	–7 24 15.8	20.94	0.55	–56.0	–13.2	57.1	3.61
000351	1 12 17.91	–7 23 52.2	20.83	0.52	–99.3	–56.6	38.7	4.77
000378	1 12 40.53	–7 23 25.3	21.15	0.69	–33.1	9.7	93.8	2.50
000451	1 13 13.45	–7 21 54.4	21.61	0.67	–105.7	–62.9	69.5	3.13
000468	1 12 45.22	–7 21 39.3	21.12	0.74	–64.0	–21.2	63.1	3.36
000491	1 12 50.32	–7 21 12.8	21.70	0.34	–60.3	–17.5	50.4	3.95
000505	1 12 20.27	–7 21 00.0	19.99	0.40	–53.9	–11.1	31.1	5.59
000507	1 12 38.68	–7 20 55.9	20.48	0.62	–161.9	–119.1	30.5	5.67

Table 3.19: Spectroscopic and Photometric Data for Objects in Field 090.1n02.7

ID	$\alpha_{J2000.0}$	$\delta_{J2000.0}$	I_0	$(V-I)_0$	$V_{\rm helio}$ (km s^{-1})	$V_{\rm gsr}$ (km s^{-1})	σ_V (km s^{-1})	R_{TD}
000351	1 21 07.16	–10 58 07.2	21.64	0.99	–44.2	–17.0	74.0	2.99
000367	1 21 23.18	–10 57 54.1	20.56	0.75	–104.2	–77.0	13.8	12.74
000380	1 20 47.00	–10 57 47.8	19.62	0.75	–89.1	–61.9	12.9	14.97
000408	1 20 37.52	–10 57 34.7	20.25	0.67	–58.0	–30.8	17.1	9.36
000413	1 20 54.97	–10 57 28.7	21.26	0.80	–64.7	–37.5	24.9	6.63
000451	1 21 36.13	–10 57 00.4	21.13	0.67	55.7	83.0	35.0	5.13
000458	1 20 51.60	–10 56 57.3	21.32	1.02	5.6	32.8	52.8	3.82
000499	1 21 15.23	–10 56 30.3	20.78	0.75	–61.5	–34.3	17.0	9.39
000533	1 20 58.46	–10 56 09.1	21.20	0.67	–23.9	3.4	43.5	4.39
000572	1 20 48.52	–10 55 44.0	20.08	0.74	–11.6	15.6	20.3	7.86
000631	1 20 52.51	–10 54 55.8	21.57	0.79	137.3	164.5	45.9	4.22
000642	1 21 00.51	–10 54 46.0	21.14	0.94	–69.6	–42.3	12.1	19.48
000678	1 21 13.85	–10 54 26.8	21.12	0.93	–122.5	–95.3	24.6	6.70
000708	1 21 01.03	–10 54 10.8	20.77	0.71	–58.8	–31.6	24.4	6.73
000746	1 21 20.98	–10 53 41.9	19.76	0.69	–161.6	–134.4	27.1	6.21
000851	1 20 50.19	–10 52 36.0	21.37	0.92	–198.2	–171.0	39.2	4.73
000897	1 21 15.99	–10 52 04.7	20.39	0.98	–6.0	21.2	47.0	4.15
000899	1 20 42.11	–10 52 05.9	20.93	0.75	17.5	44.7	21.0	7.64
000910	1 21 01.40	–10 51 59.3	20.28	0.64	–132.3	–105.1	17.7	8.99
000922	1 21 19.44	–10 51 48.2	21.38	0.57	64.2	91.5	50.4	3.95
000925	1 20 46.55	–10 51 47.2	20.77	0.72	–97.6	–70.3	16.6	9.65
000947	1 20 45.01	–10 51 29.5	20.23	0.76	–133.5	–106.3	14.0	12.34
001048	1 21 12.24	–10 50 33.9	21.94	0.93	–3.9	23.4	50.6	3.94
001069	1 20 44.43	–10 50 20.4	21.56	0.92	–65.5	–38.2	38.8	4.76
001078	1 21 11.70	–10 50 15.9	21.56	0.69	–71.8	–44.6	34.3	5.20
001123	1 21 27.79	–10 49 53.9	21.01	0.71	–147.8	–120.6	42.5	4.46
001165	1 21 28.50	–10 49 28.2	20.40	0.65	–147.9	–120.6	15.0	10.97

Table 3.20: Spectroscopic and Photometric Data for Objects in Field 105.1n02.3

ID	$\alpha_{J2000.0}$	$\delta_{J2000.0}$	I_0	$(V-I)_0$	$V_{\rm helio}$ (km s^{-1})	$V_{\rm gsr}$ (km s^{-1})	σ_V (km s^{-1})	R_{TD}
000152	2 12 04.10	–3 04 47.7	21.04	0.49	–116.7	–98.2	39.5	4.70
000167	2 12 36.06	–3 04 31.3	19.80	0.80	–134.8	–116.3	13.4	13.52
000177	2 12 14.94	–3 04 24.0	20.39	0.60	–142.5	–124.1	26.5	6.32
000183	2 12 20.11	–3 04 18.2	20.61	0.54	–54.2	–35.8	19.6	8.13
000186	2 12 07.09	–3 04 15.7	20.44	0.88	131.3	149.7	22.2	7.29
000202	2 12 37.69	–3 03 56.7	20.94	0.65	–205.2	–186.7	41.6	4.53
000210	2 12 33.02	–3 03 51.2	21.10	0.89	30.8	49.2	81.6	2.78
000216	2 12 55.67	–3 03 40.0	21.08	0.97	20.0	38.5	34.4	5.19
000229	2 12 34.44	–3 03 30.9	19.64	0.54	118.4	136.9	14.0	12.27
000236	2 12 25.92	–3 03 18.0	21.17	0.60	–142.2	–123.8	35.4	5.09
000237	2 12 36.49	–3 03 15.6	19.76	0.61	–149.4	–130.9	17.3	9.24
000241	2 12 13.98	–3 03 11.4	20.10	0.62	–93.4	–74.9	17.3	9.22
000279	2 12 25.16	–3 02 29.7	19.84	0.69	–84.8	–66.4	14.9	11.07
000314	2 12 16.66	–3 01 47.4	21.51	0.98	–28.8	–10.3	83.2	2.74
000339	2 12 35.54	–3 01 27.1	20.01	0.65	–107.9	–89.4	18.5	8.59
000353	2 12 42.07	–3 01 11.8	21.31	0.60	–172.8	–154.4	57.3	3.60
000370	2 12 11.61	–3 00 51.9	21.47	0.88	57.4	75.9	75.7	2.94
000392	2 12 22.75	–3 00 31.1	21.09	0.67	190.6	209.0	58.7	3.54
000451	2 12 24.04	–2 59 42.8	19.31	0.62	–173.2	–154.8	18.6	8.56
000490	2 12 02.26	–2 59 08.6	21.11	0.58	–103.7	–85.2	35.0	5.13
000504	2 12 21.62	–2 58 55.3	21.07	0.63	–227.9	–209.5	53.0	3.81
000548	2 12 57.33	–2 58 23.7	20.97	0.68	–259.6	–241.2	52.0	3.86
000567	2 12 45.50	–2 58 07.2	20.83	0.62	–229.1	–210.7	40.0	4.66
000586	2 12 40.84	–2 57 53.0	20.40	0.60	–148.6	–130.2	31.8	5.50
000594	2 12 14.33	–2 57 50.2	20.04	0.61	111.4	129.9	33.5	5.30
000615	2 12 49.47	–2 57 31.2	21.02	0.62	–85.6	–67.1	49.3	4.01
000641	2 12 04.61	–2 57 14.6	21.79	0.48	–176.7	–158.3	81.2	2.79
000669	2 12 45.11	–2 56 32.1	20.98	0.59	–168.7	–150.3	55.4	3.69
000687	2 12 36.90	–2 56 12.5	21.16	0.51	–166.5	–148.0	39.6	4.69

Table 3.21: Spectroscopic and Photometric Data for Objects in Field 119.9p00.0

ID	$\alpha_{J2000.0}$	$\delta_{J2000.0}$	I_0	$(V-I)_0$	$V_{\rm helio}$ (km s^{-1})	$V_{\rm gsr}$ (km s^{-1})	σ_V (km s^{-1})	R_{TD}
000277	2 58 46.46	6 24 53.1	20.53	0.60	–67.9	–52.7	53.4	3.79
000415	2 58 47.57	6 28 35.6	20.45	0.57	44.7	59.9	67.2	3.21
000664	2 58 49.47	6 23 01.3	21.17	0.68	–159.0	–143.7	80.0	2.82
000678	2 58 49.68	6 23 15.5	21.03	0.63	–146.3	–131.0	57.1	3.61
000887	2 58 50.83	6 24 11.8	21.11	0.52	–31.9	–16.7	52.8	3.82
000999	2 58 51.18	6 20 57.2	19.77	0.71	–188.1	–172.9	58.9	3.53
001067	2 58 51.29	6 32 38.4	20.46	0.53	–146.1	–130.8	28.1	6.04
001376	2 58 53.22	6 33 04.3	20.51	0.61	–80.8	–65.6	36.2	5.01
001542	2 58 54.41	6 27 54.5	20.54	0.50	–188.7	–173.5	45.3	4.26
001696	2 58 55.14	6 26 31.6	21.27	0.64	–39.3	–24.1	69.5	3.13
001701	2 58 55.15	6 32 06.3	21.70	0.61	–266.0	–250.7	79.3	2.84
001743	2 58 55.59	6 32 57.7	20.91	0.70	–151.1	–135.8	66.3	3.24
002077	2 58 57.80	6 30 11.6	21.72	0.64	–102.0	–86.7	69.2	3.14
002145	2 58 58.48	6 27 43.0	20.16	0.56	–124.3	–109.1	32.9	5.36
002167	2 58 58.63	6 31 33.4	21.30	0.55	1.9	17.1	64.4	3.31
002174	2 58 58.75	6 22 01.7	20.77	0.59	–50.8	–35.6	47.3	4.13
002235	2 58 59.16	6 29 55.0	19.33	0.63	–182.0	–166.8	16.5	9.73
002777	2 59 04.11	6 34 06.3	20.85	0.59	–227.7	–212.4	63.9	3.33
002802	2 59 04.35	6 25 43.5	21.73	0.72	–216.8	–201.5	78.9	2.85
002924	2 59 05.33	6 21 07.3	21.58	0.55	–48.9	–33.6	43.0	4.42
003047	2 59 06.46	6 26 46.2	20.27	0.65	–159.1	–143.9	30.9	5.62
003250	2 59 07.94	6 29 23.0	19.70	0.62	–114.6	–99.4	23.4	6.96
003567	2 59 10.92	6 21 37.1	20.87	0.67	–161.2	–145.9	51.8	3.87
003872	2 59 13.58	6 30 47.5	20.50	0.50	–155.5	–140.3	42.9	4.43

Table 3.22: Spectroscopic and Photometric Data for Objects in Field 135.1p00.5

ID	$\alpha_{J2000.0}$	$\delta_{J2000.0}$	I_0	$(V-I)_0$	$V_{\rm helio}$ (km s^{-1})	$V_{\rm gsr}$ (km s^{-1})	σ_V (km s^{-1})	R_{TD}
003437	3 51 47.84	14 07 13.3	21.38	0.46	–124.4	–120.6	69.2	3.14
003668	3 51 49.32	14 08 22.2	21.16	0.65	31.8	35.6	49.9	3.98
003831	3 51 50.66	14 11 09.9	19.36	0.44	–20.3	–16.5	28.4	5.98
005050	3 52 00.58	14 08 45.3	20.16	0.54	–307.1	–303.3	74.6	2.97
005681	3 52 04.88	14 17 27.6	18.98	0.71	–6.7	–2.8	23.9	6.85
005761	3 52 05.58	14 13 00.9	20.57	0.45	–72.0	–68.1	83.6	2.73
005812	3 52 06.06	14 20 29.9	19.87	0.54	–52.5	–48.6	56.7	3.63
006054	3 52 08.08	14 11 55.8	19.61	0.69	–54.9	–51.0	28.9	5.91
006088	3 52 08.25	14 08 40.1	19.82	0.80	–1.9	2.0	32.9	5.37
006206	3 52 08.86	14 10 54.6	20.51	0.48	–73.8	–69.9	72.0	3.05
006317	3 52 09.77	14 10 30.4	20.81	0.76	34.6	38.4	65.5	3.27
007525	3 52 17.90	14 12 35.1	20.66	0.51	–34.1	–30.3	52.6	3.83
007823	3 52 19.56	14 06 28.0	19.79	0.61	16.1	20.0	56.0	3.66
008654	3 52 24.60	14 13 50.4	20.51	0.70	–148.6	–144.7	23.6	6.92

Table 3.23: Spectroscopic and Photometric Data for Objects in Field 139.9n07.6

ID	$\alpha_{J2000.0}$	$\delta_{J2000.0}$	I_0	$(V-I)_0$	$V_{\rm helio}$ (km s^{-1})	$V_{\rm gsr}$ (km s^{-1})	σ_V (km s^{-1})	R_{TD}
003423	4 24 59.61	9 06 23.4	19.39	0.40	81.4	49.8	32.7	5.39
003736	4 24 57.05	9 06 16.7	19.60	0.39	–87.7	–119.3	82.0	2.77
003897	4 24 56.27	9 00 14.3	20.63	0.61	46.3	14.7	49.5	4.00
003964	4 24 55.69	9 03 59.1	20.27	0.55	27.2	–4.4	44.2	4.34
004437	4 24 52.49	9 04 53.1	19.89	0.69	7.3	–24.3	83.6	2.73
004482	4 24 51.94	9 12 30.1	19.37	0.51	37.4	5.8	21.3	7.55
004567	4 24 51.40	9 07 47.3	19.23	0.83	–3.6	–35.2	51.8	3.87
004596	4 24 51.04	9 08 23.4	21.07	0.76	1.3	–30.3	63.3	3.35
004597	4 24 51.24	8 59 41.5	20.74	0.59	49.6	18.0	80.0	2.82
004638	4 24 50.84	9 05 21.6	19.61	0.43	19.5	–12.1	23.6	6.91
004787	4 24 49.31	9 01 50.1	19.78	0.50	26.1	–5.5	50.9	3.92
005013	4 24 48.18	8 59 50.2	20.25	0.65	23.2	–8.4	70.4	3.10
005158	4 24 47.43	9 05 07.8	19.68	0.38	–2.4	–34.0	45.3	4.26
005210	4 24 47.26	9 03 17.8	19.69	0.56	57.1	25.5	46.1	4.21
005355	4 24 46.26	9 12 13.7	20.06	0.71	9.8	–21.8	60.8	3.45
005678	4 24 44.41	9 04 07.0	19.61	0.85	–20.8	–52.4	66.3	3.24
005948	4 24 42.41	9 12 23.6	20.68	0.52	353.6	322.0	75.0	2.96
006256	4 24 40.15	9 05 54.7	20.64	0.65	20.3	–11.2	74.6	2.97
006293	4 24 39.94	9 02 49.0	19.98	0.60	–16.2	–47.8	35.2	5.11
006476	4 24 38.23	9 01 43.8	18.90	0.41	7.8	–23.8	14.0	12.41
006775	4 24 35.60	9 07 59.1	21.24	0.48	36.5	5.0	84.4	2.71
007226	4 24 31.96	9 03 01.3	19.81	0.54	19.1	–12.5	75.3	2.95
007257	4 24 31.77	9 00 55.6	19.68	0.56	53.2	21.6	33.2	5.33
007387	4 24 30.82	8 59 59.7	19.34	0.85	61.4	29.8	27.1	6.20
007403	4 24 30.67	9 00 27.7	19.73	0.77	15.5	–16.0	32.8	5.38
007634	4 24 28.71	9 11 10.2	21.26	0.48	–22.8	–54.3	54.2	3.75
007919	4 24 27.11	9 02 39.6	19.44	0.59	71.5	39.9	25.9	6.42
007988	4 24 26.51	9 10 15.8	20.97	0.54	–64.7	–96.3	63.1	3.36
008093	4 24 25.55	9 12 46.4	20.21	0.58	42.3	10.7	84.8	2.70

Table 3.24: Spectroscopic and Photometric Data for Objects in Field 147.0n04.5

ID	$\alpha_{J2000.0}$	$\delta_{J2000.0}$	I_0	$(V-I)_0$	$V_{\rm helio}$ (km s^{-1})	$V_{\rm gsr}$ (km s^{-1})	σ_V (km s^{-1})	R_{TD}
000872	4 45 50.48	14 48 57.9	19.47	0.64	13.6	–12.4	41.6	4.53
001138	4 45 48.21	14 45 50.8	18.37	0.47	53.0	27.0	12.6	16.06
001158	4 45 48.06	14 45 10.1	19.13	0.62	–26.7	–52.8	20.1	7.94
001243	4 45 47.14	14 46 56.4	20.39	0.69	–17.0	–43.0	82.0	2.77
001325	4 45 46.15	14 54 00.5	19.06	0.46	–22.7	–48.7	21.3	7.55
001331	4 45 46.16	14 51 23.9	19.18	0.82	27.0	1.0	23.7	6.90
001361	4 45 45.87	14 45 57.5	18.51	0.49	28.3	2.2	17.6	9.06
001368	4 45 45.69	14 50 54.5	18.43	0.40	–22.6	–48.7	21.7	7.42
001439	4 45 44.66	14 56 43.5	18.43	0.65	–2.8	–28.9	16.7	9.60
001546	4 45 43.97	14 45 44.3	20.05	0.44	–11.1	–37.1	48.2	4.08
001600	4 45 43.23	14 52 54.9	18.39	0.39	–14.7	–40.7	15.0	11.06
001655	4 45 42.56	14 55 19.5	19.32	0.51	–3.0	–29.1	63.1	3.36
001658	4 45 42.72	14 47 01.9	18.42	0.32	7.9	–18.1	14.5	11.63
001768	4 45 41.25	14 58 43.0	18.81	0.41	42.9	16.8	29.7	5.79
001856	4 45 40.48	14 55 59.6	19.31	0.53	–20.0	–46.1	47.3	4.13
001936	4 45 39.81	14 47 21.6	18.97	0.69	88.3	62.2	32.9	5.37
001958	4 45 39.36	14 58 09.9	18.38	0.80	45.8	19.8	21.6	7.44
002223	4 45 36.83	14 53 04.0	20.73	0.38	–111.1	–137.2	49.9	3.98
002233	4 45 36.85	14 47 10.0	18.54	0.66	5.0	–21.1	17.6	9.05
002443	4 45 34.60	14 51 46.6	18.47	0.51	–67.4	–93.4	19.0	8.36
002524	4 45 34.03	14 51 13.8	18.67	0.66	39.6	13.5	18.7	8.52
002544	4 45 33.63	14 58 57.8	18.38	0.54	–2.2	–28.3	21.3	7.55
002552	4 45 33.86	14 46 16.6	20.06	0.63	61.0	35.0	56.0	3.66
002604	4 45 33.19	14 55 32.8	19.41	0.46	25.5	–0.6	30.9	5.62
002631	4 45 33.04	14 46 23.4	19.06	0.51	–4.1	–30.2	28.3	6.00
002777	4 45 31.26	14 59 16.4	19.70	0.73	41.5	15.5	54.4	3.74
002787	4 45 31.44	14 46 31.2	18.69	0.60	33.3	7.2	19.3	8.25
002805	4 45 31.04	14 54 19.4	19.12	0.52	7.0	–19.1	31.3	5.57
002810	4 45 30.98	14 55 05.5	18.81	0.65	8.4	–17.7	20.1	7.96
002893	4 45 29.99	14 53 12.1	19.80	0.65	39.4	13.4	51.7	3.88
002988	4 45 28.97	14 58 35.6	19.37	0.55	39.7	13.6	25.1	6.58
003062	4 45 28.16	14 59 42.3	18.75	0.51	–91.4	–117.5	61.1	3.44
003150	4 45 27.40	14 51 38.4	20.04	0.55	56.4	30.3	55.4	3.69
003424	4 45 23.94	14 48 01.7	20.35	0.71	104.9	78.9	78.5	2.86
003850	4 45 19.97	14 44 47.6	19.27	0.66	5.7	–20.3	50.4	3.95
003871	4 45 19.67	14 49 51.3	18.61	0.29	22.0	–4.0	50.7	3.93
004143	4 45 16.93	14 44 38.6	18.90	0.77	18.2	–7.9	54.2	3.75
004407	4 45 13.91	14 47 49.3	19.40	0.43	–2.6	–28.7	51.1	3.91

Table 3.25: Spectroscopic and Photometric Data for Objects in Field 150.0n01.1

ID	$\alpha_{J2000.0}$	$\delta_{J2000.0}$	I_0	$(V-I)_0$	$V_{\rm helio}$ (km s^{-1})	$V_{\rm gsr}$ (km s^{-1})	σ_V (km s^{-1})	R_{TD}
000145	4 51 01.18	19 21 02.6	18.93	0.76	–135.7	–151.13	65.8	3.26
000387	4 51 03.39	19 09 57.9	18.62	0.36	–61.0	–76.45	82.8	2.75
000690	4 51 06.10	19 21 46.2	19.25	0.71	–91.0	–106.45	87.4	2.64
000714	4 51 06.37	19 18 45.9	18.56	0.73	–252.3	–267.72	45.3	4.26
000885	4 51 07.90	19 10 12.7	19.02	0.80	–122.8	–138.30	64.4	3.31
001045	4 51 08.93	19 08 56.0	18.57	0.51	–192.1	–207.52	60.1	3.48
001063	4 51 09.06	19 17 38.3	19.32	0.65	–73.3	–88.79	50.7	3.93
001273	4 51 10.74	19 15 30.3	19.47	0.77	–42.7	–58.20	82.8	2.75
001820	4 51 15.80	19 11 27.6	19.14	0.69	–150.5	–165.93	60.8	3.45
002007	4 51 17.33	19 11 51.4	18.61	0.64	–126.2	–141.64	43.9	4.36
002374	4 51 20.69	19 13 23.4	19.34	0.81	–30.3	–45.78	77.1	2.90
002389	4 51 20.81	19 15 25.1	19.41	0.46	37.1	21.64	73.0	3.02
002549	4 51 22.00	19 08 36.5	18.64	0.52	–81.3	–96.74	69.2	3.14
002844	4 51 24.65	19 07 50.2	19.50	0.67	–101.6	–117.11	90.0	2.58
002910	4 51 25.13	19 13 14.0	18.76	0.43	–169.7	–185.11	36.5	4.98
003091	4 51 25.94	19 13 05.6	19.13	0.70	–81.5	–96.94	61.6	3.42
003703	4 51 30.10	19 10 54.6	19.08	0.46	9.0	–6.42	58.2	3.56
003777	4 51 30.76	19 21 28.6	18.88	0.73	–40.6	–56.08	81.2	2.79
003891	4 51 31.89	19 11 01.7	19.23	0.70	–50.5	–65.95	52.0	3.86

Table 3.26: Spectroscopic and Photometric Data for Objects in Field 150.0n08.9

ID	$\alpha_{J2000.0}$	$\delta_{J2000.0}$	I_0	$(V-I)_0$	$V_{\rm helio}$ (km s^{-1})	$V_{\rm gsr}$ (km s^{-1})	σ_V (km s^{-1})	R_{TD}
003377	5 04 03.66	11 55 54.6	19.12	0.85	75.3	30.0	25.5	6.50
003522	5 04 02.69	11 54 42.2	21.55	0.65	76.8	31.4	66.9	3.22
003571	5 04 02.26	11 54 59.0	20.00	0.57	80.2	34.9	21.1	7.60
003589	5 04 02.33	11 49 40.8	20.78	0.69	63.7	18.3	32.9	5.36
003615	5 04 02.18	11 49 54.0	21.36	0.82	75.5	30.1	42.2	4.48
003738	5 04 01.45	11 50 28.6	21.20	0.67	72.1	26.7	55.8	3.67
003756	5 04 00.99	12 01 55.0	19.50	0.47	105.8	60.4	23.4	6.97
003765	5 04 00.90	12 03 41.1	20.45	0.69	57.2	11.8	31.2	5.58
003814	5 04 00.79	11 56 09.0	20.38	0.74	90.0	44.6	26.8	6.25
003981	5 03 59.78	11 59 39.5	20.49	0.72	51.4	6.0	32.6	5.40
004124	5 03 58.98	12 01 14.7	21.26	0.60	63.2	17.8	52.6	3.83
004163	5 03 59.04	11 51 41.5	19.76	0.57	74.4	29.0	27.2	6.19
004373	5 03 57.78	12 04 17.6	21.54	0.57	80.7	35.3	82.8	2.75
004410	5 03 57.52	12 02 15.4	20.08	0.61	74.0	28.6	34.9	5.14
004478	5 03 57.17	12 03 57.3	21.03	0.81	56.0	10.6	48.3	4.07
004592	5 03 56.83	11 54 07.0	19.66	0.55	61.2	15.8	26.5	6.32
004912	5 03 54.79	12 00 23.8	20.78	0.54	78.9	33.5	40.1	4.65
005137	5 03 53.85	11 51 56.3	19.13	0.67	77.1	31.7	16.8	9.52
005138	5 03 53.52	12 03 49.5	19.98	0.49	49.1	3.7	34.8	5.15
005225	5 03 53.21	11 51 23.6	21.59	0.73	57.9	12.5	67.2	3.21
005271	5 03 52.78	11 55 28.4	19.31	0.82	82.4	37.0	46.7	4.17
005422	5 03 51.75	12 04 32.7	19.43	0.85	88.4	43.0	75.7	2.94
005534	5 03 50.80	12 04 03.9	21.40	0.80	76.3	30.9	73.3	3.01
005734	5 03 50.70	11 52 36.4	19.31	0.72	55.4	10.0	25.1	6.58
005934	5 03 50.44	11 53 28.3	20.09	0.28	76.2	30.8	77.4	2.89
006384	5 03 49.70	12 03 34.0	20.48	0.53	82.7	37.3	54.6	3.73
006849	5 03 48.60	11 53 07.3	21.50	0.71	85.6	40.2	59.2	3.52
006896	5 03 48.32	12 00 14.0	20.08	0.77	76.1	30.7	49.3	4.01
007393	5 03 47.06	11 54 16.5	19.86	0.48	50.3	4.9	25.8	6.44
008370	5 03 43.84	11 56 48.8	19.42	0.65	52.9	7.5	18.8	8.47
008414	5 03 43.66	11 58 21.3	20.08	0.60	55.1	9.7	26.8	6.26
008489	5 03 43.26	12 00 08.8	20.86	0.62	59.2	13.8	46.1	4.21
008503	5 03 43.28	11 55 16.7	19.33	0.41	36.0	–9.3	23.4	6.96
008504	5 03 43.37	11 52 04.0	19.00	0.49	26.6	–18.7	16.4	9.77
008567	5 03 43.14	11 50 41.1	20.93	0.83	64.5	19.2	34.3	5.21
008732	5 03 42.24	11 56 24.1	20.72	0.71	48.3	2.9	41.6	4.53
008750	5 03 42.27	11 52 12.1	19.02	0.63	31.6	–13.7	18.6	8.55
008843	5 03 41.66	11 57 49.9	21.38	0.62	65.0	19.6	55.4	3.69
009274	5 03 39.82	12 01 01.6	21.18	0.72	60.6	15.3	72.0	3.05
009371	5 03 39.35	12 02 29.0	19.43	0.75	75.1	29.8	16.7	9.57
009762	5 03 37.66	12 04 12.1	21.33	0.44	59.7	14.3	65.8	3.26
010041	5 03 36.19	12 04 26.7	19.28	0.90	45.0	–0.4	24.7	6.67
010281	5 03 35.28	11 56 36.3	19.83	0.90	73.5	28.1	35.9	5.04
010624	5 03 33.42	12 03 10.2	19.20	0.67	36.4	–9.0	17.6	9.05
010958	5 03 32.14	11 58 03.5	20.51	0.51	76.1	30.7	20.3	7.87
011346	5 03 30.67	11 53 35.8	20.65	0.44	58.6	13.2	89.6	2.59
011385	5 03 30.24	12 00 52.3	20.15	0.45	99.4	54.0	30.8	5.63

Continued on Next Page...

Table 3.26 – 150.0n08.9 (Continued)

ID	$\alpha_{J2000.0}$	$\delta_{J2000.0}$	I_0	$(V-I)_0$	$V_{\rm helio}$ (km s^{-1})	$V_{\rm gsr}$ (km s^{-1})	σ_V (km s^{-1})	R_{TD}
011632	5 03 29.06	11 53 49.7	20.39	0.53	70.0	24.6	33.1	5.34
011643	5 03 28.76	12 02 43.4	20.06	0.56	64.4	19.0	22.0	7.35
011712	5 03 28.53	11 58 46.1	19.41	0.85	79.1	33.7	21.2	7.56
011880	5 03 28.12	11 59 11.7	19.00	0.68	91.2	45.8	14.4	11.75
011992	5 03 27.65	11 58 11.2	19.72	0.45	60.8	15.4	23.6	6.93
012123	5 03 27.05	11 57 22.9	19.29	0.62	105.4	60.1	31.3	5.56

Table 3.27: Spectroscopic and Photometric Data for Objects in Field 177.4n02.7

ID	$\alpha_{J2000.0}$	$\delta_{J2000.0}$	I_0	$(V-I)_0$	$V_{\rm helio}$ (km s^{-1})	$V_{\rm gsr}$ (km s^{-1})	σ_V (km s^{-1})	R_{TD}
100077	6 45 26.33	25 41 44.3	18.18	0.66	29.2	–14.2	4.0	26.08
101053	6 45 30.21	25 38 41.0	18.90	0.74	21.5	–21.9	4.9	21.96
102648	6 45 37.26	25 41 18.8	19.71	0.80	76.6	33.3	10.3	12.82
103155	6 45 39.83	25 38 17.6	18.36	0.64	39.0	–4.4	4.0	26.23
104313	6 45 46.52	25 38 07.0	18.12	0.51	43.8	0.4	5.3	20.45
104710	6 45 50.73	25 36 30.2	20.07	0.73	51.5	8.1	19.3	8.38
105984	6 45 58.33	25 40 24.5	18.58	0.60	81.0	37.6	50.9	4.25
106699	6 46 03.05	25 40 11.2	18.30	0.61	–8.9	–52.3	4.9	21.75
106748	6 46 03.17	25 43 45.0	19.54	0.76	–41.1	–84.4	22.8	7.48
107350	6 46 07.17	25 41 10.1	19.57	0.85	375.4	332.1	16.2	9.42
107363	6 46 07.06	25 42 55.9	19.28	0.66	20.7	–22.7	10.9	12.33
107670	6 46 09.59	25 39 06.0	18.46	0.61	20.0	–23.4	4.6	23.16
107873	6 46 10.68	25 40 39.7	19.00	0.73	46.1	2.7	4.5	23.54
107894	6 46 10.72	25 41 58.7	19.89	0.89	23.0	–20.3	13.6	10.61
108429	6 46 15.20	25 41 19.3	19.58	0.84	–26.7	–70.1	14.6	10.14
108447	6 46 15.50	25 38 57.9	18.88	0.75	21.9	–21.5	4.3	24.11
108940	6 46 19.73	25 41 01.1	19.90	0.66	3.3	–40.1	7.6	15.71
108977	6 46 20.32	25 38 04.8	19.27	0.66	28.8	–14.5	5.3	20.42
109047	6 46 20.93	25 37 01.2	20.02	0.80	–73.8	–117.2	11.1	12.15
109177	6 46 22.00	25 36 15.6	19.56	0.71	21.8	–21.6	6.7	17.27
109482	6 46 25.26	25 37 32.6	19.38	0.70	–69.5	–112.9	4.6	23.03
110614	6 46 34.09	25 36 48.5	19.91	0.80	–10.2	–53.6	13.7	10.56
111131	6 46 38.04	25 43 02.3	18.29	0.69	70.3	26.9	3.4	31.14
111417	6 46 41.11	25 40 51.7	18.84	0.76	38.3	–5.1	3.6	29.28
111618	6 46 42.81	25 41 24.8	19.03	0.65	–53.9	–97.2	5.6	19.76
111904	6 46 44.46	25 43 38.3	19.26	0.62	44.5	1.1	5.0	21.39
112213	6 46 45.99	25 39 19.2	19.03	0.64	5.9	–37.4	3.7	27.99
200544	6 45 29.01	25 51 16.4	19.31	0.71	50.9	7.5	49.5	4.34
200816	6 45 31.08	25 44 55.8	18.24	0.54	26.1	–17.3	5.1	21.13
201979	6 45 37.25	25 52 47.2	18.46	0.59	10.6	–32.8	5.1	21.04
202383	6 45 39.79	25 47 58.8	19.22	0.75	66.8	23.4	10.0	13.04
202951	6 45 42.26	25 53 15.8	19.84	0.80	–9.9	–53.3	30.1	6.19
203362	6 45 45.22	25 50 32.0	18.50	0.60	323.2	279.8	9.1	13.97
203725	6 45 48.82	25 44 43.3	20.00	0.76	–48.4	–91.8	17.7	8.88
203838	6 45 50.08	25 48 03.4	18.27	0.62	–31.4	–74.8	3.6	28.57
203844	6 45 49.88	25 52 21.0	19.14	0.76	59.3	15.9	48.1	4.43
204186	6 45 52.62	25 46 16.0	18.22	0.53	17.2	–26.2	5.5	19.90
204415	6 45 54.45	25 48 59.5	19.25	0.57	7.8	–35.5	11.2	12.08
204588	6 45 56.34	25 52 23.4	19.32	0.73	72.7	29.3	9.0	14.00
204659	6 45 57.16	25 48 08.1	19.11	0.59	10.4	–33.0	6.2	18.29
205781	6 46 05.35	25 45 06.9	19.70	0.81	11.8	–31.6	13.2	10.85
205821	6 46 05.21	25 51 34.2	19.80	0.88	69.8	26.5	20.9	7.96
206037	6 46 06.56	25 51 17.3	18.97	0.59	60.3	16.9	5.6	19.69
207062	6 46 12.81	25 48 53.6	19.95	0.68	–43.1	–86.5	16.6	9.30
207420	6 46 14.57	25 50 12.4	19.43	0.74	46.7	3.3	5.7	19.33
207859	6 46 16.42	25 48 44.7	18.18	0.52	55.8	12.4	4.7	22.64
207878	6 46 16.72	25 46 51.0	19.04	0.61	1.3	–42.1	5.1	21.01

Continued on Next Page...

Table 3.27 – 177.4n02.7 (Continued)

ID	$\alpha_{J2000.0}$	$\delta_{J2000.0}$	I_0	$(V-I)_0$	$V_{\rm helio}$ (km s^{-1})	$V_{\rm gsr}$ (km s^{-1})	σ_V (km s^{-1})	R_{TD}
208342	6 46 20.63	25 52 28.8	18.64	0.62	67.6	24.3	4.3	24.11
210087	6 46 28.11	25 46 54.8	20.02	0.70	–63.9	–107.2	25.8	6.88
211383	6 46 35.81	25 49 54.4	19.87	0.84	–100.9	–144.3	6.2	18.17
211640	6 46 36.86	25 53 38.5	19.40	0.63	30.1	–13.3	5.2	20.73
211912	6 46 38.38	25 48 24.0	18.43	0.52	18.8	–24.6	4.2	24.66
212675	6 46 40.93	25 52 58.4	19.37	0.77	14.1	–29.3	5.2	20.74
300222	6 45 26.88	25 58 08.0	19.30	0.78	25.7	–17.7	7.2	16.32
301487	6 45 36.91	26 00 24.2	19.71	0.90	76.8	33.5	11.4	11.92
301622	6 45 38.16	25 58 22.8	20.11	0.94	–51.8	–95.1	30.9	6.07
301688	6 45 38.89	25 56 09.8	19.89	0.62	67.8	24.4	33.3	5.77
302170	6 45 42.64	25 53 52.5	18.66	0.64	44.3	0.9	5.3	20.56
302370	6 45 43.79	26 00 01.5	19.88	0.75	83.0	39.6	20.5	8.05
303266	6 45 51.76	26 02 56.0	19.41	0.81	–18.5	–61.9	11.5	11.86
303413	6 45 53.39	25 58 07.0	19.26	0.63	28.7	–14.7	14.1	10.34
303629	6 45 56.02	25 59 17.9	18.26	0.55	–5.4	–48.8	4.8	22.25
303712	6 45 57.29	25 55 21.3	19.91	0.75	85.9	42.5	14.3	10.26
303789	6 45 57.90	25 57 21.7	19.72	0.76	20.4	–22.9	22.8	7.50
304597	6 46 03.66	26 02 16.2	19.09	0.76	22.7	–20.7	4.4	24.04
305928	6 46 19.10	26 01 25.8	19.71	0.85	5.9	–37.4	10.1	12.95
306112	6 46 20.76	25 58 06.5	18.73	0.73	144.6	101.3	4.3	24.23
306176	6 46 22.26	25 55 41.5	20.03	0.72	53.5	10.1	11.9	11.58
306349	6 46 24.09	25 58 15.8	18.57	0.73	44.0	0.6	3.3	31.69
306431	6 46 25.04	25 59 04.9	19.55	0.69	49.7	6.3	7.9	15.36
306600	6 46 26.68	25 56 51.2	18.27	0.52	39.5	–3.9	5.3	20.49
306881	6 46 28.41	25 58 54.6	19.09	0.76	–24.6	–67.9	5.1	21.21
308464	6 46 40.03	25 57 09.2	19.15	0.76	35.7	–7.7	4.2	24.70
308514	6 46 40.12	25 59 19.7	19.71	0.90	19.7	–23.7	16.9	9.17
308929	6 46 43.44	25 55 50.0	19.44	0.68	–28.1	–71.5	8.6	14.51
309037	6 46 44.01	25 59 34.7	18.63	0.63	17.2	–26.2	4.2	25.01
400659	6 45 27.75	26 05 50.1	18.71	0.68	6.8	–36.6	4.6	22.84
401267	6 45 29.30	26 04 43.0	18.98	0.79	1.5	–41.9	4.8	22.21
401937	6 45 31.12	26 09 56.5	18.74	0.65	58.0	14.6	4.8	22.34
402674	6 45 32.19	26 03 06.9	19.00	0.74	–1.2	–44.6	4.0	26.13
404034	6 45 35.25	26 07 04.8	20.09	0.78	30.3	–13.1	37.0	5.35
404192	6 45 35.83	26 03 25.7	19.60	0.85	67.8	24.4	9.8	13.28
409449	6 45 47.95	26 06 38.2	18.15	0.48	41.1	–2.3	6.4	17.82
409578	6 45 48.16	26 08 13.0	18.64	0.73	–19.7	–63.0	3.5	29.47
412168	6 45 52.00	26 08 31.9	19.24	0.64	55.8	12.4	8.8	14.19
413108	6 45 53.09	26 03 50.1	19.77	0.81	53.8	10.4	15.2	9.85
413571	6 45 53.90	26 10 24.6	19.38	0.67	47.2	3.9	7.3	16.16
415397	6 45 56.28	26 07 59.4	18.40	0.60	26.3	–17.1	4.0	26.20
424483	6 46 11.27	26 11 11.4	20.08	0.96	62.3	18.9	21.8	7.73
426117	6 46 13.27	26 08 13.3	18.29	0.52	5.7	–37.6	5.9	18.90
428233	6 46 15.59	26 07 55.6	19.69	0.81	41.0	–2.4	9.9	13.13
428995	6 46 16.65	26 10 15.9	20.04	0.77	101.8	58.5	16.4	9.35
432866	6 46 20.78	26 06 11.9	19.41	0.65	24.6	–18.8	6.3	18.05
435012	6 46 22.73	26 09 35.6	19.15	0.79	21.3	–22.1	4.2	25.10
439878	6 46 27.35	26 04 24.8	18.19	0.63	51.0	7.7	4.1	25.51

Continued on Next Page...

Table 3.27 – 177.4n02.7 (Continued)

ID	$\alpha_{J2000.0}$	$\delta_{J2000.0}$	I_0	$(V-I)_0$	$V_{\rm helio}$ (km s^{-1})	$V_{\rm gsr}$ (km s^{-1})	σ_V (km s^{-1})	R_{TD}
441454	6 46 28.67	26 11 49.5	18.97	0.79	79.7	36.3	4.9	21.91
447149	6 46 35.44	26 08 05.2	18.92	0.71	73.2	29.8	4.2	24.64
449053	6 46 38.78	26 04 28.2	19.58	0.89	–9.6	–52.9	7.6	15.78
451825	6 46 43.05	26 03 38.3	19.82	0.81	16.8	–26.6	8.9	14.16
452541	6 46 44.77	26 08 24.7	19.32	0.71	38.2	–5.1	8.0	15.17
502047	6 46 53.19	25 40 01.3	18.73	0.75	36.8	–6.6	3.8	27.36
502907	6 46 56.81	25 38 40.5	20.03	0.83	19.1	–24.2	6.8	16.97
503723	6 46 59.01	25 42 55.6	19.90	0.73	146.1	102.7	8.2	14.93
504225	6 47 00.85	25 40 40.6	18.55	0.53	5.6	–37.8	5.5	19.94
504444	6 47 01.94	25 43 55.8	19.40	0.64	23.5	–19.9	4.6	22.86
505497	6 47 06.20	25 42 38.3	18.23	0.65	50.8	7.4	3.4	31.23
505559	6 47 06.66	25 35 56.6	19.39	0.80	33.4	–10.0	6.7	17.17
507881	6 47 13.24	25 43 33.3	18.15	0.54	9.7	–33.7	4.3	24.11
510001	6 47 20.09	25 41 48.6	19.85	0.84	–9.1	–52.5	8.0	15.24
511281	6 47 23.69	25 39 05.3	18.67	0.69	17.7	–25.7	4.8	22.35
514552	6 47 32.24	25 41 46.9	19.36	0.84	60.8	17.4	4.7	22.70
514976	6 47 33.52	25 42 28.3	18.70	0.71	69.7	26.3	3.3	31.44
516836	6 47 39.51	25 39 27.2	18.84	0.63	44.4	1.0	4.3	24.37
519578	6 47 49.52	25 40 51.5	19.62	0.69	36.7	–6.7	6.0	18.56
520847	6 47 54.51	25 35 41.7	18.66	0.54	11.8	–31.6	4.6	22.81
521324	6 47 56.75	25 42 33.8	18.75	0.59	–4.3	–47.7	3.8	27.13
522537	6 48 04.47	25 40 44.1	19.07	0.66	–3.6	–47.0	5.0	21.58
600958	6 46 52.37	25 44 49.8	19.82	0.57	128.4	85.0	23.0	7.45
600994	6 46 52.57	25 49 13.7	19.11	0.65	24.3	–19.1	6.7	17.16
601256	6 46 54.52	25 47 05.7	18.87	0.78	26.8	–16.6	4.2	24.85
601267	6 46 54.74	25 44 38.0	19.19	0.65	36.1	–7.3	4.4	23.66
602195	6 47 03.77	25 46 00.7	19.46	0.76	–8.9	–52.3	5.9	18.83
602877	6 47 10.22	25 45 35.9	18.97	0.63	211.0	167.6	4.8	22.32
602921	6 47 10.27	25 52 49.1	18.56	0.62	16.7	–26.7	8.5	14.59
603047	6 47 11.54	25 50 04.9	19.86	0.72	53.8	10.4	10.1	13.01
603876	6 47 16.46	25 48 27.3	20.00	0.67	–2.4	–45.7	6.7	17.31
603930	6 47 17.01	25 51 37.0	19.90	0.71	7.0	–36.4	10.8	12.39
604154	6 47 18.72	25 46 45.1	18.29	0.63	–9.6	–53.0	3.5	29.98
604330	6 47 20.15	25 47 03.9	20.07	0.71	29.1	–14.3	9.9	13.12
606155	6 47 30.24	25 49 33.6	19.34	0.66	15.2	–28.2	4.6	22.99
606284	6 47 31.33	25 46 19.3	19.24	0.60	19.7	–23.7	5.3	20.54
606285	6 47 31.33	25 47 28.4	19.61	0.70	40.2	–3.1	5.3	20.49
606567	6 47 35.08	25 47 29.2	19.42	0.85	7.2	–36.2	5.1	21.19
606592	6 47 35.43	25 48 01.8	18.45	0.71	–6.2	–49.5	3.4	30.98
607660	6 47 43.13	25 51 58.4	19.76	0.90	57.5	14.1	10.8	12.43
607843	6 47 45.21	25 48 29.3	19.15	0.70	24.8	–18.6	6.5	17.54
608273	6 47 49.45	25 53 17.0	18.94	0.63	–4.8	–48.2	4.7	22.63
608360	6 47 50.45	25 49 48.9	19.24	0.78	55.8	12.4	5.2	20.87
608386	6 47 50.67	25 46 20.4	19.37	0.86	–26.9	–70.3	7.6	15.73
608485	6 47 52.40	25 49 02.3	18.77	0.68	12.3	–31.1	4.9	21.64
608847	6 47 54.49	25 51 11.1	18.60	0.61	42.8	–0.5	4.4	23.91
608896	6 47 54.78	25 52 51.5	19.45	0.63	–10.2	–53.5	5.9	18.96
609658	6 48 00.08	25 52 23.6	18.71	0.56	40.9	–2.5	8.1	15.12

Continued on Next Page...

Table 3.27 – 177.4n02.7 (Continued)

ID	$\alpha_{J2000.0}$	$\delta_{J2000.0}$	I_0	$(V-I)_0$	$V_{\rm helio}$ (km s^{-1})	$V_{\rm gsr}$ (km s^{-1})	σ_V (km s^{-1})	R_{TD}
700030	6 46 46.65	26 03 01.8	18.27	0.66	37.0	–6.3	3.0	37.02
700330	6 46 48.93	25 58 47.5	18.53	0.63	9.7	–33.7	4.0	25.94
700434	6 46 49.50	26 00 53.1	20.11	0.07	26.3	–17.1	10.2	12.90
701168	6 46 53.80	25 59 05.9	18.74	0.67	–86.3	–129.7	6.4	17.87
702098	6 47 00.01	25 55 50.8	18.81	0.77	22.8	–20.6	4.2	24.85
702668	6 47 04.59	26 01 04.8	19.71	0.81	0.4	–43.0	14.9	10.00
702870	6 47 06.67	26 02 39.4	19.02	0.69	23.2	–20.1	5.8	19.16
703649	6 47 11.82	25 58 29.5	20.03	0.72	25.0	–18.4	11.0	12.27
703951	6 47 14.88	25 57 19.5	19.67	0.77	5.5	–37.9	7.2	16.39
704795	6 47 20.83	25 56 10.2	19.38	0.63	–5.1	–48.5	5.3	20.52
705336	6 47 23.65	25 59 59.6	19.12	0.77	73.4	30.0	5.6	19.77
705382	6 47 24.22	25 54 54.6	18.12	0.58	59.6	16.2	5.4	20.13
705879	6 47 27.96	26 01 53.7	19.40	0.84	196.4	153.0	8.0	15.16
706004	6 47 28.60	26 02 26.7	19.35	0.70	14.0	–29.4	5.4	20.22
706397	6 47 31.28	25 58 46.0	18.28	0.65	47.3	3.9	4.0	25.75
707274	6 47 37.63	26 01 13.1	20.03	0.78	–105.8	–149.2	11.4	11.97
708090	6 47 45.81	25 55 36.3	20.11	0.85	–22.0	–65.4	14.4	10.20
708489	6 47 48.16	26 00 26.0	19.88	0.66	69.2	25.8	12.9	11.00
708567	6 47 48.49	26 01 33.1	18.32	0.52	33.4	–10.0	6.1	18.37
709110	6 47 53.50	25 58 04.7	18.25	0.51	33.9	–9.5	6.1	18.39
709294	6 47 55.41	25 59 28.4	19.68	0.74	–178.7	–222.1	12.7	11.10
709408	6 47 56.45	25 57 05.3	18.17	0.64	2.2	–41.2	3.4	30.35
710097	6 48 00.64	26 03 05.9	19.81	0.83	37.7	–5.7	9.4	13.60
710146	6 48 02.00	25 54 36.2	19.01	0.67	11.9	–31.5	7.1	16.49
710438	6 48 04.21	25 57 49.3	19.79	0.69	–34.9	–78.2	17.1	9.11
801443	6 46 48.22	26 10 17.6	19.29	0.58	14.5	–28.9	6.7	17.15
804144	6 46 50.96	26 07 21.7	18.55	0.62	–15.7	–59.1	5.6	19.68
807681	6 46 57.10	26 11 59.5	19.34	0.80	52.2	8.8	5.3	20.40
808726	6 46 58.89	26 04 37.8	19.21	0.73	–6.8	–50.2	5.0	21.45
811334	6 47 04.01	26 04 42.0	18.70	0.66	–46.0	–89.4	3.9	26.78
812260	6 47 06.46	26 04 25.8	19.07	0.64	51.0	7.6	4.7	22.52
812425	6 47 06.64	26 06 32.6	19.20	0.61	213.3	169.9	9.3	13.73
813959	6 47 08.68	26 10 37.5	18.27	0.61	19.2	–24.2	4.8	22.22
816309	6 47 15.32	26 03 48.0	19.29	0.67	5.3	–38.0	12.4	11.30
817120	6 47 16.46	26 10 03.2	19.85	0.78	–3.1	–46.5	13.2	10.82
820466	6 47 24.08	26 10 10.2	19.11	0.64	86.6	43.2	9.3	13.70
823071	6 47 34.71	26 06 49.4	19.18	0.69	–7.2	–50.6	6.8	17.11
823998	6 47 38.63	26 10 16.5	19.27	0.58	–4.0	–47.4	6.3	18.07
825685	6 47 44.68	26 09 44.4	19.42	0.80	58.3	15.0	6.9	16.88
826810	6 47 48.23	26 05 23.8	19.64	0.65	37.0	–6.4	11.6	11.84
826957	6 47 49.18	26 04 28.3	19.65	0.77	59.7	16.3	8.3	14.85
827555	6 47 50.83	26 12 01.3	18.60	0.67	62.8	19.4	4.5	23.31
827794	6 47 52.16	26 08 52.2	19.64	0.67	43.6	0.2	9.6	13.45
828890	6 47 58.64	26 04 50.5	18.89	0.63	–16.9	–60.3	4.7	22.61

Table 3.28: Spectroscopic and Photometric Data for Objects in Field 180.4n11.2

ID	$\alpha_{J2000.0}$	$\delta_{J2000.0}$	I_0	$(V-I)_0$	$V_{\rm helio}$ (km s^{-1})	$V_{\rm gsr}$ (km s^{-1})	σ_V (km s^{-1})	R_{TD}
000028	7 06 11.03	18 01 21.2	20.39	0.79	–2.3	–79.4	59.4	3.51
000204	7 06 10.29	18 02 40.2	20.72	0.86	25.1	–52.0	62.3	3.39
000318	7 06 09.69	18 06 06.3	20.22	0.77	16.0	–61.2	35.3	5.10
000802	7 06 08.09	17 58 19.7	20.98	0.88	–5.8	–82.9	50.6	3.94
001477	7 06 05.66	17 59 43.5	20.94	0.81	76.1	–1.0	28.3	6.00
001573	7 06 05.06	18 06 43.6	19.61	0.96	82.8	5.6	21.3	7.55
001869	7 06 04.50	18 03 00.2	20.36	0.77	31.3	–45.9	29.9	5.76
002212	7 06 03.45	18 02 36.7	20.26	0.80	11.3	–65.9	25.6	6.49
002347	7 06 02.98	18 00 38.7	20.28	0.78	–5.3	–82.4	19.4	8.21
002430	7 06 02.53	17 59 48.7	19.98	0.62	66.3	–10.8	19.2	8.31
002524	7 06 02.00	18 02 16.6	20.24	1.04	40.2	–37.0	40.8	4.59
002736	7 06 01.11	17 59 38.1	20.26	0.76	–8.2	–85.3	20.2	7.89
002986	7 05 59.95	18 03 14.1	20.42	0.58	100.5	23.4	28.2	6.02
003080	7 05 59.41	18 02 47.9	19.89	0.63	31.3	–45.8	14.5	11.64
003774	7 05 56.21	18 00 33.2	19.96	1.25	37.4	–39.7	32.9	5.36
004163	7 05 54.31	18 06 43.5	21.02	0.87	58.5	–18.6	34.0	5.24
004488	7 05 53.23	18 02 00.8	19.81	0.58	57.0	–20.1	20.8	7.70
004760	7 05 51.87	18 04 54.4	19.76	0.70	28.8	–48.4	15.7	10.32
004917	7 05 51.17	18 04 35.5	20.44	1.25	15.1	–62.1	48.0	4.09
005073	7 05 50.44	18 06 01.3	19.79	0.80	33.2	–43.9	16.7	9.56
005253	7 05 49.69	18 03 17.1	20.57	0.63	–4.0	–81.2	24.7	6.67
005560	7 05 48.33	18 05 17.8	20.34	0.67	39.4	–37.7	30.5	5.68
005715	7 05 47.59	17 58 42.3	20.35	1.18	–29.9	–107.1	58.9	3.53
006326	7 05 44.54	18 03 42.4	20.10	0.66	39.5	–37.6	18.0	8.84
006379	7 05 44.17	18 05 19.5	20.43	0.95	20.0	–57.1	24.1	6.80
006557	7 05 43.51	18 00 34.8	20.74	1.05	31.4	–45.7	62.3	3.39
006638	7 05 42.93	18 04 53.4	19.43	0.96	94.0	16.9	18.1	8.79
006739	7 05 42.52	18 02 55.8	19.41	1.19	61.5	–15.6	38.0	4.83
006876	7 05 41.99	17 58 27.4	21.27	1.11	–26.4	–103.6	57.1	3.61
006980	7 05 41.36	18 05 07.2	20.68	0.78	47.1	–30.0	32.3	5.44
007290	7 05 39.84	18 03 26.9	20.22	0.63	37.5	–39.6	26.3	6.35
007438	7 05 38.69	18 00 41.5	19.78	0.89	70.9	–6.3	15.2	10.80
007616	7 05 37.91	18 03 48.8	21.28	0.72	113.8	36.7	38.8	4.76
007913	7 05 37.02	18 02 57.4	20.49	0.74	–31.5	–108.6	18.6	8.57
008102	7 05 36.46	18 00 32.0	20.42	1.14	74.0	–3.2	58.7	3.54
008198	7 05 36.10	17 58 20.6	20.03	1.12	18.5	–58.6	55.6	3.68
008672	7 05 33.86	18 03 23.9	20.83	0.85	47.6	–29.5	38.4	4.80
008781	7 05 33.39	18 06 19.8	20.27	0.68	26.7	–50.4	24.6	6.70
008968	7 05 32.74	18 02 51.4	20.23	0.85	32.3	–44.8	16.3	9.90
009117	7 05 32.23	18 01 42.1	20.07	0.68	46.5	–30.7	14.4	11.77
009446	7 05 30.73	18 02 29.3	20.15	0.72	–9.7	–86.8	18.5	8.60
009562	7 05 30.19	18 02 17.6	19.99	0.76	–5.6	–82.8	18.2	8.72
009673	7 05 29.60	18 01 40.0	20.01	1.18	42.3	–34.8	20.2	7.91
009740	7 05 29.13	18 06 31.4	20.13	0.62	98.7	21.6	72.7	3.03
009854	7 05 28.61	18 01 48.5	21.20	1.17	22.4	–54.7	51.8	3.87
009921	7 05 28.11	18 06 39.4	21.37	1.25	–65.0	–142.1	73.6	3.00
010252	7 05 26.45	18 03 21.7	19.57	0.60	49.8	–27.3	14.8	11.29

Continued on Next Page...

Table 3.28 – 180.4n11.2 (Continued)

ID	$\alpha_{J2000.0}$	$\delta_{J2000.0}$	I_0	$(V-I)_0$	$V_{\rm helio}$ (km s^{-1})	$V_{\rm gsr}$ (km s^{-1})	σ_V (km s^{-1})	R_{TD}
010629	7 05 24.91	18 05 27.0	19.67	1.17	–28.7	–105.9	34.0	5.24
010862	7 05 24.08	18 06 37.3	20.08	0.70	5.4	–71.7	19.4	8.19
010952	7 05 23.67	18 04 05.3	19.81	1.05	62.2	–14.9	16.6	9.68
011224	7 05 22.57	17 58 09.1	19.50	0.74	21.9	–55.2	23.7	6.90
011424	7 05 21.32	17 58 15.4	19.44	0.68	48.2	–28.9	12.3	17.92
011845	7 05 19.38	18 06 06.4	20.28	0.73	38.4	–38.7	18.1	8.81
012063	7 05 18.40	18 03 20.2	19.75	0.61	84.5	7.4	12.7	15.55
012218	7 05 17.54	18 05 34.7	19.45	1.22	48.6	–28.6	34.7	5.16
012363	7 05 17.02	18 05 04.0	19.57	0.64	42.2	–35.0	15.8	10.28
012834	7 05 14.62	18 04 36.5	20.01	1.15	34.7	–42.4	45.5	4.25
013134	7 05 13.26	17 59 32.6	19.53	0.58	153.5	76.4	16.0	10.11
013343	7 05 12.16	17 59 38.8	20.22	0.79	37.7	–39.5	23.1	7.03
013446	7 05 11.49	18 02 09.4	19.78	1.16	39.9	–37.2	22.0	7.34
013591	7 05 10.64	18 06 34.2	20.10	0.76	38.1	–39.1	19.5	8.16
013708	7 05 10.08	18 03 41.1	19.65	1.00	54.1	–23.1	16.6	9.64

Table 3.29: Spectroscopic and Photometric Data for Objects in Field 197.4n00.9

ID	$\alpha_{J2000.0}$	$\delta_{J2000.0}$	I_0	$(V-I)_0$	$V_{\rm helio}$ (km s^{-1})	$V_{\rm gsr}$ (km s^{-1})	σ_V (km s^{-1})	R_{TD}
100415	8 14 30.80	29 23 35.3	18.40	0.60	–96.8	–144.9	3.6	29.24
100516	8 14 31.96	29 22 52.7	19.07	0.49	54.9	6.8	4.2	24.82
100675	8 14 36.41	29 20 44.4	18.08	0.55	82.0	33.9	8.7	14.40
101396	8 14 48.82	29 25 27.6	17.86	0.86	20.7	–27.4	3.3	31.31
101553	8 14 52.82	29 23 02.3	19.38	0.64	19.7	–28.4	9.3	13.74
101565	8 14 52.92	29 25 27.8	20.11	0.68	41.0	–7.1	9.9	13.12
101886	8 15 01.38	29 22 54.0	19.55	0.75	36.5	–11.6	4.3	24.49
101912	8 15 01.88	29 21 02.6	19.76	0.84	11.4	–36.7	21.6	7.78
102297	8 15 11.25	29 22 10.4	18.46	0.76	–84.5	–132.6	5.4	20.27
102627	8 15 14.78	29 20 13.6	19.55	0.63	–16.4	–64.5	7.7	15.63
103282	8 15 20.30	29 17 56.6	19.52	0.88	73.5	25.4	5.3	20.36
103414	8 15 20.88	29 19 13.9	17.82	0.70	14.9	–33.2	3.0	35.58
103664	8 15 22.75	29 23 50.8	19.34	0.70	–7.7	–55.8	4.3	24.13
103860	8 15 24.99	29 17 02.4	19.60	0.65	62.6	14.5	7.6	15.74
104258	8 15 28.99	29 20 47.5	18.71	0.61	1.2	–46.9	4.6	23.18
105417	8 15 37.44	29 23 18.9	19.20	0.84	278.7	230.6	8.1	15.12
105453	8 15 37.80	29 21 21.7	19.47	0.88	–28.9	–77.0	6.4	17.79
105857	8 15 44.43	29 20 41.2	19.37	0.68	36.8	–11.3	4.3	24.52
106116	8 15 47.01	29 22 05.6	20.12	0.93	–187.1	–235.2	28.7	6.40
106472	8 15 49.21	29 20 33.0	19.39	0.62	17.8	–30.3	5.1	21.29
200573	8 14 33.82	29 28 24.6	20.21	0.78	32.0	–16.1	19.8	8.25
201332	8 14 39.17	29 28 05.0	19.57	0.66	40.3	–7.8	8.4	14.75
201916	8 14 42.86	29 33 15.8	18.62	0.75	5.9	–42.2	3.6	28.73
201942	8 14 43.45	29 27 56.6	18.35	0.53	34.1	–14.0	4.4	23.65
202257	8 14 47.08	29 27 30.1	20.03	0.71	224.9	176.8	9.4	13.66
202587	8 14 49.84	29 31 36.1	18.57	0.27	232.9	184.8	51.6	4.21
202664	8 14 51.80	29 33 13.6	19.49	0.50	–108.6	–156.7	16.4	9.35
202734	8 14 53.27	29 34 12.1	19.16	0.52	–215.1	–263.2	6.3	18.07
202826	8 14 55.23	29 34 49.1	19.56	0.65	–23.0	–71.1	26.9	6.68
202892	8 14 56.94	29 31 39.8	18.46	0.63	–9.8	–57.9	3.4	30.65
203092	8 15 01.09	29 29 21.3	18.97	0.79	18.8	–29.3	5.7	19.31
203169	8 15 03.22	29 26 40.7	18.68	0.58	–47.9	–96.0	4.5	23.57
203527	8 15 10.24	29 28 52.6	20.21	0.88	–152.4	–200.5	15.2	9.87
203581	8 15 11.33	29 29 38.3	19.01	0.59	222.8	174.7	6.4	17.89
203640	8 15 12.37	29 34 08.3	18.71	0.62	45.0	–3.1	3.6	28.75
203799	8 15 15.46	29 26 56.2	17.79	0.59	33.2	–14.9	3.6	28.73
204964	8 15 26.07	29 32 59.3	19.03	0.81	–12.5	–60.6	4.2	25.03
205548	8 15 32.71	29 33 06.3	18.92	0.59	5.8	–42.3	3.9	26.76
205713	8 15 35.84	29 26 52.2	19.87	0.72	35.6	–12.5	12.5	11.26
205739	8 15 35.50	29 35 07.7	18.63	0.57	–6.2	–54.3	10.6	12.53
205940	8 15 37.81	29 34 35.5	18.94	0.75	39.5	–8.6	6.6	17.40
206115	8 15 39.09	29 27 01.6	18.60	0.90	18.3	–29.8	4.2	25.09
206536	8 15 44.67	29 32 24.1	19.57	0.61	36.2	–11.9	5.5	19.91
300016	8 14 26.38	29 36 35.0	20.18	0.89	23.6	–24.6	19.0	8.47
300220	8 14 31.30	29 41 54.7	19.48	0.69	61.3	13.2	6.3	17.93
300353	8 14 35.84	29 37 29.5	20.21	0.85	–71.5	–119.6	39.9	5.07
300635	8 14 40.08	29 37 45.3	19.01	0.69	46.6	–1.5	4.3	24.58

Continued on Next Page...

Table 3.29 – 197.4n00.9 (Continued)

ID	$\alpha_{J2000.0}$	$\delta_{J2000.0}$	I_0	$(V-I)_0$	$V_{\rm helio}$ (km s^{-1})	$V_{\rm gsr}$ (km s^{-1})	σ_V (km s^{-1})	R_{TD}
300665	8 14 40.79	29 43 15.5	19.62	0.77	9.5	–38.6	12.2	11.42
300690	8 14 41.47	29 38 56.2	19.60	0.72	31.4	–16.7	7.7	15.64
301071	8 14 48.81	29 39 30.6	17.91	0.77	–31.1	–79.2	3.0	35.70
301475	8 14 51.72	29 41 03.1	18.46	0.50	30.7	–17.4	4.9	21.94
302129	8 14 58.92	29 36 20.3	19.64	0.83	127.6	79.5	6.7	17.21
302185	8 14 59.31	29 41 21.8	18.81	0.48	0.8	–47.3	5.4	20.10
302250	8 15 00.46	29 39 52.1	19.26	0.74	32.4	–15.7	5.4	20.24
302357	8 15 02.47	29 35 35.2	19.54	0.86	0.7	–47.4	8.8	14.21
302822	8 15 09.53	29 37 00.7	19.58	0.59	–75.7	–123.8	12.3	11.36
302875	8 15 10.94	29 41 50.3	17.89	0.54	121.6	73.5	10.0	13.07
303386	8 15 15.80	29 37 47.9	20.04	0.58	0.3	–47.8	15.5	9.73
304362	8 15 25.73	29 43 16.4	18.41	0.90	16.7	–31.4	4.1	25.50
304804	8 15 28.63	29 40 07.5	19.54	0.93	–21.8	–69.9	8.3	14.84
305227	8 15 33.32	29 38 05.4	19.89	0.84	18.0	–30.1	8.3	14.78
305389	8 15 34.89	29 43 35.1	20.02	0.57	–10.6	–58.8	13.6	10.64
305854	8 15 41.56	29 38 23.6	18.70	0.66	–36.9	–85.0	5.4	20.33
305870	8 15 41.53	29 43 37.2	19.07	0.54	12.4	–35.7	4.3	24.28
306026	8 15 44.30	29 38 52.3	18.02	0.84	19.8	–28.3	3.3	31.62
306107	8 15 45.83	29 44 23.1	19.31	0.64	58.8	10.7	6.1	18.44
400009	8 14 26.00	29 46 03.8	19.62	0.79	16.4	–31.7	6.4	17.81
400218	8 14 28.87	29 44 49.1	18.35	0.61	39.2	–8.9	4.4	24.07
400238	8 14 29.00	29 47 39.6	19.98	0.85	154.9	106.8	21.0	7.93
400795	8 14 35.72	29 49 08.1	17.95	0.96	–78.2	–126.3	4.8	22.32
401155	8 14 37.97	29 51 05.6	19.66	0.63	5.7	–42.4	33.6	5.73
401767	8 14 45.68	29 52 05.7	19.97	0.65	–80.3	–128.4	30.1	6.19
401863	8 14 47.37	29 50 42.7	18.97	0.70	35.8	–12.3	8.2	14.95
402165	8 14 49.37	29 46 50.0	18.28	0.88	32.6	–15.5	4.0	26.14
402833	8 14 54.41	29 50 52.2	19.12	0.67	38.7	–9.4	8.4	14.66
403843	8 15 05.31	29 52 20.2	20.21	0.72	–67.9	–116.0	37.9	5.26
404469	8 15 07.93	29 49 15.1	17.90	0.88	16.3	–31.8	3.9	26.63
404946	8 15 09.97	29 51 14.1	18.00	0.40	–102.2	–150.3	21.4	7.82
405795	8 15 15.38	29 49 53.6	19.52	0.74	–51.6	–99.7	4.9	21.78
407827	8 15 22.84	29 50 05.4	19.39	0.90	–81.4	–129.5	8.8	14.29
407865	8 15 23.25	29 52 39.1	20.15	0.62	–76.0	–124.1	29.1	6.34
410137	8 15 34.64	29 45 46.1	18.04	0.54	54.8	6.7	5.4	20.15
410586	8 15 36.09	29 48 32.5	19.59	0.77	–24.4	–72.5	8.2	14.91
411599	8 15 40.84	29 50 57.9	18.90	0.96	–35.1	–83.2	6.1	18.55
500432	8 15 53.38	29 25 00.9	19.32	0.82	–48.3	–96.4	7.3	16.16
500562	8 15 56.00	29 18 57.7	18.71	0.61	–137.0	–185.1	7.1	16.51
501203	8 16 02.01	29 22 59.5	19.71	0.84	–43.9	–92.0	11.3	12.03
501252	8 16 02.67	29 18 03.4	19.94	0.72	62.2	14.1	9.2	13.83
502513	8 16 08.96	29 24 37.6	19.72	0.67	36.9	–11.2	7.2	16.31
506551	8 16 29.68	29 19 12.6	19.04	0.59	21.2	–26.9	10.6	12.58
507499	8 16 32.44	29 22 31.5	19.98	0.42	19.3	–28.8	43.3	4.78
507720	8 16 33.28	29 20 00.5	18.52	0.57	28.7	–19.4	5.0	21.55
508467	8 16 36.86	29 17 24.1	18.72	0.90	–29.1	–77.2	4.8	22.00
508595	8 16 37.55	29 23 44.4	20.01	0.82	21.4	–26.7	14.3	10.25
508914	8 16 38.58	29 17 31.4	19.32	0.74	18.0	–30.1	4.9	21.99

Continued on Next Page...

Table 3.29 – 197.4n00.9 (Continued)

ID	$\alpha_{J2000.0}$	$\delta_{J2000.0}$	I_0	$(V-I)_0$	$V_{\rm helio}$ (km s^{-1})	$V_{\rm gsr}$ (km s^{-1})	σ_V (km s^{-1})	R_{TD}
509312	8 16 40.50	29 18 14.6	19.62	0.73	70.4	22.3	9.7	13.36
510531	8 16 51.25	29 25 09.9	18.29	0.65	–8.6	–56.7	3.8	27.58
510711	8 16 52.33	29 19 45.9	17.99	0.56	15.8	–32.3	5.1	21.12
511793	8 17 01.40	29 25 56.5	17.85	0.78	–4.1	–52.2	4.0	25.94
511806	8 17 01.44	29 21 09.4	19.15	0.67	–20.3	–68.4	5.4	20.12
600782	8 16 02.10	29 28 28.7	19.97	0.65	137.8	89.7	10.5	12.60
601099	8 16 09.65	29 26 11.5	18.43	0.74	–10.0	–58.1	3.1	34.10
601204	8 16 10.97	29 28 21.2	18.25	0.63	–40.1	–88.2	3.4	31.19
601638	8 16 18.69	29 34 09.9	19.84	0.64	30.6	–17.5	17.4	9.00
602009	8 16 25.94	29 32 39.8	18.75	0.63	–29.9	–78.0	4.8	22.28
602144	8 16 28.61	29 31 15.9	17.97	0.87	61.2	13.1	3.9	26.34
602325	8 16 30.83	29 27 05.9	18.92	0.58	215.0	166.9	12.4	11.29
602688	8 16 33.31	29 31 19.5	18.54	0.81	4.5	–43.6	4.2	24.87
603111	8 16 38.56	29 26 28.3	17.93	0.63	–41.5	–89.6	3.4	30.79
603590	8 16 44.25	29 28 05.7	19.30	0.90	6.9	–41.2	6.2	18.32
603640	8 16 45.62	29 32 26.2	18.59	0.60	3.8	–44.3	5.0	21.62
603737	8 16 46.49	29 35 05.2	17.90	0.71	–5.2	–53.3	3.6	29.04
604296	8 16 53.43	29 31 12.7	18.94	0.59	–107.2	–155.3	6.9	16.93
604483	8 16 56.39	29 33 09.8	19.82	0.73	3.7	–44.4	16.9	9.19
604749	8 17 03.31	29 30 22.6	20.09	0.79	80.8	32.7	12.6	11.16
604984	8 17 05.36	29 27 23.3	17.83	0.52	62.7	14.6	5.2	20.84
605194	8 17 06.83	29 26 28.7	18.16	0.80	33.1	–15.0	3.4	30.58
605518	8 17 11.13	29 32 12.8	18.68	0.62	133.1	85.0	7.8	15.49
605583	8 17 11.94	29 33 10.0	20.20	0.61	38.4	–9.7	39.3	5.13
700086	8 15 50.77	29 41 29.9	19.45	0.66	–41.0	–89.1	5.4	20.35
700363	8 15 52.98	29 41 31.2	19.70	0.33	–78.0	–126.1	27.8	6.53
700687	8 15 56.43	29 37 11.7	19.74	0.58	6.6	–41.5	10.3	12.77
700832	8 15 57.07	29 41 07.6	19.14	0.83	32.7	–15.4	5.4	20.07
701064	8 15 58.83	29 41 57.2	19.98	0.66	81.7	33.6	15.9	9.56
701373	8 16 00.58	29 37 25.8	19.68	0.27	38.8	–9.3	17.3	9.02
701985	8 16 06.61	29 41 32.6	18.65	0.82	183.0	134.9	4.3	24.39
702047	8 16 08.16	29 37 05.3	19.64	0.93	–0.3	–48.4	13.9	10.45
702457	8 16 14.18	29 44 30.4	19.82	0.60	10.5	–37.6	8.2	14.99
703265	8 16 23.10	29 39 06.7	18.09	0.66	2.4	–45.7	3.5	29.35
703561	8 16 26.48	29 44 27.6	17.90	0.87	–12.1	–60.2	4.1	25.49
703678	8 16 28.15	29 44 05.8	19.93	0.59	–44.7	–92.8	19.9	8.21
705642	8 16 41.37	29 38 20.7	19.86	0.58	–2.2	–50.3	27.2	6.64
705712	8 16 41.77	29 39 23.3	19.12	0.63	–25.1	–73.2	4.3	24.12
705938	8 16 44.32	29 42 49.7	19.73	0.69	19.7	–28.4	12.6	11.19
707137	8 16 56.96	29 43 06.7	18.95	0.64	–21.1	–69.2	3.5	29.53
707387	8 16 59.06	29 35 56.0	19.09	0.67	65.5	17.4	5.6	19.62
707942	8 17 01.42	29 44 44.2	18.18	0.57	–70.3	–118.4	3.6	29.00
708541	8 17 05.58	29 37 15.3	18.79	0.80	–137.0	–185.1	8.0	15.19
709196	8 17 13.04	29 39 14.8	18.91	0.61	–105.7	–153.8	7.4	16.00
800570	8 15 51.89	29 46 17.5	20.06	0.83	33.1	–15.0	12.2	11.39
801621	8 15 57.91	29 47 55.3	20.08	0.71	–17.7	–65.8	31.6	5.98
802823	8 16 04.00	29 49 35.4	18.13	0.90	8.1	–40.0	4.3	24.13
804658	8 16 11.42	29 49 45.4	19.86	0.79	169.5	121.4	15.4	9.77

Continued on Next Page...

Table 3.29 – 197.4n00.9 (Continued)

ID	$\alpha_{J2000.0}$	$\delta_{J2000.0}$	I_0	$(V-I)_0$	$V_{\rm helio}$ (km s^{-1})	$V_{\rm gsr}$ (km s^{-1})	σ_V (km s^{-1})	R_{TD}
804837	8 16 12.82	29 47 52.0	20.17	0.89	183.3	135.2	23.4	7.36
805168	8 16 15.58	29 48 43.6	20.25	0.68	50.7	2.6	14.3	10.28
805970	8 16 23.77	29 47 00.0	20.11	0.74	75.6	27.5	20.6	8.03
806123	8 16 24.61	29 51 54.4	18.88	0.77	89.7	41.6	4.7	22.58
806590	8 16 27.67	29 46 59.4	19.10	0.64	117.5	69.4	31.6	5.98
806943	8 16 29.58	29 48 20.1	19.55	0.68	17.4	–30.7	12.3	11.38
808714	8 16 39.06	29 52 58.5	18.54	0.63	22.0	–26.1	4.7	22.69
809577	8 16 44.78	29 52 31.3	18.54	0.81	–22.9	–71.0	3.9	26.40
809674	8 16 45.96	29 49 09.8	19.95	0.68	–60.0	–108.1	11.1	12.20
810218	8 16 49.51	29 51 36.9	20.00	0.80	–224.8	–272.9	10.2	12.92
810832	8 16 56.01	29 48 08.6	18.68	0.92	–41.2	–89.3	5.7	19.32

Table 3.30: Spectroscopic and Photometric Data for Objects in Field 198.4n10.9

ID	$\alpha_{J2000.0}$	$\delta_{J2000.0}$	I_0	$(V-I)_0$	$V_{\rm helio}$ (km s^{-1})	$V_{\rm gsr}$ (km s^{-1})	σ_V (km s^{-1})	R_{TD}
000717	8 19 30.36	19 36 17.0	20.22	0.64	–64.2	–150.1	61.3	3.43
001427	8 20 26.90	19 35 05.6	19.43	0.70	–572.0	–657.9	59.6	3.50
002805	8 20 07.83	19 33 03.6	19.57	0.72	39.2	–46.7	60.3	3.47
003741	8 19 51.11	19 31 48.6	20.21	0.65	–49.4	–135.4	58.7	3.54
004044	8 20 13.39	19 31 35.9	19.62	0.62	124.6	38.7	52.4	3.84
005360	8 20 04.96	19 29 31.3	21.40	0.72	–15.1	–101.0	77.1	2.90

Table 3.31: Spectroscopic and Photometric Data for Objects in Field 207.1p00.2

ID	$\alpha_{J2000.0}$	$\delta_{J2000.0}$	I_0	$(V-I)_0$	$V_{\rm helio}$ (km s^{-1})	$V_{\rm gsr}$ (km s^{-1})	σ_V (km s^{-1})	R_{TD}
001123	9 02 47.25	30 17 29.3	19.57	0.79	100.7	53.0	18.2	8.73
001439	9 00 48.03	30 15 15.8	18.60	0.63	86.9	39.2	4.3	24.13
001656	9 02 45.53	30 16 19.4	19.89	0.56	–92.4	–140.1	8.7	14.34
002071	9 00 45.61	29 52 20.6	18.53	1.12	–13.0	–60.7	4.8	22.23
002400	9 02 36.15	29 52 08.0	19.57	0.70	–46.6	–94.4	14.3	10.26
002673	9 00 39.15	30 16 35.4	18.50	0.66	55.0	7.3	4.8	22.15
002765	9 00 40.46	29 49 25.1	17.73	1.32	0.0	–47.7	8.9	14.08
003032	9 00 38.94	29 53 02.6	16.63	0.65	–38.7	–86.4	2.9	37.57
003090	9 02 31.64	29 53 11.2	18.20	0.65	219.1	171.4	3.8	27.12
003405	9 00 32.77	30 17 29.1	16.23	0.59	25.9	–21.8	3.1	35.01
003449	9 00 32.30	30 13 33.0	16.44	1.01	24.8	–22.9	3.8	27.40
003644	9 00 34.78	29 51 30.0	19.49	0.84	–62.5	–110.2	6.7	17.27
004126	9 00 26.10	30 18 33.2	18.20	0.60	29.8	–17.9	5.1	20.99
004349	9 00 30.43	29 53 00.6	16.51	0.85	–36.1	–83.8	3.1	34.91
004805	9 00 19.12	30 18 04.9	16.31	0.65	40.4	–7.3	3.0	36.46
004972	9 02 17.82	29 52 02.0	17.15	0.99	–49.0	–96.7	4.4	23.91
004996	9 02 17.65	29 49 06.2	19.29	0.64	108.9	61.2	6.9	16.89
005247	9 00 15.96	30 14 21.9	17.02	0.92	95.3	47.6	3.7	27.67
005248	9 00 15.93	30 16 23.3	16.76	0.70	82.3	34.6	3.1	34.00
006007	9 02 28.17	30 14 07.4	19.04	0.59	–47.2	–94.9	6.7	17.23
006223	9 00 18.82	29 52 17.1	18.36	1.02	136.4	88.7	5.0	21.59
006703	9 00 05.51	30 18 59.0	16.25	0.69	–25.0	–72.8	3.1	35.24
006806	9 02 07.06	29 50 39.3	18.42	0.70	–17.0	–64.7	3.4	30.76
008145	9 00 05.93	29 50 25.0	16.64	0.67	3.1	–44.6	2.9	39.10
010783	9 02 07.10	30 16 59.0	18.33	0.48	31.7	–16.0	3.4	30.23
012858	9 01 59.20	30 14 33.2	19.05	0.95	97.8	50.0	4.9	21.84
100023	9 00 56.70	30 24 03.7	17.11	0.86	61.2	13.5	3.1	35.12
100207	9 00 55.23	30 20 42.4	17.34	0.99	12.0	–35.7	4.2	24.98
100388	9 02 48.56	29 55 37.6	19.98	1.06	–101.8	–149.5	24.5	7.14
100598	9 00 50.58	30 22 11.6	18.95	0.72	61.6	13.9	5.7	19.35
101325	9 00 39.52	30 20 19.2	19.01	1.15	196.0	148.3	20.2	8.13
101543	9 00 41.23	29 56 43.3	16.98	0.82	19.7	–28.0	2.9	37.42
101560	9 00 35.21	30 24 14.5	18.37	0.78	–87.5	–135.2	4.8	22.29
101746	9 02 34.93	29 57 20.9	17.70	0.88	28.1	–19.6	3.3	31.99
102019	9 02 40.26	30 19 12.1	17.50	0.49	129.0	81.3	11.8	11.67
102361	9 00 22.89	30 23 46.6	18.10	0.88	12.8	–34.9	4.8	22.24
102734	9 00 16.31	30 19 43.0	17.32	0.60	40.6	–7.1	12.5	11.26
102893	9 00 27.15	29 56 00.0	19.05	0.59	–31.9	–79.6	7.4	16.09
102997	9 02 20.64	29 56 26.9	17.05	0.86	22.7	–25.0	3.3	31.95
103159	9 02 18.75	29 57 45.4	17.07	0.58	92.0	44.3	3.4	30.72
103227	9 02 17.99	29 59 23.6	19.29	1.09	166.1	118.4	10.0	13.08
103298	9 02 17.08	29 54 19.1	18.31	0.90	–20.7	–68.4	3.8	27.56
103406	9 02 30.91	30 22 31.7	18.34	0.53	123.3	75.6	6.1	18.50
103450	9 00 04.52	30 24 50.0	16.13	1.04	–36.1	–83.8	4.4	23.74
103879	9 02 09.47	29 57 09.3	19.21	0.62	81.8	34.1	4.6	23.13
104604	9 02 01.66	29 54 49.7	17.45	0.59	–46.1	–93.8	3.5	29.93
104901	9 00 03.67	29 56 29.4	16.75	0.84	55.6	7.9	3.0	35.95

Continued on Next Page...

Table 3.31 – 207.1p00.2 (Continued)

ID	$\alpha_{J2000.0}$	$\delta_{J2000.0}$	I_0	$(V-I)_0$	$V_{\rm helio}$ (km s^{-1})	$V_{\rm gsr}$ (km s^{-1})	σ_V (km s^{-1})	R_{TD}
105585	9 02 13.73	30 24 04.8	16.94	0.81	47.2	–0.5	3.1	34.58
106925	9 02 03.84	30 24 48.9	18.37	0.67	63.9	16.2	3.5	30.00
107192	9 02 01.80	30 21 57.8	18.50	1.00	61.3	13.6	4.8	22.33
200599	9 00 49.64	30 29 02.5	19.16	0.55	–160.3	–208.0	9.1	13.88
200805	9 00 51.25	30 02 31.5	20.18	0.62	–37.4	–85.2	17.4	8.98
200816	9 00 46.98	30 31 00.4	20.24	0.03	109.2	61.5	17.7	8.89
201419	9 00 36.93	30 27 47.5	18.71	0.59	224.7	177.0	6.6	17.33
201637	9 02 44.93	30 26 37.0	19.98	0.71	210.1	162.4	41.5	4.93
201675	9 00 44.57	30 01 00.0	18.06	0.46	–169.4	–217.1	3.5	29.54
201853	9 00 43.15	30 02 40.4	19.04	0.56	4.3	–43.4	3.9	26.90
202030	9 00 24.40	30 27 31.7	17.80	0.56	163.1	115.4	4.5	23.49
202171	9 00 21.15	30 30 13.5	17.62	0.60	141.2	93.5	4.7	22.72
202220	9 00 20.19	30 28 34.7	18.56	0.61	335.2	287.5	8.7	14.39
202269	9 00 39.75	30 04 15.2	18.12	0.70	14.7	–33.0	3.3	31.98
202425	9 02 35.62	30 05 21.7	18.56	0.52	–81.3	–129.1	8.1	15.02
202698	9 02 33.34	30 00 47.4	18.49	0.59	30.6	–17.1	3.2	32.67
202810	9 00 34.94	30 03 54.3	18.82	1.04	87.4	39.7	5.2	20.88
203133	9 00 32.53	30 04 32.6	19.21	0.61	–57.1	–104.8	3.9	26.45
203648	9 00 27.45	30 05 40.1	19.50	1.02	173.2	125.4	13.0	10.93
203863	9 00 25.26	30 02 30.7	17.28	0.55	54.1	6.4	3.0	36.54
204952	9 02 14.60	30 01 33.9	18.29	0.88	–89.7	–137.4	4.7	22.52
206073	9 00 05.13	30 05 22.0	17.42	0.86	42.6	–5.1	3.1	35.14
206296	9 02 04.35	30 05 17.5	18.94	0.73	–5.4	–53.1	5.2	20.86
206379	9 00 01.97	30 02 32.1	19.61	0.74	28.3	–19.4	4.4	23.92
207071	9 01 58.56	30 03 30.8	19.06	0.71	82.6	34.9	5.4	20.28
208304	9 02 07.95	30 28 49.6	19.01	0.54	29.6	–18.1	4.7	22.43
210200	9 01 57.33	30 29 51.5	20.05	0.51	–210.9	–258.6	25.2	7.00
401967	9 01 09.14	30 10 50.9	19.49	0.72	237.9	190.2	6.9	16.92
402532	9 01 11.41	30 09 50.3	17.84	0.80	–74.7	–122.4	3.8	27.45
402630	8 59 13.76	30 08 33.1	17.90	1.05	–44.9	–92.6	52.9	4.13
403355	9 01 15.62	30 09 23.0	18.20	1.02	122.5	74.8	4.5	23.28
403686	9 01 11.67	30 33 59.2	20.64	0.87	–115.5	–163.2	50.1	4.30
403713	8 59 16.94	30 06 43.3	19.30	0.63	32.8	–14.9	7.2	16.33
404983	8 59 51.94	30 33 16.3	20.34	0.64	32.1	–15.6	25.1	7.01
405823	9 01 29.60	30 11 37.2	18.67	0.53	–125.5	–173.2	5.4	20.26
405891	9 01 29.95	30 07 44.1	18.01	0.44	100.7	53.0	8.5	14.55
406496	8 59 26.19	30 09 19.9	19.66	0.58	–115.5	–163.2	6.6	17.35
407411	9 01 37.91	30 10 41.2	19.06	0.63	19.6	–28.1	4.1	25.13
410837	9 01 53.77	30 10 44.8	17.93	0.61	–9.3	–57.0	4.0	26.24
411366	9 01 56.14	30 08 42.0	20.33	0.71	–41.4	–89.1	12.0	11.57
411468	9 01 56.70	30 09 47.9	17.69	0.61	–7.5	–55.2	3.1	34.40
412392	8 59 44.40	30 09 37.5	18.01	0.97	227.8	180.1	5.0	21.55
413640	8 59 48.14	30 10 21.8	18.23	0.69	29.4	–18.3	6.2	18.30
414866	9 01 49.97	30 35 08.3	18.24	0.51	25.2	–22.5	4.5	23.54
414954	9 01 50.22	30 33 45.3	20.24	0.76	–202.0	–249.7	8.8	14.29
415993	8 59 54.86	30 07 36.4	18.58	0.52	44.8	–2.9	3.6	28.65
500893	8 59 14.52	30 27 17.1	16.68	0.92	67.6	19.9	3.3	31.42
501774	9 01 08.34	30 26 30.9	18.31	0.75	6.7	–41.0	3.6	28.63

Continued on Next Page...

Table 3.31 – 207.1p00.2 (Continued)

ID	$\alpha_{J2000.0}$	$\delta_{J2000.0}$	I_0	$(V-I)_0$	$V_{\rm helio}$ (km s^{-1})	$V_{\rm gsr}$ (km s^{-1})	σ_V (km s^{-1})	R_{TD}
502110	9 01 14.68	30 01 07.3	19.19	0.64	40.2	–7.5	4.5	23.61
502936	8 59 34.67	30 25 54.7	19.18	0.94	100.8	53.1	10.6	12.54
503096	8 59 36.80	30 28 02.0	18.70	0.55	–19.3	–67.0	5.3	20.50
503201	8 59 26.73	30 03 58.3	17.32	0.93	–24.3	–72.0	3.7	28.38
503209	9 01 20.70	30 02 48.4	17.78	0.73	40.2	–7.5	3.2	33.52
503764	8 59 41.38	30 28 57.7	16.23	0.67	75.3	27.6	3.2	32.92
504116	9 01 18.82	30 25 43.8	19.89	0.45	101.5	53.8	19.1	8.45
504400	8 59 36.35	30 02 58.7	17.85	0.58	255.3	207.6	3.2	32.83
504417	8 59 36.48	30 03 59.5	16.70	0.94	12.2	–35.5	3.5	29.30
504502	9 01 20.57	30 30 29.9	19.37	0.52	–49.3	–97.0	5.1	21.07
505091	8 59 42.55	30 05 40.7	17.78	0.92	66.8	19.1	3.6	29.07
505183	8 59 43.77	30 01 38.9	18.35	0.56	63.4	15.7	3.2	33.13
505823	9 01 40.32	30 03 34.6	17.41	0.84	65.4	17.6	3.2	33.07
506060	8 59 53.20	30 02 04.0	19.17	0.53	–107.4	–155.1	4.5	23.40
506229	8 59 54.87	30 05 30.4	16.86	0.62	48.7	1.0	2.8	39.54
506432	8 59 57.24	30 01 46.8	19.16	0.67	58.9	11.2	4.4	23.73
506752	9 01 51.47	30 00 22.4	18.07	0.70	225.8	178.1	3.6	28.80
506922	9 01 53.15	30 03 09.0	19.24	0.61	–96.4	–144.1	4.6	22.92
507034	9 01 53.85	30 01 52.9	17.47	0.69	–110.0	–157.7	3.0	36.35
507194	9 01 55.61	30 04 44.5	17.74	0.84	187.3	139.6	4.1	25.15
507596	9 01 37.00	30 29 49.6	17.53	0.75	–60.1	–107.8	3.3	31.69
508024	9 01 40.26	30 30 40.8	17.04	0.70	–25.5	–73.2	2.9	39.38
600158	9 01 03.58	29 58 20.1	17.38	0.59	220.5	172.8	6.0	18.72
600289	8 59 09.66	30 23 23.9	16.07	0.79	–27.3	–75.1	3.0	36.62
600384	8 59 10.64	30 20 30.7	18.61	0.78	–88.3	–136.0	6.7	17.25
600610	9 01 06.70	29 57 21.6	18.74	0.77	7.2	–40.5	4.4	24.08
600677	9 01 07.31	29 59 21.1	19.17	0.67	–75.7	–123.4	8.1	15.06
600877	8 59 11.32	29 59 34.5	18.81	0.79	191.0	143.3	3.3	31.44
600963	8 59 15.63	30 23 28.9	16.74	0.70	31.9	–15.8	3.1	34.82
601262	8 59 18.56	30 20 24.5	16.77	0.55	187.9	140.2	4.5	23.34
601776	8 59 24.19	30 23 46.1	17.53	0.94	–41.4	–89.1	3.5	29.38
602181	9 01 10.19	30 23 22.0	17.31	0.48	11.6	–36.1	5.1	21.12
602994	9 01 22.33	29 55 10.9	18.53	1.01	43.2	–4.5	4.7	22.47
603199	8 59 37.99	30 21 16.2	19.19	0.50	148.7	101.0	6.7	17.26
603382	9 01 25.91	29 58 52.1	19.67	1.05	–301.8	–349.5	9.9	13.13
603883	9 01 29.93	29 55 34.1	19.33	0.47	–54.5	–102.2	20.3	8.11
604494	9 01 34.24	29 58 11.1	17.67	0.90	28.6	–19.1	3.7	28.39
604906	8 59 58.67	30 23 39.9	16.77	0.61	93.8	46.0	4.9	21.87
605458	9 01 40.66	29 54 55.1	19.92	0.91	–11.6	–59.3	8.0	15.23
605611	8 59 44.64	29 59 09.9	17.46	0.75	95.2	47.5	3.2	32.77
606032	9 01 27.09	30 21 10.6	19.55	0.84	–47.4	–95.1	7.7	15.63
606066	8 59 48.52	29 57 21.0	19.44	0.76	–12.8	–60.5	4.8	22.16
606251	8 59 50.18	29 55 23.2	17.50	0.51	–7.8	–55.5	3.1	33.81
606986	9 01 54.07	29 54 37.3	17.03	0.92	54.9	7.2	3.5	29.95
607179	9 01 56.55	29 54 54.6	17.36	0.96	52.6	4.9	3.6	28.58
607309	8 59 58.72	29 57 20.1	16.53	0.64	31.5	–16.2	3.0	35.43
607476	9 01 33.52	30 20 03.0	17.44	0.70	–29.7	–77.5	2.9	37.33
607919	9 01 34.88	30 21 14.1	19.40	0.54	184.7	137.0	27.1	6.66

Continued on Next Page...

Table 3.31 – 207.1p00.2 (Continued)

ID	$\alpha_{J2000.0}$	$\delta_{J2000.0}$	I_0	$(V-I)_0$	$V_{\rm helio}$ (km s^{-1})	$V_{\rm gsr}$ (km s^{-1})	σ_V (km s^{-1})	R_{TD}
607953	9 01 35.05	30 19 15.1	19.54	0.65	241.2	193.5	4.9	21.81
608053	9 01 35.43	30 22 46.3	17.60	0.88	85.5	37.8	3.5	30.02
608705	9 01 38.97	30 21 06.2	16.92	0.87	29.9	–17.8	2.9	37.87
611622	9 01 56.01	30 19 56.9	17.23	1.07	–18.2	–65.9	4.2	24.85
700408	8 59 12.66	30 16 12.4	18.84	0.59	–42.1	–89.8	13.4	10.73
700664	8 59 13.62	29 53 35.0	17.14	0.94	–30.4	–78.1	3.5	29.94
700716	8 59 17.99	30 17 34.7	18.32	0.54	88.1	40.3	6.1	18.35
700828	8 59 19.70	30 15 02.1	18.65	0.58	–12.8	–60.5	4.6	22.95
700837	9 01 10.19	29 51 55.6	17.11	0.88	34.5	–13.2	3.8	27.19
700936	9 01 08.61	30 14 42.3	17.51	0.56	31.7	–16.0	4.0	26.02
700973	8 59 17.81	29 53 03.1	17.15	0.77	–6.2	–54.0	3.3	32.35
701103	9 01 09.62	30 18 13.3	16.81	0.70	93.0	45.3	3.3	32.03
701447	9 01 17.57	29 49 58.4	18.54	0.98	31.3	–16.4	4.4	23.92
701560	8 59 32.73	30 18 25.7	17.05	0.49	–98.0	–145.7	3.4	31.05
701751	9 01 21.78	29 50 15.0	16.55	0.46	1.9	–45.8	7.6	15.71
701813	8 59 37.57	30 13 18.1	16.20	0.57	–78.8	–126.5	7.5	15.89
701865	9 01 23.19	29 51 11.4	17.08	0.59	31.4	–16.3	3.0	36.39
701977	8 59 41.07	30 16 41.9	17.63	0.85	3.0	–44.7	3.5	30.06
702528	9 01 32.63	29 50 00.4	18.43	0.88	42.0	–5.7	4.1	25.66
702680	9 01 34.95	29 48 00.1	17.30	0.60	10.0	–37.7	3.5	29.72
702793	9 01 23.60	30 13 59.8	18.99	0.69	–69.1	–116.8	5.6	19.61
702822	9 01 37.39	29 49 01.8	19.64	0.45	51.2	3.4	13.4	10.72
702893	9 01 38.89	29 53 06.4	17.12	0.87	–10.7	–58.4	3.3	32.00
703236	8 59 48.21	29 53 31.9	18.31	0.87	16.9	–30.8	3.5	29.50
703251	9 01 43.89	29 48 31.8	17.82	0.58	20.2	–27.5	4.4	23.91
703398	9 01 45.78	29 51 45.2	17.82	0.55	90.7	43.0	3.9	26.31
704002	8 59 57.77	29 54 00.2	16.40	0.77	–51.7	–99.4	3.5	30.12
704124	8 59 59.44	29 51 06.0	17.67	0.78	2.6	–45.1	3.3	32.41
704279	9 01 34.88	30 15 19.4	17.23	0.74	27.2	–20.5	3.6	28.75
704985	9 01 41.16	30 18 18.9	17.74	0.90	–7.0	–54.7	4.3	24.19
705660	9 01 46.96	30 15 34.8	16.84	0.70	14.3	–33.4	2.9	39.43
705827	9 01 48.25	30 16 20.0	19.17	0.69	–101.4	–149.1	4.9	21.77

Table 3.32: Spectroscopic and Photometric Data for Objects in Field 215.1p00.8

ID	$\alpha_{J2000.0}$	$\delta_{J2000.0}$	I_0	$(V-I)_0$	$V_{\rm helio}$ (km s^{-1})	$V_{\rm gsr}$ (km s^{-1})	σ_V (km s^{-1})	R_{TD}
001149	9 39 31.76	29 13 50.2	17.18	0.91	–26.4	–73.9	3.7	28.21
001351	9 37 39.93	29 38 50.0	18.84	0.57	12.8	–34.6	6.1	18.51
001457	9 39 38.34	29 39 13.5	17.60	0.48	–30.2	–77.6	3.1	34.97
001461	9 39 28.48	29 13 54.3	19.64	0.71	6.3	–41.1	12.8	11.05
002405	9 39 18.66	29 15 52.3	17.31	1.06	–111.9	–159.3	3.9	26.62
003361	9 39 08.08	29 15 40.8	17.58	0.92	–70.8	–118.2	3.6	28.88
004112	9 37 36.12	29 14 31.3	19.95	0.79	2.8	–44.6	46.0	4.58
004706	9 39 27.61	29 40 17.5	18.67	0.97	–54.7	–102.1	14.2	10.33
004980	9 39 26.74	29 41 28.5	17.77	0.50	70.3	22.9	6.6	17.33
005858	9 39 23.63	29 37 10.9	18.96	0.46	192.4	145.0	19.2	8.42
006574	9 37 28.85	29 13 27.8	17.24	0.79	7.4	–40.0	3.2	33.56
006722	9 39 20.42	29 41 47.9	19.62	0.82	–85.6	–133.0	23.1	7.43
007554	9 39 17.30	29 36 33.7	18.50	1.13	77.6	30.2	6.6	17.46
008270	9 39 14.63	29 38 02.3	19.08	0.84	78.3	30.9	7.7	15.66
008983	9 37 22.68	29 15 58.8	19.81	0.86	–71.5	–118.9	15.6	9.70
012739	9 37 11.98	29 17 14.6	20.06	0.81	96.7	49.3	21.3	7.85
014593	9 37 06.99	29 17 30.8	19.18	0.66	28.7	–18.8	9.4	13.62
017320	9 36 59.77	29 14 15.2	17.06	0.98	–58.6	–106.0	4.0	25.78
100003	9 37 50.45	29 46 54.9	18.10	0.66	–127.3	–174.7	5.6	19.57
100197	9 39 40.37	29 21 12.8	18.16	0.57	149.5	102.1	4.5	23.62
100198	9 37 46.42	29 22 35.5	19.36	0.67	14.7	–32.7	11.4	11.96
100238	9 39 39.88	29 22 02.6	19.73	0.59	204.7	157.3	17.1	9.10
100870	9 39 40.08	29 47 33.9	19.87	0.61	–126.6	–174.0	16.6	9.29
100941	9 39 29.24	29 19 59.1	17.62	0.74	209.6	162.2	3.9	26.81
101190	9 39 26.28	29 18 20.4	19.42	1.05	245.8	198.4	22.2	7.63
101388	9 37 41.97	29 21 24.5	18.84	0.78	155.5	108.1	7.3	16.24
101441	9 39 37.75	29 42 33.2	17.69	0.78	–12.1	–59.5	3.2	33.22
101599	9 39 21.40	29 18 01.4	18.59	1.15	–40.1	–87.5	8.3	14.89
102053	9 37 26.60	29 44 52.6	19.47	0.72	–107.2	–154.6	17.4	9.00
102608	9 37 19.80	29 44 31.9	18.96	0.61	55.6	8.2	5.3	20.39
102684	9 39 32.15	29 45 21.8	19.54	0.91	–6.5	–53.9	14.1	10.35
103014	9 38 59.52	29 18 24.1	17.04	0.75	–30.5	–77.9	3.1	34.04
103691	9 37 04.93	29 43 23.0	19.49	0.64	121.3	73.9	33.9	5.69
104782	9 37 28.19	29 23 22.7	17.90	0.73	58.6	11.2	3.8	27.10
107320	9 39 11.07	29 44 14.7	18.59	0.65	125.4	78.0	10.3	12.80
107622	9 39 09.80	29 46 42.5	17.98	1.19	72.7	25.3	6.5	17.63
108545	9 39 06.24	29 45 00.6	19.57	0.68	92.8	45.4	13.9	10.48
109101	9 39 03.75	29 44 12.1	18.79	0.66	21.0	–26.4	5.3	20.53
109713	9 37 06.11	29 22 23.9	19.02	0.82	96.7	49.3	10.8	12.40
200266	9 39 40.94	29 23 44.7	19.03	0.90	90.1	42.7	15.2	9.84
200766	9 39 36.18	29 26 21.4	20.44	0.70	49.8	2.4	5.1	21.01
201047	9 39 33.70	29 25 19.1	18.46	0.79	–74.2	–121.6	7.2	16.34
202567	9 39 19.66	29 27 29.3	18.43	0.56	–96.3	–143.7	5.0	21.35
202724	9 39 18.27	29 28 18.3	17.83	0.63	51.4	4.0	3.2	33.58
203323	9 37 25.09	29 49 52.9	20.05	0.56	154.1	106.7	23.9	7.26
204519	9 39 01.38	29 24 56.3	19.06	0.67	–40.5	–87.9	7.8	15.52
204587	9 37 13.50	29 53 36.1	17.55	0.67	–188.7	–236.1	12.8	11.03

Continued on Next Page...

Table 3.32 – 215.1p00.8 (Continued)

ID	$\alpha_{J2000.0}$	$\delta_{J2000.0}$	I_0	$(V-I)_0$	$V_{\rm helio}$ (km s^{-1})	$V_{\rm gsr}$ (km s^{-1})	σ_V (km s^{-1})	R_{TD}
204631	9 38 59.83	29 25 54.3	19.22	0.53	131.6	84.2	10.8	12.36
204641	9 37 32.12	29 27 05.4	19.75	0.57	–114.6	–162.0	15.6	9.70
205308	9 39 23.52	29 50 32.9	19.25	0.57	–104.8	–152.2	10.6	12.54
206057	9 37 27.60	29 26 51.0	19.15	0.96	190.5	143.1	10.6	12.54
206165	9 37 27.29	29 27 55.8	18.71	0.59	–141.0	–188.4	6.2	18.33
207007	9 39 19.00	29 50 27.4	18.26	0.56	12.4	–35.0	4.4	23.73
211103	9 37 10.81	29 25 07.5	18.11	0.82	67.3	19.9	5.5	19.97
211733	9 37 08.58	29 26 37.4	19.31	0.52	–108.5	–155.9	16.5	9.33
214138	9 39 02.51	29 53 49.1	20.58	0.47	–48.3	–95.7	23.7	7.30
214421	9 39 01.86	29 50 12.1	20.87	0.88	–24.9	–72.3	46.1	4.57
214855	9 36 58.10	29 30 11.3	20.17	0.89	97.2	49.7	41.2	4.96
218189	9 38 52.10	29 54 07.5	19.98	0.71	–52.7	–100.1	21.6	7.76
401645	9 36 01.05	29 35 22.0	19.37	0.69	–81.0	–128.5	12.3	11.38
402455	9 38 10.68	29 34 38.1	19.02	0.54	33.9	–13.5	7.1	16.48
403053	9 37 58.70	29 57 11.6	19.16	0.88	54.4	7.0	9.3	13.76
404213	9 38 23.94	29 30 29.5	17.97	0.46	175.2	127.8	4.3	24.25
404282	9 36 24.64	29 55 35.0	18.73	0.65	–80.3	–127.7	8.0	15.15
405127	9 38 31.19	29 31 06.6	17.83	0.42	239.4	192.0	6.0	18.68
405963	9 38 37.34	29 35 13.8	19.41	0.84	4.8	–42.6	7.9	15.28
406150	9 38 38.96	29 31 02.2	19.64	0.47	87.2	39.8	11.8	11.66
406346	9 36 10.64	29 33 28.1	20.39	0.61	–49.6	–97.0	23.5	7.34
407859	9 36 14.49	29 32 17.7	18.50	1.08	131.3	83.9	16.1	9.49
408549	9 36 50.33	30 00 30.2	20.42	0.73	–24.6	–72.0	45.6	4.61
412658	9 36 26.87	29 30 52.8	19.45	0.82	54.1	6.7	16.0	9.50
412836	9 36 27.34	29 34 29.2	19.42	0.53	181.6	134.2	13.8	10.52
415892	9 36 34.23	29 32 21.8	18.57	0.46	304.0	256.6	15.5	9.73
417576	9 38 19.27	29 57 55.7	18.54	0.92	166.8	119.4	15.1	9.89
420726	9 38 23.82	29 56 09.2	20.05	0.54	–124.7	–172.1	30.2	6.18
422682	9 36 51.19	29 36 09.9	20.01	0.71	–22.6	–70.0	26.0	6.85
422805	9 36 51.49	29 32 50.6	17.92	0.99	–44.8	–92.2	4.6	22.97
422908	9 36 51.73	29 31 26.8	19.69	0.56	–63.0	–110.4	20.4	8.07
432326	9 38 40.41	29 57 57.7	18.04	0.59	74.7	27.3	3.5	30.19
433409	9 38 42.20	29 59 40.7	18.44	0.99	280.7	233.3	8.4	14.71
436542	9 38 47.06	29 57 38.6	20.05	0.58	–27.0	–74.4	20.3	8.11
501166	9 38 04.64	29 28 10.3	18.75	0.68	94.3	46.9	5.8	19.26
502458	9 38 18.59	29 27 32.9	18.84	0.73	203.6	156.1	5.2	20.83
503690	9 36 10.71	29 26 09.9	18.62	0.88	–106.5	–153.9	7.6	15.73
504610	9 36 38.94	29 52 01.6	18.46	0.57	–16.0	–63.4	7.8	15.54
504988	9 36 14.83	29 29 37.2	17.52	0.76	–24.9	–72.3	3.0	37.02
508708	9 38 22.89	29 50 35.3	19.73	0.89	–16.6	–64.0	25.8	6.89
510890	9 38 32.58	29 49 36.3	17.79	0.67	85.8	38.4	4.6	22.95
511308	9 38 34.59	29 53 25.9	19.70	0.72	35.1	–12.3	8.1	15.08
514086	9 38 45.65	29 48 53.8	16.85	0.87	14.4	–33.0	3.8	27.28
514966	9 36 50.09	29 24 46.6	18.63	0.60	–13.7	–61.1	3.6	28.93
600143	9 37 55.88	29 20 57.4	17.97	0.59	117.2	69.7	5.8	19.13
600341	9 37 58.09	29 21 26.5	18.97	0.71	59.0	11.6	8.8	14.23
600632	9 38 01.36	29 19 29.8	18.81	0.85	87.6	40.2	5.5	19.81
600672	9 36 06.57	29 43 42.2	18.35	0.60	291.5	244.1	5.8	19.11

Continued on Next Page...

Table 3.32 – 215.1p00.8 (Continued)

ID	$\alpha_{J2000.0}$	$\delta_{J2000.0}$	I_0	$(V-I)_0$	$V_{\rm helio}$ (km s^{-1})	$V_{\rm gsr}$ (km s^{-1})	σ_V (km s^{-1})	R_{TD}
600673	9 37 56.84	29 43 53.5	18.57	0.54	57.0	9.6	3.5	29.75
600808	9 38 03.16	29 20 22.7	18.61	0.75	63.2	15.8	5.0	21.43
601115	9 38 06.25	29 23 20.2	16.56	0.76	8.5	–38.9	3.4	31.04
601616	9 36 14.57	29 45 47.8	17.27	0.64	93.7	46.3	3.8	27.17
601702	9 36 03.34	29 23 43.4	19.20	0.62	–97.9	–145.3	14.0	10.40
601719	9 36 03.44	29 22 09.0	19.14	0.71	220.2	172.8	9.4	13.65
602433	9 36 22.62	29 43 21.7	18.91	0.58	–26.2	–73.6	12.7	11.14
602826	9 36 06.99	29 18 28.5	19.49	0.56	21.3	–26.1	41.4	4.94
603009	9 38 04.29	29 47 53.3	19.57	0.64	–118.4	–165.8	19.9	8.23
603071	9 38 26.38	29 23 14.1	19.06	0.45	–67.6	–115.0	11.9	11.59
603170	9 36 29.67	29 46 34.8	19.56	0.47	102.1	54.7	28.4	6.44
603172	9 38 27.81	29 19 40.7	18.87	0.78	174.6	127.2	6.9	16.80
603207	9 38 04.95	29 43 31.2	18.54	1.01	11.9	–35.5	6.3	18.11
604592	9 38 09.06	29 48 08.5	19.25	0.90	127.4	80.0	10.8	12.39
607370	9 36 20.85	29 19 31.6	17.72	0.58	–32.8	–80.2	5.3	20.45
607421	9 38 18.87	29 43 00.9	18.02	0.66	–157.1	–204.5	4.0	25.69
609289	9 36 26.79	29 18 36.7	20.02	0.59	–93.1	–140.5	18.4	8.65
609903	9 36 28.83	29 23 37.4	19.80	0.61	–10.0	–57.4	15.6	9.69
611629	9 36 34.91	29 21 22.4	18.68	0.57	18.1	–29.3	11.9	11.60
614155	9 38 44.94	29 43 13.6	17.67	0.54	35.8	–11.6	5.6	19.70
616042	9 36 50.86	29 19 32.3	18.01	0.98	–31.6	–79.0	6.7	17.18
700189	9 37 57.09	29 12 01.2	19.10	0.56	–79.1	–126.5	8.4	14.72
700812	9 36 12.68	29 39 23.8	18.71	0.52	–103.4	–150.8	8.9	14.17
701304	9 38 13.99	29 15 43.1	16.74	0.65	–9.2	–56.6	3.3	32.32
701859	9 38 24.21	29 12 20.7	18.24	0.55	21.6	–25.8	4.5	23.21
702062	9 36 29.47	29 39 24.2	18.69	0.65	2.4	–45.0	7.8	15.51
702069	9 38 28.58	29 11 38.8	16.55	0.96	39.3	–8.1	3.7	27.91
702207	9 36 31.74	29 38 49.4	17.37	0.77	–2.8	–50.2	3.3	31.78
702256	9 38 32.71	29 12 12.2	17.69	0.75	30.5	–16.9	3.4	30.71
702306	9 36 33.34	29 41 21.5	18.61	0.59	18.3	–29.1	9.8	13.23
702421	9 38 10.06	29 40 58.4	18.87	0.61	48.6	1.1	3.6	28.77
702539	9 36 36.90	29 38 21.5	18.31	0.76	–29.1	–76.5	4.7	22.52
703251	9 36 48.54	29 39 08.1	18.62	0.74	142.5	95.1	6.7	17.29
703352	9 38 16.40	29 38 17.8	19.44	0.78	58.4	11.0	21.7	7.74
704258	9 38 22.78	29 41 53.6	19.59	0.76	46.3	–1.1	17.6	8.91
704825	9 38 26.92	29 39 03.1	19.62	0.53	230.7	183.3	26.4	6.77
705060	9 38 28.47	29 38 32.3	16.87	0.62	33.3	–14.2	3.0	35.54
705929	9 36 33.06	29 13 39.5	16.59	1.14	42.2	–5.2	4.5	23.53
706282	9 38 38.10	29 40 28.1	18.83	0.58	67.6	20.2	6.1	18.44
706538	9 38 39.89	29 36 55.5	18.50	0.71	–75.6	–123.0	7.0	16.69
706888	9 38 42.48	29 38 16.6	19.88	0.65	–112.2	–159.6	20.7	8.00
707314	9 36 40.97	29 15 10.5	18.08	0.82	–55.2	–102.6	4.0	25.73

Table 3.33: Spectroscopic and Photometric Data for Objects in Field 222.2n09.1

ID	$\alpha_{J2000.0}$	$\delta_{J2000.0}$	I_0	$(V-I)_0$	$V_{\rm helio}$ (km s^{-1})	$V_{\rm gsr}$ (km s^{-1})	σ_V (km s^{-1})	R_{TD}
202269	10 00 09.34	18 27 02.8	19.32	0.64	133.4	48.0	14.6	11.53
202281	10 00 08.94	18 29 06.8	19.73	0.80	72.0	–13.3	21.1	7.62
202312	10 00 08.50	18 28 13.4	20.10	0.55	180.3	94.9	25.9	6.42
202490	10 00 05.92	18 24 32.7	20.50	0.94	94.7	9.3	87.8	2.63
202537	10 00 04.47	18 28 04.4	19.05	0.58	87.1	1.7	12.2	18.45
400321	9 59 13.61	18 30 15.3	19.19	0.81	9.2	–76.1	43.6	4.38
400454	9 59 14.67	18 32 04.5	17.74	1.14	14.9	–70.5	12.7	15.60
400582	9 59 15.87	18 30 57.6	19.26	0.68	15.3	–70.1	14.9	11.11
400612	9 59 16.04	18 30 33.3	19.22	0.78	55.5	–29.8	19.7	8.09
401259	9 59 25.90	18 31 23.6	18.63	0.65	59.9	–25.5	13.0	14.72
401779	9 59 34.32	18 34 49.9	19.45	0.30	42.0	–43.4	49.3	4.01
402157	9 59 38.99	18 31 05.0	20.58	0.87	60.2	–25.2	33.4	5.31
402199	9 59 39.87	18 32 03.4	20.68	0.59	240.9	155.5	76.4	2.92
402348	9 59 42.54	18 30 37.0	18.81	0.83	190.8	105.5	12.1	19.50
402978	9 59 48.80	18 31 51.6	17.50	0.60	233.8	148.5	16.5	9.73
500742	9 59 24.89	18 27 18.0	18.70	0.85	224.8	139.4	17.8	8.95
500915	9 59 27.50	18 26 38.5	17.97	0.57	284.3	198.9	13.2	13.99
501033	9 59 30.08	18 28 33.6	16.99	0.80	133.1	47.8	12.1	19.99
501317	9 59 37.84	18 26 54.7	18.21	0.80	135.8	50.4	16.0	10.12
501673	9 59 48.99	18 24 51.5	19.59	0.11	42.8	–42.6	36.8	4.95

Table 3.34: Spectroscopic and Photometric Data for Objects in Field 235.1p01.8

ID	$\alpha_{J2000.0}$	$\delta_{J2000.0}$	I_0	$(V-I)_0$	$V_{\rm helio}$ (km s^{-1})	$V_{\rm gsr}$ (km s^{-1})	σ_V (km s^{-1})	R_{TD}
000059	11 06 15.01	24 46 31.0	19.31	0.67	233.1	188.9	5.4	20.08
000148	11 06 11.76	24 45 17.6	18.33	0.59	218.3	174.0	7.2	16.41
000250	11 06 06.96	24 45 57.6	17.34	0.62	–54.6	–98.9	3.4	30.58
000604	11 05 53.59	24 45 44.2	16.70	0.67	–47.2	–91.5	3.4	30.92
001016	11 05 46.01	24 47 57.9	19.15	0.85	–69.1	–113.3	5.8	19.17
002483	11 06 06.16	25 13 16.0	18.21	0.71	23.8	–20.4	5.9	18.85
003667	11 07 57.78	25 12 19.8	18.41	0.41	–120.3	–164.6	17.0	9.15
004673	11 05 49.69	25 12 04.7	16.84	0.64	144.4	100.1	5.2	20.69
004709	11 05 49.46	25 11 24.5	19.36	0.75	–118.5	–162.7	10.7	12.46
004768	11 07 53.24	25 13 33.7	20.25	1.16	140.6	96.3	33.9	5.69
004845	11 07 52.96	25 15 34.2	18.98	0.61	329.1	284.8	6.4	17.72
007994	11 07 39.11	25 14 41.1	19.52	0.57	338.9	294.7	16.0	9.52
009120	11 05 33.47	25 15 00.6	18.37	0.83	133.4	89.1	4.5	23.41
009726	11 05 29.82	25 11 39.1	18.79	0.62	269.7	225.4	17.4	9.01
011331	11 07 26.21	25 10 28.7	17.88	0.86	55.5	11.2	3.7	28.09
012238	11 07 23.06	25 14 25.4	18.25	0.94	241.2	196.9	3.8	27.60
100187	11 06 05.61	24 51 09.9	17.51	0.96	44.5	0.3	4.4	23.63
100316	11 06 18.23	25 17 06.0	19.08	1.05	–75.5	–119.8	6.3	18.04
100498	11 06 16.57	25 20 24.7	18.80	1.19	–8.1	–52.3	7.5	15.94
100512	11 05 57.26	24 53 42.7	16.44	0.78	50.6	6.3	3.4	31.20
100557	11 06 16.07	25 18 10.7	18.43	0.73	–94.5	–138.7	5.3	20.46
100663	11 05 46.93	24 52 03.9	17.89	0.72	22.4	–21.9	3.9	26.74
100675	11 08 08.44	25 20 29.2	18.50	0.82	–114.1	–158.4	38.3	5.22
100752	11 05 41.38	24 55 23.0	17.00	0.64	37.3	–7.0	3.6	28.51
101024	11 06 10.81	25 21 38.1	17.59	0.73	67.1	22.8	3.3	31.52
101080	11 08 06.40	25 16 26.4	18.35	0.70	152.1	107.9	4.8	22.33
101113	11 06 09.90	25 18 41.6	18.65	0.81	134.9	90.6	5.5	19.81
101119	11 06 09.83	25 16 24.6	17.97	0.70	–39.4	–83.6	11.6	11.80
101308	11 08 05.13	25 19 48.4	17.98	0.57	–90.8	–135.0	6.2	18.27
101472	11 06 04.59	25 21 26.5	17.12	0.71	96.5	52.3	4.1	25.67
101790	11 08 01.91	25 17 45.7	18.51	1.01	–8.8	–53.1	4.3	24.49
102620	11 05 49.03	25 17 09.3	18.55	0.84	–45.5	–89.7	6.9	16.80
102714	11 05 47.61	25 21 46.3	16.77	0.71	59.4	15.2	4.1	25.63
103207	11 07 53.40	25 20 26.4	19.65	0.59	–50.1	–94.4	10.6	12.52
103805	11 07 49.79	25 20 59.8	19.02	0.61	100.0	55.8	7.6	15.79
105709	11 07 36.08	25 16 41.9	19.43	0.74	162.9	118.7	5.7	19.43
107196	11 07 24.00	25 19 31.7	19.72	0.55	–103.2	–147.4	13.9	10.44
200083	11 06 20.11	25 24 38.6	19.20	0.69	–102.0	–146.3	5.0	21.55
200214	11 06 07.64	25 01 12.8	20.31	0.66	235.8	191.6	21.4	7.81
200376	11 06 00.82	24 58 42.6	19.91	0.67	–93.5	–137.7	13.3	10.77
200556	11 08 09.07	25 25 28.2	18.98	0.68	271.5	227.2	8.0	15.25
200745	11 05 40.97	25 01 38.8	19.49	0.65	11.8	–32.4	10.4	12.73
201292	11 06 11.07	25 22 39.6	19.68	0.64	–34.4	–78.6	17.4	8.98
202024	11 08 02.64	25 22 50.2	20.61	0.49	66.5	22.3	44.8	4.67
203703	11 05 52.55	25 27 22.3	17.09	0.71	–43.8	–88.0	4.7	22.68
204149	11 05 49.17	25 22 03.5	17.38	0.90	0.3	–44.0	4.8	22.06
204826	11 07 47.74	25 24 38.7	18.48	0.62	–61.8	–106.1	6.9	16.95

Continued on Next Page...

Table 3.34 – 235.1p01.8 (Continued)

ID	$\alpha_{J2000.0}$	$\delta_{J2000.0}$	I_0	$(V-I)_0$	$V_{\rm helio}$ (km s^{-1})	$V_{\rm gsr}$ (km s^{-1})	σ_V (km s^{-1})	R_{TD}
205208	11 05 41.20	25 26 02.0	18.27	0.41	288.5	244.2	27.7	6.55
205248	11 07 45.12	25 26 29.2	20.69	0.53	83.8	39.6	32.8	5.83
205452	11 05 39.52	25 23 32.7	19.92	0.93	125.4	81.2	11.4	11.94
208681	11 05 32.09	25 22 00.8	17.87	0.70	113.6	69.3	5.2	20.76
402528	11 05 22.15	25 07 55.6	19.52	0.70	–31.2	–75.4	14.2	10.31
403993	11 06 38.15	25 32 28.5	20.00	0.53	280.9	236.7	24.7	7.09
406053	11 05 05.13	25 30 30.2	18.15	0.57	198.7	154.5	14.8	10.05
408362	11 05 17.36	25 28 46.3	17.12	0.68	36.8	–7.4	4.3	24.18
408801	11 05 19.74	25 33 45.8	19.10	0.78	212.5	168.2	9.0	13.98
409044	11 06 54.11	25 31 01.6	19.38	1.08	–20.5	–64.8	34.5	5.62
410705	11 06 59.32	25 30 48.7	19.47	1.03	–8.4	–52.6	4.9	21.77
414568	11 07 03.81	25 30 07.0	20.79	0.94	–26.3	–70.5	24.8	7.08
421682	11 07 18.03	25 32 34.3	20.33	0.59	58.9	14.7	21.2	7.86
500075	11 04 36.83	25 02 18.7	18.26	0.61	76.2	31.9	6.3	18.02
500187	11 04 41.30	25 02 04.5	19.35	0.54	182.9	138.7	11.8	11.69
500235	11 04 38.11	25 22 00.1	18.62	0.56	27.5	–16.7	32.0	5.93
500265	11 04 38.30	25 26 00.9	18.63	0.66	192.1	147.9	6.5	17.54
500479	11 04 52.99	24 59 22.9	16.87	0.78	48.0	3.7	4.8	22.16
500507	11 04 54.57	24 57 21.2	16.38	0.57	91.9	47.7	3.8	27.49
500618	11 05 00.06	25 00 47.1	16.70	0.51	183.2	138.9	11.6	11.80
500673	11 05 03.68	25 01 52.0	17.49	0.53	–98.6	–142.9	12.0	11.54
500714	11 04 41.80	25 23 25.2	18.49	0.59	0.1	–44.2	20.7	8.01
500981	11 05 15.56	25 00 36.5	17.26	0.84	55.5	11.3	5.0	21.32
501136	11 05 21.98	24 58 47.3	18.04	0.78	–41.0	–85.2	3.4	30.26
502231	11 04 53.80	25 27 29.0	16.76	0.65	21.2	–23.0	3.9	26.86
504200	11 05 14.58	25 25 14.8	18.46	0.69	–43.4	–87.6	8.4	14.65
504238	11 05 15.11	25 26 10.4	16.37	0.67	41.3	–2.9	4.4	24.06
504512	11 05 19.29	25 22 05.6	17.75	0.72	–43.4	–87.7	4.4	24.09
504913	11 05 24.42	25 24 59.0	16.45	0.75	94.9	50.7	3.7	27.75
505701	11 06 54.43	25 23 56.9	19.29	0.83	316.6	272.3	10.7	12.48
508577	11 07 15.51	25 23 47.8	17.34	0.71	–52.6	–96.8	4.4	24.00
600321	11 04 46.43	24 56 38.2	16.28	0.60	–18.6	–62.8	3.5	29.83
600399	11 04 48.80	24 54 58.6	17.57	0.83	–3.8	–48.1	5.2	20.73
600752	11 04 42.13	25 16 01.4	16.90	0.59	–17.2	–61.4	4.8	22.15
600786	11 05 10.24	24 54 01.8	17.15	0.87	–9.3	–53.5	4.4	23.89
600883	11 05 15.15	24 52 27.6	19.30	0.56	113.5	69.3	12.8	11.05
600927	11 05 17.57	24 52 10.0	16.89	0.80	–65.4	–109.7	5.0	21.51
600994	11 04 43.87	25 16 36.2	18.40	0.70	62.4	18.2	4.9	21.76
601533	11 06 32.93	25 20 49.0	19.64	0.56	–96.9	–141.2	13.3	10.80
602104	11 04 52.80	25 21 36.2	16.41	0.81	66.6	22.4	3.8	27.20
602116	11 06 35.42	25 17 59.7	18.94	0.59	–152.7	–196.9	9.5	13.51
603313	11 06 40.81	25 21 05.4	17.15	0.81	109.0	64.7	4.0	25.73
603399	11 06 41.25	25 18 42.0	19.07	0.55	165.1	120.8	6.8	17.08
604629	11 06 47.28	25 19 59.2	19.45	0.91	21.1	–23.2	15.9	9.55
606868	11 06 58.72	25 21 13.7	20.01	0.95	159.5	115.3	16.9	9.18
609023	11 07 10.72	25 19 41.2	17.90	0.59	2.1	–42.2	4.2	25.06
609120	11 07 11.43	25 20 45.1	18.45	0.55	276.6	232.4	8.2	14.91
700058	11 06 27.34	25 10 52.0	18.64	0.80	–51.3	–95.5	4.3	24.16

Continued on Next Page...

Table 3.34 – 235.1p01.8 (Continued)

ID	$\alpha_{J2000.0}$	$\delta_{J2000.0}$	I_0	$(V-I)_0$	$V_{\rm helio}$ (km s^{-1})	$V_{\rm gsr}$ (km s^{-1})	σ_V (km s^{-1})	R_{TD}
700391	11 04 41.58	25 13 13.3	16.69	0.78	–40.4	–84.7	4.2	25.08
700655	11 06 31.66	25 15 30.1	19.96	1.03	–69.9	–114.2	12.9	10.98
700668	11 06 31.70	25 14 02.2	19.86	0.66	–50.2	–94.4	19.7	8.27
700906	11 06 33.63	25 11 25.3	18.90	0.46	198.0	153.8	6.0	18.63
701193	11 06 36.07	25 14 20.8	16.70	0.60	–23.8	–68.0	4.5	23.59
701287	11 05 22.52	24 49 52.8	17.44	0.61	34.5	–9.8	4.4	23.97
701289	11 05 22.55	24 47 49.1	18.12	0.73	79.7	35.4	3.9	26.43
701717	11 06 40.72	25 11 57.9	17.50	0.66	–173.5	–217.7	5.9	18.85
702142	11 06 44.42	25 13 58.1	18.91	0.86	94.4	50.1	5.1	21.17
702350	11 05 03.82	25 12 48.9	16.34	0.50	44.7	0.5	3.8	27.30
703068	11 05 11.77	25 14 16.4	17.73	0.51	40.5	–3.7	12.7	11.13
704055	11 05 17.69	25 10 17.1	16.46	0.87	–25.2	–69.5	4.0	26.25
704170	11 05 19.50	25 13 30.0	17.45	0.53	–119.5	–163.7	20.0	8.18
704302	11 05 20.67	25 11 08.8	18.89	0.85	120.3	76.1	22.9	7.47
704931	11 07 06.69	25 15 02.0	18.83	0.56	17.3	–27.0	7.1	16.56

Table 3.35: Spectroscopic and Photometric Data for Objects in Field 245.0p01.3

ID	$\alpha_{J2000.0}$	$\delta_{J2000.0}$	I_0	$(V-I)_0$	$V_{\rm helio}$ (km s^{-1})	$V_{\rm gsr}$ (km s^{-1})	σ_V (km s^{-1})	R_{TD}
000405	11 45 17.39	21 00 55.2	21.49	0.82	–7.2	–51.1	72.3	3.04
000429	11 45 43.15	21 01 08.4	20.49	0.82	59.4	15.5	13.3	13.75
000481	11 45 13.30	21 01 40.4	19.89	0.87	27.7	–16.2	68.3	3.17
000520	11 45 28.24	21 02 03.7	21.26	0.52	63.1	19.2	70.4	3.10
000556	11 45 04.22	21 02 26.3	20.17	0.66	184.0	140.1	34.2	5.22
000623	11 45 35.00	21 03 32.4	21.52	0.68	–45.8	–89.7	68.3	3.17
000628	11 45 49.24	21 03 35.2	20.20	0.73	–0.8	–44.7	24.2	6.78
000633	11 45 10.34	21 03 41.4	20.81	0.63	–34.9	–78.8	22.3	7.25
000650	11 44 55.32	21 03 56.0	20.64	0.70	173.5	129.6	69.2	3.14
000688	11 45 03.32	21 04 18.9	21.86	0.76	–21.9	–65.9	78.2	2.87
000692	11 45 12.76	21 04 21.2	21.19	0.63	–262.6	–306.5	41.0	4.58
000706	11 45 22.67	21 04 36.5	19.87	0.77	32.5	–11.4	12.9	14.83
000713	11 45 25.37	21 04 40.3	19.80	0.77	–46.6	–90.6	13.9	12.45
000783	11 44 59.34	21 05 34.0	21.27	0.59	–18.2	–62.1	38.4	4.80
000786	11 45 48.17	21 05 38.6	21.50	0.68	–79.6	–123.5	88.7	2.61
000793	11 45 26.03	21 05 44.6	20.28	0.61	35.3	–8.6	16.5	9.72
000809	11 45 34.04	21 05 59.4	20.84	0.50	26.9	–17.0	30.7	5.65
000821	11 45 44.01	21 06 06.6	20.98	0.40	–27.9	–71.8	37.0	4.93
000825	11 45 11.24	21 06 07.6	21.70	0.56	–68.3	–112.2	65.8	3.26
000898	11 45 05.21	21 07 11.4	19.36	0.67	297.6	253.7	12.8	15.48
000918	11 45 15.34	21 07 27.5	21.66	0.97	–22.3	–66.2	86.9	2.65
000952	11 45 24.79	21 07 51.0	21.63	0.93	267.7	223.8	82.8	2.75
000961	11 45 12.18	21 07 56.6	19.85	0.62	–54.5	–98.4	14.1	12.21
000973	11 45 29.62	21 08 03.2	21.65	0.69	–59.6	–103.5	45.3	4.26
000980	11 45 56.20	21 08 07.1	19.43	0.64	1.9	–42.0	37.4	4.89
001092	11 45 34.56	21 09 17.3	20.09	0.91	–13.7	–57.6	13.8	12.62
001093	11 45 53.49	21 09 18.1	21.20	0.83	–87.7	–131.6	60.6	3.46
001106	11 45 00.29	21 09 27.4	20.78	0.54	27.0	–16.9	69.2	3.14
001119	11 45 19.77	21 09 35.5	20.60	0.80	233.0	189.1	24.8	6.64
001132	11 45 44.57	21 09 51.1	19.88	0.81	–37.4	–81.3	13.4	13.49

Table 3.36: Spectroscopic and Photometric Data for Objects in Field 246.8n05.9

ID	$\alpha_{J2000.0}$	$\delta_{J2000.0}$	I_0	$(V-I)_0$	$V_{\rm helio}$ (km s^{-1})	$V_{\rm gsr}$ (km s^{-1})	σ_V (km s^{-1})	R_{TD}
100692	11 40 40.51	13 43 59.2	20.18	0.77	43.6	–27.2	54.4	3.74
100724	11 40 40.15	13 43 00.7	17.50	1.02	145.5	74.7	13.0	14.54
100969	11 40 36.98	13 43 06.4	17.53	1.13	–41.8	–112.6	13.3	13.69
101473	11 40 30.71	13 43 49.5	20.02	0.77	–19.0	–89.7	77.8	2.88
103368	11 40 07.92	13 42 52.9	19.02	0.43	–63.9	–134.7	25.7	6.47
200492	11 40 45.02	13 46 21.7	19.99	0.80	99.4	28.6	75.0	2.96
200551	11 40 44.50	13 48 29.0	17.94	0.68	26.8	–44.0	18.1	8.78
200757	11 40 42.43	13 44 58.6	17.95	1.12	–115.6	–186.4	15.2	10.85
201217	11 40 37.99	13 46 55.5	20.66	0.84	79.9	9.1	75.0	2.96
201313	11 40 37.32	13 48 34.6	20.23	1.15	–115.9	–186.6	15.0	11.01
203988	11 40 10.84	13 48 01.3	18.76	0.42	25.9	–44.8	46.7	4.17
204343	11 40 06.96	13 45 28.6	18.38	1.07	–2.2	–72.9	24.7	6.66
204842	11 40 01.57	13 46 28.7	18.82	0.28	–23.0	–93.7	13.6	13.15

Table 3.37: Spectroscopic and Photometric Data for Objects in Field 250.1p01.2

ID	$\alpha_{J2000.0}$	$\delta_{J2000.0}$	I_0	$(V-I)_0$	$V_{\rm helio}$ (km s^{-1})	$V_{\rm gsr}$ (km s^{-1})	σ_V (km s^{-1})	R_{TD}
000087	12 05 05.91	18 46 23.9	20.04	0.71	53.6	10.9	20.2	7.90
000285	12 05 03.92	18 49 27.2	20.49	0.64	–11.7	–54.4	20.3	7.86
000337	12 04 57.70	18 50 21.2	21.68	0.67	4.2	–38.6	54.6	3.73
000385	12 05 01.90	18 51 02.6	20.64	0.76	60.9	18.1	26.2	6.37
000400	12 05 00.45	18 51 21.0	21.59	0.57	21.1	–21.6	50.7	3.93
000408	12 04 40.23	18 51 37.9	20.34	0.76	309.0	266.3	21.1	7.61
000602	12 04 34.76	18 54 09.1	21.18	0.64	301.2	258.5	60.3	3.47
000605	12 05 00.12	18 54 11.5	19.32	1.02	256.4	213.6	26.3	6.35
000648	12 04 58.80	18 54 43.7	20.26	0.67	52.6	9.9	48.0	4.09
000654	12 04 33.26	18 54 47.6	20.53	0.94	519.1	476.3	54.2	3.75
000690	12 04 31.83	18 55 17.1	19.92	0.61	–108.9	–151.6	35.3	5.10
000729	12 04 33.83	18 55 55.2	20.47	0.71	281.1	238.4	30.3	5.70
000742	12 04 30.80	18 56 11.6	19.68	0.63	–58.5	–101.2	19.2	8.28
000876	12 04 47.43	18 58 24.8	21.84	0.57	61.4	18.7	37.8	4.85
000936	12 04 57.44	18 59 25.9	19.62	0.73	92.9	50.2	13.0	14.53
000947	12 04 26.41	18 59 33.2	20.13	0.95	114.3	71.6	60.3	3.47

Table 3.38: Spectroscopic and Photometric Data for Objects in Field 255.0n00.9

ID	$\alpha_{J2000.0}$	$\delta_{J2000.0}$	I_0	$(V-I)_0$	$V_{\rm helio}$ (km s^{-1})	$V_{\rm gsr}$ (km s^{-1})	σ_V (km s^{-1})	R_{TD}
000381	12 19 23.36	14 47 12.4	21.62	0.85	500.7	451.8	71.7	3.06
000386	12 19 13.33	14 47 15.0	21.57	0.77	–17.2	–66.0	59.6	3.50
000398	12 19 27.38	14 47 25.4	19.76	0.63	–52.0	–100.9	16.3	9.88
000420	12 19 40.95	14 47 41.8	20.21	0.71	–10.9	–59.7	21.8	7.38
000451	12 19 35.16	14 48 11.3	20.20	0.62	–37.4	–86.3	20.1	7.96
000455	12 19 36.59	14 48 13.2	21.41	0.57	–62.1	–111.0	80.8	2.80
000459	12 19 20.59	14 48 18.0	21.22	0.92	223.1	174.3	44.9	4.29
000475	12 19 54.15	14 48 39.6	20.79	0.86	209.4	160.5	56.9	3.62
000478	12 19 16.68	14 48 41.1	19.37	0.54	–23.6	–72.5	20.6	7.77
000484	12 19 38.35	14 48 47.6	19.86	0.62	131.5	82.7	30.1	5.73
000560	12 19 18.07	14 49 57.6	20.84	0.97	–6.9	–55.7	53.2	3.80
000585	12 19 04.79	14 50 15.0	20.65	0.76	–35.1	–83.9	33.4	5.31
000651	12 19 10.86	14 50 57.2	21.72	0.63	27.5	–21.3	82.4	2.76
000655	12 19 13.76	14 51 00.7	19.84	0.63	–131.1	–179.9	27.6	6.11
000742	12 19 18.67	14 52 02.3	21.62	0.94	–44.1	–93.0	70.7	3.09
000745	12 19 33.28	14 52 04.2	20.63	0.84	63.6	14.8	33.2	5.33
000752	12 19 48.41	14 52 12.4	19.39	0.65	118.3	69.5	15.6	10.39
000773	12 19 08.22	14 52 27.3	21.06	0.84	–425.9	–474.7	68.3	3.17
000779	12 19 59.34	14 52 32.8	20.88	0.90	20.8	–28.0	81.6	2.78
000787	12 19 39.64	14 52 36.5	20.10	0.89	1421.1	1372.3	36.3	5.00
000874	12 19 10.22	14 53 28.8	21.26	0.96	2468.9	2420.1	55.6	3.68
000885	12 20 00.60	14 53 36.0	20.81	0.71	58.6	9.7	38.3	4.81
000892	12 19 43.11	14 53 40.9	21.05	0.74	–18.8	–67.7	58.2	3.56
000893	12 19 26.68	14 53 40.6	21.26	0.60	170.5	121.7	46.5	4.18
000913	12 19 39.10	14 53 56.3	21.18	0.57	–56.5	–105.3	27.6	6.12
000916	12 19 32.82	14 53 57.2	19.45	0.94	–56.5	–105.4	13.6	12.97
000927	12 19 53.67	14 54 10.9	20.94	0.89	2.0	–46.9	27.0	6.22
000930	12 19 45.72	14 54 13.2	21.08	0.92	1523.2	1474.3	53.4	3.79
000938	12 19 30.60	14 54 22.0	21.21	0.81	33.2	–15.7	42.8	4.44
000941	12 19 46.76	14 54 22.7	19.84	0.56	645.1	596.2	70.7	3.09
000968	12 19 42.50	14 54 43.5	20.17	0.89	1356.3	1307.5	50.6	3.94
001007	12 19 37.67	14 55 17.6	20.85	0.63	0.4	–48.5	39.5	4.70
001052	12 19 21.51	14 55 55.4	19.43	0.66	111.2	62.3	18.6	8.54
001057	12 19 55.68	14 55 58.2	20.67	0.93	1507.7	1458.8	57.6	3.59
001077	12 19 29.23	14 56 07.9	19.24	0.83	145.9	97.0	14.0	12.35
001082	12 19 59.89	14 56 10.1	19.99	0.60	23.2	–25.7	22.7	7.15
001083	12 19 01.65	14 56 08.8	20.30	0.69	47.1	–1.8	64.1	3.32

Table 3.39: Spectroscopic and Photometric Data for Objects in Field 255.1p03.1

ID	$\alpha_{J2000.0}$	$\delta_{J2000.0}$	I_0	$(V-I)_0$	$V_{\rm helio}$ (km s^{-1})	$V_{\rm gsr}$ (km s^{-1})	σ_V (km s^{-1})	R_{TD}
000050	12 27 10.59	18 15 11.5	21.51	0.93	175.6	142.1	84.8	2.70
000105	12 27 45.93	18 16 19.8	20.07	0.80	–71.3	–104.7	36.7	4.96
000160	12 27 44.91	18 17 13.4	21.06	1.02	–10.1	–43.6	83.6	2.73
000228	12 27 31.15	18 18 19.5	20.31	0.91	–54.2	–87.7	62.1	3.40
000327	12 27 26.76	18 19 54.1	19.33	0.64	22.8	–10.6	26.7	6.28
000360	12 27 40.63	18 20 21.1	20.21	0.60	–3.3	–36.7	74.6	2.97
000387	12 27 21.71	18 20 35.6	20.31	0.67	–21.9	–55.4	60.1	3.48
000479	12 27 31.49	18 21 43.6	20.53	0.46	72.7	39.3	42.8	4.44
000768	12 27 26.86	18 25 31.4	21.51	0.82	–373.9	–407.4	84.0	2.72

Table 3.40: Spectroscopic and Photometric Data for Objects in Field 256.7n04.1

ID	$\alpha_{J2000.0}$	$\delta_{J2000.0}$	I_0	$(V-I)_0$	$V_{\rm helio}$ (km s^{-1})	$V_{\rm gsr}$ (km s^{-1})	σ_V (km s^{-1})	R_{TD}
102893	12 20 05.70	11 08 44.9	17.31	0.60	272.7	212.3	17.7	9.01
203252	12 20 06.64	11 11 55.6	19.24	0.82	104.2	43.8	14.2	12.04
203293	12 20 05.84	11 13 25.6	20.14	0.58	266.1	205.7	17.5	9.12
402280	12 19 38.99	11 17 24.3	20.79	0.58	8.1	–52.3	29.1	5.88
402455	12 19 40.65	11 20 05.8	18.84	0.72	–85.0	–145.4	13.9	12.45
402460	12 19 40.68	11 19 04.1	19.31	0.42	–16.4	–76.7	15.1	10.94
403328	12 19 48.64	11 18 17.2	20.32	1.02	2.7	–57.7	40.6	4.61
403463	12 19 49.67	11 18 32.5	19.94	0.44	187.4	127.0	23.3	6.99
404407	12 19 58.08	11 16 21.9	20.48	0.78	2.0	–58.4	28.8	5.92
404608	12 20 00.07	11 18 26.3	17.75	0.33	140.7	80.4	12.9	14.80
404719	12 20 01.29	11 17 08.9	19.70	1.00	–21.2	–81.6	17.6	9.02
500915	12 19 31.02	11 14 05.7	19.52	0.54	230.3	169.9	22.5	7.20
501029	12 19 33.11	11 13 48.4	19.82	0.48	172.1	111.7	17.5	9.12
501074	12 19 33.90	11 09 12.3	17.33	0.86	176.2	115.9	12.0	20.75
501246	12 19 36.64	11 12 30.3	17.00	0.66	153.5	93.1	13.1	14.36
501268	12 19 37.06	11 12 17.2	19.14	0.52	127.6	67.2	16.8	9.52
501276	12 19 37.12	11 13 12.5	20.01	0.55	150.7	90.3	32.0	5.48
501369	12 19 38.39	11 11 25.2	18.16	0.70	–20.1	–80.5	12.6	16.24
502017	12 19 49.66	11 13 05.7	17.36	0.75	–61.6	–122.0	12.3	17.62
502194	12 19 53.20	11 09 57.7	19.77	0.87	–4.7	–65.1	17.0	9.41
502241	12 19 54.54	11 14 31.8	18.84	0.55	122.0	61.6	16.2	9.91
502726	12 20 01.70	11 14 21.1	18.61	0.54	335.1	274.8	15.8	10.29
502793	12 20 02.53	11 14 38.4	17.36	0.61	14.7	–45.7	14.0	12.30
602193	12 19 36.81	11 07 13.3	18.72	0.84	–19.4	–79.8	14.5	11.67
602988	12 19 43.27	11 08 06.3	18.52	0.39	–38.3	–98.7	20.2	7.89
603727	12 19 50.93	11 07 45.1	18.15	0.63	–124.0	–184.4	13.9	12.51
604179	12 19 56.71	11 06 42.2	16.75	0.70	63.4	3.0	11.9	23.20
604766	12 20 03.95	11 05 25.4	16.52	0.80	–76.6	–137.0	19.7	8.10

Table 3.41: Spectroscopic and Photometric Data for Objects in Field 260.0p01.0

ID	$\alpha_{J2000.0}$	$\delta_{J2000.0}$	I_0	$(V-I)_0$	$V_{\rm helio}$ (km s^{-1})	$V_{\rm gsr}$ (km s^{-1})	σ_V (km s^{-1})	R_{TD}
000042	12 41 40.46	14 05 37.7	20.70	0.64	–159.0	–198.5	20.5	7.79
000075	12 41 34.53	14 05 57.4	19.29	0.71	96.1	56.6	13.2	13.91
000127	12 41 06.29	14 06 38.6	21.11	0.53	–31.7	–71.2	26.6	6.30
000143	12 41 22.31	14 06 49.0	20.96	0.91	–54.0	–93.5	27.6	6.11
000150	12 41 29.75	14 06 56.2	19.72	0.57	73.1	33.6	14.1	12.17
000168	12 41 19.37	14 07 10.1	20.92	0.62	86.3	46.8	31.9	5.49
000272	12 41 11.29	14 08 28.6	20.71	0.58	–26.9	–66.4	30.9	5.62
000301	12 41 37.76	14 08 53.8	20.67	0.74	–19.2	–58.8	31.3	5.56
000324	12 41 34.71	14 09 07.5	19.68	0.73	–57.4	–97.0	14.0	12.36
000351	12 41 20.58	14 09 22.6	21.32	0.59	–42.6	–82.2	31.7	5.51
000372	12 41 42.80	14 09 32.7	19.88	0.63	13.4	–26.1	13.7	12.92
000409	12 41 34.31	14 10 02.0	20.83	0.59	–45.8	–85.3	30.9	5.62
000433	12 41 08.43	14 10 25.0	21.03	0.72	–95.7	–135.3	38.1	4.82
000456	12 41 20.89	14 10 43.6	19.56	0.60	175.0	135.5	15.0	11.06
000471	12 41 26.77	14 10 52.1	21.02	0.76	–114.1	–153.6	29.2	5.86
000492	12 41 09.02	14 11 15.0	21.72	0.59	–32.8	–72.3	72.7	3.03
000513	12 41 39.52	14 11 28.5	19.94	0.70	140.7	101.2	13.5	13.28
000527	12 41 22.55	14 11 37.8	19.55	0.79	–8.2	–47.7	14.7	11.41
000548	12 41 38.83	14 11 43.6	20.97	0.59	–62.2	–101.7	27.2	6.19
000554	12 41 39.89	14 11 49.9	20.27	0.75	–70.8	–110.3	29.3	5.84
000570	12 41 15.89	14 12 00.1	20.92	0.71	136.5	96.9	40.3	4.63
000653	12 41 38.82	14 13 16.2	19.86	0.85	–86.1	–125.7	14.2	12.01
000699	12 41 19.82	14 14 12.4	20.99	0.92	234.5	195.0	29.3	5.84
000760	12 41 36.51	14 14 58.9	21.02	0.65	88.9	49.4	42.6	4.45
000783	12 41 24.17	14 15 17.3	21.07	0.77	234.7	195.1	40.5	4.62
000791	12 41 30.12	14 15 23.5	21.14	0.86	–9.4	–48.9	60.6	3.46
000810	12 41 30.16	14 15 35.5	21.43	0.74	–60.2	–99.7	71.1	3.08
000859	12 41 15.21	14 16 02.7	19.88	0.61	265.1	225.6	30.9	5.62
000910	12 41 25.49	14 16 41.7	19.26	0.61	–100.3	–139.8	13.8	12.64
000967	12 41 37.77	14 17 15.0	21.07	0.73	–45.1	–84.7	49.3	4.01
000998	12 41 39.29	14 17 40.4	20.48	0.80	250.5	210.9	34.3	5.21
001026	12 41 22.72	14 17 59.2	21.77	0.55	–32.0	–71.6	47.5	4.12
001079	12 41 34.78	14 18 40.9	19.45	0.63	–66.2	–105.8	19.4	8.19
001129	12 41 28.40	14 19 19.3	20.68	0.90	–217.1	–256.7	31.3	5.57
001199	12 41 41.98	14 20 19.7	20.49	0.63	–52.3	–91.8	31.3	5.57

Table 3.42: Spectroscopic and Photometric Data for Objects in Field 265.0p00.9

ID	$\alpha_{J2000.0}$	$\delta_{J2000.0}$	I_0	$(V-I)_0$	$V_{\rm helio}$ (km s^{-1})	$V_{\rm gsr}$ (km s^{-1})	σ_V (km s^{-1})	R_{TD}
000027	12 59 32.21	11 39 06.2	20.16	0.99	265.3	228.1	44.0	4.35
000066	12 59 26.18	11 39 27.8	21.09	0.68	109.2	72.0	57.6	3.59
000084	12 59 09.44	11 39 37.6	19.86	0.72	16.1	–21.1	21.7	7.43
000133	12 59 20.22	11 40 09.9	20.51	0.67	–66.3	–103.5	30.4	5.69
000140	12 59 34.22	11 40 17.3	19.67	0.93	19.2	–18.0	17.9	8.90
000210	12 59 41.87	11 41 01.9	20.26	0.54	150.7	113.4	22.7	7.14
000230	12 59 08.63	11 41 23.9	20.83	0.45	–53.3	–90.5	84.4	2.71
000242	12 59 39.37	11 41 33.2	20.93	0.75	209.5	172.3	62.8	3.37
000262	12 59 42.06	11 41 45.3	20.97	0.65	–75.2	–112.5	29.2	5.86
000288	12 59 36.39	11 42 03.2	21.76	0.86	–26.3	–63.5	85.2	2.69
000300	12 59 36.91	11 42 09.5	20.21	0.64	–19.9	–57.1	34.9	5.14
000315	12 59 17.37	11 42 19.1	21.37	0.49	2.4	–34.8	35.7	5.06
000322	12 59 34.94	11 42 26.2	19.50	0.87	–155.6	–192.8	17.5	9.08
000337	12 59 11.29	11 42 38.0	19.63	0.55	241.6	204.4	15.9	10.17
000379	12 59 41.92	11 43 08.6	21.69	0.45	20.6	–16.6	54.0	3.76
000384	12 59 31.71	11 43 15.7	21.58	1.01	48.1	10.9	86.5	2.66
000422	12 59 09.27	11 43 35.6	20.96	0.51	–168.2	–205.4	38.7	4.77
000456	12 59 07.49	11 44 04.3	20.63	0.89	–57.6	–94.8	28.9	5.91
000487	12 59 23.28	11 44 28.5	21.19	0.57	68.5	31.3	48.5	4.06
000531	12 59 38.89	11 45 07.5	20.19	0.54	134.2	97.0	34.3	5.20
000545	12 59 12.15	11 45 18.2	19.51	0.61	218.9	181.7	17.0	9.41
000594	12 59 05.94	11 45 52.9	20.25	0.74	–56.0	–93.2	29.5	5.82
000724	12 59 35.93	11 47 03.5	19.91	0.76	26.7	–10.5	25.4	6.53
000795	12 59 34.09	11 47 40.9	20.57	0.74	52.7	15.5	42.8	4.44
000845	12 59 12.51	11 48 03.9	21.31	0.65	36.2	–1.0	68.6	3.16
000919	12 59 10.73	11 49 02.2	21.12	0.56	–209.8	–247.0	40.8	4.59
000964	12 59 20.51	11 49 35.5	20.68	0.76	–30.9	–68.1	53.6	3.78
000976	12 59 39.49	11 49 43.6	20.59	0.92	19.6	–17.6	25.5	6.50
000998	12 59 15.36	11 49 57.5	21.72	0.64	18.9	–18.3	75.3	2.95
001121	12 59 18.47	11 51 12.0	21.12	0.64	84.4	47.2	45.5	4.25
001234	12 59 07.04	11 52 40.1	20.64	0.51	–3.5	–40.7	43.9	4.36
001241	12 59 14.03	11 52 46.2	21.27	0.66	80.4	43.2	67.2	3.21
001272	12 59 27.03	11 53 12.1	19.69	0.62	196.0	158.8	14.1	12.15
001295	12 59 14.07	11 53 20.1	20.93	0.62	–50.2	–87.5	32.0	5.48
001304	12 59 22.19	11 53 26.1	21.80	0.64	119.6	82.4	44.0	4.35
001356	12 59 09.97	11 53 56.1	19.83	0.55	102.2	64.9	17.3	9.23

Table 3.43: Spectroscopic and Photometric Data for Objects in Field 275.1p00.6

ID	$\alpha_{J2000.0}$	$\delta_{J2000.0}$	I_0	$(V-I)_0$	$V_{\rm helio}$ (km s^{-1})	$V_{\rm gsr}$ (km s^{-1})	σ_V (km s^{-1})	R_{TD}
000072	13 34 28.92	6 29 28.4	21.62	0.52	–42.7	–74.8	50.6	3.94
000098	13 34 21.30	6 29 41.3	19.64	0.69	–103.9	–136.1	16.8	9.52
000143	13 34 35.40	6 30 03.8	21.24	0.65	–93.7	–125.8	30.5	5.68
000165	13 34 04.13	6 30 14.7	20.16	0.85	20.1	–12.0	21.4	7.52
000182	13 34 02.52	6 30 25.5	20.25	0.53	188.8	156.7	28.9	5.90
000240	13 34 23.81	6 30 54.3	21.31	0.60	–41.0	–73.1	37.5	4.88
000364	13 34 05.59	6 32 03.9	19.38	0.73	135.7	103.6	13.2	14.12
000424	13 34 14.79	6 32 39.0	19.82	0.85	–46.5	–78.7	15.7	10.34
000465	13 34 34.60	6 33 07.0	21.02	0.61	0.0	–32.1	32.0	5.48
000482	13 34 21.37	6 33 15.4	21.35	0.52	–9.0	–41.2	19.1	8.33
000506	13 34 17.77	6 33 32.3	21.90	0.57	–36.8	–69.0	41.3	4.55
000530	13 34 37.32	6 33 56.4	20.37	0.75	91.0	58.9	18.6	8.56
000572	13 34 27.07	6 34 18.3	21.18	0.65	–41.0	–73.1	60.3	3.47
000589	13 34 23.68	6 34 25.4	20.25	0.82	107.0	74.8	19.7	8.09
000641	13 34 31.32	6 34 49.0	19.83	0.96	43.1	11.0	34.6	5.17
000652	13 34 02.38	6 34 54.7	21.18	0.46	8.2	–23.9	28.6	5.96
000722	13 34 21.60	6 35 37.6	21.18	1.00	–47.0	–79.1	77.4	2.89
000777	13 34 25.83	6 36 10.0	20.16	0.61	–0.6	–32.7	46.9	4.16
000976	13 34 25.97	6 38 11.0	21.22	0.54	–82.4	–114.6	59.6	3.50
001009	13 34 08.76	6 38 26.5	19.29	0.54	239.5	207.4	15.6	10.40
001130	13 34 17.56	6 39 34.8	19.70	0.83	–18.6	–50.7	14.2	12.03
001141	13 34 06.33	6 39 42.7	21.19	0.88	7.4	–24.8	54.6	3.73
001176	13 34 16.23	6 39 59.8	20.30	0.62	–88.3	–120.4	16.6	9.64
001218	13 34 13.57	6 40 27.5	19.76	0.68	216.3	184.2	13.4	13.45
001314	13 34 14.53	6 41 26.4	19.99	0.60	–177.1	–209.2	16.2	9.95
001338	13 34 20.44	6 41 37.7	21.43	0.54	–56.6	–88.7	38.1	4.82
001423	13 34 33.08	6 42 32.7	20.44	0.66	–21.3	–53.4	17.3	9.23
001537	13 34 10.75	6 43 30.0	19.87	0.56	–14.8	–46.9	17.8	8.92
001555	13 34 10.55	6 43 41.6	19.90	1.02	114.8	82.6	27.2	6.18
001566	13 34 14.90	6 43 49.1	19.63	0.63	–83.5	–115.6	26.3	6.34
001575	13 34 19.24	6 43 55.6	19.79	0.72	162.9	130.8	18.7	8.49

Table 3.44: Spectroscopic and Photometric Data for Objects in Field 285.0p00.3

ID	$\alpha_{J2000.0}$	$\delta_{J2000.0}$	I_0	$(V-I)_0$	$V_{\rm helio}$ (km s^{-1})	$V_{\rm gsr}$ (km s^{-1})	σ_V (km s^{-1})	R_{TD}
000056	14 08 17.72	1 12 15.2	21.04	0.75	51.9	25.7	84.8	2.70
000079	14 08 16.18	1 12 31.4	20.56	0.85	19.8	–6.4	42.8	4.44
000096	14 07 56.98	1 12 38.2	21.33	0.65	46.5	20.3	78.9	2.85
000141	14 07 52.40	1 12 52.4	21.92	0.62	401.7	375.5	88.7	2.61
000157	14 07 57.17	1 13 01.9	19.95	0.60	–217.4	–243.6	19.0	8.39
000194	14 07 57.09	1 13 17.6	21.18	0.72	97.1	70.9	61.3	3.43
000209	14 07 59.85	1 13 24.6	19.89	0.72	–134.4	–160.6	17.6	9.06
000223	14 08 08.86	1 13 31.3	21.69	1.03	–25.0	–51.2	73.3	3.01
000319	14 08 06.42	1 14 16.5	20.81	0.79	–189.4	–215.6	30.7	5.65
000342	14 08 05.03	1 14 31.2	19.62	0.70	93.6	67.4	21.1	7.61
000353	14 08 01.73	1 14 38.1	19.26	0.76	–278.8	–305.0	17.0	9.38
000389	14 08 13.92	1 15 01.0	20.81	0.88	111.4	85.2	34.8	5.15
000407	14 08 03.64	1 15 12.2	19.86	0.59	–76.3	–102.5	22.3	7.24
000423	14 08 18.54	1 15 20.0	21.03	0.67	–136.5	–162.7	45.2	4.27
000445	14 08 27.93	1 15 34.2	19.35	0.64	24.8	–1.4	13.6	13.16
000463	14 08 19.40	1 15 43.8	20.84	0.64	295.1	268.9	69.5	3.13
000495	14 08 05.11	1 16 05.8	20.33	0.73	73.8	47.6	38.1	4.82
000515	14 08 13.70	1 16 14.8	20.96	0.90	21.7	–4.5	59.6	3.50
000525	14 08 15.11	1 16 23.4	21.89	0.74	–22.4	–48.6	62.8	3.37
000558	14 08 05.30	1 16 36.3	20.79	0.77	109.6	83.4	65.2	3.28
000581	14 08 01.88	1 16 49.7	19.44	0.59	–109.7	–135.9	14.2	12.04
000587	14 08 26.81	1 16 56.4	21.71	0.91	14.3	–11.9	79.3	2.84
000598	14 07 53.76	1 17 02.8	20.69	0.66	–75.7	–101.9	85.6	2.68
000631	14 08 27.75	1 17 17.3	20.21	0.68	149.9	123.7	21.3	7.55
000663	14 08 12.89	1 17 27.7	21.12	0.87	83.0	56.8	84.8	2.70
000692	14 08 16.29	1 17 42.8	21.91	0.53	192.0	165.8	84.0	2.72
000712	14 08 15.51	1 17 51.4	21.38	1.02	98.5	72.3	90.5	2.57
000743	14 08 06.92	1 18 03.9	21.80	0.77	–26.4	–52.6	96.3	2.45
000773	14 08 15.46	1 18 19.6	21.20	0.54	28.0	1.8	33.5	5.29
000801	14 08 11.46	1 18 29.1	19.49	0.82	–63.9	–90.1	13.9	12.56
000826	14 08 27.67	1 18 41.6	19.43	0.75	–125.4	–151.6	21.1	7.62
000919	14 08 26.51	1 19 24.7	19.56	0.59	35.6	9.4	19.3	8.24
000980	14 07 58.44	1 19 53.8	21.26	0.55	–10.7	–36.9	31.9	5.49
001042	14 07 57.11	1 20 26.7	20.44	0.66	–152.1	–178.3	95.8	2.46
001063	14 08 15.16	1 20 34.3	21.62	0.47	1.3	–24.9	58.9	3.53
001093	14 08 21.07	1 20 42.6	21.83	0.60	–26.5	–52.7	95.3	2.47
001151	14 08 08.82	1 21 04.4	21.09	0.96	1.1	–25.1	91.9	2.54
001217	14 08 09.30	1 21 31.2	21.67	0.77	–8.1	–34.3	62.3	3.39
001243	14 07 55.65	1 21 39.5	19.78	0.82	198.6	172.4	17.4	9.14
001262	14 08 02.68	1 21 47.4	21.00	0.73	14.6	–11.6	53.2	3.80
001329	14 08 16.65	1 22 16.6	21.72	0.64	–57.3	–83.5	70.4	3.10
001355	14 08 25.42	1 22 32.0	21.59	0.55	–7.2	–33.4	69.2	3.14
001463	14 08 00.30	1 23 28.4	20.64	0.71	217.2	191.0	32.5	5.41
001480	14 08 23.02	1 23 37.5	21.29	0.64	–19.2	–45.4	70.4	3.10
001505	14 08 20.12	1 23 52.5	21.36	0.81	173.3	147.1	53.4	3.79
001545	14 08 16.13	1 24 16.9	20.55	0.89	49.1	22.9	37.5	4.88
001620	14 07 55.20	1 24 57.8	20.52	0.54	103.8	77.6	60.6	3.46

Continued on Next Page...

Table 3.44 – 285.0p00.3 (Continued)

ID	$\alpha_{J2000.0}$	$\delta_{J2000.0}$	I_0	$(V-I)_0$	$V_{\rm helio}$ (km s^{-1})	$V_{\rm gsr}$ (km s^{-1})	σ_V (km s^{-1})	R_{TD}
001674	14 08 27.43	1 25 43.5	20.49	0.58	42.7	16.5	34.9	5.14
001681	14 08 16.92	1 25 51.0	21.07	0.66	–20.9	–47.1	37.0	4.93
001692	14 08 06.41	1 25 57.5	20.48	0.71	–132.0	–158.2	25.7	6.46
001711	14 08 07.01	1 26 17.0	19.82	0.77	11.8	–14.4	19.6	8.13
001738	14 08 01.62	1 26 37.1	21.59	0.55	–16.3	–42.5	75.0	2.96

Table 3.45: Spectroscopic and Photometric Data for Objects in Field 295.0p00.0

ID	$\alpha_{J2000.0}$	$\delta_{J2000.0}$	I_0	$(V-I)_0$	$V_{\rm helio}$ (km s^{-1})	$V_{\rm gsr}$ (km s^{-1})	σ_V (km s^{-1})	R_{TD}
000230	14 42 36.94	–4 04 42.0	20.51	0.57	18.1	–1.2	42.9	4.43
000260	14 42 15.05	–4 04 25.7	21.17	0.63	240.1	220.8	59.9	3.49
000262	14 42 27.94	–4 04 24.7	20.11	0.66	–111.0	–130.3	21.3	7.55
000309	14 41 57.92	–4 03 59.6	21.79	0.51	21.7	2.4	52.6	3.83
000322	14 42 38.57	–4 03 50.8	21.45	0.56	80.7	61.3	65.2	3.28
000334	14 41 50.65	–4 03 44.3	20.12	0.77	29.8	10.4	19.2	8.31
000339	14 42 20.44	–4 03 42.5	20.32	0.91	285.1	265.7	29.8	5.77
000343	14 42 32.83	–4 03 40.0	21.31	0.36	21.1	1.8	31.8	5.50
000367	14 41 42.92	–4 03 31.9	20.78	0.65	–60.4	–79.7	52.6	3.83
000390	14 42 03.72	–4 03 22.6	21.34	0.60	19.1	–0.2	46.2	4.20
000392	14 42 17.96	–4 03 21.2	19.69	0.65	–23.9	–43.3	23.9	6.84
000397	14 42 01.92	–4 03 20.1	21.05	0.72	21.7	2.3	32.3	5.44
000417	14 42 35.28	–4 03 13.4	21.80	0.45	–10.5	–29.8	57.8	3.58
000430	14 41 58.80	–4 03 08.4	21.10	0.79	57.4	38.0	37.6	4.87
000437	14 41 41.31	–4 03 07.1	20.56	0.80	351.2	331.9	52.6	3.83
000457	14 42 00.37	–4 03 01.9	19.40	0.63	172.4	153.0	17.4	9.17
000496	14 42 00.72	–4 02 47.1	19.96	0.68	–78.7	–98.1	52.0	3.86
000503	14 41 55.66	–4 02 44.4	20.65	0.51	10.4	–9.0	40.6	4.61
000543	14 42 23.11	–4 02 21.3	21.49	0.46	21.0	1.7	52.4	3.84
000582	14 42 05.37	–4 02 05.0	21.62	0.51	–5.7	–25.1	48.8	4.04
000584	14 42 22.08	–4 02 03.1	19.16	0.49	–118.3	–137.6	16.1	10.00
000640	14 42 32.26	–4 01 40.3	20.28	0.58	383.6	364.3	47.0	4.15
000757	14 41 52.89	–4 00 46.8	19.86	0.84	23.1	3.7	34.4	5.19
000759	14 41 48.99	–4 00 46.3	19.74	0.88	7.1	–12.3	26.7	6.28
000877	14 42 16.03	–3 59 48.5	20.01	0.74	–25.5	–44.8	42.2	4.48
000927	14 42 37.83	–3 59 24.7	20.92	0.39	–30.6	–50.0	63.6	3.34
000946	14 41 40.72	–3 59 18.3	19.95	0.56	233.5	214.1	70.4	3.10
000962	14 41 46.43	–3 59 13.2	20.78	0.80	–187.4	–206.7	84.0	2.72
001041	14 42 12.81	–3 58 34.6	19.80	0.79	–5.6	–25.0	17.4	9.13
001048	14 42 04.26	–3 58 31.5	21.13	0.69	50.8	31.5	55.6	3.68
001117	14 41 48.02	–3 58 04.9	21.26	0.61	1.2	–18.1	51.1	3.91
001168	14 42 26.25	–3 57 43.1	20.41	0.76	105.2	85.8	42.1	4.49
001196	14 41 56.15	–3 57 27.8	19.38	0.56	–108.2	–127.6	21.3	7.53
001207	14 42 34.39	–3 57 19.1	21.84	0.67	6.2	–13.2	77.1	2.90
001257	14 41 40.24	–3 56 55.8	20.78	0.72	–1.4	–20.8	41.2	4.56
001291	14 42 19.97	–3 56 39.0	20.08	0.48	–49.9	–69.3	43.9	4.36
001303	14 42 11.35	–3 56 30.3	20.94	0.71	44.6	25.2	62.1	3.40

Table 3.46: Spectroscopic and Photometric Data for Objects in Field 305.0n00.2

ID	$\alpha_{J2000.0}$	$\delta_{J2000.0}$	I_0	$(V-I)_0$	$V_{\rm helio}$ (km s^{-1})	$V_{\rm gsr}$ (km s^{-1})	σ_V (km s^{-1})	R_{TD}
000445	15 16 15.63	–9 16 54.0	20.73	0.36	117.6	105.8	45.2	4.27
000447	15 16 48.78	–9 16 53.0	20.76	0.91	–31.4	–43.2	54.8	3.72
000450	15 16 53.98	–9 16 50.4	19.75	0.60	258.4	246.6	24.0	6.83
000457	15 16 45.90	–9 16 48.7	20.01	0.71	44.6	32.8	21.7	7.43
000503	15 17 00.00	–9 16 29.2	19.53	0.77	–13.0	–24.8	21.5	7.48
000519	15 16 07.62	–9 16 23.3	20.75	0.76	13.4	1.6	49.2	4.02
000547	15 16 27.36	–9 16 11.6	21.62	0.57	–8.6	–20.4	63.9	3.33
000595	15 16 18.94	–9 15 50.2	21.55	0.61	33.6	21.8	43.6	4.38
000597	15 16 57.32	–9 15 49.1	20.50	0.88	–13.8	–25.6	66.6	3.23
000738	15 16 22.29	–9 14 45.9	21.06	0.85	42.1	30.3	40.0	4.66
000747	15 16 06.56	–9 14 41.7	21.34	0.80	–7.0	–18.8	84.8	2.70
000791	15 16 50.07	–9 14 21.5	19.29	0.76	61.5	49.7	27.6	6.12
000793	15 16 32.69	–9 14 21.0	20.49	0.52	425.4	413.6	49.2	4.02
000902	15 16 43.80	–9 13 35.4	20.43	0.61	–12.6	–24.4	60.3	3.47
000927	15 16 21.73	–9 13 26.5	21.54	0.60	29.0	17.2	46.4	4.19
000936	15 16 13.65	–9 13 23.1	19.18	0.86	83.7	71.9	24.3	6.75
000938	15 16 05.09	–9 13 21.7	21.64	0.70	7.7	–4.1	75.3	2.95
000964	15 16 36.86	–9 13 08.9	20.66	0.61	–31.2	–43.1	36.0	5.03
000967	15 16 58.89	–9 13 06.7	21.16	0.74	21.9	10.1	77.8	2.88
001026	15 16 52.45	–9 12 50.5	21.24	0.85	–27.8	–39.6	49.2	4.02
001064	15 16 08.13	–9 12 39.7	19.85	0.59	–35.1	–46.9	37.6	4.87
001071	15 16 01.26	–9 12 36.3	21.44	0.60	30.7	18.9	58.9	3.53
001098	15 16 38.78	–9 12 17.4	19.95	0.87	42.7	30.9	32.0	5.47
001108	15 16 27.82	–9 12 13.3	19.26	0.87	43.5	31.6	20.6	7.77
001129	15 16 06.97	–9 12 05.5	19.43	0.85	192.1	180.3	17.0	9.40
001156	15 16 10.41	–9 11 55.5	20.50	0.71	41.5	29.7	26.2	6.37
001169	15 16 25.88	–9 11 50.2	20.59	0.71	326.7	314.9	38.1	4.82
001173	15 16 41.65	–9 11 47.2	21.83	0.52	–8.1	–19.9	79.3	2.84
001195	15 16 49.38	–9 11 32.6	21.24	0.53	–3.3	–15.1	79.3	2.84
001202	15 16 39.89	–9 11 27.5	21.21	0.72	–279.1	–290.9	76.4	2.92
001206	15 16 50.96	–9 11 25.2	20.00	0.71	–188.1	–199.9	27.6	6.11
001209	15 16 21.30	–9 11 24.9	19.41	0.86	–13.0	–24.8	16.3	9.87
001237	15 16 36.47	–9 11 12.2	19.47	0.42	–20.9	–32.7	37.3	4.90
001247	15 16 42.56	–9 11 06.8	20.87	0.51	31.8	19.9	38.1	4.82
001292	15 16 23.02	–9 10 46.8	20.01	0.57	68.2	56.4	31.6	5.53
001349	15 16 55.57	–9 10 23.7	19.37	0.53	–143.9	–155.7	25.5	6.51
001361	15 16 44.70	–9 10 18.4	21.61	0.54	6.1	–5.8	49.3	4.01
001386	15 16 24.89	–9 10 08.3	21.21	0.48	262.3	250.5	49.9	3.98
001439	15 16 09.73	–9 09 46.4	21.84	0.97	–13.7	–25.6	59.4	3.51
001482	15 16 26.79	–9 09 27.0	20.09	0.29	33.6	21.7	21.3	7.55
001487	15 16 26.36	–9 09 25.0	20.33	0.92	–3.8	–15.6	70.7	3.09
001518	15 16 10.79	–9 09 14.7	20.42	0.56	12.6	0.8	31.7	5.52
001523	15 16 00.67	–9 09 12.1	20.70	0.36	–2.8	–14.6	56.7	3.63
001540	15 16 25.37	–9 09 04.9	21.62	0.64	6.8	–5.0	49.5	4.00
001549	15 16 09.02	–9 09 02.9	20.29	0.76	245.4	233.6	37.4	4.89
001558	15 16 34.68	–9 08 58.5	21.55	0.47	31.3	19.5	84.0	2.72
001574	15 16 52.96	–9 08 52.3	20.82	0.63	41.0	29.1	78.2	2.87

Continued on Next Page...

Table 3.46 – 305.0n00.2 (Continued)

ID	$\alpha_{J2000.0}$	$\delta_{J2000.0}$	I_0	$(V-I)_0$	$V_{\rm helio}$ (km s^{-1})	$V_{\rm gsr}$ (km s^{-1})	σ_V (km s^{-1})	R_{TD}
001617	15 16 24.48	–9 08 37.6	20.94	0.60	–92.8	–104.6	63.9	3.33
001637	15 16 55.17	–9 08 30.6	19.66	0.81	117.0	105.1	25.5	6.50
001656	15 16 23.76	–9 08 23.8	20.49	0.54	62.1	50.3	47.2	4.14
001664	15 16 28.87	–9 08 19.0	19.64	0.76	18.6	6.7	23.8	6.88
001679	15 16 18.07	–9 08 14.9	21.27	0.51	29.5	17.6	63.3	3.35
001685	15 16 20.11	–9 08 11.1	19.80	0.60	29.2	17.4	25.4	6.53

Table 3.47: Spectroscopic and Photometric Data for Objects in Field 315.1n00.6

ID	$\alpha_{J2000.0}$	$\delta_{J2000.0}$	I_0	$(V-I)_0$	$V_{\rm helio}$ (km s^{-1})	$V_{\rm gsr}$ (km s^{-1})	σ_V (km s^{-1})	R_{TD}
000530	15 51 43.30	–14 24 49.4	20.09	0.70	282.3	278.0	22.2	7.29
000535	15 51 53.31	–14 24 48.1	20.70	0.74	63.3	58.9	72.0	3.05
000545	15 51 45.39	–14 24 45.3	20.29	0.82	13.6	9.2	19.4	8.22
000550	15 51 30.20	–14 24 43.7	20.60	0.82	–6.4	–10.7	17.5	9.11
000581	15 51 30.76	–14 24 32.0	20.80	0.50	101.7	97.3	45.3	4.26
000587	15 51 22.71	–14 24 30.7	21.25	0.83	–26.6	–31.0	50.2	3.96
000596	15 51 44.38	–14 24 28.5	20.73	0.59	–1.6	–5.9	44.2	4.34
000608	15 51 50.28	–14 24 26.2	21.15	0.61	–3.6	–8.0	54.2	3.75
000648	15 51 45.78	–14 24 14.3	21.40	0.60	29.4	25.0	42.0	4.50
000670	15 51 56.58	–14 24 07.9	20.06	0.63	19.2	14.8	17.0	9.41
000687	15 52 15.49	–14 24 03.6	19.57	0.54	–85.5	–89.8	22.9	7.10
000705	15 52 18.34	–14 24 00.0	19.84	0.69	–181.4	–185.7	34.0	5.24
000715	15 51 57.04	–14 23 57.3	20.44	0.61	174.4	170.0	24.7	6.68
000746	15 51 33.32	–14 23 47.1	20.83	0.85	27.7	23.3	38.3	4.81
000815	15 51 52.05	–14 23 29.0	21.23	0.61	–8.1	–12.5	76.7	2.91
000821	15 52 06.38	–14 23 27.2	19.31	0.67	34.4	30.0	13.2	14.08
000857	15 51 55.85	–14 23 17.1	20.83	0.38	218.1	213.8	39.4	4.71
000862	15 52 03.68	–14 23 15.5	20.97	0.56	23.7	19.3	48.3	4.07
000913	15 52 14.85	–14 23 04.7	20.53	0.82	–10.0	–14.3	49.7	3.99
000919	15 51 51.69	–14 23 03.0	20.61	0.82	13.8	9.5	30.7	5.64
000940	15 51 24.85	–14 22 57.8	19.05	0.61	4.9	0.5	11.9	22.03
000946	15 51 34.32	–14 22 55.9	20.95	0.72	23.9	19.5	56.3	3.65
000997	15 52 13.88	–14 22 42.5	19.76	0.69	–18.7	–23.0	16.4	9.82
001009	15 52 20.17	–14 22 39.1	21.04	0.54	3.2	–1.2	79.7	2.83
001074	15 51 29.21	–14 22 23.0	19.97	0.80	33.0	28.7	14.1	12.25
001076	15 51 49.21	–14 22 22.2	19.33	0.73	47.7	43.3	13.4	13.58
001088	15 52 18.93	–14 22 16.8	21.30	0.54	77.3	72.9	58.7	3.54
001150	15 51 21.64	–14 22 03.2	21.36	0.63	–55.2	–59.5	43.7	4.37
001182	15 52 19.65	–14 21 49.0	19.55	0.67	84.9	80.5	15.1	10.87
001194	15 51 33.73	–14 21 48.1	20.07	0.67	225.4	221.1	25.6	6.48
001205	15 52 16.60	–14 21 44.1	19.63	0.48	12.1	7.7	27.6	6.12
001276	15 52 10.07	–14 21 26.4	21.30	0.86	42.1	37.7	86.1	2.67
001421	15 51 49.56	–14 20 54.9	20.84	0.60	52.1	47.7	49.3	4.01
001437	15 52 00.14	–14 20 51.9	20.61	0.68	–6.7	–11.1	50.4	3.95
001494	15 51 44.81	–14 20 37.9	20.91	0.86	25.9	21.5	39.4	4.71
001501	15 51 38.00	–14 20 36.2	20.98	0.60	17.3	12.9	58.0	3.57
001520	15 52 06.00	–14 20 31.1	20.56	0.78	19.8	15.4	43.2	4.41
001529	15 51 25.33	–14 20 29.8	19.65	0.84	–4.6	–9.0	14.0	12.31
001578	15 51 48.33	–14 20 15.9	21.08	0.80	6.6	2.3	52.6	3.83
001624	15 51 55.43	–14 20 06.2	21.25	0.47	16.3	12.0	54.8	3.72
001625	15 51 31.94	–14 20 06.4	21.58	0.66	26.2	21.9	77.1	2.90
001631	15 51 57.76	–14 20 05.0	20.60	0.47	28.7	24.3	37.3	4.90
001667	15 52 17.75	–14 19 58.3	20.57	0.70	–16.3	–20.7	82.8	2.75
001683	15 51 36.63	–14 19 55.6	21.64	0.22	0.7	–3.6	49.3	4.01
001744	15 52 07.28	–14 19 44.4	21.10	0.56	35.4	31.0	85.2	2.69
001761	15 51 42.90	–14 19 42.4	20.31	0.86	62.4	58.0	37.3	4.90
001767	15 52 23.82	–14 19 40.0	21.48	0.86	40.2	35.8	68.3	3.17

Continued on Next Page...

Table 3.47 – 315.1n00.6 (Continued)

ID	$\alpha_{J2000.0}$	$\delta_{J2000.0}$	I_0	$(V-I)_0$	$V_{\rm helio}$ (km s^{-1})	$V_{\rm gsr}$ (km s^{-1})	σ_V (km s^{-1})	R_{TD}
001809	15 51 58.44	–14 19 27.8	19.90	0.81	–145.7	–150.1	28.0	6.05
001816	15 51 23.45	–14 19 26.4	21.44	0.73	7.0	2.6	68.3	3.17
001866	15 52 10.69	–14 19 16.7	20.88	0.76	19.0	14.6	66.3	3.24
001869	15 52 21.21	–14 19 15.3	21.52	0.53	28.8	24.4	60.1	3.48
001892	15 52 21.77	–14 19 09.7	19.19	0.51	–189.7	–194.0	28.2	6.01
001951	15 51 26.69	–14 18 58.9	21.11	0.68	9.9	5.6	25.8	6.44
001977	15 51 40.12	–14 18 52.3	21.60	0.53	25.0	20.7	44.6	4.31
001994	15 51 54.26	–14 18 48.7	19.55	0.69	–41.8	–46.1	34.5	5.18
002030	15 52 05.24	–14 18 40.1	21.11	0.53	36.1	31.8	40.0	4.66
002070	15 51 50.81	–14 18 32.9	19.50	0.53	–51.6	–55.9	37.1	4.92
002085	15 51 46.22	–14 18 29.1	19.25	0.80	–17.0	–21.4	19.5	8.18
002126	15 51 47.68	–14 18 19.9	20.02	0.86	111.1	106.7	56.0	3.66
002134	15 52 13.35	–14 18 18.2	20.37	0.57	–10.9	–15.3	43.5	4.39
002249	15 51 46.76	–14 17 55.4	20.83	0.58	73.3	68.9	30.5	5.67
002251	15 52 01.40	–14 17 54.7	21.58	0.51	31.1	26.8	61.6	3.42
002272	15 52 07.90	–14 17 47.9	19.63	0.85	29.4	25.1	16.2	9.94
002274	15 52 22.24	–14 17 47.5	20.75	0.39	17.3	13.0	59.4	3.51
002338	15 52 09.20	–14 17 33.9	21.36	0.56	238.5	234.2	55.2	3.70
002395	15 51 35.66	–14 17 21.8	19.82	0.73	–285.6	–290.0	28.6	5.96
002397	15 52 17.40	–14 17 20.2	20.01	0.84	–44.9	–49.2	50.7	3.93
002440	15 51 53.69	–14 17 08.1	20.69	0.70	40.3	36.0	43.5	4.39
002459	15 52 01.78	–14 17 03.3	21.33	0.47	17.4	13.0	66.9	3.22
002575	15 51 28.23	–14 16 31.7	20.11	0.87	–0.5	–4.8	22.0	7.35
002584	15 51 31.20	–14 16 28.9	20.25	0.67	–13.8	–18.1	25.3	6.54
002627	15 52 16.00	–14 16 18.9	19.89	0.65	63.0	58.7	18.6	8.55
002639	15 51 34.87	–14 16 15.1	19.82	0.73	–19.3	–23.6	18.6	8.53
002649	15 51 59.34	–14 16 11.4	20.19	0.77	45.5	41.1	21.8	7.39
002657	15 52 02.43	–14 16 09.7	20.57	0.71	69.0	64.6	38.9	4.75
002669	15 52 00.77	–14 16 06.7	19.81	0.70	27.5	23.1	16.8	9.54
002715	15 52 03.16	–14 15 51.7	20.89	0.85	36.0	31.7	28.8	5.93

CHAPTER 4

The Sgr Stream in Virgo

4.1 Introduction

The recent search for substructure in the Galactic halo, sparked by the discovery of the Sagittarius dwarf spheroidal galaxy (Sgr; Ibata et al., 1994) and its prominent tidal tails (Majewski et al., 2003; Belokurov et al., 2006; Yanny et al., 2009), has led to the discoveries of numerous dwarf galaxies and stellar streams. Some of the most intriguing of these discoveries have been made in the constellation of Virgo, where numerous features have been identified.

The first evidence of substructure in Virgo was revealed by the QUasar Equatorial Survey Team (QUEST) RR Lyrae survey, which scanned a narrow band around the sky (right ascension, $\alpha \sim 62°$–$92°$, $120°$–$255°$), centered on the celestial equator (declination, $\delta \sim$ –2.3°–0°). They initially identified a small, concentrated clump of just five RR Lyrae variables (RRLs) at $\alpha \sim 200°$ (Vivas et al., 2001). Continued work in the field by the team expanded the feature's membership to 21 RRLs spread over $\alpha \sim 175°$–$200°$, and placed the group at a heliocentric distance of 19 kpc (Vivas & Zinn, 2003; Zinn et al., 2004). Given that the group was centered at $\alpha \sim 186°$, they named this feature the "$12^{\rm h}.4$ clump." Upon expanding its potential membership

to 42 RRLs, the QUEST team revised their distance estimate to the $12^{\rm h}.4$ clump, revealing it to extend from 12 kpc out to 20 kpc from the Sun, with a mean distance of 17 kpc (Vivas & Zinn, 2006). Duffau et al. (2006) obtained spectra for a sample of 18 RRLs in the $12^{\rm h}.4$ clump and supplemented their data with Sloan Digital Sky Survey (SDSS) spectra of 10 blue horizontal branch (BHB) stars discovered by Sirko et al. (2004) in the same region. They found 13 of these 28 stars to have similar kinematics. In particular, a highly localized cluster of six stars (five RRLs and one BHB), with a mean heliocentric distance of 19.6 kpc, was found to have a mean velocity of $\langle V_{\rm gsr} \rangle = 99.8$ km s^{-1} and a velocity dispersion of $\sigma_{\rm v} = 17.3$ km s^{-1}. This provided proof that the $12^{\rm h}.4$ clump was in fact a comoving group, which the QUEST team decided to rename the "Virgo Stellar Stream" (VSS). It is also worth noting that their Figure 2 shows a peak comprised of nine stars with a mean velocity of $\langle V_{\rm gsr} \rangle \sim$ –70 km s^{-1}.

Concurrently, extensive work with SDSS data was done to search for halo substructure in Virgo. Newberg et al. (2002) identified an overdensity of F-type turnoff stars centered near (α, δ) $\sim$ (190°, 0°) at a distance of $\sim$20 kpc. They noted that this feature, named S297+63–20.5, had a turnoff color redder than that of Sgr, but bluer than that of the spheroid. In the same region, Jurić et al. (2008) identified an expansive ($\sim$1000 deg^2) low surface brightness overdensity of mostly main-sequence turnoff stars. Using the method of photometric parallax they found this feature, named the "Virgo overdensity" (VOD), to be centered at a distance of $\sim$10 kpc, but to extend over the entire range of the survey, $\sim$6–20 kpc. They note the possibility

that the VOD could extend down to the Galactic plane, and perhaps even into the southern Galactic hemisphere.

Majewski et al. (2003), using Two Micron All Sky Survey (2MASS) M-giants to trace the tidal arms of Sgr, noted that the leading portion of their best-fit Sgr orbital plane appears to pierce the Galactic disk in the solar neighborhood. Subsequent models assuming oblate halo potentials demonstrated this scenario quite nicely (Martínez-Delgado et al., 2004; Law et al., 2005). Martínez-Delgado et al. (2007) have shown that an oblate halo model can explain the observed substructure in Virgo as being the leading tidal tail of Sgr descending down from the northern Galactic hemisphere on to and through the solar neighborhood. The authors note that the observation of highly negative radial velocities ($V_{\rm gsr} \lesssim$ –200 km s^{-1}) toward Virgo would provide strong evidence in support of their hypothesis.

Contradicting these predictions, Newberg et al. (2007, hereafter NYC07) used SDSS photometry of F-type turnoff stars to trace the leading arm of Sgr through the northern Galactic hemisphere, over the position of the Sun, and down toward the Galactic plane at least 15 kpc outside of the solar circle and in the general direction of the Galactic anticenter. Using SDSS photometry of K/M-giants, Yanny et al. (2009) reached the same conclusion. Also, using SDSS and SEGUE (Sloan Extension for Galactic Understanding and Evolution) spectra of F turnoff stars within S297+62–20.5 NYC07 found the feature to have a radial velocity of $\langle V_{\rm gsr} \rangle = 130 \pm 10$ km s^{-1}. This is fairly consistent with the radial velocity of the VSS, but markedly inconsistent with the aforementioned model that predicted infalling debris from the

leading tidal tail of Sgr into the solar neighborhood. However, it is worth noting that the faint limit of their spectra was $g_0 = 20.5$, and the main-sequence turnoff for Sgr is about a magnitude fainter, so the velocity signature of Sgr was most likely greatly diminished in their spectral data. Since S297+63–20.5 roughly occupies the same volume in the Galactic halo as the VSS and the VOD (NYC07 place it at a distance of ∼18 kpc), and has a velocity similar to that of the VSS, the authors conclude that the three features are most likely one and the same. However, they also see evidence for additional as-yet unidentified Virgo substructures in the form of two other radial velocity peaks of lesser significance at $\langle V_{\rm gsr} \rangle$ = –76 ± 10 km s^{-1} and $\langle V_{\rm gsr} \rangle$ = –168 ± 10 km s^{-1}.

Like Duffau et al. (2006) and NYC07, several recent studies have also found kinematic evidence of multiple halo substructures in Virgo. Vivas et al. (2008) discovered three peaks in the radial velocity distributions of a sample of 43 QUEST RRLs and 38 SDSS BHBs at $\langle V_{\rm gsr} \rangle$ = 215, –49, and –171 km s^{-1} having relatively high, moderate, and low significance, respectively. The stars that constitute these three features have distances that range from ∼7 to 13 kpc. Starkenburg et al. (2009) found two pairs of K-giant stars in the Spaghetti survey data set with mean velocities of $\langle V_{\rm gsr} \rangle$ = 162 and –129 km s^{-1} and distances ranging from ∼13 to 17 kpc. Prior et al. (2009b) observed two peaks in the radial velocity distribution of 11 RRLs at $\langle V_{\rm gsr} \rangle$ = 127 ± 10 and –175 ± 10 km s^{-1} with distances that range from 16 to 22 kpc (see also Prior et al. 2009a).

This volume of the Galactic halo has also recently been spatially resolved into

numerous substructures. Keller et al. (2008) identified two overdensities of SEKBO RRLs, "VOD clump 1" and "VOD clump 2", at distances of 16 and 19 kpc, respectively. Keller et al. (2009) combine distance estimates from SEKBO RRLs with SEKBO and SDSS photometry of main-sequence and red giant branch stars to reveal three overdensities: "feature A" (associated with VOD clump 2, at a distance of $D \sim 20$ kpc), "feature B" (associated with VOD clump 1, $D \sim 17$ kpc), and the newly discovered "feature C" (whose distance is indeterminate due to a lack of RRLs). Most recently, in a tomographic survey of the Virgo region, Keller (2010) used SDSS photometry of subgiants to reveal four substructures which they identify as: the VOD (associated with feature B of Keller et al. 2009, $D \sim 16$ kpc), the "180° overdensity" (associated with feature C of Keller et al. 2009, $D \sim 19$ kpc), and the newly discovered "160° overdensity" ($D \sim 17$ kpc) and "Virgo Equatorial Stream" (VES, $D \sim 28$ kpc).

In addition, Walsh et al. (2009) report the potential discovery of a new extremely low surface brightness dwarf spheroidal galaxy, Virgo Z, at a distance of ∼40 kpc, near (in projection) to the VOD of Keller (2010), and within ∼1° of the field explored in the present study.

What is clear from this discussion is that the Galactic halo in the direction of Virgo is filled with substructures of unknown or uncertain origin and relation. In this study, we present the kinematic results obtained from a sample of 111 faint (median magnitude of $g_0 \sim 20.5$) probable main-sequence stars located in a small field centered on the core of the VSS of Duffau et al. (2006). We find a peak of high

significance in the radial velocity distribution at $V_{\rm gsr} \sim -75$ km s^{-1}, and we interpret this finding in the context of the previous discoveries in Virgo and the extant models of the destruction of Sagittarius.

4.2 Observations and Reductions

To select candidates for spectroscopic follow-up, we obtained multiple exposures in B (3×900 s) and r (4×600 s) in a single field centered on the VSS at (α, δ) $\sim$ (185.°9, –1.°0), and in a control field as well. These images were obtained by David Martínez-Delgado with the Wide Field Camera (WFC) on the 2.5 m Isaac Newton Telescope in 2004 May and 2000 June, respectively. Due to the possible association between Sgr debris and the stellar overdensity in Virgo (Martínez-Delgado et al., 2007), the control field, centered at (α, δ) $\sim$ (228.°5, 9.°9), was chosen to be at a similar Sagittarius longitude (Majewski et al., 2003) to our Virgo field, but reflected about the Sagittarius debris plane.

Candidates in the Virgo and control fields were selected from (B, $B - r$) color–magnitude diagrams, which were later tied directly to the Sloan g_0 and r_0 filters using the SDSS magnitudes of these stars (Abazajian et al., 2009). The selection region (Figure 4.1) was designed to identify probable main-sequence stars in the halo of the Milky Way. We chose stars over a fairly broad color range, and with $g_0 < 21.8$ to minimize the possibility of contamination by background galaxies. There were a total of 328 candidates in the Virgo field, and 272 in the control field. To further minimize contamination by background galaxies, each of these candidates was visually inspected and extended sources were removed from the candidate list.

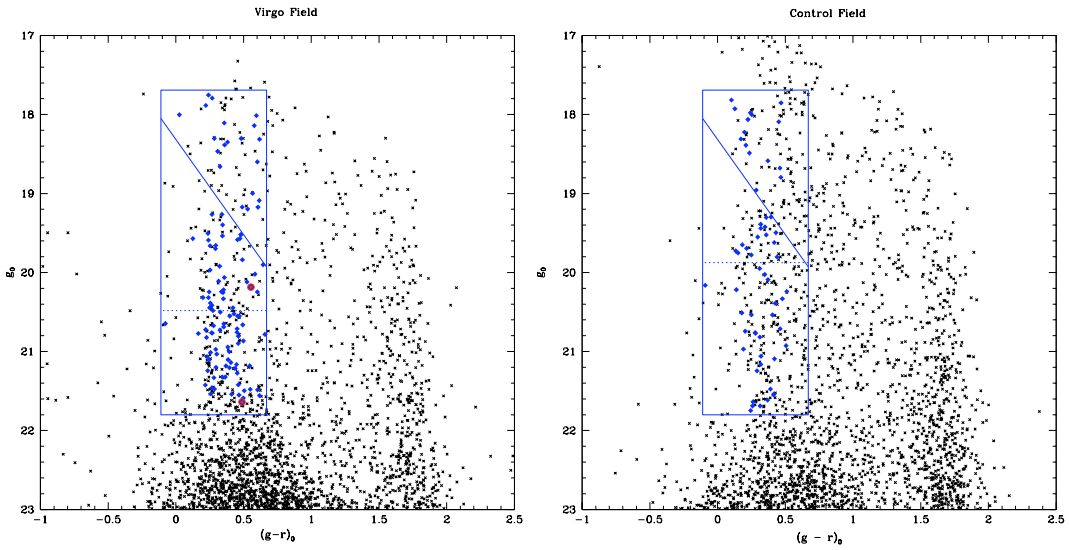

Figure 4.1: Color–magnitude diagrams for the Virgo and control fields. Candidates for spectroscopic follow-up were chosen from inside the rectangular regions, which were designed to identify probable main-sequence stars in the Galactic halo. Stars for which we measured reliable radial velocities are designated with a blue diamond. The dashed line in each field indicates the median apparent magnitude of these stars. The diagonal lines in the selection boxes represent a secondary photometric criterion as explained in Section 4.3. The red circles in the Virgo field designate two stars from our data set whose spectra and Fourier cross-correlations are shown in Figure 4.4.

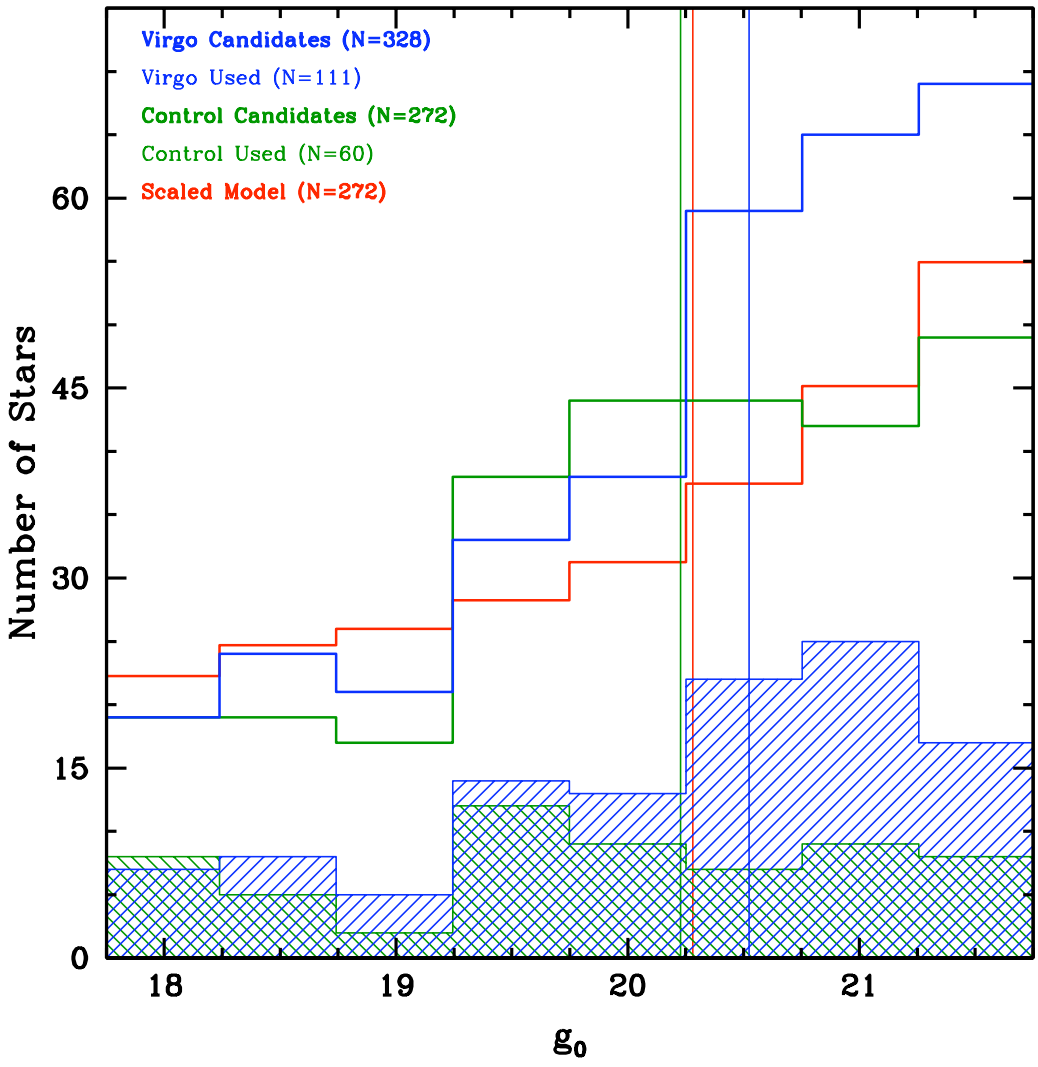

Figure 4.2: Virgo and control field apparent magnitude (g_0) histograms. The candidates in Virgo (blue), the control field (green), and the Besançon model (red) are all shown. The shaded histograms represent the distributions in the Virgo field (blue) and control field (green) of the stars for which we obtained radial velocities. The vertical lines represent the median values of the candidate samples.

The color–magnitude diagrams provide our first hint that there may be substructure within the Virgo field. In Figure 4.2, we plot the distribution of apparent magnitudes for the candidate stars in both fields. For comparison, we also show the expected distribution in the Virgo field as predicted by the so-called Besançon Milky Way model (Robin et al., 2003) (we defer further discussion of this model to Section 4.3). The distributions are quite similar down to $g_0 \sim 20$, below which the Virgo field shows a significant excess of faint stars relative to both the control field and the model. The astrometric transformations from CCD pixel coordinates to standard coordinates, (ξ, η), were performed by the IRAF tasks `tfinder` and `cctrans` using several hundred USNO-B stars (Monet et al., 2003) per field.

All spectra were obtained using multi-slit masks fabricated for use with the Inamori-Magellan Areal Camera and Spectrograph (IMACS) with the $f/4.3$ camera, on the 6.5 m Baade telescope at Las Campanas Observatory. We used the 600 lines mm^{-1} grating in first order centered at 4550 Å. All spectra spanned at least 3800–5300 Å. This region was chosen to include several Balmer lines as well as absorption lines from Ca II, Ca I, Fe I, and others. Slit widths were all $0\farcs8$ and the dispersion was 0.755 Å pixel^{-1} when binned 2×2, corresponding to a spectral resolution of 2.7 Å.

Despite the $15\farcm4 \times 15\farcm4$ field of view of IMACS, the self-imposed restriction that for each slit we obtain our entire desired wavelength range of 3800–5300 Å limits the effective area each mask can cover to about only $15' \times 9'$; much smaller than the $34\farcm2 \times 34\farcm2$ field of view of the WFC. We therefore chose to fabricate multiple masks

in each field: four in Virgo and two in the control field. Figure 4.3 details the spatial distribution of the candidates on each of the four Virgo masks and the unobserved candidates as well. The masks virgo1_1 and virgo1_2 were observed in 2006 April, the control field masks were observed in 2006 June, and the mask virgo1_3 was observed in 2008 May. We were unable to observe the mask virgo1_4 in 2008 May due to poor weather. Four 30 minute exposures were taken with each mask, the only exception being virgo1_3, for which the weather only allowed three 30 minute exposures. Each series of science exposures was preceded by an He–Ne–Ar arc spectrum, and followed by another arc, and finally a quartz–halogen spectroscopic flat. These calibration spectra were all taken using the screen located at the pupil image generated in the Gregorian optical system of the telescope.

All spectra were reduced using the Carnegie Observatories System for Multi-Object Spectroscopy (COSMOS). With COSMOS the data were: overscan subtracted, trimmed, bias subtracted, flattened (using the quartz), sky subtracted, wavelength calibrated (using the nearest arc), extracted to individual two-dimensional spectra, and finally co-added with cosmic ray rejection. These two-dimensional spectra were then collapsed to one-dimensional spectra using the IRAF task `apall`. Radial velocities for each stellar spectrum were then measured using the IRAF task `fxcor`, which performs a Fourier cross-correlation between the input spectrum and a radial velocity template spectrum. For the template, we used a high-resolution synthetic stellar spectrum with properties similar to that of a G0 dwarf (Coelho et al., 2005). In Figure 4.4, we present stellar spectra and cross-correlation results for two stars in

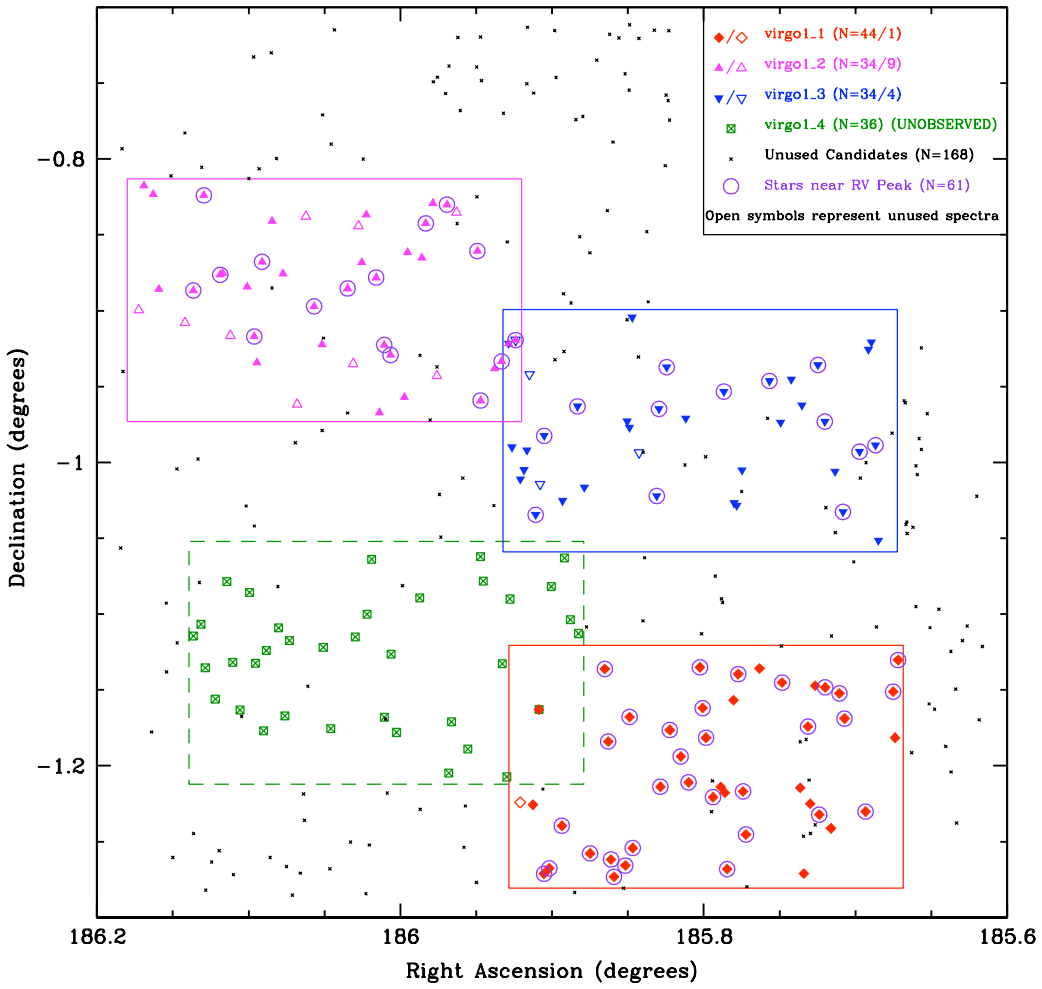

Figure 4.3: Spatial distribution of all of the candidate stars in the Virgo field. Also indicated are the locations of the four masks, the stars with measured radial velocities (both usable—filled symbols and unusable—open symbols), and the stars that ultimately fell near the radial velocity peak (see Section 4.3), broadly taken to be –162 km s^{-1} < $V_{\rm gsr}$ < –26 km s^{-1}.

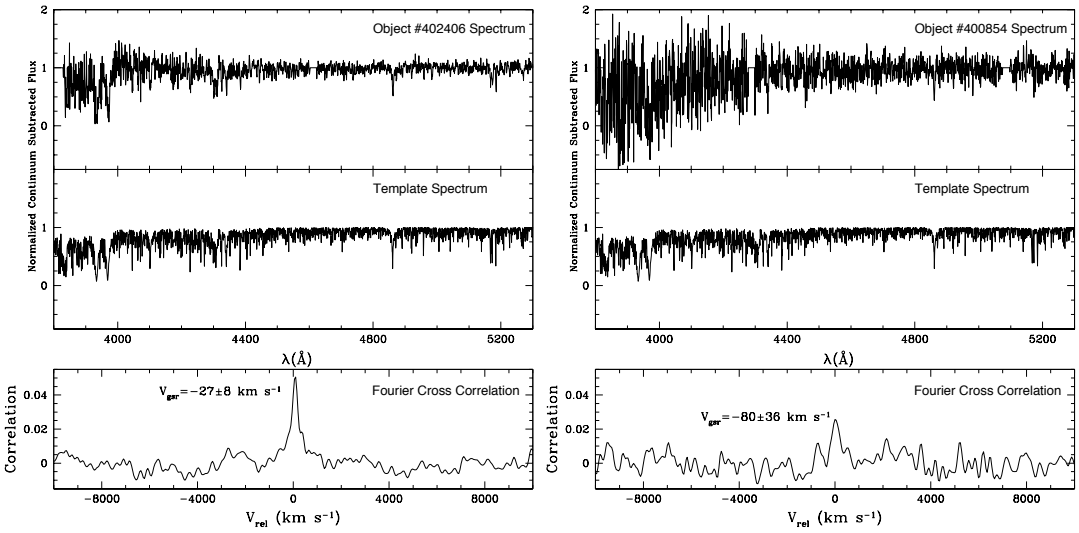

Figure 4.4: Sample IMACS spectra in Virgo. The object spectra (top), the radial velocity template (middle), and the results of their cross-correlations (bottom) for a star of typical brightness (left) and for the faintest star in our Virgo field (right) are all shown. These two stars are designated by the red circles in the Virgo field color–magnitude diagram of Figure 4.1.

our Virgo field (one is of typical brightness, and the other is the faintest in the field, as marked in Figure 4.1).

Of the 126 objects in Virgo on to which we placed slits, only 14 had to be removed from our sample: five were background galaxies, and nine were stellar sources that failed to produce reliable radial velocities when cross-correlated. The contaminating galaxies were identified based on the appearance of their spectra and the object type classification of the SDSS (Abazajian et al., 2009). In the control field, 12 of our 72 spectra were removed from our sample: seven were background galaxies and five were stellar sources that yielded poor quality cross-correlations. The uncertainties in our velocity measurements, σ, were calculated by assuming a functional relationship between it and the Tonry–Davis R value (Tonry & Davis, 1979) as described in Walker et al. (2006). Our measured uncertainties ranged from 4 to 58 km s^{-1}, with a median

value of 17 km s^{-1}. Figure 4.5 shows how our measurement uncertainties vary as a function of g_0 magnitude.

All data are presented in Tables 4.1 and 4.2 for Virgo and the control field, respectively. We report velocities in the Galactic standard of rest frame. This frame of reference is centered on the Sun and at rest with respect to the Galactic center (i.e., the local-standard-of-rest rotation velocity of 220 km s^{-1} and a solar peculiar velocity of (u, v, w) = (–10.00, 5.25, 7.17) km s^{-1} (Dehnen & Binney, 1998) has been removed from the heliocentric radial velocity). Relative to their heliocentric velocities, the Galactic standard of rest radial velocities are ∼96 km s^{-1} lower in the Virgo field and ∼42 km s^{-1} higher in the control field.

4.3 Analysis

The Besançon stellar population synthesis model of the Milky Way galaxy (Robin et al., 2003) is a powerful tool for predicting the properties of various Galactic stellar populations. We used the Besançon model to produce two very large sets of model stars (∼65,000 each) for both the Virgo and control fields. The model stars were restricted to have the same color–magnitude constraints as our spectroscopic candidates. In both of our fields, the model predicted that our generous photometric selection box (Figure 4.1) would allow a significant number of foreground (mostly thick disk) stars to contaminate the upper right corner of the selection region. To more effectively isolate the desired halo stars from the foreground contaminants, we applied a secondary photometric criterion in the form of a diagonal cut through the selection box, as depicted in Figure 4.1. The boundaries for this photometric selec-

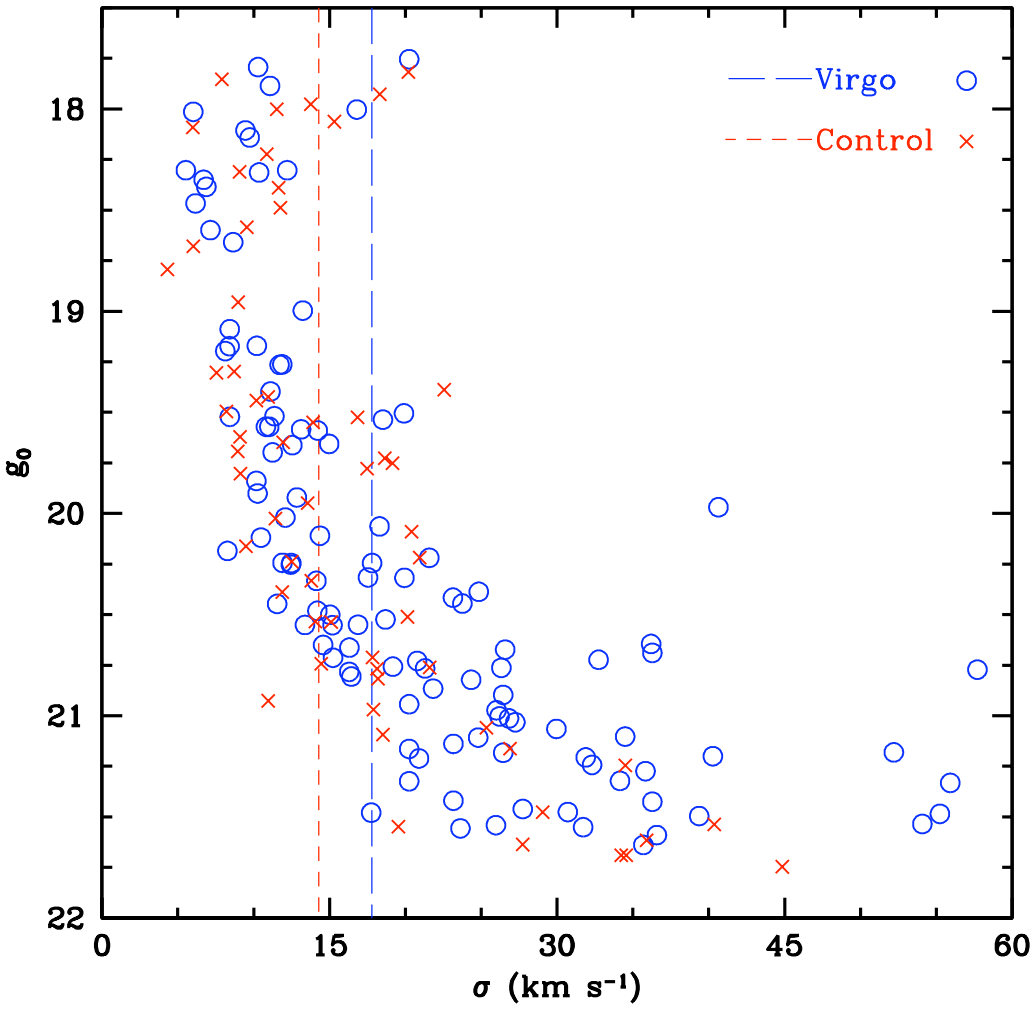

Figure 4.5: Radial velocity uncertainties as a function of g_0 magnitude. Virgo stars (open circles) and control field stars (crosses) are plotted separately. The vertical lines represent the median values of the Virgo (long dash) and control field (short dash) radial velocity uncertainties.

Table 4.1: Virgo Data

ID	Field	g_0	r_0	$\alpha_{J2000.0}$	$\delta_{J2000.0}$	$V_{\rm gsr}$ (km s^{-1})	σ (km s^{-1})	$R_{\rm TD}$
103180	virgo1_1	19.59	19.35	12 23 39.03	–1 13 32.6	4.6	14.2	11.39
103256	virgo1_1	19.54	19.19	12 23 38.07	–1 09 46.6	–276.3	18.5	8.71
103284	virgo1_1	20.48	20.21	12 23 37.27	–1 16 16.3	–88.4	14.2	11.42
103329	virgo1_1	21.07	20.84	12 23 36.43	–1 16 03.3	–96.6	30.0	5.22
103435	virgo1_1	18.35	17.97	12 23 34.45	–1 14 22.2	–62.9	6.7	23.91
103745	virgo1_1	20.90	20.44	12 23 29.98	–1 15 28.0	–70.3	26.5	5.98
103894	virgo1_1	18.01	17.42	12 23 27.64	–1 08 10.1	–48.5	6.0	26.48
103906	virgo1_1	21.18	20.64	12 23 27.12	–1 11 02.4	–83.9	52.2	2.72
103923	virgo1_1	21.11	20.86	12 23 26.66	–1 15 42.2	–76.9	24.8	6.41
103951	virgo1_1	21.48	21.19	12 23 26.20	–1 16 23.6	–88.0	30.7	5.08
104084	virgo1_1	21.46	21.20	12 23 24.41	–1 15 56.8	–86.0	27.7	5.68
104131	virgo1_1	21.16	20.72	12 23 23.74	–1 10 04.0	–93.4	20.2	7.94
104138	virgo1_1	21.24	21.01	12 23 23.24	–1 15 15.1	–79.0	32.3	4.80
104425	virgo1_1	21.42	20.96	12 23 18.87	–1 12 49.6	–109.8	23.2	6.89
104502	virgo1_1	20.55	20.08	12 23 17.37	–1 10 35.0	–103.7	15.2	10.66
104592	virgo1_1	20.32	20.12	12 23 15.64	–1 11 38.0	–109.9	17.5	9.21
104661	virgo1_1	21.18	20.81	12 23 14.41	–1 12 39.2	–52.6	26.5	5.98
200145	virgo1_3	20.42	20.15	12 22 45.49	–0 55 14.4	83.8	23.1	6.90
200203	virgo1_3	20.39	20.13	12 22 45.95	–0 55 31.8	78.5	24.8	6.40
200372	virgo1_3	21.48	20.88	12 22 53.94	–0 56 08.7	–65.1	55.2	2.53
200589	virgo1_3	19.92	19.60	12 22 58.16	–0 56 43.2	62.3	12.9	12.62
200602	virgo1_3	19.57	19.45	12 23 01.61	–0 56 46.7	–62.2	10.8	14.98
200693	virgo1_3	19.90	19.26	12 23 08.82	–0 57 12.0	–38.7	10.3	15.78
200830	virgo1_3	20.72	20.50	12 22 56.47	–0 57 44.7	149.7	32.7	4.73
201001	virgo1_3	21.54	21.28	12 22 52.85	–0 58 23.0	–63.3	54.1	2.60
201005	virgo1_3	20.73	20.40	12 22 59.83	–0 58 25.7	190.0	20.8	7.73
201212	virgo1_3	20.12	19.59	12 22 44.82	–0 59 19.3	–55.9	10.5	15.45
201298	virgo1_3	20.69	20.34	12 22 47.35	–0 59 34.4	–44.9	36.3	4.21
201451	virgo1_3	17.89	17.66	12 23 05.93	–1 00 18.5	145.0	11.1	14.63

Continued on Next Page...

Table 4.1 – Virgo Data (Continued)

ID	Field	g_0	r_0	$\alpha_{J2000.0}$	$\delta_{J2000.0}$	$V_{\rm gsr}$ (km s^{-1})	σ (km s^{-1})	$R_{\rm TD}$
201462	virgo1_3	18.11	17.75	12 22 51.23	–1 00 21.4	113.7	9.5	17.09
201756	virgo1_3	21.03	20.73	12 23 07.20	–1 01 36.6	225.4	27.3	5.79
201769	virgo1_3	21.32	20.98	12 23 06.76	–1 01 42.2	107.0	34.2	4.51
201816	virgo1_3	21.01	20.76	12 22 49.98	–1 01 57.4	–96.8	26.8	5.89
202075	virgo1_3	21.20	20.90	12 22 44.37	–1 03 05.1	151.6	40.3	3.73
203098	virgo1_1	20.06	19.71	12 22 41.26	–1 07 49.1	–95.2	18.3	8.82
203139	virgo1_1	21.54	21.13	12 23 12.59	–1 08 06.3	–71.0	26.0	6.10
203150	virgo1_1	19.20	18.67	12 23 03.17	–1 08 09.3	25.2	8.1	19.82
203230	virgo1_1	21.32	20.96	12 23 06.54	–1 08 22.4	–93.9	20.2	7.94
203310	virgo1_1	18.47	18.16	12 22 59.59	–1 08 42.6	–74.6	6.2	25.85
203331	virgo1_1	17.79	17.52	12 22 54.35	–1 08 50.1	11.0	10.3	15.73
203344	virgo1_1	20.77	20.50	12 22 52.79	–1 08 53.8	–64.3	21.3	7.53
203383	virgo1_1	20.67	20.39	12 22 42.03	–1 09 04.1	–73.7	26.6	5.95
203394	virgo1_1	20.81	20.35	12 22 50.54	–1 09 08.1	–98.7	16.4	9.84
203423	virgo1_1	19.66	19.36	12 23 07.29	–1 09 24.5	238.6	15.0	10.82
203470	virgo1_1	20.94	20.56	12 23 12.17	–1 09 43.1	–82.1	20.2	7.94
203533	virgo1_1	19.26	18.92	12 22 49.73	–1 10 07.9	–58.3	11.9	13.64
203601	virgo1_1	20.50	20.17	12 22 55.50	–1 10 26.8	–77.4	15.0	10.77
203698	virgo1_1	19.97	19.72	12 23 11.64	–1 10 53.3	–95.5	40.6	3.69
203711	virgo1_1	19.17	18.57	12 22 41.71	–1 10 53.4	250.3	8.4	19.17
204550	virgo1_1	19.70	19.40	12 23 09.29	–1 12 50.5	132.5	11.3	14.40
204574	virgo1_1	19.40	19.05	12 22 56.74	–1 12 52.2	109.7	11.1	14.59
204638	virgo1_1	20.25	19.64	12 23 05.77	–1 13 00.7	–143.7	12.5	12.99
204663	virgo1_1	19.84	19.35	12 23 08.64	–1 13 04.2	167.6	10.2	15.90
204750	virgo1_1	20.25	20.00	12 23 10.54	–1 13 14.5	–136.7	17.8	9.07
204883	virgo1_1	18.66	18.33	12 22 55.15	–1 13 29.8	–13.8	8.6	18.66
205028	virgo1_1	20.52	20.10	12 22 46.40	–1 13 48.7	–121.5	18.7	8.63
205060	virgo1_1	20.65	20.30	12 22 53.74	–1 13 56.0	–94.5	14.6	11.12
205161	virgo1_1	18.30	18.02	12 22 51.89	–1 14 28.5	21.5	12.2	13.28
205211	virgo1_1	20.65	20.72	12 23 05.32	–1 14 43.0	–68.2	36.2	4.22

Continued on Next Page...

Table 4.1 – Virgo Data (Continued)

ID	Field	g_0	r_0	$\alpha_{J2000.0}$	$\delta_{J2000.0}$	$V_{\rm gsr}$ (km s^{-1})	σ (km s^{-1})	$R_{\rm TD}$
205467	virgo1_1	20.24	19.91	12 23 08.30	–1 16 05.2	–89.5	11.9	13.63
205501	virgo1_1	19.57	19.10	12 22 56.18	–1 16 15.5	74.8	11.0	14.69
300086	virgo1_2	21.43	21.21	12 24 40.56	–0 49 03.4	22.0	36.3	4.21
300115	virgo1_2	20.78	20.13	12 24 39.08	–0 49 24.1	280.1	16.3	9.93
300133	virgo1_2	21.56	20.94	12 24 38.20	–0 53 08.9	145.2	23.6	6.75
300336	virgo1_2	20.97	20.68	12 24 32.76	–0 53 12.0	–44.3	26.0	6.09
300397	virgo1_2	21.21	20.77	12 24 31.08	–0 49 26.2	–39.1	20.9	7.68
300450	virgo1_2	21.00	20.61	12 24 28.49	–0 52 34.8	–126.5	26.2	6.04
300461	virgo1_2	19.27	19.00	12 24 28.10	–0 52 30.9	–19.7	11.7	13.84
300560	virgo1_2	20.25	19.90	12 24 24.22	–0 53 03.5	44.4	12.4	13.03
300642	virgo1_2	20.32	20.08	12 24 21.88	–0 52 03.8	–160.3	19.9	8.07
300695	virgo1_2	20.82	20.60	12 24 20.28	–0 50 26.9	169.2	24.3	6.54
300744	virgo1_2	20.55	20.10	12 24 18.58	–0 52 32.4	121.5	16.9	9.58
300881	virgo1_2	18.60	18.00	12 24 13.65	–0 53 49.6	–81.2	7.1	22.45
301071	virgo1_2	21.48	20.93	12 24 08.34	–0 53 07.2	–49.4	17.7	9.10
301150	virgo1_2	20.87	20.37	12 24 06.12	–0 52 04.9	149.5	21.8	7.34
301188	virgo1_2	19.09	18.47	12 24 05.37	–0 50 12.1	–0.5	8.4	19.14
301241	virgo1_2	19.66	19.41	12 24 03.82	–0 52 41.3	–145.9	12.6	12.92
301397	virgo1_2	18.00	17.98	12 23 58.84	–0 51 41.5	54.3	16.8	9.63
301474	virgo1_2	20.71	20.26	12 23 56.60	–0 51 54.4	242.2	15.2	10.64
301508	virgo1_2	20.45	20.20	12 23 55.97	–0 50 32.9	–129.3	23.8	6.71
301553	virgo1_2	21.59	21.09	12 23 54.83	–0 49 44.6	201.6	36.6	4.17
301634	virgo1_2	20.02	19.44	12 23 52.63	–0 49 48.3	–45.1	12.1	13.41
301817	virgo1_2	19.00	18.43	12 23 47.82	–0 51 38.5	–129.5	13.2	12.25
400854	virgo1_2	21.64	21.15	12 24 23.11	–0 55 01.1	–80.0	35.7	4.29
400880	virgo1_2	18.14	17.56	12 24 22.70	–0 56 03.1	234.9	9.7	16.60
401312	virgo1_2	20.76	20.31	12 24 12.38	–0 55 20.4	52.0	19.2	8.40
401682	virgo1_2	18.30	17.82	12 24 03.30	–0 58 01.6	41.7	5.5	28.73
401711	virgo1_2	21.14	20.73	12 24 02.55	–0 55 21.3	–51.8	23.2	6.89
401758	virgo1_2	20.55	20.15	12 24 01.55	–0 55 45.2	–162.0	13.4	12.12

Continued on Next Page...

Table 4.1 – Virgo Data (Continued)

ID	Field	g_0	r_0	$\alpha_{J2000.0}$	$\delta_{J2000.0}$	$V_{\rm gsr}$ (km s^{-1})	σ (km s^{-1})	$R_{\rm TD}$
401837	virgo1_2	20.45	20.03	12 23 59.37	–0 57 24.9	131.5	11.6	14.03
402406	virgo1_2	20.18	19.63	12 23 47.31	–0 57 33.1	–26.8	8.3	19.48
402492	virgo1_2	20.11	19.79	12 23 45.08	–0 56 17.3	160.7	14.4	11.28
402529	virgo1_2	19.52	19.04	12 23 43.97	–0 56 00.4	–46.1	11.4	14.25
402582	virgo1_2	17.75	17.51	12 23 42.87	–0 55 17.9	434.1	20.2	7.94
402582	virgo1_3	17.75	17.51	12 23 42.87	–0 55 17.9	418.3	33.4	4.62
402594	virgo1_3	21.50	20.99	12 23 42.33	–0 59 24.0	48.5	39.4	3.83
402645	virgo1_2	20.77	20.61	12 23 41.77	–0 55 09.7	–74.8	57.7	2.39
402667	virgo1_3	21.55	21.08	12 23 41.02	–1 00 39.6	32.9	31.7	4.90
402693	virgo1_3	18.31	17.70	12 23 40.46	–1 00 17.8	109.5	10.4	15.63
402708	virgo1_3	19.58	19.13	12 23 39.97	–0 59 31.5	115.8	13.1	12.35
402749	virgo1_3	20.66	20.17	12 23 38.59	–1 02 04.3	–33.2	16.3	9.92
402812	virgo1_3	21.27	20.82	12 23 37.24	–0 58 57.0	–137.2	35.8	4.27
402925	virgo1_3	19.17	18.68	12 23 34.34	–1 01 31.0	62.1	10.2	15.85
403016	virgo1_3	20.33	19.98	12 23 31.97	–0 57 47.1	–157.1	14.1	11.47
403061	virgo1_3	19.52	19.04	12 23 30.88	–1 00 59.0	110.2	8.4	19.13
403435	virgo1_3	18.38	18.02	12 23 24.11	–0 58 22.7	6.9	6.9	23.29
403465	virgo1_3	19.50	19.27	12 23 23.76	–0 58 37.4	263.9	19.9	8.08
403491	virgo1_3	20.22	19.87	12 23 23.33	–0 54 16.0	8.8	21.6	7.43
403661	virgo1_3	21.33	21.05	12 23 19.43	–1 01 19.6	–129.4	55.9	2.49
403691	virgo1_3	21.10	20.72	12 23 19.07	–0 57 53.0	–28.4	34.5	4.46
403758	virgo1_3	21.21	20.81	12 23 17.86	–0 56 13.9	–43.9	31.9	4.87
403879	virgo1_3	20.76	20.50	12 23 14.84	–0 58 15.9	–4.2	26.3	6.01

Table 4.2: Control Field Data

ID	Field	g_0	r_0	$\alpha_{J2000.0}$	$\delta_{J2000.0}$	$V_{\rm gsr}$ (km s^{-1})	σ (km s^{-1})	$R_{\rm TD}$
11205	vircont1	18.31	18.14	15 14 45.10	9 51 12.5	40.8	9.1	17.83
11223	vircont1	17.82	17.71	15 14 44.44	9 53 43.7	–20.2	20.2	7.96
11303	vircont1	21.75	21.50	15 14 41.93	9 50 42.1	77.1	44.9	3.28
11473	vircont1	20.74	20.54	15 14 36.62	9 52 48.4	–111.8	14.5	11.21
11553	vircont1	18.09	17.64	15 14 34.20	9 51 57.0	–3.0	6.0	26.59
11621	vircont1	20.53	20.28	15 14 31.97	9 51 00.4	–22.0	14.1	11.53
12001	vircont1	21.09	20.67	15 14 21.86	9 52 39.4	–110.7	18.5	8.71
12011	vircont1	21.06	20.74	15 14 21.29	9 50 54.4	84.1	25.4	6.26
12078	vircont1	19.52	19.16	15 14 19.18	9 53 31.7	126.6	16.8	9.60
20276	vircont2	18.68	18.22	15 13 48.39	9 58 52.3	–69.5	6.0	26.43
20288	vircont2	18.39	18.18	15 13 49.38	9 58 38.3	14.7	11.6	13.92
20390	vircont2	17.93	17.80	15 13 36.52	9 56 05.2	–1.9	18.3	8.81
20399	vircont2	21.62	21.25	15 13 18.69	9 55 53.5	–41.9	35.9	4.26
20429	vircont2	19.75	19.60	15 13 24.13	9 55 12.6	–68.8	19.2	8.41
20440	vircont2	21.55	21.14	15 13 45.74	9 54 46.2	53.1	19.5	8.24
20455	vircont2	19.65	19.47	15 13 49.83	9 54 25.4	77.3	11.9	13.59
20465	vircont2	19.69	19.48	15 13 48.99	9 54 15.7	–53.0	8.9	18.04
20504	vircont2	21.64	21.38	15 13 42.31	9 53 15.0	95.4	27.7	5.68
20509	vircont2	18.06	17.84	15 13 14.29	9 53 08.1	–5.9	15.3	10.57
20515	vircont2	19.62	19.20	15 13 49.38	9 53 02.7	22.0	9.1	17.76
20543	vircont2	20.33	19.85	15 13 15.80	9 52 27.4	–122.5	13.8	11.74
20575	vircont2	20.39	19.96	15 13 41.49	9 51 50.1	–34.2	11.9	13.64
20578	vircont2	19.50	19.07	15 13 25.69	9 51 44.1	31.0	8.2	19.65
20613	vircont2	19.78	19.53	15 13 27.81	9 51 06.4	–221.1	17.5	9.24
20626	vircont2	20.71	20.25	15 13 28.05	9 50 41.8	–54.1	17.8	9.05
20638	vircont2	19.95	19.64	15 13 15.72	9 50 31.2	–150.0	13.6	11.95
20667	vircont2	19.42	19.07	15 13 44.28	9 49 52.6	–162.0	11.0	14.79
20673	vircont2	19.73	19.59	15 13 31.80	9 49 47.4	–185.7	18.6	8.65
20699	vircont2	18.22	18.02	15 13 30.25	9 49 23.9	–152.6	10.9	14.92
20719	vircont2	20.97	20.78	15 13 49.11	9 48 57.9	25.7	17.9	9.02

Continued on Next Page...

Table 4.2 – Control Field Data (Continued)

ID	Field	g_0	r_0	$\alpha_{J2000.0}$	$\delta_{J2000.0}$	$V_{\rm gsr}$ (km s^{-1})	σ (km s^{-1})	$R_{\rm TD}$
20729	vircont2	21.25	20.95	15 13 14.68	9 48 47.0	208.1	34.5	4.46
20747	vircont2	20.22	20.08	15 13 36.88	9 48 33.6	89.7	21.0	7.66
20778	vircont2	17.85	17.39	15 13 17.83	9 48 05.8	–44.1	7.9	20.39
20790	vircont2	20.51	20.33	15 13 22.03	9 47 47.7	–55.4	20.1	7.99
20804	vircont2	20.93	20.42	15 13 42.78	9 47 36.4	97.3	11.0	14.77
20824	vircont2	19.80	19.36	15 13 43.45	9 47 11.2	97.0	9.1	17.68
20883	vircont2	21.69	21.43	15 13 23.34	9 45 48.8	–137.5	34.6	4.45
20886	vircont2	20.82	20.50	15 13 21.46	9 45 37.4	223.5	18.2	8.87
20904	vircont2	20.03	19.68	15 13 21.79	9 45 14.8	–155.9	11.4	14.19
20921	vircont2	20.77	20.49	15 13 45.83	9 44 47.9	–50.9	18.1	8.90
20944	vircont2	20.76	20.49	15 13 30.17	9 44 12.5	–164.0	21.6	7.42
40504	vircont1	21.69	21.38	15 14 46.30	9 59 20.8	115.0	34.2	4.50
40514	vircont1	20.24	19.73	15 14 45.76	10 03 22.8	–46.5	12.5	12.95
40598	vircont1	20.09	19.72	15 14 38.70	9 58 22.4	–37.1	20.4	7.88
40601	vircont1	18.00	17.75	15 14 38.84	10 04 22.2	120.4	11.5	14.06
40644	vircont1	21.54	21.12	15 14 36.55	10 04 56.6	–138.6	40.4	3.72
40651	vircont1	18.59	18.21	15 14 36.26	10 03 49.5	–32.1	9.6	16.92
40692	vircont1	21.48	21.09	15 14 32.64	10 03 16.1	20.6	29.1	5.40
40721	vircont1	20.16	20.25	15 14 30.66	10 02 44.0	–123.6	9.5	17.06
40749	vircont1	19.44	19.12	15 14 29.22	10 00 11.2	–128.7	10.2	15.89
40755	vircont1	19.30	18.90	15 14 29.31	10 04 40.5	178.8	8.7	18.51
40759	vircont1	18.96	18.67	15 14 28.60	10 02 29.1	–281.3	9.0	17.96
40772	vircont1	21.16	20.84	15 14 27.22	10 03 29.5	148.9	26.9	5.87
40790	vircont1	18.49	18.25	15 14 25.43	10 02 12.3	–131.4	11.8	13.79
40839	vircont1	20.54	20.13	15 14 21.55	10 01 06.6	–53.9	15.1	10.73
40841	vircont1	17.98	17.74	15 14 21.39	10 00 45.1	–39.3	13.8	11.78
40860	vircont1	19.55	19.25	15 14 20.21	9 58 06.9	64.3	13.9	11.64
40885	vircont1	19.39	19.07	15 14 18.63	9 56 45.3	–11.1	22.6	7.09
40934	vircont1	18.79	18.33	15 14 15.80	10 01 57.2	–76.6	4.3	36.40
40960	vircont1	19.30	18.94	15 14 13.38	10 03 03.1	–12.9	7.5	21.29

tion region are consistent with the findings of Jurić et al. (2008, see their Figure 37, lower left panel) and Newberg et al. (2002, see their Figure 11). As expected, once separated, the velocity distributions of the model stars from above and below the diagonal cuts can be described remarkably well by Gaussian profiles.

We present the Galactic standard of rest radial velocity distributions in the Virgo field in Figure 4.6 and the control field in Figure 4.7. In these histograms, each individual star is plotted as a normalized Gaussian centered at the measured velocity and with a standard deviation equal to the measurement uncertainty (see Tables 4.1 and 4.2). The resulting distribution is then the sum total of these individual Gaussians. In comparison with standard histograms, plots of this nature have several advantages. Their appearances are independent of both bin size and of the locations of bin boundaries, and they appropriately take into account the individual measurement uncertainties. We also plot the velocity distributions of the nearest stars from the SDSS (Abazajian et al., 2009) in each field. To get an equal number of SDSS stars as in our data set, we chose all SDSS stars with kinematic information located within $\sim 105'$ of the center of the Virgo field, and within $\sim 98'$ of the center of the control field. We also plot the theoretical velocity distributions as predicted by the Besançon model. The top three panels in Figures 4.6 and 4.7 show these distributions for (A) all of the stars, (B) the stars below the diagonal photometric cut (Figure 4.1), and (C) the stars above the diagonal photometric cut. In the control field (Figure 4.7), the Besançon model's distribution has been scaled to represent the same number of stars as in our data set, 60/45/15 for A/B/C. However, in the Virgo field, since there is an apparent

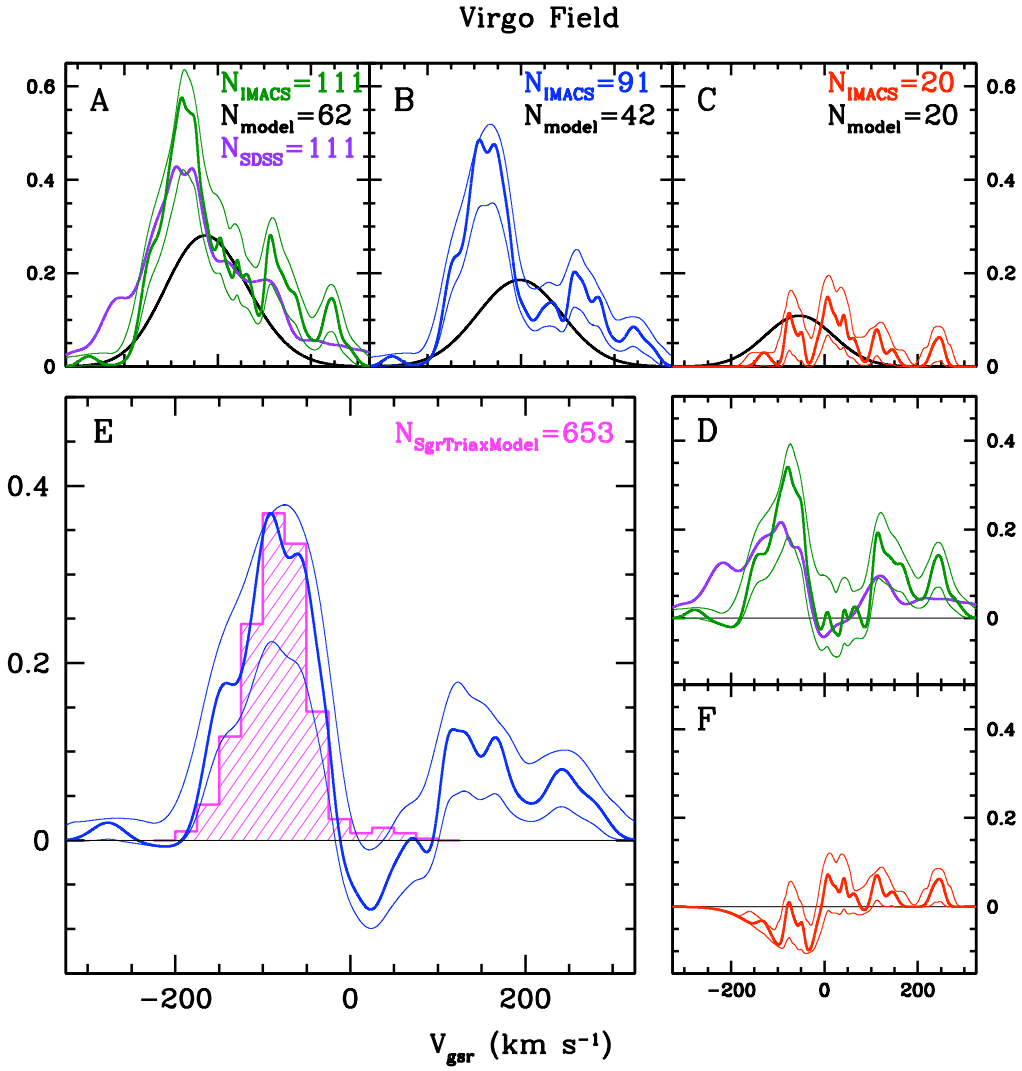

Figure 4.6: Radial velocity distributions of various Virgo samples. (A) Galactic standard of rest radial velocity distributions for all Virgo stars (green), SDSS stars (purple), and the Besançon model (black). (B) Velocity distribution for Virgo stars below the diagonal photometric cut (blue), and the Besançon model stars that satisfy the same photometric criteria (black). (C) Velocity distribution for Virgo stars above the diagonal photometric cut (red), and the Besançon model stars that satisfy the same photometric criteria (black). (D, E, and F) The results of subtracting the Besançon models from the corresponding distributions in (A), (B), and (C), respectively. Panel (E) also displays a scaled-down histogram of the 653 Law & Majewski (2010) Sgr model stars within 10° of our field (magenta). In panels (A) and (B), the model has not been scaled to the same number of stars as in the associated data sets (see the text for details). All panels include 95% confidence bounds (thin lines) on the Virgo distributions. The number of stars (N) in each distribution in panels (A), (B), (C), and (E) is indicated.

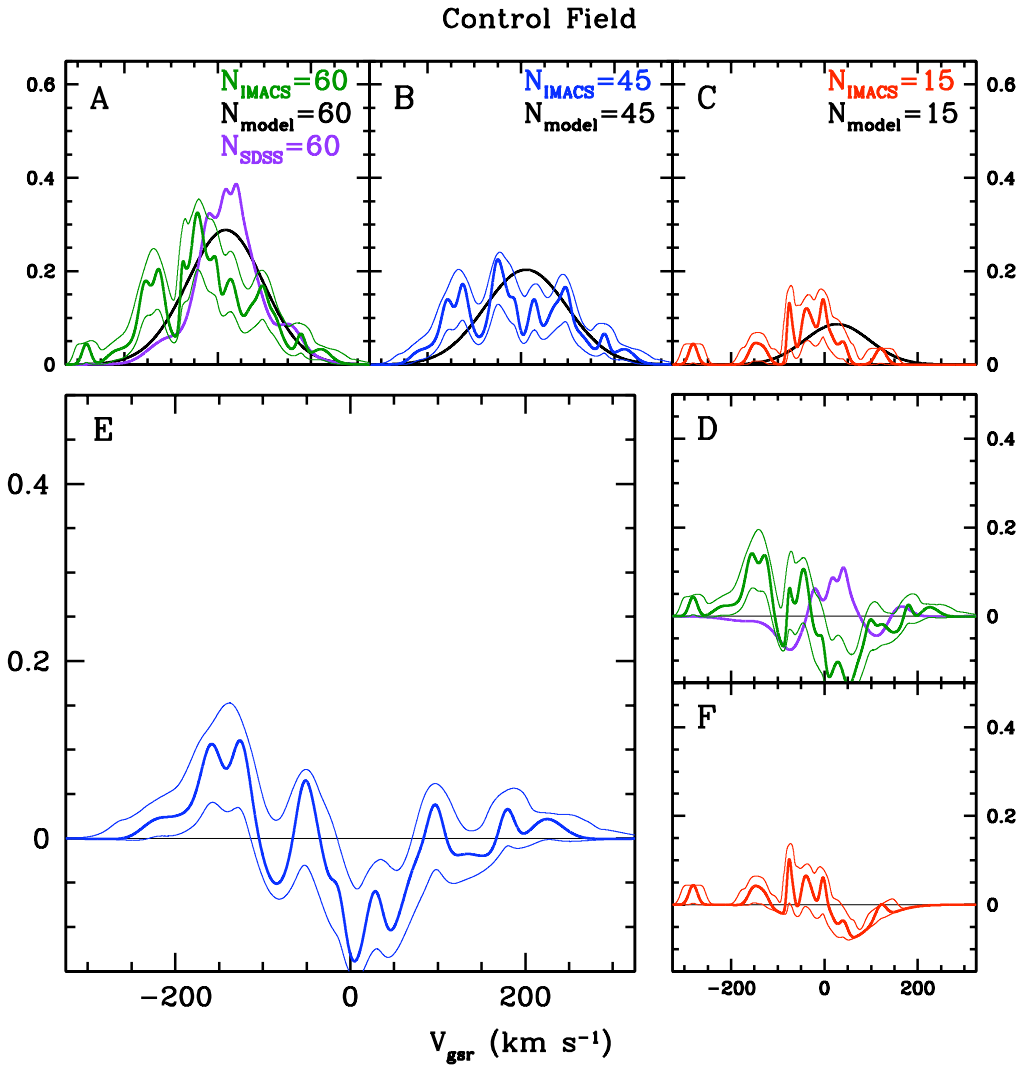

Figure 4.7: Radial velocity distributions of various control field samples. (A) Galactic standard of rest radial velocity distributions for all control field stars (green), SDSS stars (purple), and the Besançon model (black). (B) Velocity distribution for control field stars below the diagonal photometric cut (blue), and the Besançon model stars that satisfy the same photometric criteria (black). (C) Velocity distribution for control field stars above the diagonal photometric cut (red), and the Besançon model stars that satisfy the same photometric criteria (black). (D, E, and F) The results of subtracting the Besançon models from the corresponding distributions in (A), (B), and (C), respectively. All panels include 95% confidence bounds (thin lines) on the control field distributions. The number of stars (N) in each distribution in panels (A), (B), and (C) is indicated.

kinematic excess with negative velocities, we scaled the Besançon model's distribution in Figure 4.6(B) using a least-squares fit to best match the data in the region $V_{\rm gsr} > 0$. In Figure 4.6(C), the model is scaled to the same number of stars as the data (20), and in Figure 4.6(A) the model is the sum of the models from Figures 4.6(B) and (C). The lower panels of Figures 4.6 and 4.7 show the results of subtracting the Besançon models from the corresponding velocity distributions. In Figure 4.6(E), we also compare our data to the recent model of Sgr destruction in a triaxial Galactic halo by Law & Majewski (2010). We include all Sgr model stars within 10° of our field ($N = 653$), and scale the histogram so that its peak height matches that of our data. In all panels of Figures 4.6 and 4.7, we include 95% confidence bounds on our data, which were estimated via Monte Carlo simulations with 100,000 trials each. Each trial ultimately generated a new velocity distribution curve by providing a random offset to each star's measured velocity in such a way that, over all of the trials, the 100,000 offsets for any given star had a Gaussian distribution with a mean value of zero and a standard deviation equal to the star's velocity uncertainty.

We applied the Kolmogorov–Smirnov (K-S) test to the distributions shown in Figures 4.6(A) and (B), and provide the results in Table 4.3. The K-S test results suggest that while the IMACS and SDSS distributions are more likely to have been drawn from the same parent distribution, they were not drawn from the same parent distribution as the model.

Ten of the stars in our kinematic data set also have velocity measurements in the SDSS (though, unfortunately, none of the stars in the control field have SDSS

Table 4.3: K-S Test Probabilities

Figure	Distributions	Probability
4.6(A)	IMACS-SDSS	0.06066
4.6(A)	IMACS-Model	0.01554
4.6(A)	SDSS-Model	0.00072
4.6(B)	IMACS-Model	0.00008

velocities). In Figure 4.8, we demonstrate the reliability of our velocity measurements by plotting the differences between our measured velocities ($V_{\rm IMACS}$) and the SDSS's velocities ($V_{\rm SDSS}$). We find a mean offset of 15.2 km s^{-1}, and just 7.6 km s^{-1} if the faintest star is excluded.

4.4 Discussion

The principal result of this study in summarized in Figure 4.6(E) which shows a highly significant peak in the radial velocity distribution at $V_{\rm gsr} \sim$ –75 km s^{-1}. This kinematic excess cannot be explained by a smooth halo distribution model. In a control field located on the opposite side of the Sgr debris plane we find no significant peaks in the radial velocity distribution (Figure 4.7), and we show that it is consistent with a smooth halo population. In Figures 4.6 and 4.7, we also show the radial velocity distributions of the nearest SDSS stars with radial velocity measurements. We find the SDSS velocity distributions to match that of our data. It is difficult to accurately measure the velocity dispersion of this feature due to significant measurement uncertainty and the fact that its membership is not well defined due to contamination by non-members in the field (an effect which is expected to occur preferentially closer to $V_{\rm gsr} = 0$). If we first consider a very inclusive requirement for membership (beneath

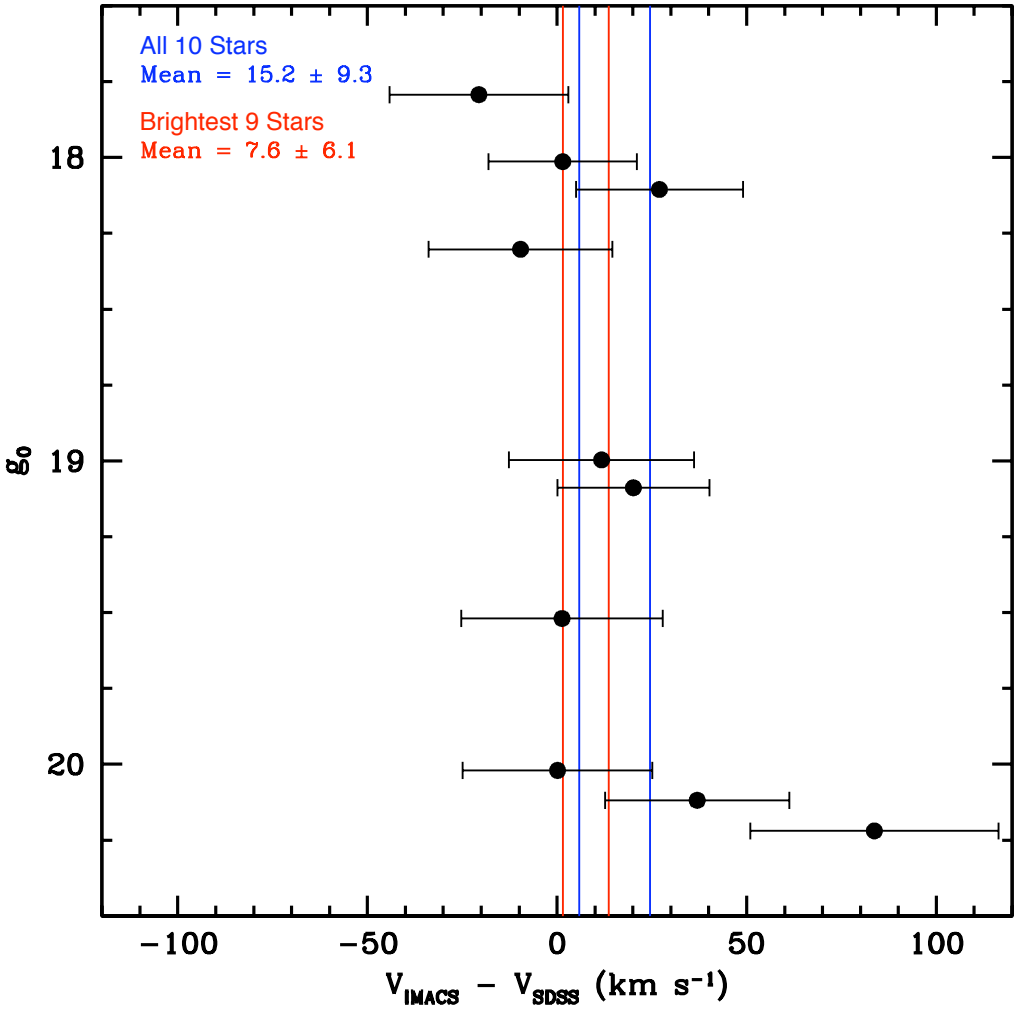

Figure 4.8: Comparison to SDSS radial velocities. The plotted points represent the differences between our measured velocities ($V_{\rm IMACS}$) and SDSS's velocities ($V_{\rm SDSS}$) for the 10 stars in both data sets. They are plotted against their g_0 magnitudes. The error bars represent the sum in quadrature of the uncertainties in the individual velocity measurements. We find a mean offset of $\langle V_{\rm IMACS} - V_{\rm SDSS} \rangle = 15.2$ km s^{-1}, and 7.6 km s^{-1} if the faintest star in excluded. The vertical lines are placed one standard deviation above and below the mean offsets.

Table 4.4: Comparison of Virgo Data and the Triaxial Halo Model

Sample	$N_{\rm stars}$	$\langle V_{\rm gsr} \rangle$ (km s^{-1})	$\sigma_{\rm v}$ (km s^{-1})	D (kpc)
Sgr model (*L1*[a])	569	–81	33	46
Sgr model (*L2*[b])	63	–116	36	9
Virgo data (inclusive[c])	49	–75	27	···
Sgr model (inclusive[c])	555	–80	24	···
Virgo data (exclusive[d])	40	–76	20	···
Sgr model (exclusive[d])	466	–77	19	···

Note: The Sgr model utilized is the triaxial halo model of Law & Majewski (2010)
[a] The *L1* stream lies 0°–360° from the dwarf in the leading direction
[b] The *L2* stream lies 360°–720° from the dwarf in the leading direction
[c] Applied the radial velocity criteria: –130 km s^{-1} $< V_{\rm gsr} <$ –25 km s^{-1}
[d] Applied the radial velocity criteria: –110 km s^{-1} $< V_{\rm gsr} <$ –40 km s^{-1}

our diagonal photometric cut and satisfying –130 km s^{-1} $< V_{\rm gsr} <$ –25 km s^{-1}) there are 49 stars with a mean velocity of $\langle V_{\rm gsr} \rangle$ = –75 km s^{-1} and an observed velocity dispersion of $\sigma_{\rm v}$ = 27 km s^{-1}. The true velocity dispersion is likely less than the measured value, which has been inflated by the somewhat large measurement uncertainties. A more exclusive requirement for membership (beneath our diagonal photometric cut and satisfying –110 km s^{-1} $< V_{\rm gsr} <$ –40 km s^{-1}) produces 40 stars with a mean velocity of $\langle V_{\rm gsr} \rangle$ = –76 km s^{-1} and an observed velocity dispersion of just $\sigma_{\rm v}$ = 20 km s^{-1}. These numbers are summarized in Table 4.4.

As mentioned in Section 4.1, other spectroscopic studies in Virgo have found low significance velocity peaks at $V_{\rm gsr} \sim$ –75 km s^{-1} (Duffau et al., 2006; NYC07). However, the most prominent radial velocity peaks in those studies were in the range of 100–130 km s^{-1}, which those authors associated with the VSS and S297+63–20.5, respectively. In Figure 4.6(E), there does appear to be a very mild excess of stars in this velocity range, however it is of rather low significance in our data

set. If we consider only stars beneath our diagonal photometric cut that also satisfy 105 km s^{-1} $< V_{\rm gsr} <$ 170 km s^{-1} we find 14 stars that have a mean velocity of $\langle V_{\rm gsr} \rangle$ = 137 km s^{-1} and an observed velocity dispersion of $\sigma_{\rm v}$ = 22 km s^{-1}. We may in fact be seeing the same feature as the previous studies, but it certainly does not dominate our sample as it does theirs. This is most likely due to the greater depth of our data, but our limited areal coverage may also be a contributing factor.

The key difference between the spectroscopic study of main-sequence stars in Virgo presented here and in the NYC07 study is that we have gone ∼1.3 mag fainter. The median magnitude in our Virgo field, $g_0 = 20.5$, is equal to the faint limit in their SDSS+SEGUE data set. In Figure 4.9, we divide our full sample of 111 stars in half to create a bright subsample ($g_0 < 20.5$) and a faint subsample ($g_0 > 20.5$). The velocity distributions of the bright and faint subsamples are plotted along with the expected distribution for a smooth halo population. In the faint subsample, the negative velocity peak is once again prominent at $\langle V_{\rm gsr} \rangle$ = –77 km s^{-1} ($\sigma_{\rm v}$ = 25 km s^{-1}), the positive velocity peak is barely present at $\langle V_{\rm gsr} \rangle$ = 137 km s^{-1} ($\sigma_{\rm v}$ = 19 km s^{-1}), and there appears to be very little contamination by foreground or smooth halo stars. The bright subsample appears to be consistent with the model of the smooth halo distribution, with just the hint of a kinematic excess at $V_{\rm gsr} \sim$ 115 km s^{-1}. This suggests that the NYC07 study did not go faint enough to sample many of the stars in the negative velocity peak, which likely lie beyond the ∼18 kpc limit of their spectroscopic data set.

When working with main-sequence stars, one of the tradeoffs made in exchange for

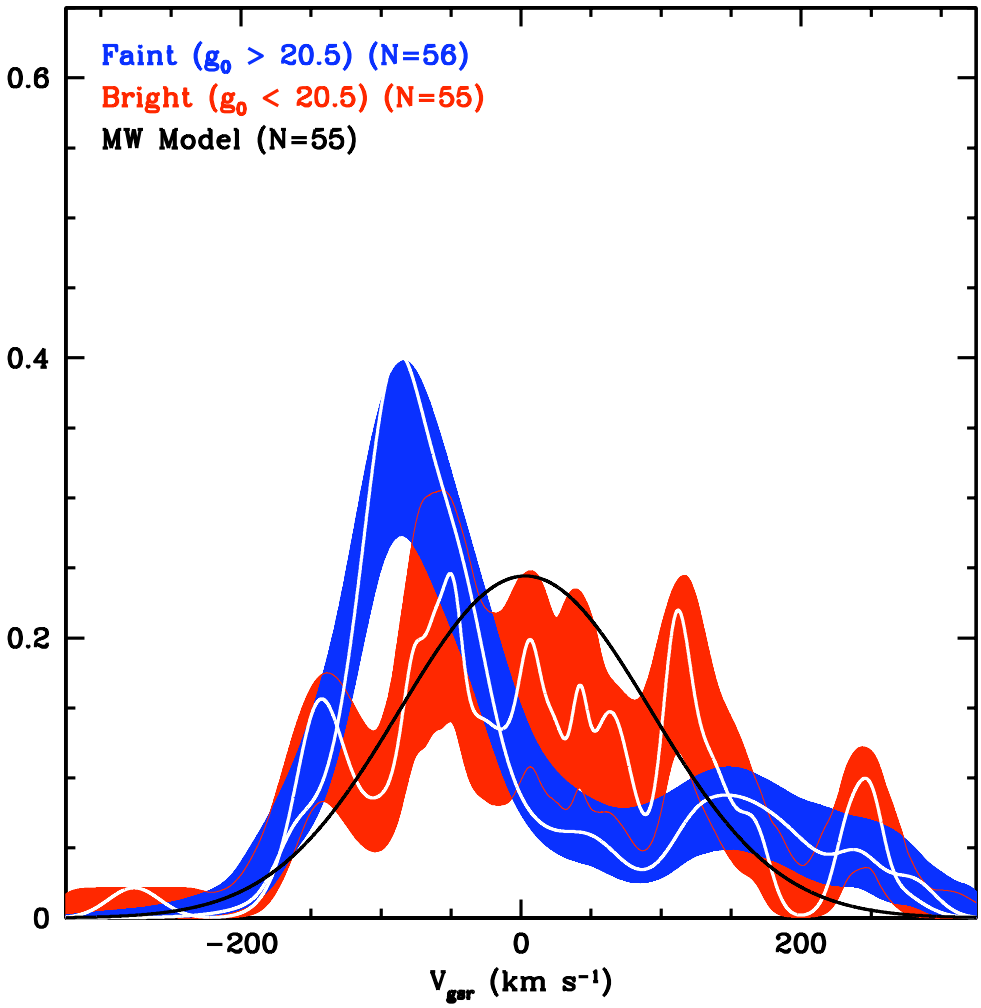

Figure 4.9: Radial velocity distributions by brightness. The Galactic standard of rest radial velocity distributions with 95% confidence bounds are shown for our 56 brightest (red) and 55 faintest (blue) targets. The Besançon model (black) of the Milky Way is also shown.

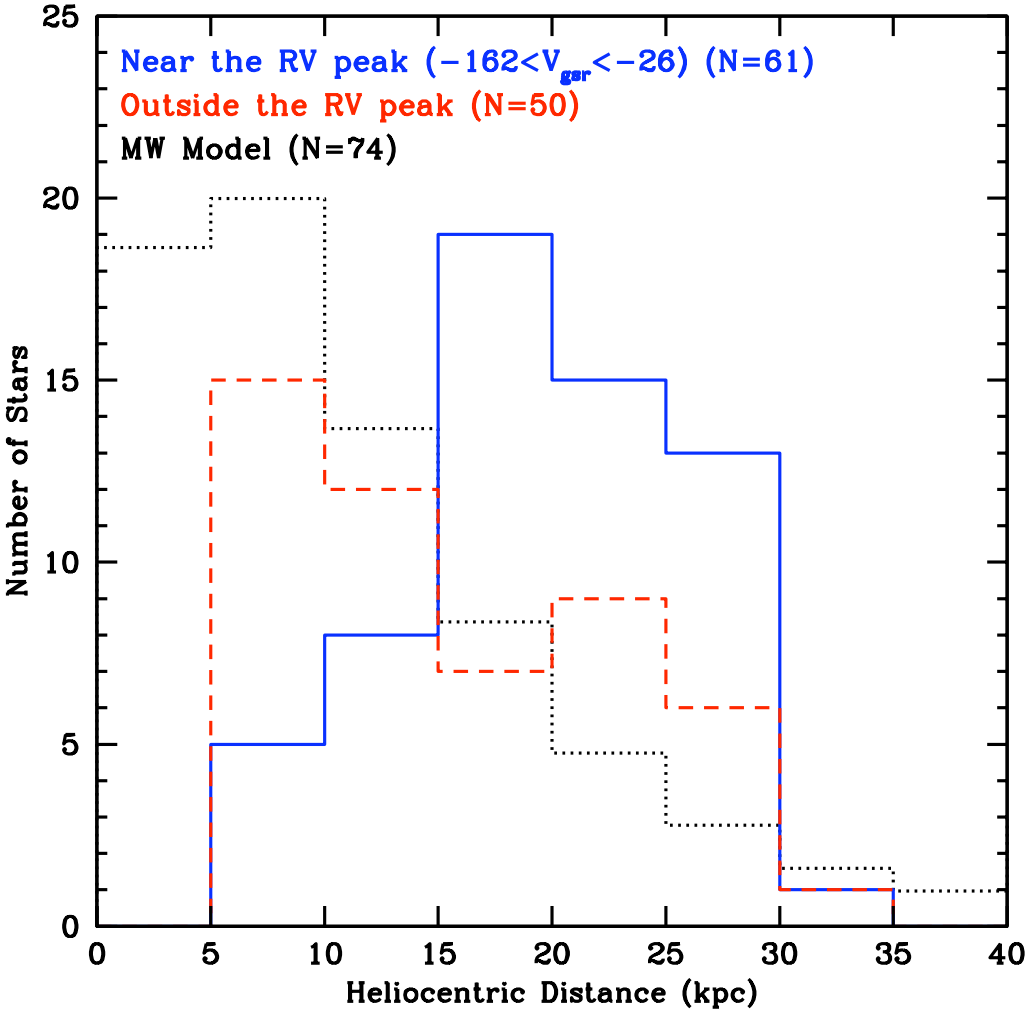

Figure 4.10: Distance histograms of Virgo stars. Histograms of the estimated heliocentric distances for the 61 targets near the kinematic excess region, and the 50 targets that are not are both presented. The prediction from the Besançon model is also shown. The model has been scaled to match the combined height of the target stars in the 5–10 kpc bin.

their relatively high numbers is the inherent difficulty in accurately determining their distances. Under the assumption that most of our sample is comprised of turnoff stars, we adopt the Newberg et al. (2002) value (see also NYC07; Yanny et al., 2009) for their typical absolute magnitude ($M_{g_0} = 4.2$), and use it to estimate the distances to the stars in our data set. In Figure 4.10, we present heliocentric distance histograms for stars that have velocities near the center of the negative velocity peak, stars that are not near that peak, and the predictions from the Besançon model of the Milky Way. The stars outside of the primary kinematic feature show the expected falloff in number with increasing distance. However, a very different distribution is found for stars near the peak velocity. Many more stars than expected appear in the bins ranging from 15 to 30 kpc. Although the number of stars in each of these three bins decreases with increasing distance, note that the model, which estimates the number of contaminating stars, also decreases with increasing distance at about the same rate. Therefore, the excess of stars above the model (i.e., the number of stars that can be attributed to the kinematic feature) is nearly constant ($\sim$10 stars) across these three bins. Since we only acquired spectra for stars in Virgo out to a distance of $\sim$31 kpc we cannot be certain how far out into the halo this feature extends. However, this suggests that the kinematic feature identified here lies beyond the previously identified substructures in Virgo, which are mostly within 20 kpc of the Sun (the lone exceptions being the VES of Keller, 2010, and Virgo Z of Walsh et al., 2009).

Given the proximity of our Virgo field to the Sgr orbital plane,[1] and the afore-

[1]In the Sgr coordinate system (Majewski et al., 2003), our Virgo field has a longitude and latitude

mentioned models that predict Sgr leading tidal tail debris in Virgo, it is tempting to see if the kinematic feature seen in our data is consistent with existing velocity measurements of Sgr. Two surveys have been done that trace the kinematics of the leading stream of Sgr: the 2MASS M-giant survey (Law et al., 2005; Chou et al., 2007), and the more recent SDSS+SEGUE survey of BHBs and K/M-giants (Yanny et al., 2009). Both studies found the velocity of Sgr debris in the leading stream at our Sgr longitude ($\Lambda_\odot \sim 263^\circ$) to be $V_{\rm gsr} \sim -75$ km s^{-1}. Both studies also show a large velocity dispersion along the leading stream, especially when compared with the dispersion along the trailing stream (Majewski et al., 2004). This matches extremely well with the prominent peak we observed at $V_{\rm gsr} = -75$ km s^{-1}. Distance estimates in this work and the larger surveys are fairly consistent given the substantial uncertainties inherent in the photometric parallax technique (especially when applied to main-sequence stars, as in the present study). In addition, the stars comprising our velocity peak have apparent magnitudes that are in agreement with the expected turnoff magnitude ($g_0 \sim 21.5$) for Sgr debris in the area (NYC07). Based on the similarities to known detections of Sgr, we conclude that the prominent kinematic feature we observed at $V_{\rm gsr} \sim -75$ km s^{-1} is likely due to the leading tidal tail of Sgr.

Early models of the destruction of Sgr, which assumed an axisymmetric Galactic halo potential, have shown that this velocity, and the leading stream velocity trends seen in the 2MASS and SDSS+SEGUE surveys, can only be produced by a prolate shaped dark matter halo (Helmi, 2004b; Law et al., 2005). This result, in agreement

of $(\Lambda, B)_\odot = (263\overset{\circ}{.}2, -14\overset{\circ}{.}6)$. This Sgr latitude corresponds to a height of ∼5 kpc above the Sgr plane at a distance of 20 kpc.

with previous studies (NYC07; Seabroke et al., 2008; Yanny et al., 2009), contradicts the proposed explanation of the stellar overdensities in Virgo as being due to the leading tidal tail of Sgr as it descends down from the northern Galactic hemisphere on to and through the solar neighborhood, which requires an oblate halo and predicts highly negative ($V_{\rm gsr} \lesssim$ –200 km s^{-1}) radial velocities (Martínez-Delgado et al., 2007). Alternatively, data presented in NYC07 and Yanny et al. (2009) show the leading arm of the Sgr stream arcing over the position of the Sun, and eventually falling down to the Galactic plane at least 15 kpc outside of the solar circle.

The recently published model for the destruction of Sgr in a triaxial Galactic halo (Law & Majewski, 2010) does an excellent job of reproducing this and other observational constraints on the Sgr steam. In Figure 4.6(E), we compare the observed radial velocity distribution in our Virgo field with the predictions of this model. We chose all model stars within 10° of our field. There are 653 model stars in total, most of which (87%) lie along the *L1* stream (0°–360° from the dwarf in the leading direction). In addition, 10% of the model stars lie along the *L2* stream (360°–720° from the dwarf in the leading direction), and the remaining 3% lie along the *L3* or trailing streams (*T1* and *T2*). Model stars from the *L1* stream have a mean velocity, velocity dispersion, and median distance of ($\langle V_{\rm gsr} \rangle$, $\sigma_{\rm v}$, D) = (–81 km s^{-1}, 33 km s^{-1}, 46 kpc). These same values for the less prominent *L2* stream are (–116 km s^{-1}, 36 km s^{-1}, 9 kpc). If we consider all model stars satisfying the "inclusive" velocity requirement for membership in our observed radial velocity peak (defined at the beginning of this section as –130 km s^{-1} $< V_{\rm gsr} <$ –25 km s^{-1}), we find that they have a mean

velocity and velocity dispersion of ($\langle V_{\rm gsr} \rangle$, $\sigma_{\rm v}$) = (–80 km s^{-1}, 24 km s^{-1}). Using the more "exclusive" requirement for membership (defined earlier as –110 km s^{-1} < $V_{\rm gsr}$ < –40 km s^{-1}), these values are (–77 km s^{-1}, 19 km s^{-1}). Both pairs of results agree remarkably well with the findings in our kinematic data set as seen in Figure 4.6(E). These numbers are summarized, along with our empirical results, in Table 4.4. Even the slight asymmetry in the shape of the radial velocity peak predicted by the model (due to the small contribution of *L2* stars with slightly more negative radial velocities) is seen in our data, indicating a detection of the second wrap of the leading stream. However, our highly uncertain distance estimates and the distance to the *L1* stream as predicted by the model are somewhat discrepant, and remain an issue to be reconciled.

Overall, the agreement between our observations and the predictions of the triaxial model is quite striking, and represents another success for the model, and further evidence supporting our interpretation of these stars as debris from the leading tidal tail of Sgr, which we find to make a significant contribution to the stellar overdensity in Virgo. Despite the remarkable similarities to the models and previous detections of Sgr, at this point we can not entirely rule out the possibility that we have detected the kinematic signature of a new or previously discovered substructure in Virgo which conspires to have similar characteristics to those of Sgr. Clearly, much more spectroscopic work needs to be done throughout Virgo in order to determine the true multicomponent nature of its stellar content.

CHAPTER 5

Velocities Along the Sgr Stream

5.1 Velocity Distribution Profiles

The 39 Sgr fields observed in this study contain the radial velocity measurements of anywhere from six (fields 198.4n10.9 and 255.1p03.1) to 372 (field 000.1n01.5) unique stars. In this section we present the Galactic standard of rest radial velocity distributions for each of these fields. Throughout this Chapter, all references to radial velocity measurements, be they in the text, tables, or figures, are taken with the respect to the Galactic standard of rest frame. For brevity, we therefore drop the "gsr" subscript, and refer to the Galactic standard of rest radial velocity as simply V henceforth.

We construct the velocity distribution, $D_i(V)$, in a given field, i, containing N_i stars, by plotting each individual star, j, as a normalized Gaussian centered at its measured velocity, V_{ij}, and with a standard deviation equal to the object's measurement uncertainty $\sigma_{V_{ij}}$. The resulting velocity distribution is then the sum total of each of the individual Gaussians, and can be expressed as:

$$D_i(V) = \sum_{j=0}^{N_i} \frac{1}{\sqrt{2\pi}\sigma_{V_{ij}}} e^{-\frac{(V-V_{ij})^2}{2\sigma^2_{V_{ij}}}}. \tag{5.1}$$

The radial velocity measurements and their corresponding measurement uncertainties for every object in every field are listed in the field tables (Tables 3.10 to 3.47) at the end of Chapter 3.

Generating continuous velocity distributions for each field in this way offers several significant advantages over the more traditional, discrete, histograms. First, the appearance of the velocity distributions when plotted are independent of an individual's choice for the bin size and the locations of the bin boundaries. Second, traditional histograms do not take in to account each object's measurement uncertainty. For data sets like the one presented in this study, for which the individual measurement uncertainties span a very wide range, it is important that the measurement uncertainties be properly accounted for in order to provide an accurate graphical representation of the velocity distribution.

After all of the velocity distributions were generated, the individual measurement uncertainties were again utilized to determine 95% confidence bounds for each distribution. The confidence bounds for each field were estimated via Monte Carlo simulation with 25,000 trials. Each trial ultimately generated a new velocity distribution curve by providing a random offset to each star's measured velocity in such a way that, over all of the trials, the 25,000 offsets for any given star had a Gaussian distribution with a mean value of zero and a standard deviation equal to the star's velocity uncertainty. Then, at each position along the velocity axis, the upper and lower limits of the 95% confidence bounds were defined so as to exclude the highest and lowest 2.5% of the trials.

The two spectrographs used to measure stelar velocities, IMACS and Hectospec, had markedly different measurement uncertainties, as discussed in Section 3.3.1, and depicted graphically in Figures 3.21, 3.22, 3.36, and 3.37. Specifically, the Hectospec data, though smaller, with only five fields, had velocity measurement uncertainties that were uniformly superior to those of IMACS. Figure 5.1 illustrates how this consequential difference manifests itself graphically in the velocity distributions calculated with Equation 5.1. The Gaussian velocity distribution profiles are shown for six hypothetical stars from both the IMACS and Hectospec data sets. These particular six stars were chosen because they span the full range of velocity measurement uncertainties, σ_V, for each data set, ranging from the minimum to the maximum values, with four in-between at each quintile. The 95% confidence bounds around each star's distribution are also shown in the expanded view panels. Figure 5.1 illustrates the differing contributions made by individual stars, due to their varying velocity uncertainties, to a field's aggregated velocity distribution profile.

In addition to detailing the range of individual stellar Gaussian velocity distribution profiles for each of the two spectrographs utilized, Figure 5.1 also highlights just how superior the velocity measurements from the Hectospec data set were compared to the those from the IMACS data set. Given the relatively tall, narrow Gaussian profiles of the majority of the Hectospec stars, the resulting aggregated velocity distribution profiles for the Hectospec fields, $D_{\mathrm{Hecto}}(V)$, are, not surprisingly, observed to contain many fluctuations, resulting in numerous local maxima and minima. The velocity distribution for the five Hectospec fields are presented in Figure 5.2. In

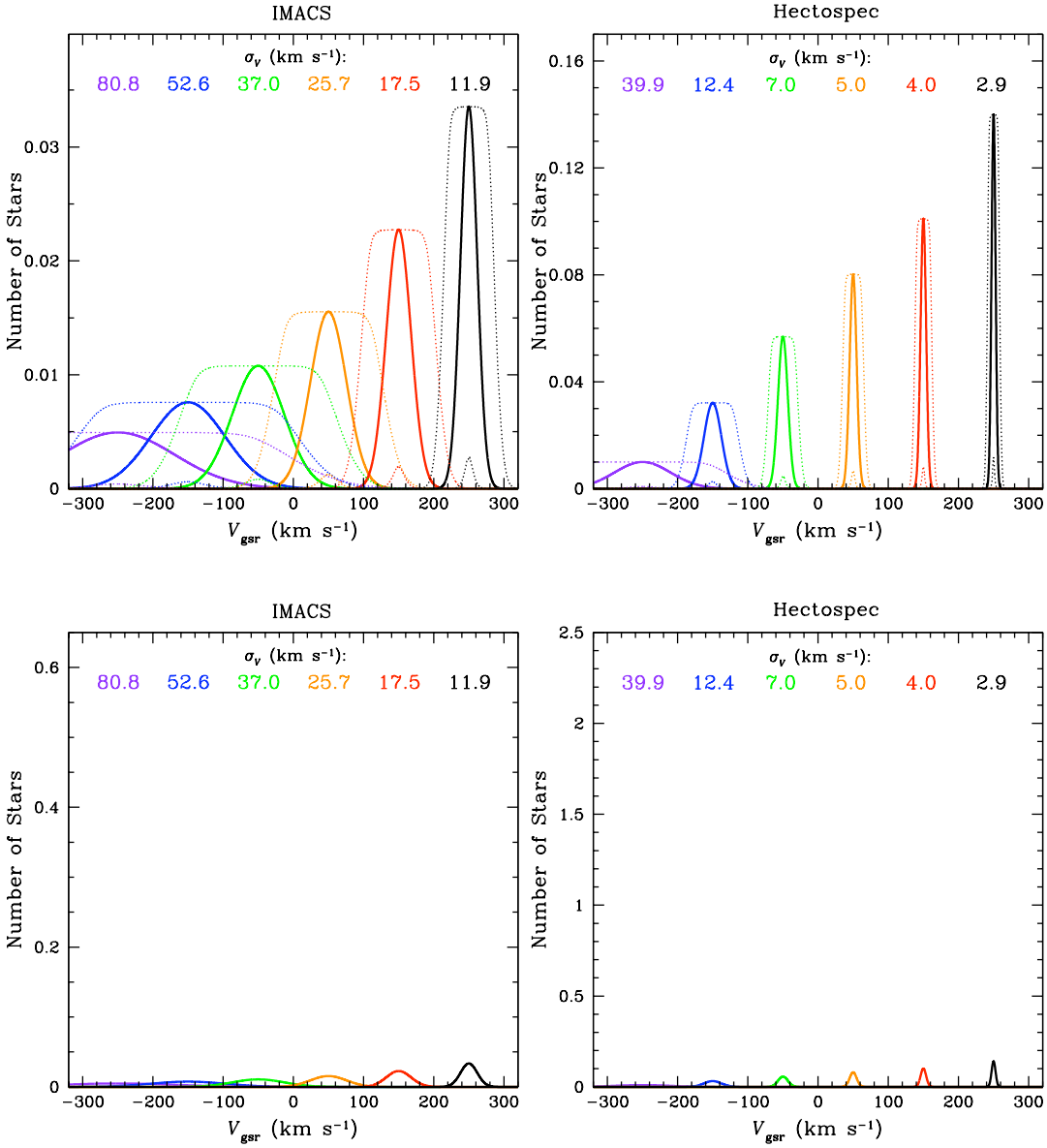

Figure 5.1: Example velocity distributions for individual stars. The Gaussian velocity distribution profiles are shown for six hypothetical stars from both the IMACS (left) and Hectospec (right) data sets. In each panel the stars are presented in order of decreasing σ_V from left to right (labeled along the top of each panel). They are spaced exactly 100 km s^{-1} apart starting at $V_{\rm gsr}$ = –250 km s^{-1}. The σ_V values range from the minimum to the maximum values in each data set, with four in-between at each quintile . The upper panels show an expanded view of the distributions and include 95% confidence bounds for each star. The lower panels show the same distributions plotted with the same y-axis scales used for the field plots included at the end of this section. For clarity, the 95% confidence bounds are not included in the lower panel plots.

general, in a given field, the smaller the velocity measurement uncertainties are, the greater the number of observed stars that are required to create a qualitatively smooth aggregated velocity distribution profile. In this sense, the Hectospec fields, despite containing on average 2.5 times the number of stars as the average IMACS field, were undersampled relative to the typical Hectospec velocity measurement uncertainty.

To account for this issue, we chose to smooth the Hectospec field's velocity distribution profiles in such a way as to make them comparable to the IMACS field's velocity distribution profiles. To do this, a logarithmic relationship was fit to seven representative $(\sigma_{V_{\rm Hecto}}, \sigma_{V_{\rm IMACS}})$ data points consisting of the minimum, maximum, median, and four quintile values of the velocity measurement uncertainties, σ_V, in each data set (most of which are depicted in Figure 5.1). A plot of this fit can be seen in the upper right panel of Figure 5.2. The best fit relationship was found to be:

$$\sigma_{V_{\rm IMACS}} = 61.9 \log_{10} [\sigma_{V_{\rm Hecto}}] - 16.9. \tag{5.2}$$

This functional relationship was then used to convert the velocity measurement uncertainty for each star in the Hectospec data set to a comparable (in a distributional sense) IMACS velocity measurement uncertainty. Using these artificially inflated velocity measurement uncertainties, new, smoothed velocity distribution profiles were generated (using Equation 5.1 again) for the Hectospec fields. The smoothed Hectospec velocity distributions, along with all of the IMACS distributions, are presented in Figures 5.3 to 5.12.

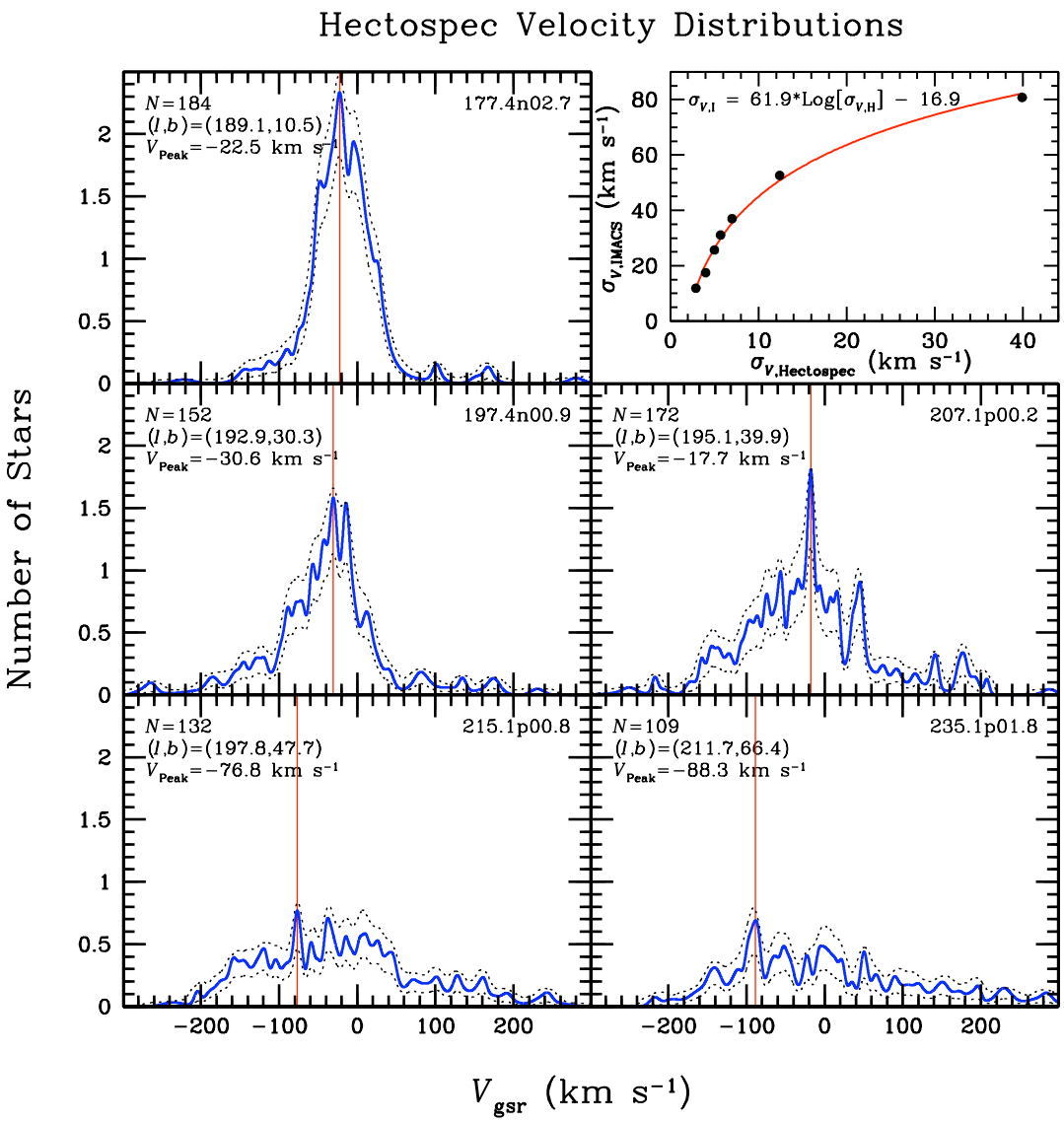

Figure 5.2: Hectospec velocity distributions. The Galactic standard of rest radial velocity distributions (solid blue lines) are presented along with their 95% confidence bounds (black dotted lines) for the five Hectospec fields. The velocity at which the peak in each distribution occurs is marked with a vertical red line and is listed with the information in the upper left hand corner. Additional information provided includes the number of stars in the field and the field's galactic coordinates. The name of each field is listed in the upper right hand corner. The smaller plot in the upper right hand panel shows the functional relationship used to smooth these five Hectospec velocity distributions to make them more comparable to the IMACS distributions (the smoothed Hectospec plots are presented later). This was done by fitting a logarithmic relationship between the maximum, minimum, median, and four quintile values of the velocity uncertainty, σ_V, for each spectrograph.

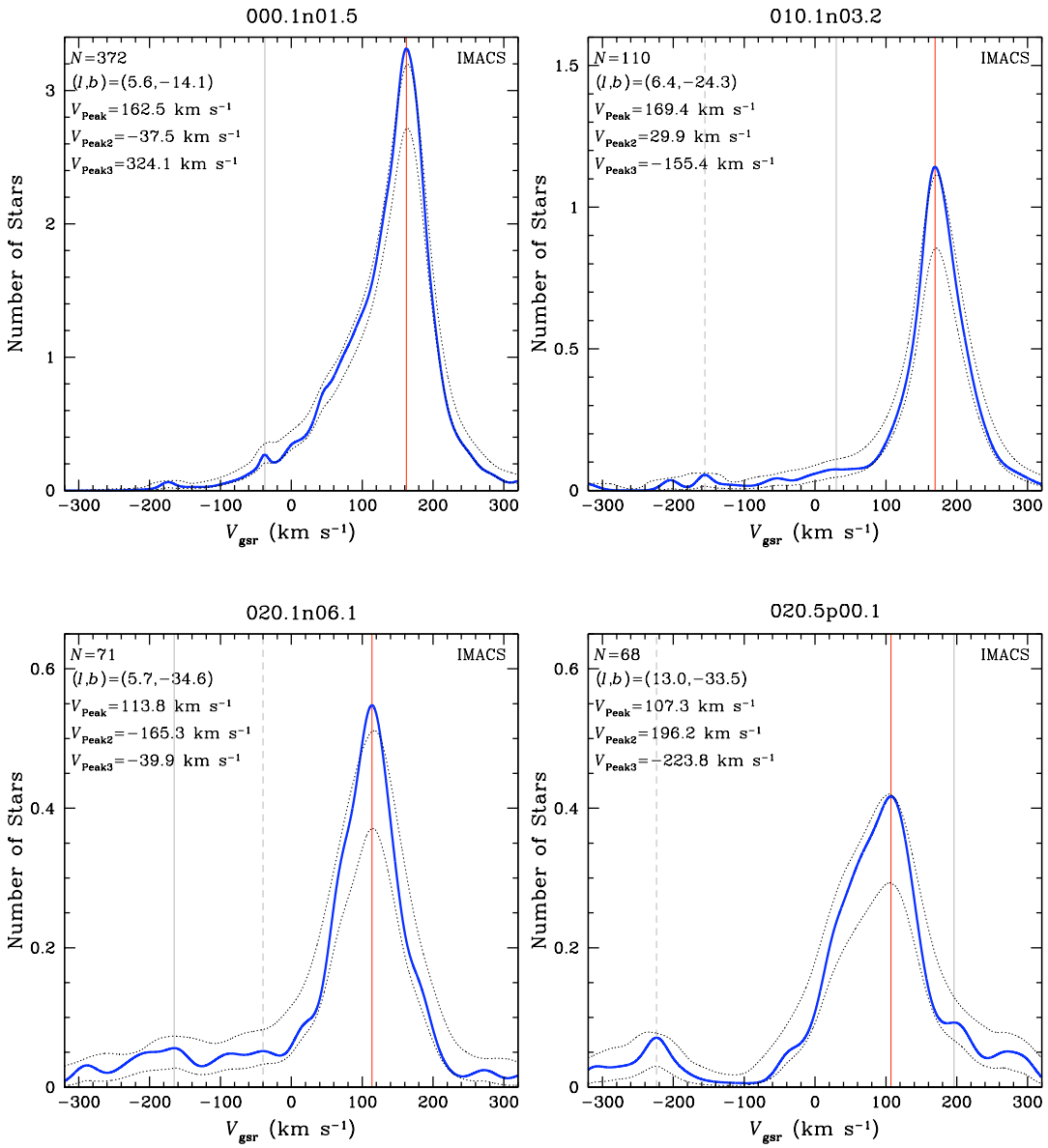

Figure 5.3: Radial velocity distributions in four fields. The Galactic standard of rest radial velocity distributions (solid blue lines) are presented along with their 95% confidence bounds (black dotted lines) for four fields. The velocity at which the peak in each distribution occurs is marked with a vertical red line and is listed with the information in the upper left hand corner. Secondary (solid gray line) and tertiary (gray dashed line) peaks, if present, are also marked and labeled in the upper left hand corner. Additional information provided includes the number of stars in the field and the field's galactic coordinates. The instrument used to acquire the spectroscopy is labeled in the upper right hand corner.

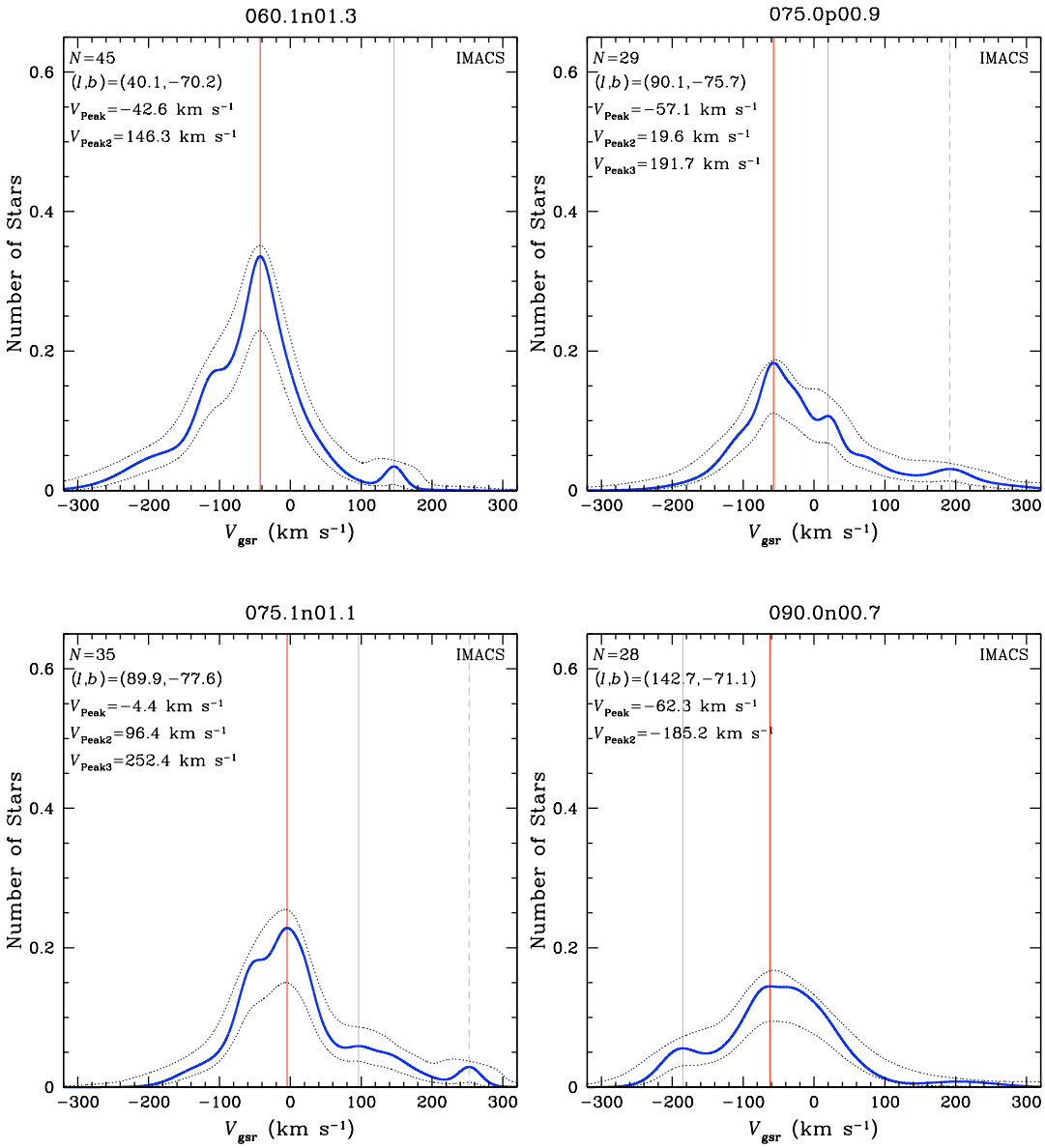

Figure 5.4: Radial velocity distributions in four fields. The Galactic standard of rest radial velocity distributions (solid blue lines) are presented along with their 95% confidence bounds (black dotted lines) for four fields. The velocity at which the peak in each distribution occurs is marked with a vertical red line and is listed with the information in the upper left hand corner. Secondary (solid gray line) and tertiary (gray dashed line) peaks, if present, are also marked and labeled in the upper left hand corner. Additional information provided includes the number of stars in the field and the field's galactic coordinates. The instrument used to acquire the spectroscopy is labeled in the upper right hand corner.

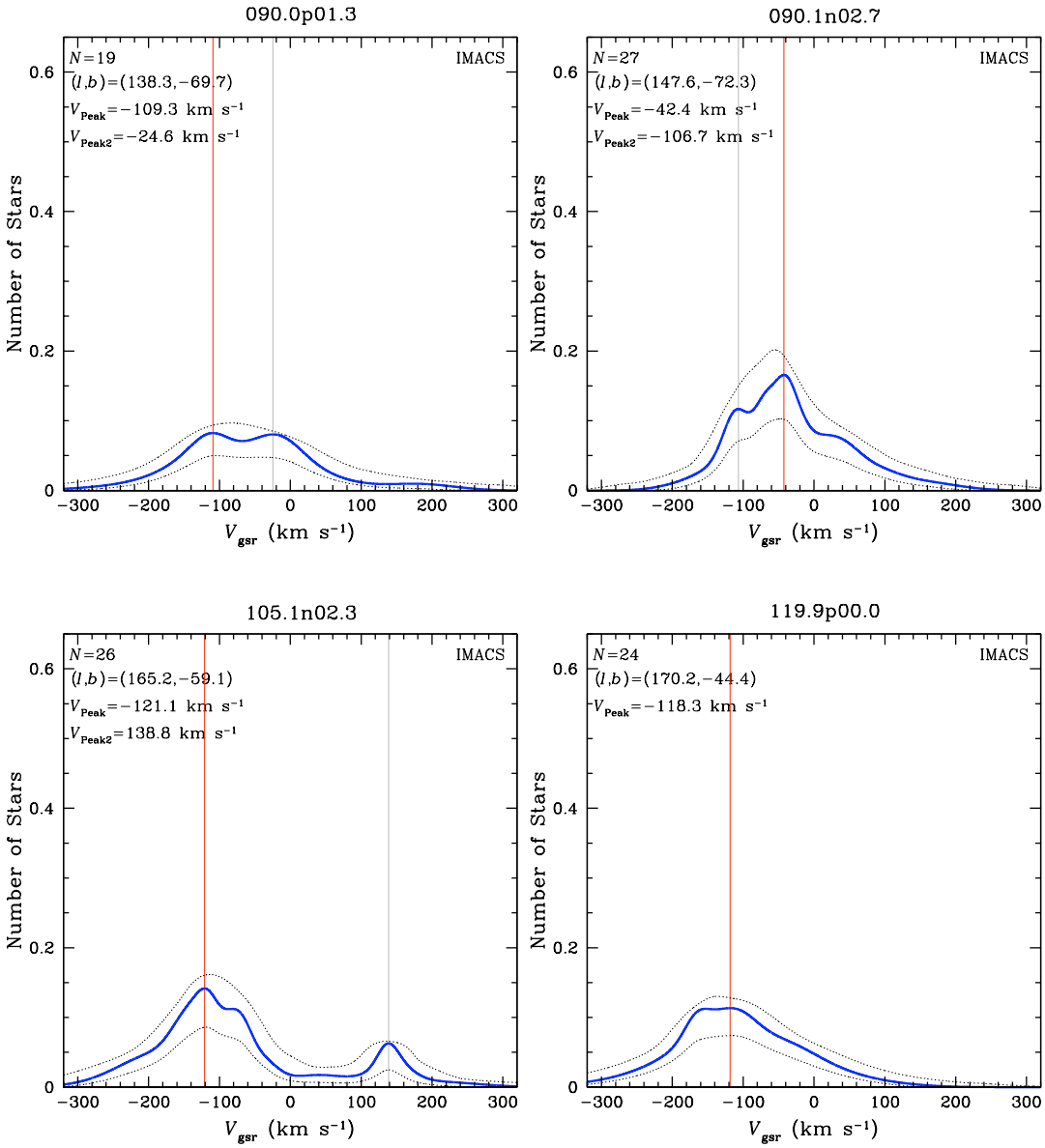

Figure 5.5: Radial velocity distributions in four fields. The Galactic standard of rest radial velocity distributions (solid blue lines) are presented along with their 95% confidence bounds (black dotted lines) for four fields. The velocity at which the peak in each distribution occurs is marked with a vertical red line and is listed with the information in the upper left hand corner. Secondary (solid gray line) and tertiary (gray dashed line) peaks, if present, are also marked and labeled in the upper left hand corner. Additional information provided includes the number of stars in the field and the field's galactic coordinates. The instrument used to acquire the spectroscopy is labeled in the upper right hand corner

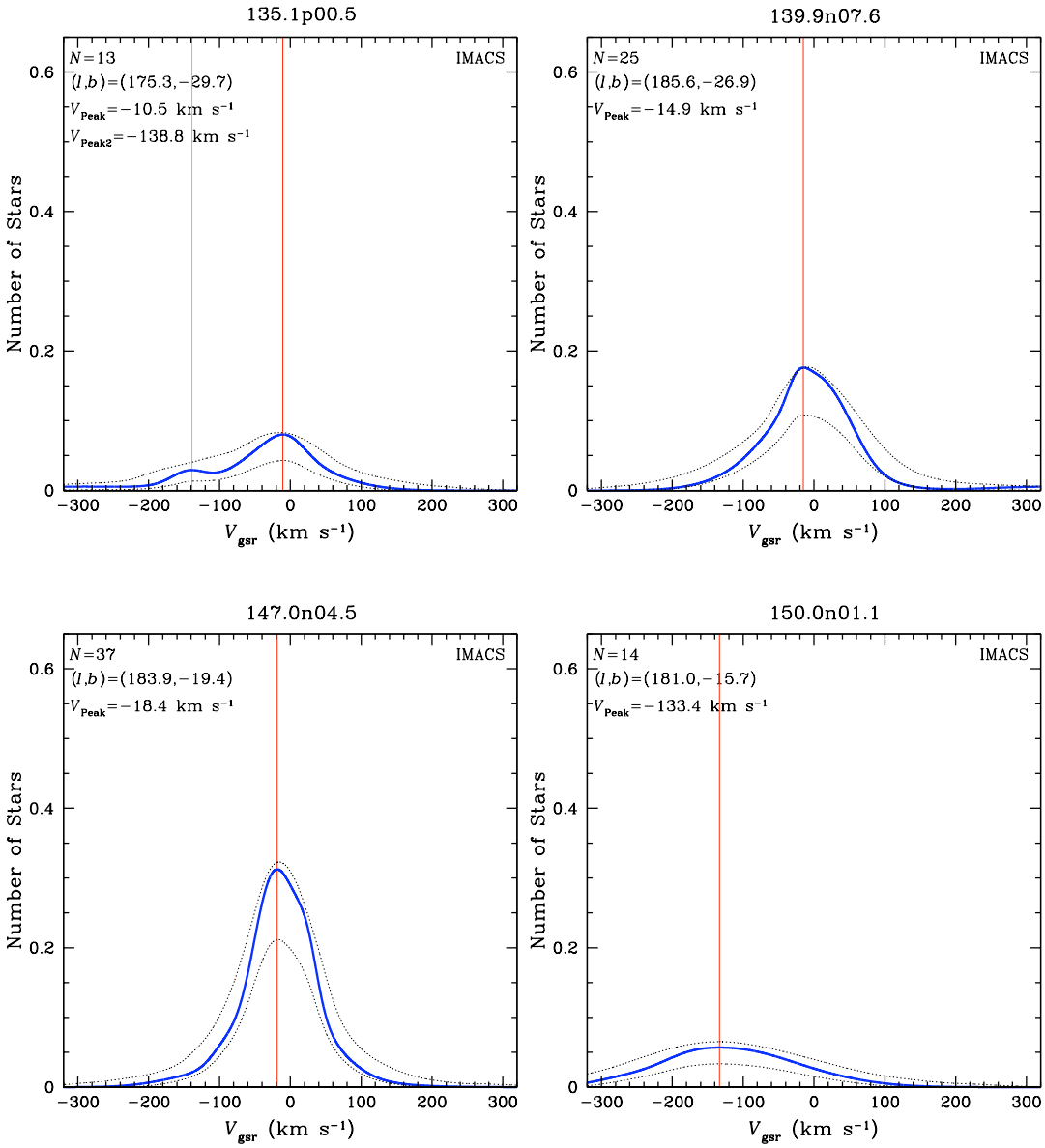

Figure 5.6: Radial velocity distributions in four fields. The Galactic standard of rest radial velocity distributions (solid blue lines) are presented along with their 95% confidence bounds (black dotted lines) for four fields. The velocity at which the peak in each distribution occurs is marked with a vertical red line and is listed with the information in the upper left hand corner. Secondary (solid gray line) and tertiary (gray dashed line) peaks, if present, are also marked and labeled in the upper left hand corner. Additional information provided includes the number of stars in the field and the field's galactic coordinates. The instrument used to acquire the spectroscopy is labeled in the upper right hand corner.

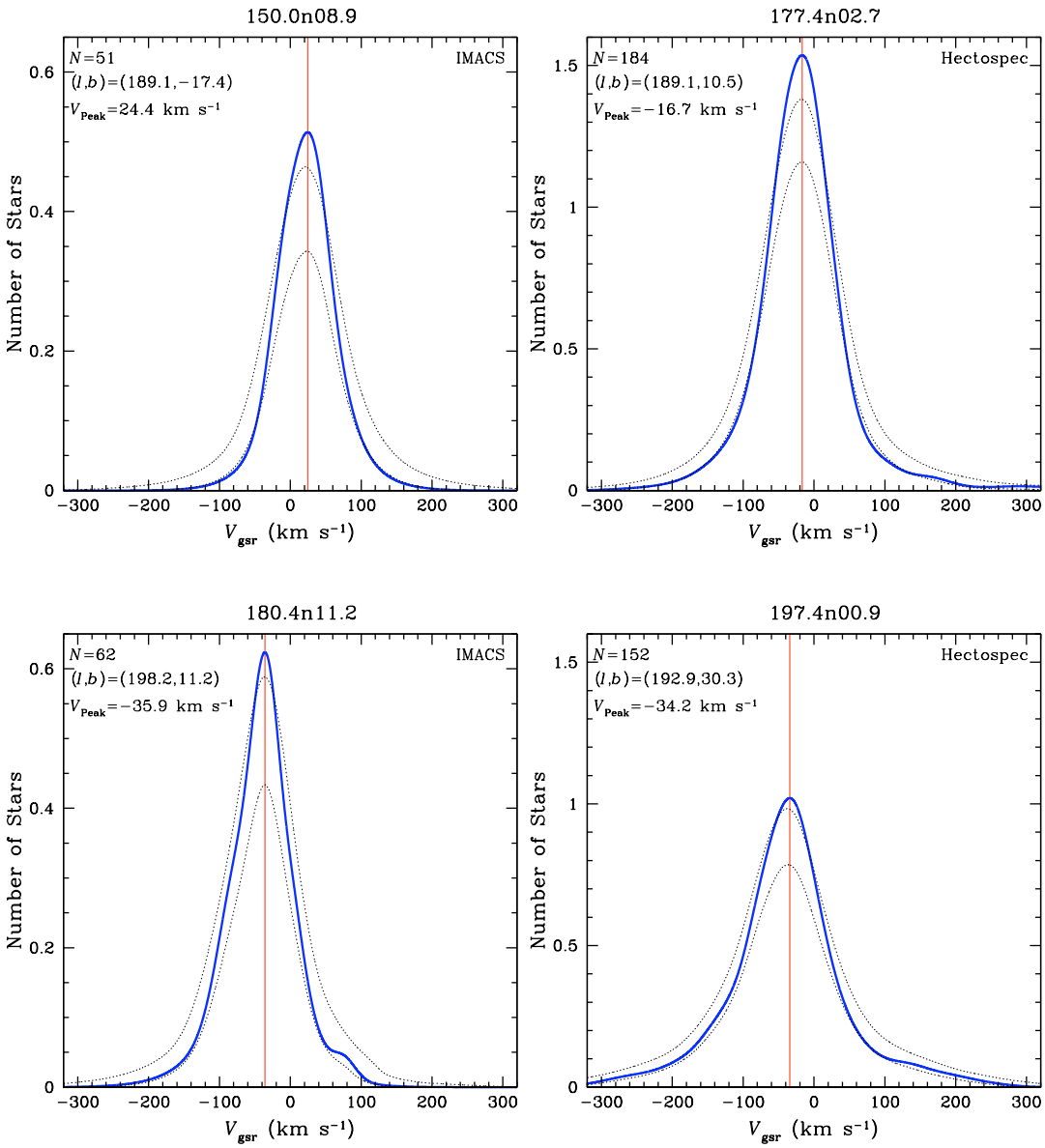

Figure 5.7: Radial velocity distributions in four fields. The Galactic standard of rest radial velocity distributions (solid blue lines) are presented along with their 95% confidence bounds (black dotted lines) for four fields. The velocity at which the peak in each distribution occurs is marked with a vertical red line and is listed with the information in the upper left hand corner. Secondary (solid gray line) and tertiary (gray dashed line) peaks, if present, are also marked and labeled in the upper left hand corner. Additional information provided includes the number of stars in the field and the field's galactic coordinates. The instrument used to acquire the spectroscopy is labeled in the upper right hand corner.

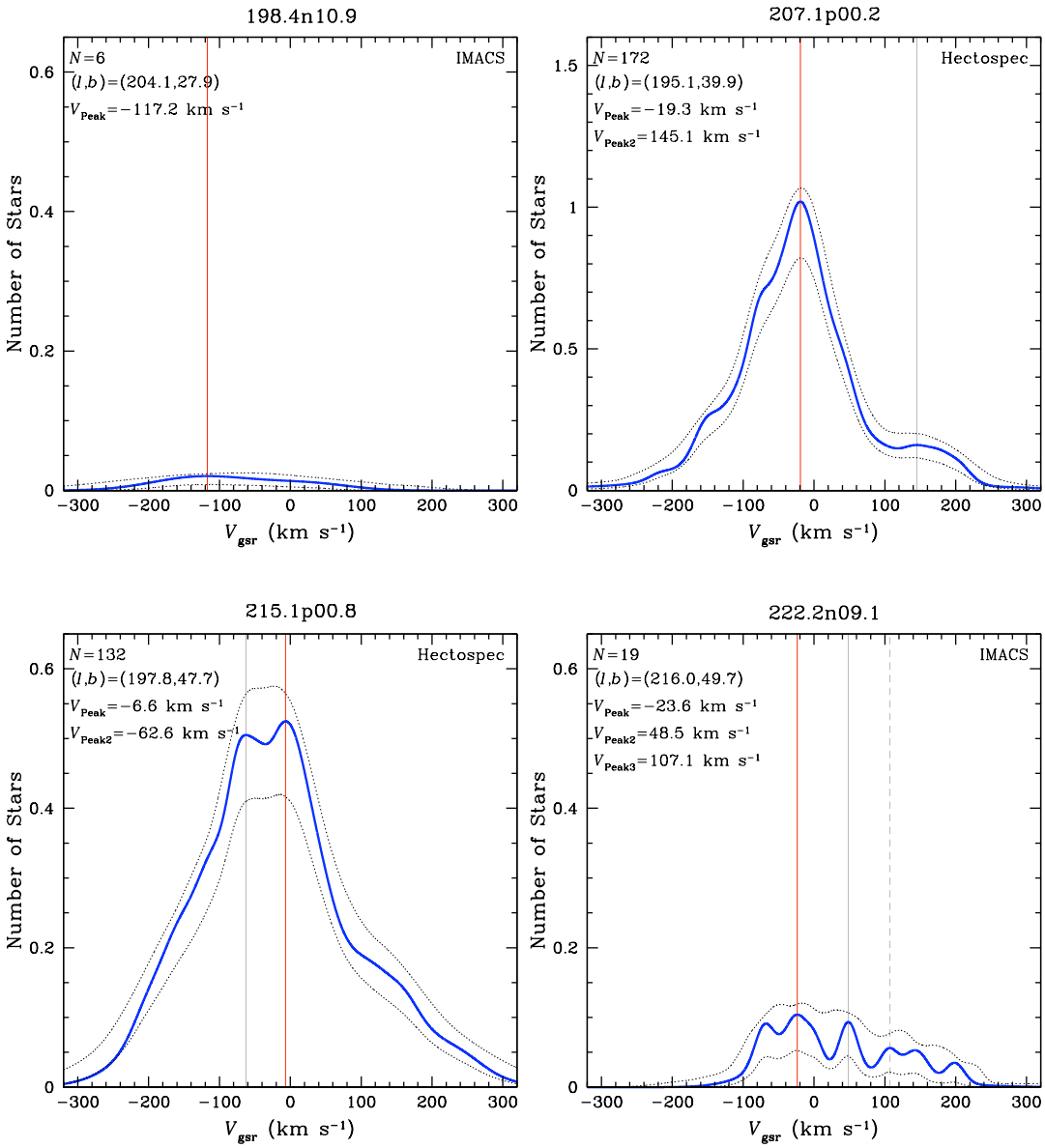

Figure 5.8: Radial velocity distributions in four fields. The Galactic standard of rest radial velocity distributions (solid blue lines) are presented along with their 95% confidence bounds (black dotted lines) for four fields. The velocity at which the peak in each distribution occurs is marked with a vertical red line and is listed with the information in the upper left hand corner. Secondary (solid gray line) and tertiary (gray dashed line) peaks, if present, are also marked and labeled in the upper left hand corner. Additional information provided includes the number of stars in the field and the field's galactic coordinates. The instrument used to acquire the spectroscopy is labeled in the upper right hand corner.

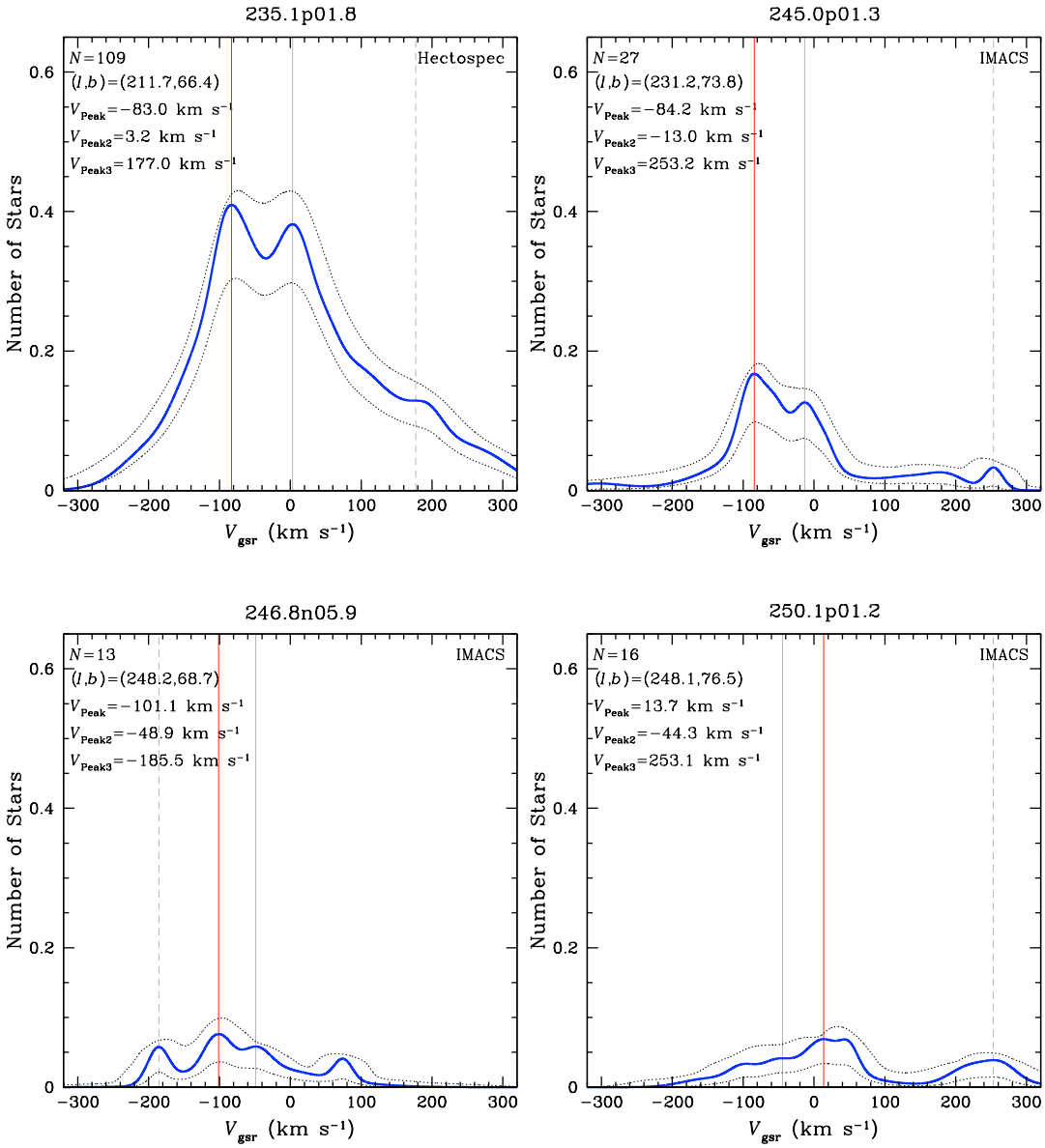

Figure 5.9: Radial velocity distributions in four fields. The Galactic standard of rest radial velocity distributions (solid blue lines) are presented along with their 95% confidence bounds (black dotted lines) for four fields. The velocity at which the peak in each distribution occurs is marked with a vertical red line and is listed with the information in the upper left hand corner. Secondary (solid gray line) and tertiary (gray dashed line) peaks, if present, are also marked and labeled in the upper left hand corner. Additional information provided includes the number of stars in the field and the field's galactic coordinates. The instrument used to acquire the spectroscopy is labeled in the upper right hand corner.

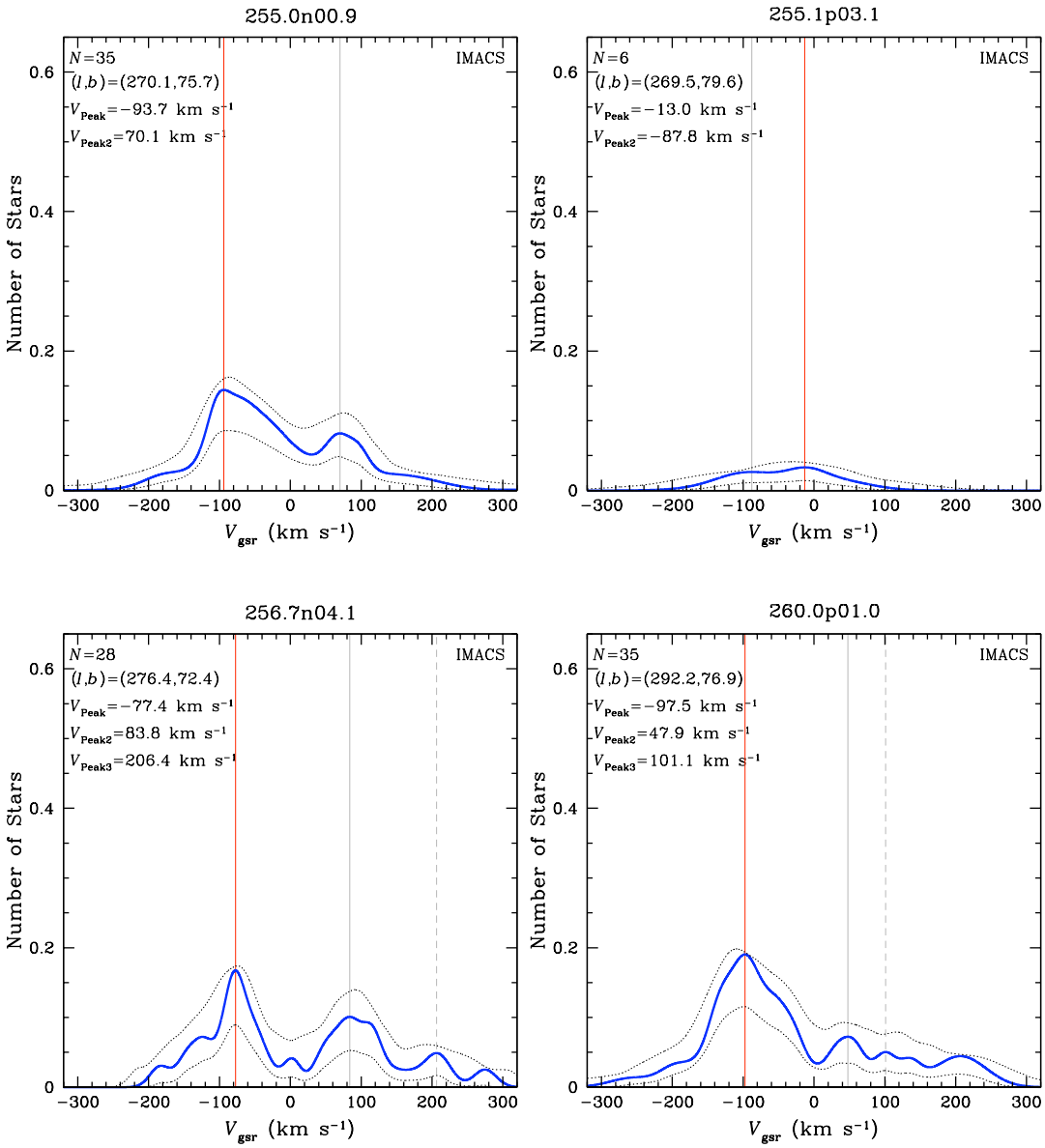

Figure 5.10: Radial velocity distributions in four fields. The Galactic standard of rest radial velocity distributions (solid blue lines) are presented along with their 95% confidence bounds (black dotted lines) for four fields. The velocity at which the peak in each distribution occurs is marked with a vertical red line and is listed with the information in the upper left hand corner. Secondary (solid gray line) and tertiary (gray dashed line) peaks, if present, are also marked and labeled in the upper left hand corner. Additional information provided includes the number of stars in the field and the field's galactic coordinates. The instrument used to acquire the spectroscopy is labeled in the upper right hand corner.

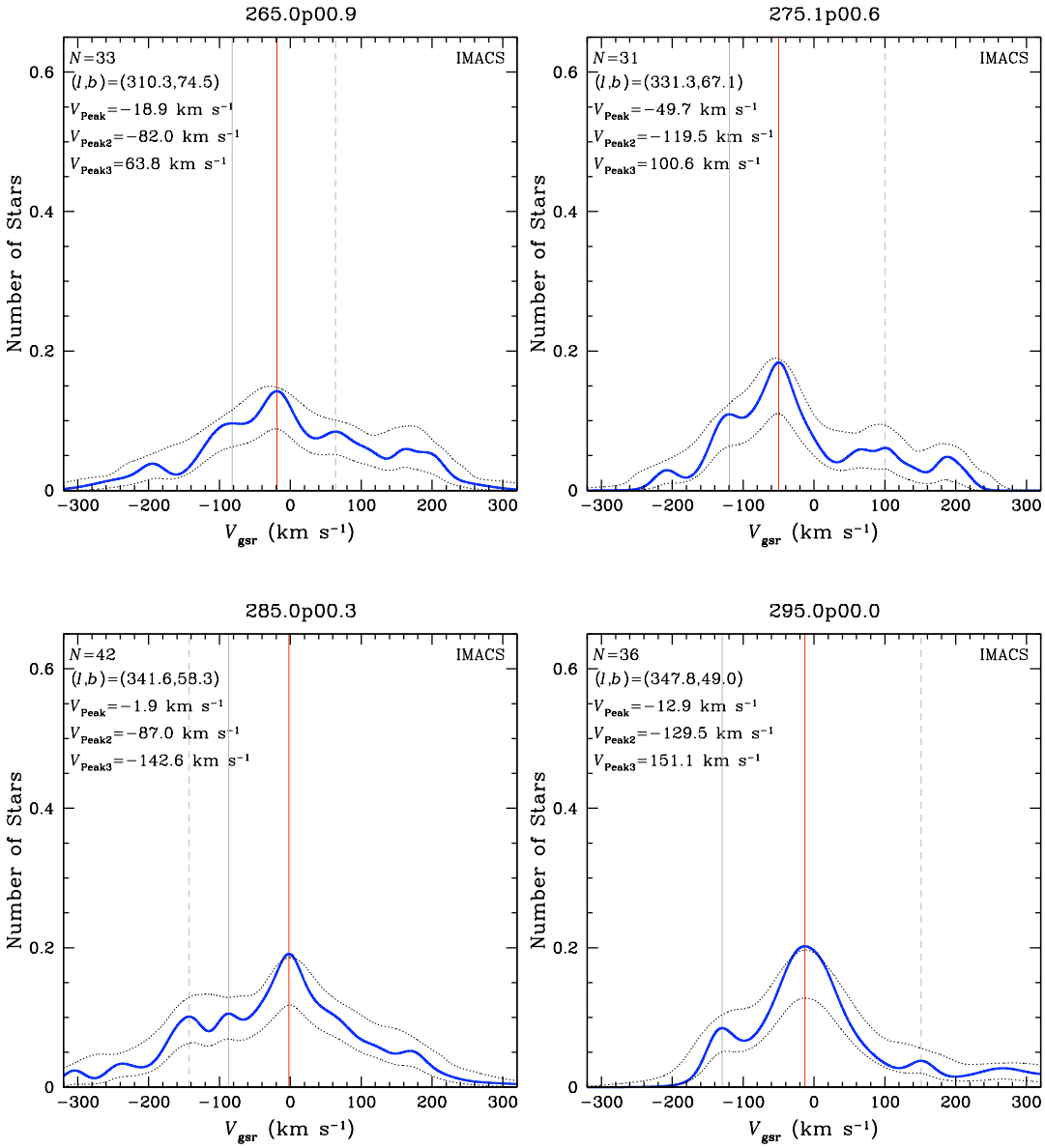

Figure 5.11: Radial velocity distributions in four fields. The Galactic standard of rest radial velocity distributions (solid blue lines) are presented along with their 95% confidence bounds (black dotted lines) for four fields. The velocity at which the peak in each distribution occurs is marked with a vertical red line and is listed with the information in the upper left hand corner. Secondary (solid gray line) and tertiary (gray dashed line) peaks, if present, are also marked and labeled in the upper left hand corner. Additional information provided includes the number of stars in the field and the field's galactic coordinates. The instrument used to acquire the spectroscopy is labeled in the upper right hand corner.

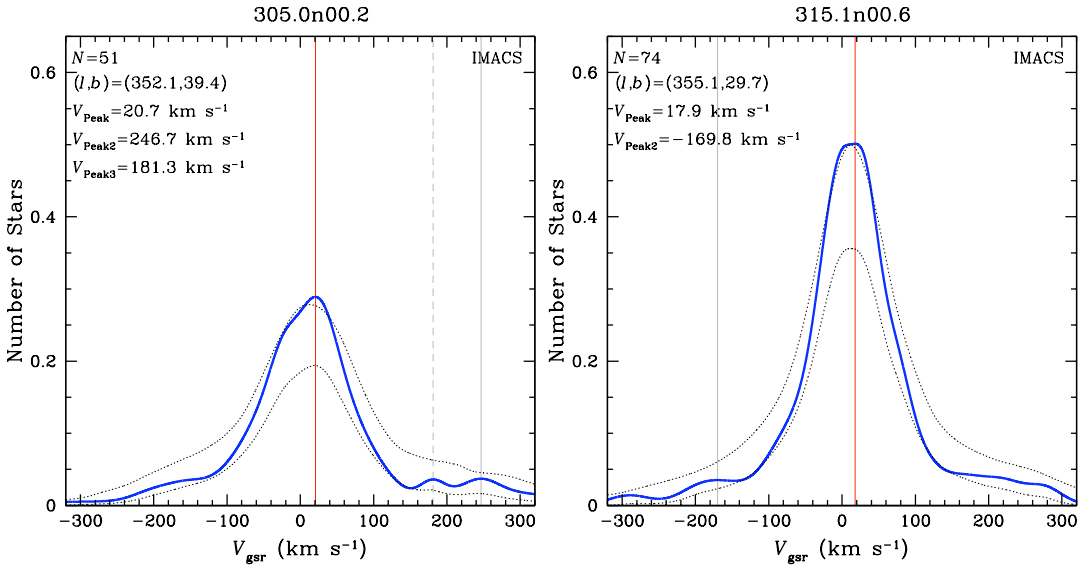

Figure 5.12: Radial velocity distributions in two fields. The Galactic standard of rest radial velocity distributions (solid blue lines) are presented along with their 95% confidence bounds (black dotted lines) for two fields. The velocity at which the peak in each distribution occurs is marked with a vertical red line and is listed with the information in the upper left hand corner. Secondary (solid gray line) and tertiary (gray dashed line) peaks, if present, are also marked and labeled in the upper left hand corner. Additional information provided includes the number of stars in the field and the field's galactic coordinates. The instrument used to acquire the spectroscopy is labeled in the upper right hand corner.

Table 5.1: Hectospec Peak Velocities and Asymmetry Statistics

Field	$N_{\rm Stars}$	$V_{\rm Peak}$ (km s^{-1})	$D(V_{\rm Peak})$	$[\Sigma D]$			$[\Sigma D \cdot \Delta V]$		
				$Left$	$Right$	L/R	$Left$	$Right$	L/R
177.4n02.7	184	$-22.5\ ^{+20.3}_{-10.2}$	2.33	0.460	0.540	0.852	0.403	0.597	0.675
197.4n00.9	152	$-30.6\ ^{+18.3}_{-10.4}$	1.58	0.547	0.453	1.208	0.567	0.433	1.309
207.1p00.2	172	$-17.7\ ^{+3.9}_{-5.7}$	1.81	0.541	0.459	1.179	0.520	0.480	1.083
215.1p00.8	132	$-76.8\ ^{+89.9}_{-2.7}$	0.77	0.313	0.687	0.456	0.188	0.812	0.232
235.1p01.8	109	$-88.3\ ^{+95.3}_{-10.3}$	0.69	0.245	0.755	0.325	0.090	0.910	0.099

We characterize the typical radial velocity of Sgr debris in each field as the velocity at which the distribution profile, $D(V)$, reaches its absolute maximum. This velocity will be referred to as $V_{\rm Peak}$ hereafter. The peak velocities are marked with vertical lines and labeled on all of the velocity distribution plots in Figures 5.2 to 5.12. Table 5.1 lists the locations, $V_{\rm Peak}$, and heights, $D(V_{\rm Peak})$, of the primary peaks in each of the five unsmoothed Hectospec fields. Table 5.2 lists the same information for the IMACS and smoothed Hectospec velocity distributions. Also included in Tables 5.1 and 5.2 are 95% confidence bounds on the peak velocities. These asymmetric uncertainties were estimated using the results of the aforementioned Monte Carlo simulation with 25,000 realizations.

Given the likelihood of the presence of additional halo substructure in the observed fields, possibly due to a wrap of the Sgr streams or an unrelated kinematic feature, we also choose to mark secondary and tertiary peaks that may be of potential interest. Each of these additional peaks had to meet several quantitative criteria to merit their identification and inclusion. The additional peaks were required to be the highest remaining local maxima in their velocity distribution profile, reside at least 50 km s^{-1} away from all previously identified peaks, and contain an integrated area

Table 5.2: Peak Velocities

Field	$N_{\rm Stars}$	$V_{\rm Peak}$ (km s^{-1})	$D(V_{\rm Peak})$	$V_{\rm Peak2}$ (km s^{-1})	$D(V_{\rm Peak2})$	$V_{\rm Peak3}$ (km s^{-1})	$D(V_{\rm Peak3})$
000.1n01.5	372	$162.5^{+8.4}_{-5.7}$	3.31	$-37.5^{+13.4}_{-19.7}$	0.27	$324.1^{+16.5}_{-15.0}$	0.07
010.1n03.2	110	$169.4^{+12.6}_{-7.0}$	1.14	$29.9^{+8.0}_{-56.7}$	0.07	$-155.4^{+17.4}_{-13.8}$	0.06
020.1n06.1	71	$113.8^{+17.9}_{-18.8}$	0.55	$-165.3^{+38.9}_{-76.6}$	0.06	$-39.9^{+23.6}_{-26.7}$	0.05
020.5p00.1	68	$107.3^{+16.8}_{-39.3}$	0.42	$196.2^{+37.2}_{-9.9}$	0.09	$-223.8^{+28.3}_{-32.1}$	0.07
060.1n01.3	45	$-42.6^{+18.5}_{-21.2}$	0.34	$146.3^{+16.9}_{-18.7}$	0.03	...	...
075.0p00.9	29	$-57.1^{+66.2}_{-19.5}$	0.18	$19.6^{+36.3}_{-14.4}$	0.11	$191.7^{+43.8}_{-47.1}$	0.03
075.1n01.1	35	$-4.4^{+19.8}_{-44.1}$	0.23	$96.4^{+74.6}_{-18.6}$	0.06	$252.4^{+19.5}_{-22.6}$	0.03
090.0n00.7	28	$-62.3^{+107.5}_{-26.8}$	0.14	$-185.2^{+32.7}_{-35.9}$	0.06	...	...
090.0p01.3	19	$-109.3^{+55.1}_{-28.5}$	0.08	$-24.6^{+59.4}_{-43.3}$	0.08	...	...
090.1n02.7	27	$-42.4^{+17.3}_{-56.6}$	0.17	$-106.7^{+13.9}_{-30.3}$	0.12	...	...
105.1n02.3	26	$-121.1^{+54.7}_{-27.3}$	0.14	$138.8^{+27.3}_{-24.2}$	0.06	...	...
119.9p00.0	24	$-118.3^{+41.7}_{-57.8}$	0.11	...	...	...	...
135.1p00.5	13	$-10.5^{+34.7}_{-47.8}$	0.08	$-138.8^{+29.8}_{-38.2}$	0.03	...	...
139.9n07.6	25	$-14.9^{+42.2}_{-23.1}$	0.18	...	...	...	...
147.0n04.5	37	$-18.4^{+31.9}_{-19.6}$	0.31	...	...	...	...
150.0n01.1	14	$-133.4^{+81.5}_{-74.6}$	0.06	...	...	...	...
150.0n08.9	51	$24.4^{+14.3}_{-20.6}$	0.51	...	...	...	...
177.4n02.7	184	$-16.7^{+10.1}_{-12.5}$	1.54	...	...	...	...
180.4n11.2	62	$-35.9^{+14.3}_{-15.0}$	0.62	...	...	...	...
197.4n00.9	152	$-34.2^{+11.5}_{-20.3}$	1.02	...	...	...	...
198.4n10.9	6	$-117.2^{+158.2}_{-80.8}$	0.02	...	...	...	...
207.1p00.2	172	$-19.3^{+18.2}_{-22.0}$	1.02	$145.1^{+69.3}_{-27.0}$	0.16	...	...
215.1p00.8	132	$-6.6^{+13.1}_{-66.1}$	0.52	$-62.6^{+27.5}_{-88.7}$	0.51	...	...
222.2n09.1	19	$-23.6^{+83.5}_{-48.9}$	0.10	$48.5^{+19.1}_{-19.8}$	0.09	$107.1^{+18.2}_{-26.3}$	0.06
235.1p01.8	109	$-83.0^{+105.9}_{-8.5}$	0.41	$3.2^{+82.7}_{-37.7}$	0.38	$177.0^{+81.3}_{-3.2}$	0.13
245.0p01.3	27	$-84.2^{+81.3}_{-16.0}$	0.17	$-13.0^{+37.1}_{-20.4}$	0.13	$253.2^{+15.6}_{-17.5}$	0.03
246.8n05.9	13	$-101.1^{+43.3}_{-82.7}$	0.08	$-48.9^{+41.7}_{-19.1}$	0.06	$-185.5^{+22.5}_{-18.8}$	0.06
250.1p01.2	16	$13.7^{+51.2}_{-83.0}$	0.07	$-44.3^{+7.0}_{-39.2}$	0.04	$253.1^{+36.6}_{-61.2}$	0.04
255.0n00.9	35	$-93.7^{+63.7}_{-18.8}$	0.14	$70.1^{+44.2}_{-40.0}$	0.08	...	...
255.1p03.1	6	$-13.0^{+48.4}_{-104.8}$	0.03	$-87.8^{+23.0}_{-60.1}$	0.03	...	...
256.7n04.1	28	$-77.4^{+175.3}_{-26.9}$	0.17	$83.8^{+48.9}_{-42.9}$	0.10	$206.4^{+22.9}_{-43.3}$	0.05
260.0p01.0	35	$-97.5^{+48.3}_{-36.0}$	0.19	$47.9^{+33.3}_{-37.1}$	0.07	$101.1^{+22.2}_{-20.0}$	0.05
265.0p00.9	33	$-18.9^{+37.3}_{-49.6}$	0.14	$-82.0^{+12.8}_{-49.7}$	0.10	$63.8^{+72.1}_{-27.5}$	0.08
275.1p00.6	31	$-49.7^{+20.9}_{-36.7}$	0.18	$-119.5^{+17.8}_{-32.3}$	0.11	$100.6^{+44.6}_{-17.5}$	0.06
285.0p00.3	42	$-1.9^{+27.0}_{-34.5}$	0.19	$-87.0^{+20.4}_{-28.1}$	0.11	$-142.6^{+27.5}_{-39.6}$	0.10
295.0p00.0	36	$-12.9^{+30.8}_{-28.1}$	0.20	$-129.5^{+30.9}_{-26.4}$	0.08	$151.1^{+31.4}_{-31.0}$	0.04
305.0n00.2	51	$20.7^{+22.2}_{-38.0}$	0.29	$246.7^{+54.5}_{-36.6}$	0.04	$181.3^{+28.8}_{-30.5}$	0.04
315.1n00.6	74	$17.9^{+17.9}_{-27.4}$	0.50	$-169.8^{+22.6}_{-51.1}$	0.04	...	...

Note: The peaks listed for the Hectospec fields refer to the smoothed distributions. The primary peak information for the unsmoothed Hectospec distributions are given in Table 5.1.

within ± 25 km s^{-1} of the peak that is greater than the areal equivalent of one star. These additional peaks are marked with vertical lines and labeled on all of the velocity distribution plots in Figures 5.3 to 5.12. Table 5.2 lists the locations, $V_{\mathrm{Peak}N}$, and heights, $D(V_{\mathrm{Peak}N})$, of each of the additionally identified peaks in the IMACS and smoothed Hectospec velocity distribution profiles (where N is used to index the peaks in order of decreasing height).

Also included in Table 5.2 are asymmetric uncertainties in the locations of the additional velocity peaks. The uncertainty on either side of each additional peak is estimated to be the distance away from the peak at which the velocity distribution profile falls to one-half of the peak's maximum height. But, if the velocity distribution profile does not monotonically decrease from the peak down to one-half of the maximum height, then the uncertainty in that direction is taken to be the location of the first local minimum. This method likely underestimates the uncertainties in the peak velocity locations. Attempts to use the more robust results from the Monte Carlo simulation to estimate their uncertainties were unsuccessful, as the relative heights and locations of the peaks frequently varied wildly. This result suggests that the existence of some of the secondary and most of the tertiary peaks should be viewed with great skepticism.

We note the high degree of asymmetry, relative to the peak velocity, V_{Peak}, apparent in some of the velocity distributions. This may be due to contamination by foreground thick disk stars or Milky Way halo stars, or possibly the presence of a wrap of the Sgr debris streams or other substructure within the halo. To help quan-

tify this we define several statistical measures of the asymmetry in a given velocity distribution, $D(V)$.

First, the normalized statistics $[\Sigma D]_L$ and $[\Sigma D]_R$ are defined to be the percentages of the velocity distribution, $D(V)$, that fall to the left and right, respectively, of the peak velocity, V_{Peak}. They, and their ratio, can be expressed mathematically as:

$$[\Sigma D]_L \equiv \frac{\int_{-\infty}^{V_{\text{Peak}}} D(V)}{\int_{-\infty}^{\infty} D(V)} = 1 - [\Sigma D]_R \tag{5.3a}$$

$$[\Sigma D]_R = 1 - [\Sigma D]_L \tag{5.3b}$$

$$[\Sigma D]_{L/R} \equiv \frac{[\Sigma D]_L}{[\Sigma D]_R} = \frac{\int_{-\infty}^{V_{\text{Peak}}} D(V)}{\int_{V_{\text{Peak}}}^{\infty} D(V)}. \tag{5.3c}$$

Likewise, the normalized statistics $[\Sigma(D \cdot \Delta V)]_L$ and $[\Sigma(D \cdot \Delta V)]_R$ are defined to be the percentages of the weighted velocity distribution, $D(V) \cdot \Delta V$, that fall to the left and right, respectively, of the peak velocity, V_{Peak}. In this case, the values of the velocity distribution, $D(V)$, are weighted by their distance from the peak velocity, ΔV, defined as $\Delta V \equiv |V - V_{\text{Peak}}|$. The $[\Sigma(D \cdot \Delta V)]_L$ and $[\Sigma(D \cdot \Delta V)]_R$ statistics, and their ratio, can be expressed mathematically as:

$$[\Sigma(D \cdot \Delta V)]_L \equiv \frac{\int_{-\infty}^{V_{\rm Peak}} D(V) \cdot \Delta V}{\int_{-\infty}^{\infty} D(V) \cdot \Delta V} = 1 - [\Sigma D \cdot \Delta V]_R \tag{5.4a}$$

$$[\Sigma(D \cdot \Delta V)]_R = 1 - [\Sigma D \cdot \Delta V]_L \tag{5.4b}$$

$$[\Sigma(D \cdot \Delta V)]_{L/R} \equiv \frac{[\Sigma(D \cdot \Delta V)]_L}{[\Sigma(D \cdot \Delta V)]_R} = \frac{\int_{-\infty}^{V_{\rm Peak}} D(V) \cdot \Delta V}{\int_{V_{\rm Peak}}^{\infty} D(V) \cdot \Delta V}. \tag{5.4c}$$

All six of the statistics defined in Equations 5.3 and 5.4 are summarized in Table 5.1, for the unsmoothed Hectospec distributions, and Table 5.3, for the IMACS and smoothed Hectospec distributions. Figure 5.13 provides plots of the $[\Sigma D]_L$ and $[\Sigma(D \cdot \Delta V)]_L$ statistics against both the Sagittarius longitude, $\Lambda_\odot$, and the peak velocity, $V_{\rm Peak}$. Finally, Figures 5.14 and 5.15 show the cumulative distribution functions of the $[\Sigma D]$ and $[\Sigma(D \cdot \Delta V)]$ statistics for all Sgr fields. The location of the peak velocity in each field is marked on the *cdfs*. For clarity, they are split between four panels, with each field's *cdf* plotted in the same panel (e.g. top-left, bottom-right, etc.) as its velocity distribution profile in Figures 5.3 to 5.12. Additionally, the (typically four) *cdfs* plotted in the same color (of which there are at most one per panel) can be found in the same velocity distribution figure. For example, the four red *cdfs* represent the four velocity distributions presented in Figure 5.3. Note that for Figures 5.13 to 5.15 the statistics plotted for the Hectospec fields are derived from the unsmoothed distributions.

Table 5.3: Field Asymmetry Statistics

Field	$N_{\rm Stars}$	$[\Sigma D]$			$[\Sigma D \cdot \Delta V]$		
		$Left$	$Right$	L/R	$Left$	$Right$	L/R
000.1n01.5	372	0.629	0.371	1.695	0.769	0.231	3.329
010.1n03.2	110	0.504	0.496	1.016	0.682	0.318	2.145
020.1n06.1	71	0.600	0.400	1.500	0.773	0.227	3.405
020.5p00.1	68	0.614	0.386	1.591	0.733	0.267	2.745
060.1n01.3	45	0.566	0.434	1.304	0.628	0.372	1.688
075.0p00.9	29	0.331	0.669	0.495	0.179	0.821	0.218
075.1n01.1	35	0.494	0.506	0.976	0.386	0.614	0.629
090.0n00.7	28	0.433	0.567	0.764	0.407	0.593	0.686
090.0p01.3	19	0.310	0.690	0.449	0.199	0.801	0.248
090.1n02.7	27	0.497	0.503	0.988	0.417	0.583	0.715
105.1n02.3	26	0.400	0.600	0.667	0.239	0.761	0.314
119.9p00.0	24	0.477	0.523	0.912	0.430	0.570	0.754
135.1p00.5	13	0.620	0.380	1.632	0.776	0.224	3.464
139.9n07.6	25	0.433	0.567	0.764	0.354	0.646	0.548
147.0n04.5	37	0.462	0.538	0.859	0.459	0.541	0.848
150.0n01.1	14	0.446	0.554	0.805	0.394	0.606	0.650
150.0n08.9	51	0.528	0.472	1.119	0.532	0.468	1.137
177.4n02.7	184	0.515	0.485	1.062	0.486	0.514	0.946
180.4n11.2	62	0.539	0.461	1.169	0.573	0.427	1.342
197.4n00.9	152	0.526	0.474	1.110	0.529	0.471	1.123
198.4n10.9	6	0.374	0.626	0.597	0.264	0.736	0.359
207.1p00.2	172	0.526	0.474	1.110	0.508	0.492	1.033
215.1p00.8	132	0.575	0.425	1.353	0.571	0.429	1.331
222.2n09.1	19	0.331	0.669	0.495	0.158	0.842	0.188
235.1p01.8	109	0.260	0.740	0.351	0.122	0.878	0.139
245.0p01.3	27	0.296	0.704	0.420	0.199	0.801	0.248
246.8n05.9	13	0.376	0.624	0.603	0.271	0.729	0.372
250.1p01.2	16	0.429	0.571	0.751	0.268	0.732	0.366
255.0n00.9	35	0.245	0.755	0.325	0.149	0.851	0.175
255.1p03.1	6	0.640	0.360	1.778	0.738	0.262	2.817
256.7n04.1	28	0.289	0.711	0.406	0.108	0.892	0.121
260.0p01.0	35	0.340	0.660	0.515	0.169	0.831	0.203
265.0p00.9	33	0.453	0.547	0.828	0.392	0.608	0.645
275.1p00.6	31	0.457	0.543	0.842	0.328	0.672	0.488
285.0p00.3	42	0.550	0.450	1.222	0.590	0.410	1.439
295.0p00.0	36	0.445	0.555	0.802	0.294	0.706	0.416
305.0n00.2	51	0.539	0.461	1.169	0.481	0.519	0.927
315.1n00.6	74	0.524	0.476	1.101	0.515	0.485	1.062

Note: The statistics for the Hectospec fields refer to the smoothed distributions. The statistics for the unsmoothed Hectospec distributions are given in Table 5.1.

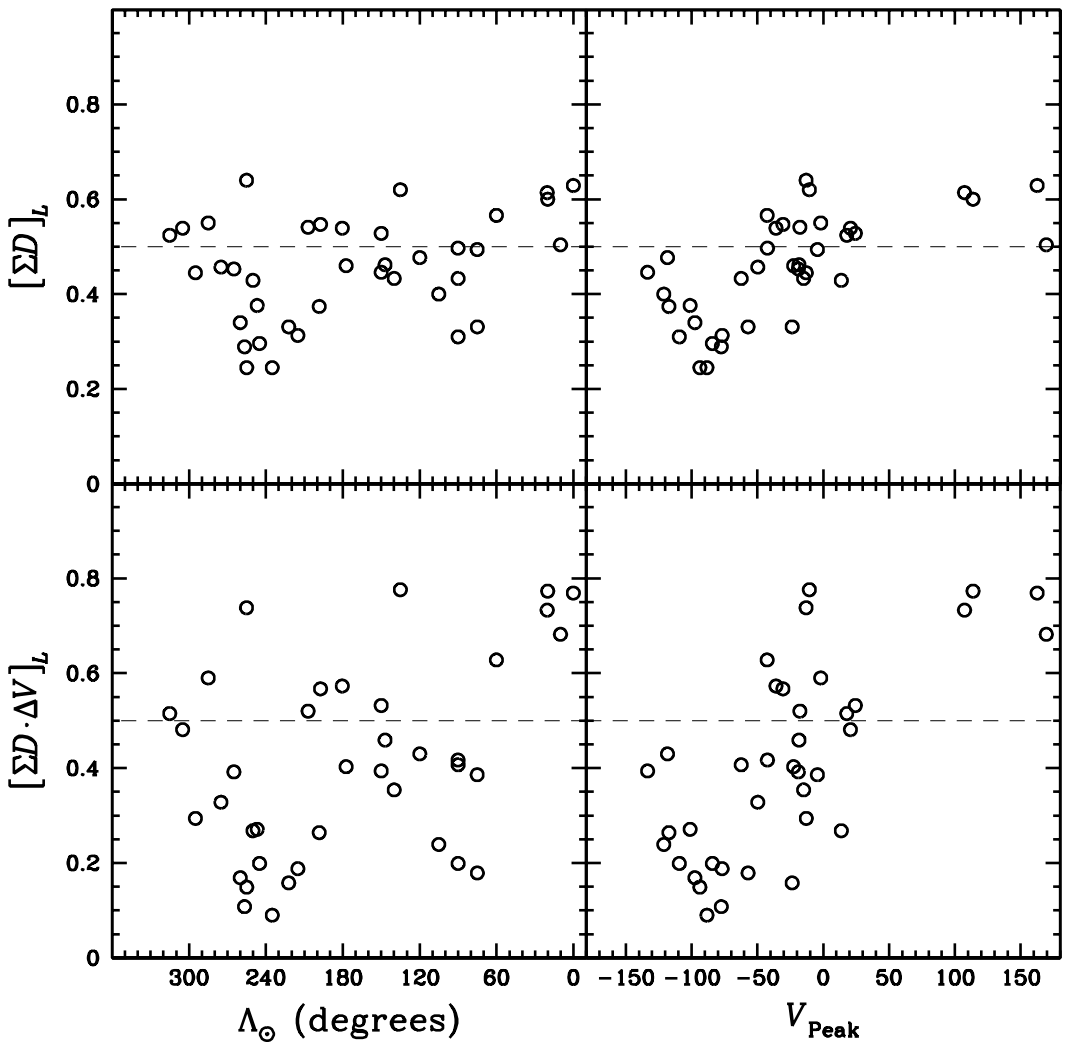

Figure 5.13: Field asymmetry statistics. The $[\Sigma D]_L$ and $[\Sigma(D{\cdot}\Delta V)]_L$ statistics are plotted against both the Sagittarius longitude, $\Lambda_\odot$ (left panels), and the peak velocity, $V_{\rm Peak}$ (right panels), for all Sgr fields. The statistics plotted for the Hectospec fields are derived from the unsmoothed distributions.

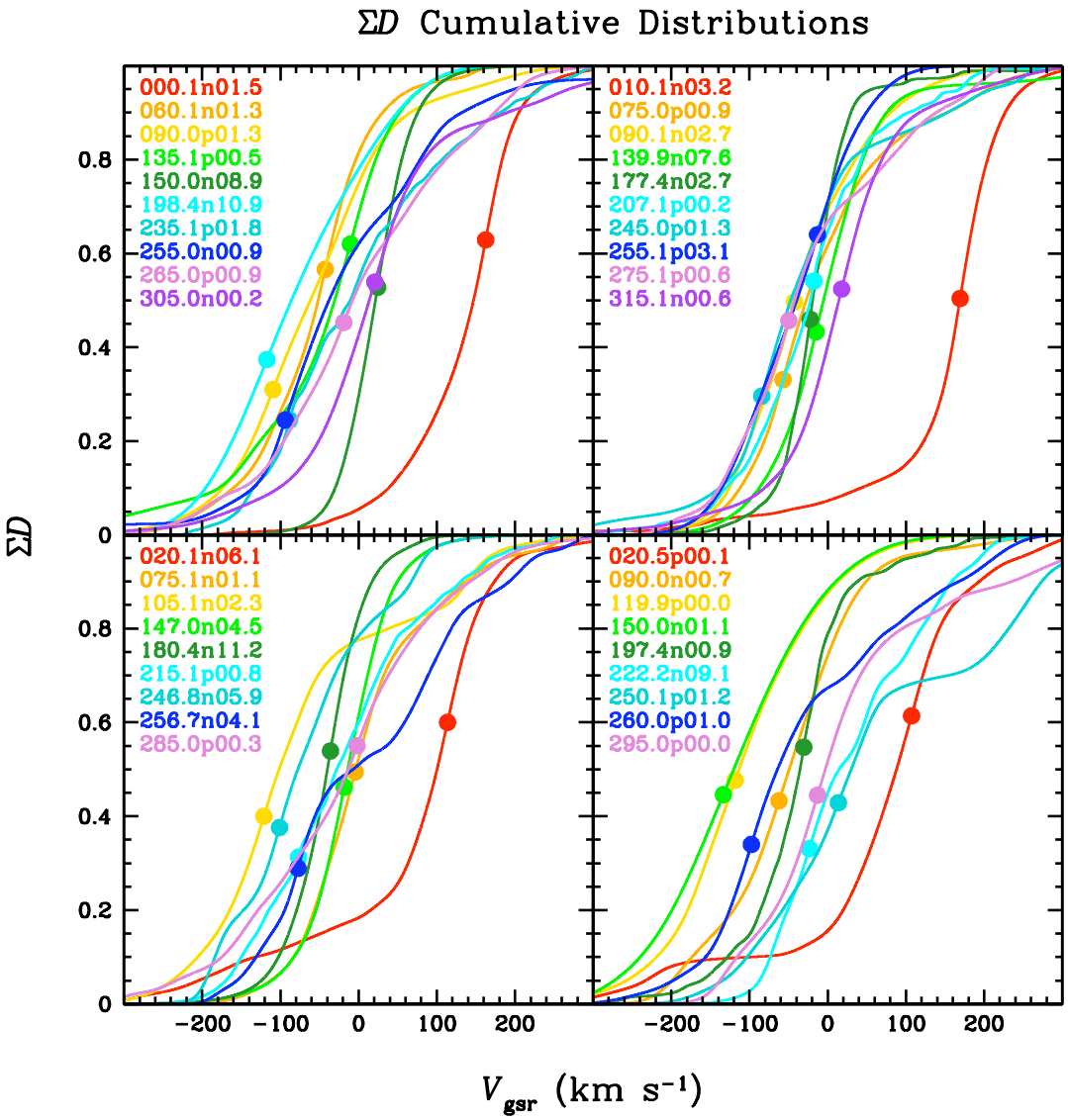

Figure 5.14: [ΣD] cumulative distribution functions. The cumulative distribution functions of the [ΣD] statistics are plotted for all Sgr fields. The location of the peak velocity in each field is marked on its *cdf* with a solid point. For clarity, they are split between four panels, with each field's *cdf* plotted in the same panel (e.g. top-left, bottom-right, etc.) as its velocity distribution profile in Figures 5.3 to 5.12. Additionally, the (typically four) *cdf s* plotted in the same color (of which there are at most one per panel) can be found in the same velocity distribution figure. For example, the four red *cdf s* represent the four velocity distributions presented in Figure 5.3. A color-coded list of the fields plotted in each panel is provided in the upper left hand corner of the corresponding panel. The *cdf s* plotted for the Hectospec fields are derived from the unsmoothed distributions.

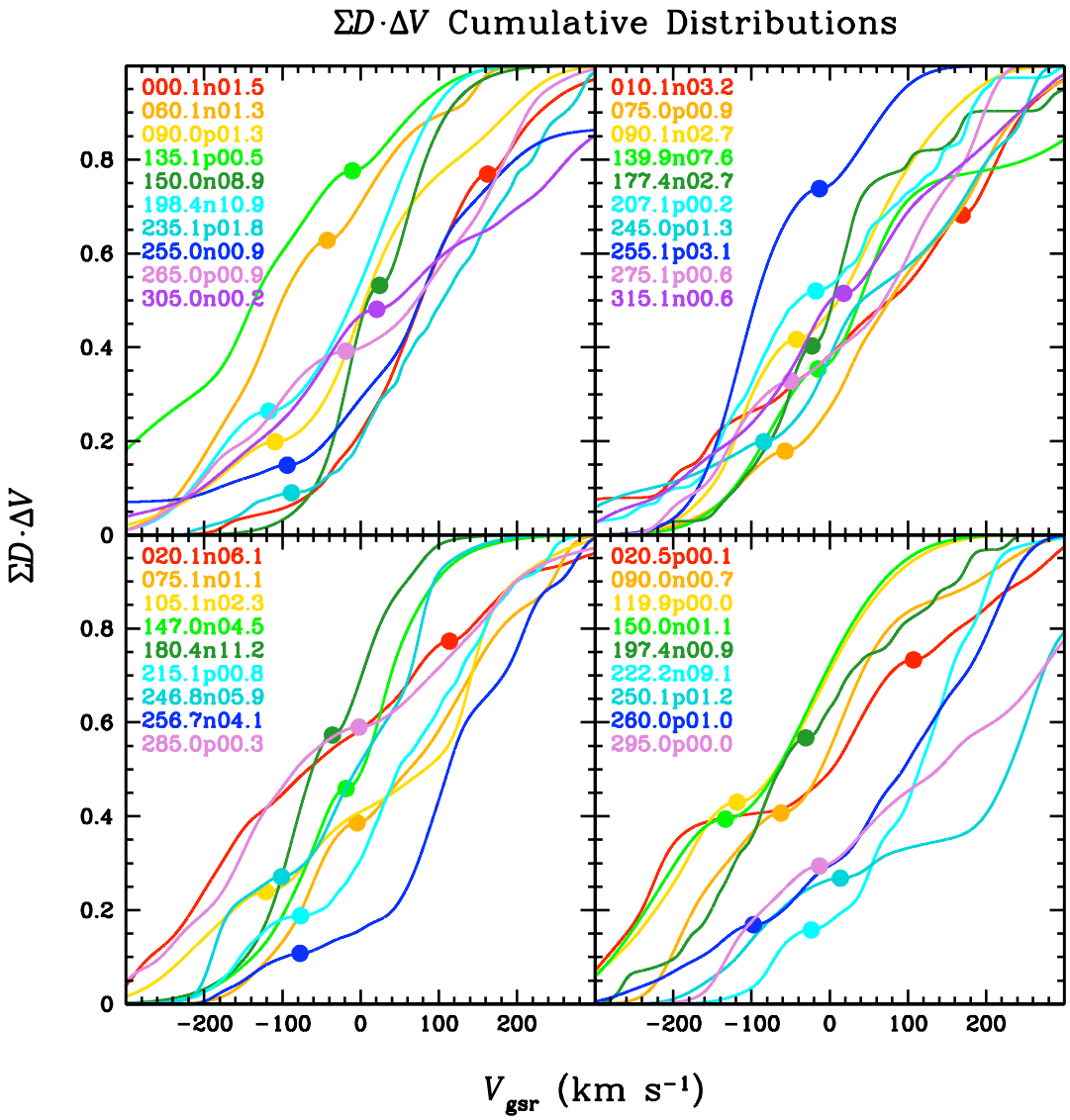

Figure 5.15: $[\Sigma(D \cdot \Delta V)]$ cumulative distribution functions. The cumulative distribution functions of the $[\Sigma(D \cdot \Delta V)]$ statistic are plotted for all Sgr fields. The location of the peak velocity in each field is marked on its *cdf* with a solid point. For clarity, they are split between four panels, with each field's *cdf* plotted in the same panel (e.g. top-left, bottom-right, etc.) as its velocity distribution profile in Figures 5.3 to 5.12. Additionally, the (typically four) *cdf s* plotted in the same color (of which there are at most one per panel) can be found in the same velocity distribution figure. For example, the four red *cdf s* represent the four velocity distributions presented in Figure 5.3. A color-coded list of the fields plotted in each panel is provided in the upper left hand corner of the corresponding panel. The *cdf s* plotted for the Hectospec fields are derived from the unsmoothed distributions.

5.2 Comparisons to Models

As discussed in Chapter 1, many attempts have been made to model the destruction of Sgr, leading to dramatically contradictory results. Most glaring, Sgr data has been interpreted to favor all possible shapes for the Milky Way's dark matter halo: oblate, spherical, prolate, and triaxial. In this section we compare the results of our comprehensive kinematic survey of the Sgr streams with the predictions of models featuring halo potentials of various shapes.

5.2.1 Descriptions of the Available Models

While many models of the destruction of Sgr have been published (see 1.2 for a summary), disappointingly few authors have made available the full results for all model particles from their N-body simulations. To date, only the oblate, spherical, and prolate halo models from Law et al. (2005, hereafter LJM05) and the triaxial halo model from Law & Majewski (2010, hereafter LM10) are available[1] for comparisons with observational studies.

The authors of these models have provided full three-dimensional spatial and kinematic information for all of the 10^5 particles in each model. Each particle is also tagged with a "color" that indicates on which orbit it became unbound from the core of Sgr. For this purpose each orbit is defined to begin at one apogalacticon and end at the following apogalacticon. This definition conveniently places the time when the mass loss rate it greatest, during each orbit's perigalactic passage, in the middle of each orbital period. The core of Sgr is currently located near perigalacticon, and is

[1]Results from all four models have been posted at http://www.astro.virginia.edu/∼srm4n/Sgr/

therefore only halfway through its current orbital period. All four models estimate the orbital period of Sgr to be ∼0.9 Gyr. However, a notable difference between the models is the time period over which they were integrated: only ∼4 Gyr for the earlier oblate, prolate, and spherical models of LJM05, and ∼7.8 Gyr for the triaxial model of LM10.

In their most recent model LM10 have provided additional information for each particle that can be valuable when making comparisons with our kinematic survey. To help discriminate between leading ("L") and trailing ("T") stream debris, and their multiple wraps (1,2, or 3) each particle is tagged as belonging to the $L1$ (young leading), $T1$ (young trailing), $L2$ (old leading), $T2$ (old trailing), or $L3$ (very old leading) streams. By definition the primary $L1$ and $T1$ streams range from $0° - 360°$ in angular separation from the core, the secondary $L2$ and $T2$ wraps range from $360° - 720°$, and the $L3$ wrap ranges from $720° - 1080°$ in angular separation from the core. In addition to classifying all of the particles based on which stream and wrap they belong to, as well as on which orbit they became unbound, the precise time (measured backwards from the present) at which they became unbound is also provided. Finally, the authors also provide the full orbital history of the core of Sgr over the last ∼7.8 Gyr. None of this additional information was provided with the earlier set of axisymmetric models released by LJM05.

It is instructive to see how the models compare to each other before further complicating the picture by including the results of our kinematic survey. In Figure 5.16 the velocities of all 10^5 particles are plotted as a function of their Sgr longitude ($\Lambda_\odot$)

for all four models. Color coding is used to classify the debris based on which orbit it became unbound from the core of Sgr. In all four panels the red debris represents particles lost from Sgr since its last apogalactic passage about one-half of a period (0.5 Gyr) ago. For the older oblate, spherical, and prolate models the orange (0.5–1.4 Gyr), yellow (1.4–2.2 Gyr), green (2.2–3.1 Gyr), and blue (3.1–4.0 Gyr) debris represent particles lost over the four most recent complete orbits of Sgr around the Milky Way. The color coding for the triaxial model is slightly different. Particles lost over the course of the eight most recent complete orbits of Sgr are designated as orange (0.5–1.3 Gyr), yellow (1.4–2.3 Gyr), green (2.4–3.2 Gyr), dark green (3.2–4.2 Gyr), cyan (4.2–5.0 Gyr), blue (5.1–6.0 Gyr), navy blue (6.0–6.9 Gyr), and purple (6.9–7.8 Gyr) points in the triaxial model panel. Particles still bound to the core of Sgr at the present time are represented as grey points in the triaxial model. However, in the oblate, spherical, and prolate models LJM05 use the same designation for the presently bound particles as for the recently lost red colored debris. The color coding system described above is adopted without variation throughout this chapter.

To help disentangle the contributions to Figure 5.16 from debris lost over the multiple orbital periods depicted, Figures 5.17 and 5.18 are provided. Figure 5.17 shows, for each of the three axisymmetric halo models, the particle velocities as a function of their Sgr longitude for the debris lost during the current and four previous orbits or Sgr split in to five separate panels. The same information is shown in Figure 5.18 for the triaxial halo mode. In Figure 5.18 the currently bound particles

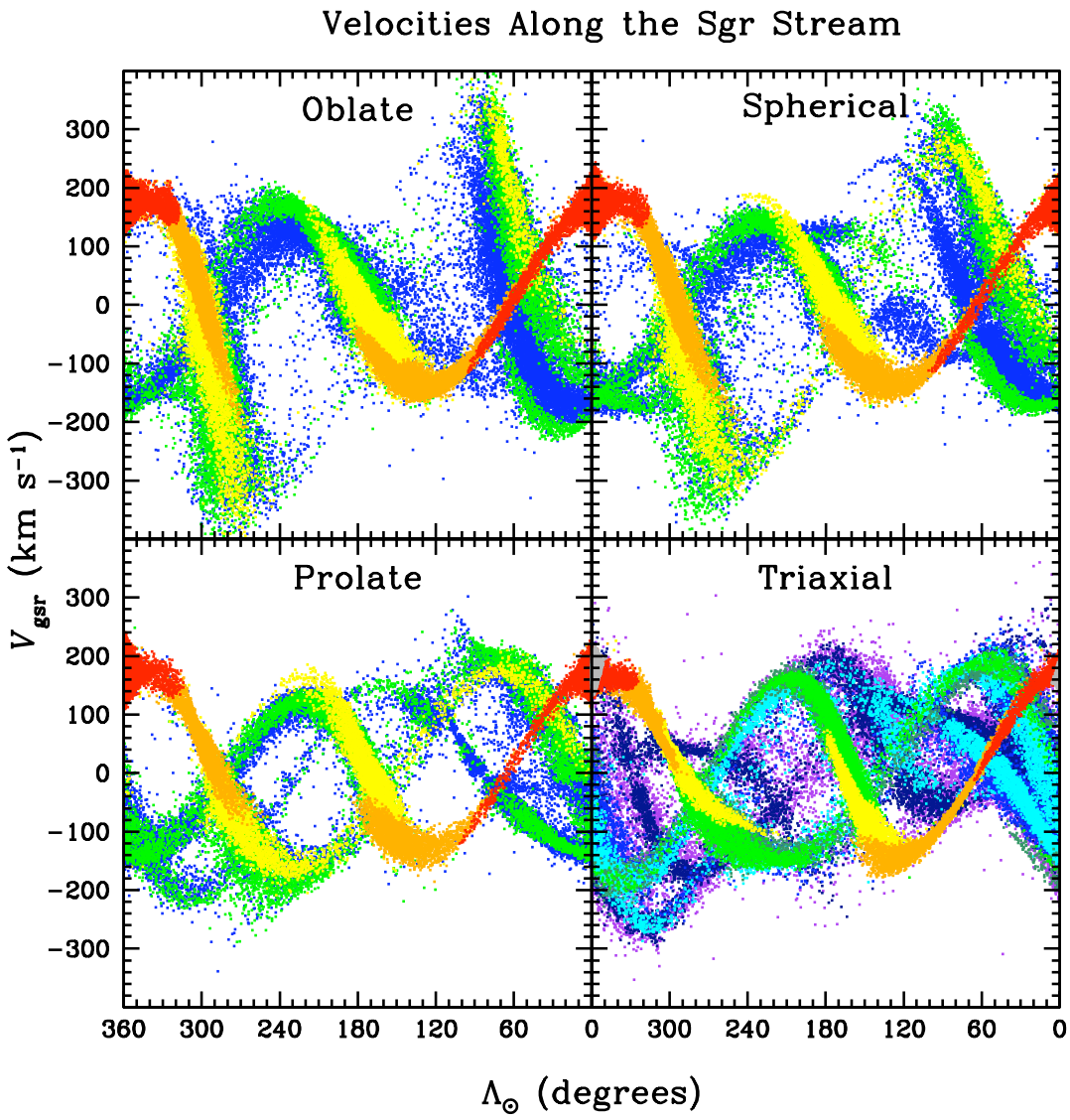

Figure 5.16: Velocities of Sgr debris in all four halo models. The Galactic standard of rest radial velocities for the 10^5 particles in the oblate, spherical, and prolate halo models of LJM05 and triaxial halo model of LM10 are shown as a function of their Sgr longitude. Color coding of the particles is used to designate the orbit on which they became unbound from the core of Sgr. For the axisymmetric models red is used to designate debris that is still bound or was lost on the current orbital period (0–0.5 Gyr ago). Orange (0.5–1.4 Gyr), yellow (1.4–2.2 Gyr), green (2.2–3.1 Gyr), and blue (3.1–4.0 Gyr) debris represent particles lost over the four most recent complete orbits of Sgr around the Milky Way. For the triaxial model (lower left) grey is used to represent particles still bound to the core of Sgr and red represents debris lost on the current orbital period (0–0.5 Gyr ago). Orange (0.5–1.3 Gyr), yellow (1.4–2.3 Gyr), green (2.4–3.2 Gyr), dark green (3.2–4.2 Gyr), cyan (4.2–5.0 Gyr), blue (5.1–6.0 Gyr), navy blue (6.0–6.9 Gyr), and purple (6.9–7.8 Gyr) debris represent particles lost over the eight most recent complete orbits of Sgr.

as well as the debris lost during the current and eight previous orbits or Sgr are split in to ten separate panels.

Several important conclusions can be drawn from the differing radial velocity trends predicted by these models. First, the radial velocities of debris lost within the last ∼1.4 Gyr (red and orange particles) are nearly identical between the four models, and thus can not provide a useful constraint on the shape of the Milky Way's halo. Noticeable differences between the models start to emerge with the debris that has been unbound for > 1.4 Gyr (yellow and later particles). Specifically, the oblate model predicts highly positive and highly negative velocities near $\Lambda_{\odot} = 90^{\circ}$ and 270° respectively. The radial velocities of the debris in these areas are predicted to be less extreme in the spherical halo model, and lesser still in the prolate and triaxial models. This underscores the importance of using long-lived, dynamically old stellar tracers of the Sgr stream, as the youngest debris has not been unbound from the Sgr core long enough to have noticeably experienced the effects of precession induced by the Milky Way's gravitational potential.

The additional information provided with the triaxial halo model allows for a closer examination of the mass loss history of Sgr. The histograms of Figure 5.19 were constructed using the recorded time that each particle has been unbound from the core. The three histograms show the total number of particles lost from Sgr during each time step of the model (∼0.05 Gyr, top panel), the fractional loss over each time step (bottom panel, shorter histogram), and the fractional loss over each orbit (bottom panel, taller histogram), using the same color coding as previously

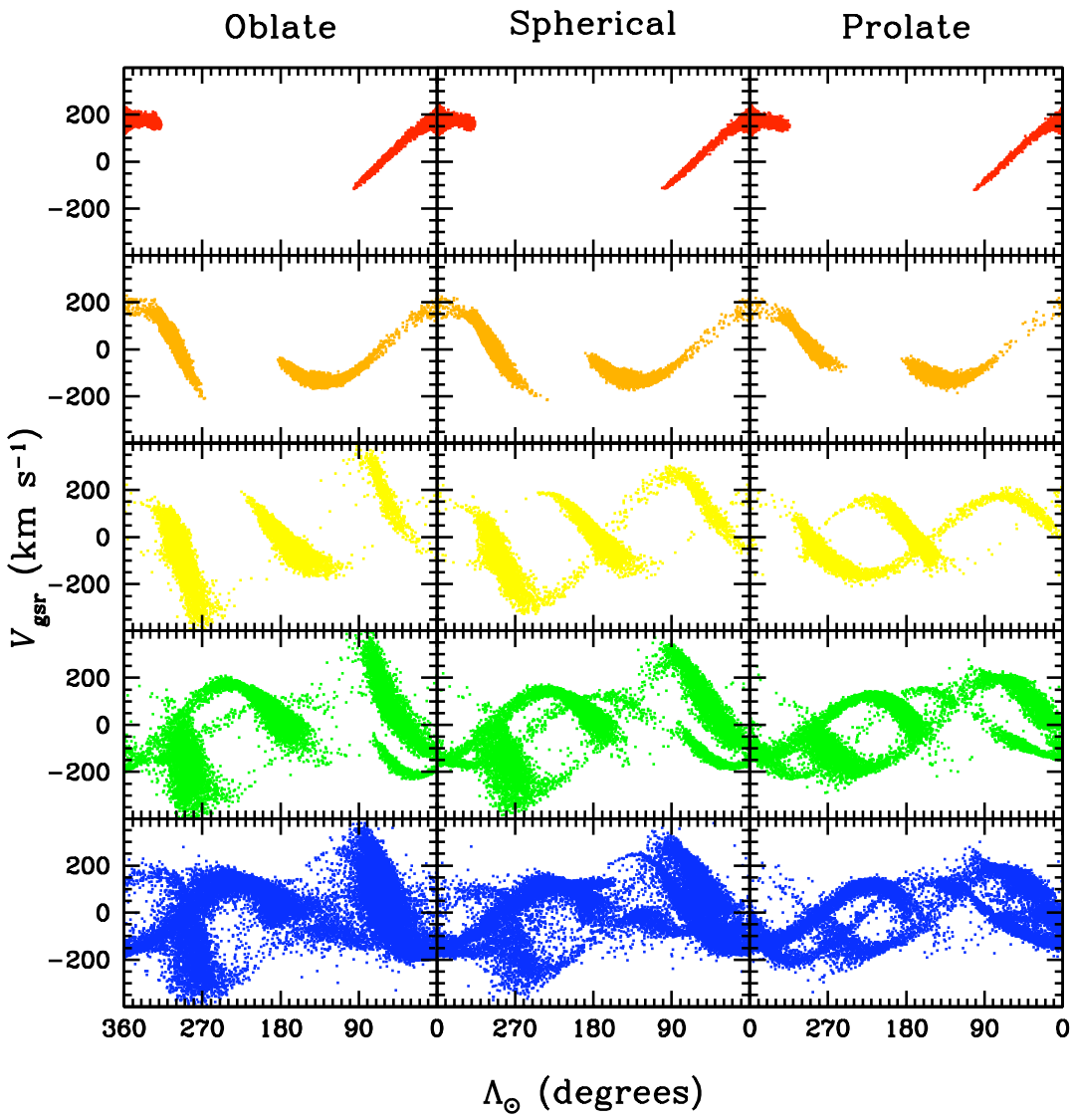

Figure 5.17: Velocities of debris from each orbit in the axisymmetric halo models. The radial velocities of Sgr debris lost during the current (top panels, red particles) and four previous orbits (orange, yellow, green, and blue particles) are shown as a function of their longitudinal coordinate for the three axisymmetric halo models of LJM05 (left: oblate, center: spherical, right: prolate). The dynamical ages of the debris are red (0–0.5 Gyr), orange (0.5–1.4 Gyr), yellow (1.4–2.2 Gyr), green (2.2–3.1 Gyr), and blue (3.1–4.0 Gyr).

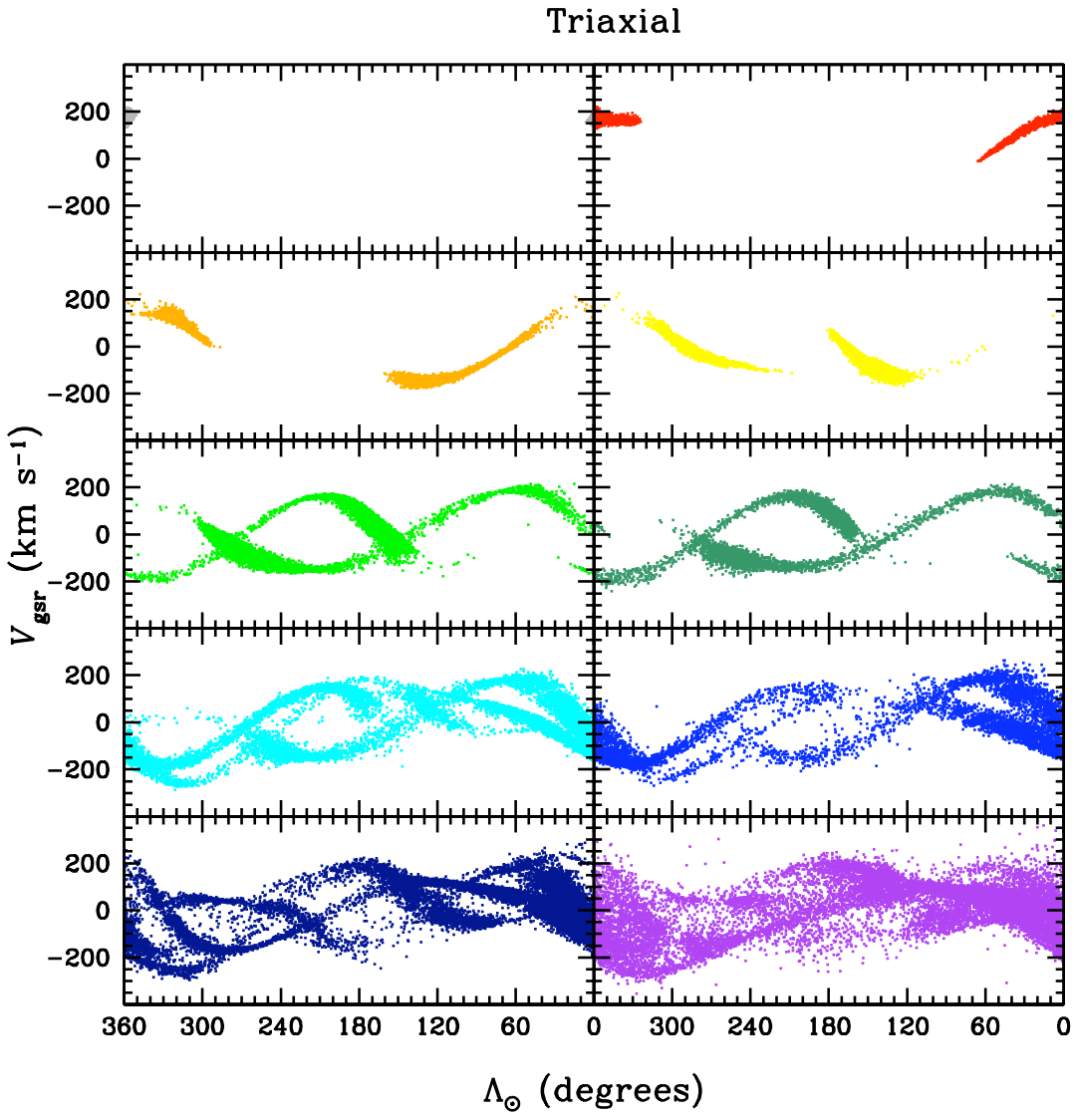

Figure 5.18: Velocities of debris from each orbit in the triaxial halo model. The radial velocities of currently bound Sgr stars (upper left panel, grey particles), and debris lost during the current (upper right panel, red particles) and eight previous orbits (orange, yellow, green, dark green, cyan, blue, navy blue, and purple particles) are shown as a function of their longitudinal coordinate for the triaxial halo model of LM10. The dynamical ages of the debris are red (0–0.5 Gyr), orange (0.5–1.3 Gyr), yellow (1.4–2.3 Gyr), green (2.4–3.2 Gyr), dark green (3.2–4.2 Gyr), cyan (4.2–5.0 Gyr), blue (5.1–6.0 Gyr), navy blue (6.0–6.9 Gyr), and purple (6.9–7.8 Gyr).

adopted for the triaxial model results. The radial distance of Sgr from the Galactic center over the course of the ∼8.5 orbits considered by the model is overplotted for reference.

As expected, the loss of Sgr debris from the Sgr core is greatest during the perigalactic passage of each orbit. While the apogalactic distance of the core is consistently near 60 kpc, the perigalactic distance in seen to alternate between ∼12 and ∼28 kpc. Typically, the orbits over which the greatest debris is lost occur subsequent to (not during) a close perigalactic passage. The bottom panel of Figure 5.19 shows that on average ∼14% of the bound particles are lost over the course of each orbital period – a rate which has fluctuated, but does not appear to be appreciably increasing or decreasing with time.

A final feature of the Sgr streams to consider is the number density of particles along the stream as predicted by the models. The histograms in Figure 5.20 show the total number of debris particles as a function of their Sgr longitude for each of the four models. The particles have been divided in to 4° wide bins and color-coded as before. The bins that contain fields observed in this survey are indicated with vertical grey bands of varying weight, as described in the caption.

It is notable that all four models predict the existence of exactly three peaks in the number density, and the models predict them to occur at similar locations along the stream: $\Lambda_\odot \sim 20°$–$70°$, $160°$–$180°$, and $290°$–$300°$. These regions of high density correspond to the locations along the stream where the debris is near apogalacticon (see Section 5.2.2). As the stars approach and pass through apogalacticon on their

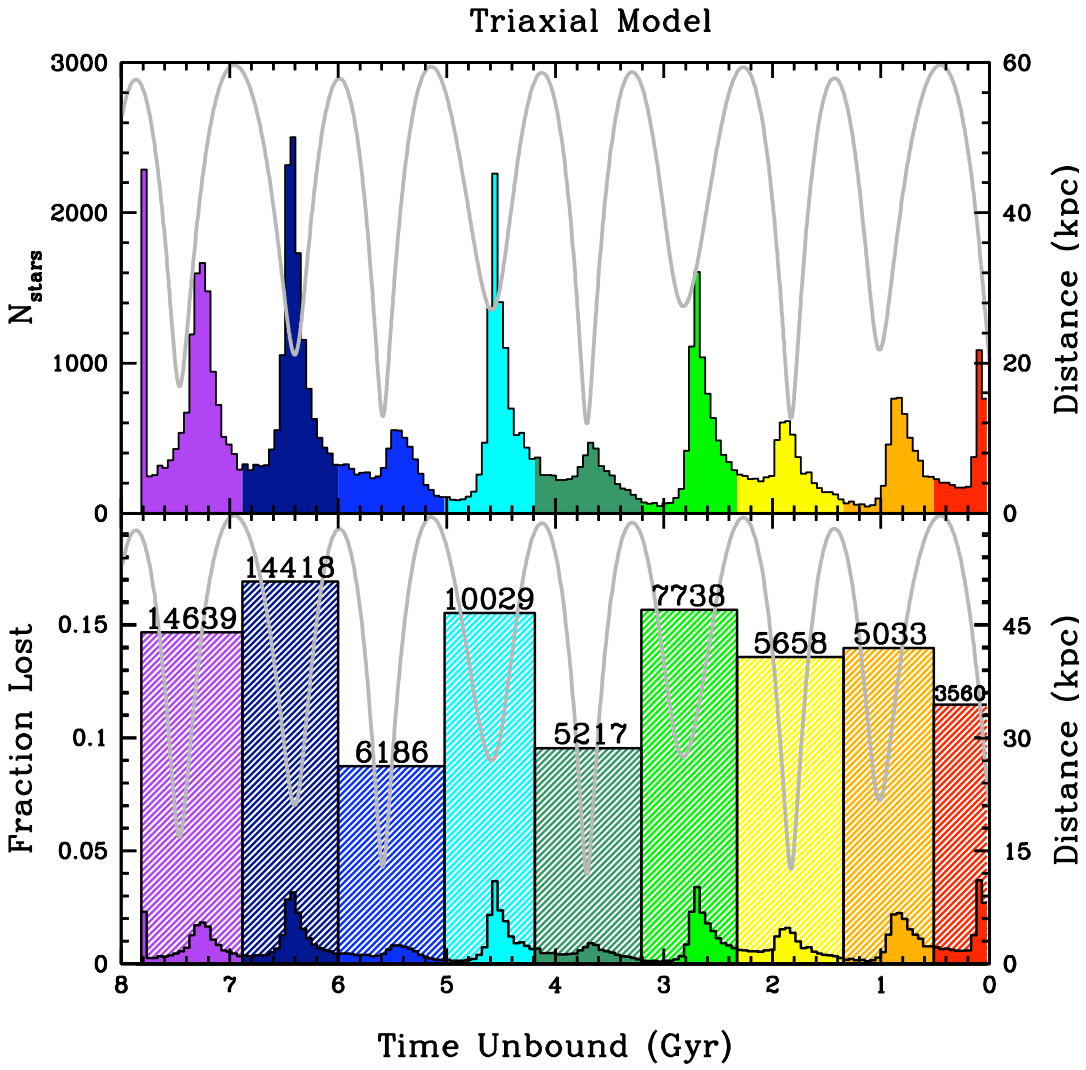

Figure 5.19: Mass loss history of Sgr in the triaxial halo model. The upper panel shows the number of particles lost from Sgr during each time step of the model (∼0.05 Gyr), using the same color coding as previously adopted for the triaxial model results. The tall histogram in the lower panel (with individual bins corresponding to full orbital periods) shows the fraction of bound stars at the beginning of each orbital period that were eventually lost over the course of the subsequent orbital period. The number of stars lost on each orbit is shown at the top of each orbital bin. The shorter histogram in the lower panel (with bin sizes of ∼0.05 Gyr) shows the fraction of bound stars at the beginning of each time step that were eventually lost over the course of the subsequent time step. The radial distance of Sgr from the Galactic center over the course of the ∼8.5 orbits considered by the model is overplotted in both panels for reference.

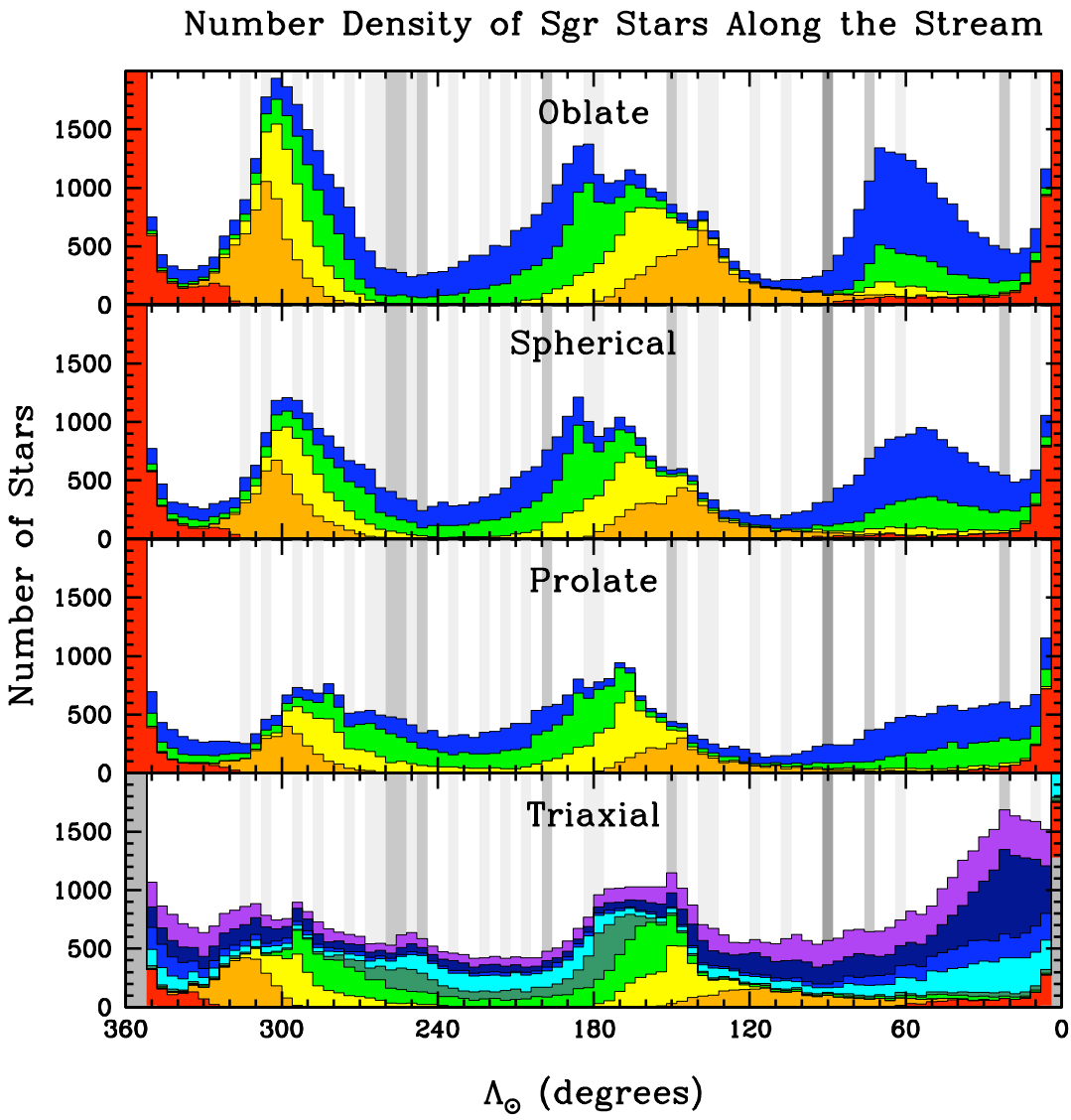

Figure 5.20: Number density along the Sgr stream in all four models. Each panel shows multiple histograms of the Sgr particles as a function of their Sgr longitude. The individual histograms are color-coded (as before) to indicate on which orbit the particles became unbound from the core. The particles have been divided in to 4° wide bins. The contribution in each bin from stars lost during any individual orbit are displayed as an incremental addition above that of the previous orbit. The bins that contain fields observed in this survey are indicated with vertical grey bands of varying weight. Light grey is used for the majority (21) of the $\Lambda_\odot$ bins which contain just one of our observed fields, medium grey is used for the seven bins that contain two of our fields, and dark grey is used for the one bin with three fields. The name of each model is centered near the top of its panel.

Keplerian orbits around the Milky Way, they slow down, and their space velocities reach a minimum, before accelerating back down towards the Galaxy. This slow down results in a buildup of Sgr debris near apogalacticon. From the solar vantage point this coincides with the time when their observed radial velocities will be near zero (at $\gtrsim$50 kpc the effect of galactocentric parallax is small) as can be seen in Figure 5.16. As expected, within any of the number density peaks the younger debris is offset closer to the core, while older debris is offset further from the core. This effect is most pronounced within the central peak near $\Lambda_\odot \sim 170°$, which is created by debris from the trailing stream. A clear distinction between the models is the relative heights of the number density peaks, which tend to decrease as the halo flattening parameter q increases (from oblate to spherical to prolate/triaxial).

Note that in each model there are many stars still bound to the core. The bound stars are located in the bins with $\Lambda_\odot < 8°$ and $\Lambda_\odot > 352°$ whose heights exceed the limits of the plot. The number of bound stars increases as the halo flattening parameter q increases (from oblate to spherical to prolate), thus there are more unbound stars in the models with lower flattening values (see Table 5.5 in the following section). This explains why there appear to be different numbers of stars in each panel – the flatter models (upper panels) are "hiding" fewer of their stars in the core.

5.2.2 Spatial Coincidence of Model Debris and Survey Stars

5.2.2.1 Coincidence in Celestial Coordinates

The specific locations of the fields observed in this survey were chosen based on a slightly modified version of the the best-fit Sgr debris plane from the 2MASS M-giant

study of Majewski et al. (2003) (see Section 2.1). The three-dimensional positions of those stars were also used as a constraint in the development of the models of LJM05 and LM10. Since their positions were derived from the same source, it is expected that our observed fields should closely follow the path of Sgr debris across the sky as predicted by the models.

In Figure 5.21 the Sgr-based celestial coordinates $(\Lambda_\odot, B_\odot)$ are plotted for all of the 10^5 particles in each of the four models. The model particles are color-coded in accordance with the system adopted in Section 5.2.1, which uses the orbit on which the particles became unbound from the core as an indicator of their dynamical age. The coordinates of each of our fields (see Table 2.1) are overplotted in each panel for comparison. As expected, our fields closely trace the equator of the model debris in each panel. The seven fields offset to lower latitudes (denoted by solid squares) trace the northern hemisphere bifurcation in the stream (Belokurov et al., 2006). The single field in Virgo (denoted by an asterisk at $\Lambda_\odot = 263°$), which is discussed in Chapter 4, is near the edge of the debris plane in most of the models.

The positions of the young (red/orange/yellow) debris differ very little between the four models. However significant differences between the models can be seen with the older (green, and especially blue) debris. Most noticeably, the oldest (blue) debris covers a large swath of the sky in the oblate halo model. In this model the leading stream of Sgr is predicted to pierce the Galactic plane very near the solar neighborhood. This descending column of stars would effectively fill most of the celestial sphere with Sgr debris as it passes through the solar position. This prediction

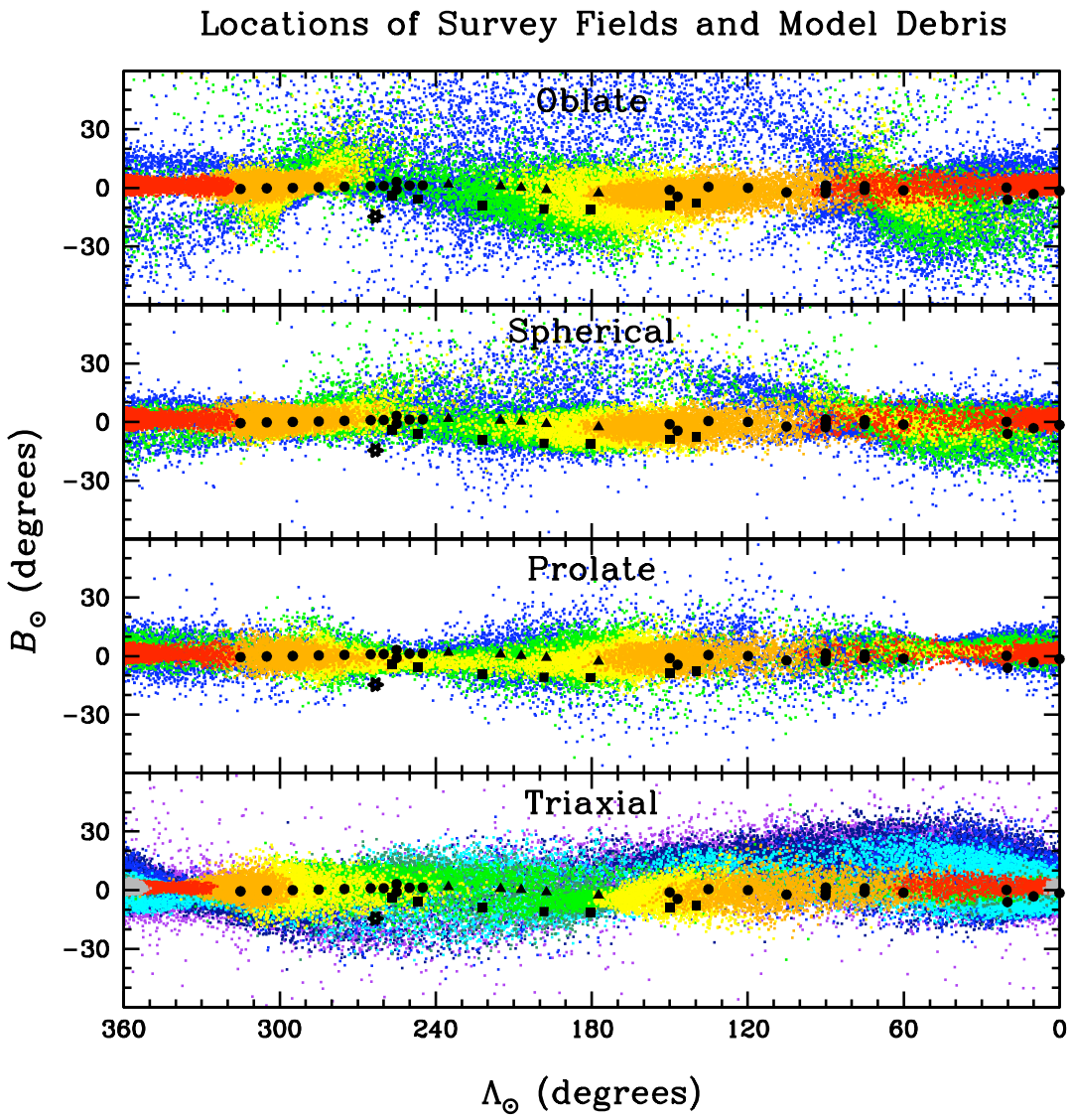

Figure 5.21: Sgr coordinates of model particles and survey fields. The Sgr-based celestial coordinates are plotted for all of the 10^5 particles in each of the four models. The name of each model is centered near the top of its panel. The model particles are color-coded as before to indicate on which orbit they became unbound. The coordinates of each of our fields are overplotted in each panel for comparison. The five solid black triangles with $177^\circ < \Lambda_\odot < 235^\circ$ represent the Hectospec fields. The seven solid black squares with $140^\circ < \Lambda_\odot < 257^\circ$ which are offset to lower latitudes represent the fields along the northern hemisphere bifurcation in the stream (Belokurov et al., 2006). The black star at $\Lambda_\odot = 263^\circ$ denotes the Virgo field discussed in Chapter 4. The 26 solid black circles represent the remaining field locations.

was tested, and rejected, by the observations in Virgo (Chapter 4). Another noticeable difference between the models is the increased breadth of the streams in the triaxial halo model. Much of the old (cyan/blue/navy blue/purple) debris can be found in high concentrations $20° - 30°$ from the stream equator. This is likely a result of the longer ($\sim$ 7.8 Gyr) integration time used for the triaxial model, which allowed the oldest debris to traverse the Galactic halo under the influence of its gravitational potential for nearly twice as long as the axisymmetric models ($\sim$ 4 Gyr). Over time the precession induced by the asymmetric potential resulted in a significant broadening of the streams.

5.2.2.2 Estimating Distances of Survey Stars

In the previous section we confirmed the general agreement between the models' predictions for the coordinates of Sgr debris and the locations of our targeted fields. It is also necessary to examine their correspondence along the additional dimension of their heliocentric distances. To accomplish this it was first necessary to estimate the heliocentric distances of the stars in the final kinematic data set using the technique of photometric parallax.

Assuming that our observed stars are in the main-sequence phase of their stellar evolutions, as they were initially selected to be (see Section 2.2), their observed, calibrated $(V - I)$ colors can be used to classify them as a particular main-sequence spectral type[2] (Ducati et al., 2001; Bessell, 1979). Their main-sequence spectral types can in turn be used to estimate their V-band absolute magnitudes, M_V (Carroll &

[2]The transformation equations published by Bessell (1979) were used to convert from the Johnson magnitude system used by Ducati et al. (2001) to the Cousins magnitude system used in this study.

Ostlie, 1996). The absolute magnitude of each star can then be used along with its observed, calibrated apparent V-band magnitude, V, to estimate its distance using the distance modulus equation:

$$d = 10^{(V-M_V+5)/5} \text{ pc} \tag{5.5a}$$

$$= 10^{(V-M_V-10)/5} \text{ kpc.} \tag{5.5b}$$

A table was constructed (using the aforementioned references) to facilitate the conversions from $(V-I)$ color to V-band absolute magnitude for all of the stars in the kinematic sample. Table 5.4 lists the corresponding V-band absolute magnitude for all $(V-I)$ colors ranging from –0.31 to 2.23 in steps of 0.01 magnitudes. Specific spectral types are noted in the table next to their corresponding $(V-I)$ color. Linear interpolation was used to estimate the absolute magnitudes for the intermediary colors that fell between the published values for the listed spectral types.

The empirically derived relationship between the $(V-I)$ color and the absolute V-band magnitude for main-sequence stars is depicted graphically in Figure 5.22. The solid black circles are plotted at the $(V-I, M_V)$ values published in the referenced literature, and they are labeled with their corresponding spectral type. The points whose absolute magnitudes were estimated via linear interpolation are denoted by the small dots that lie between the labeled circles. These points are placed at intervals of 0.01 magnitudes. Also shown in Figure 5.22 is a histogram of the $(V-I)$ colors for all 2008 unique stars in the final kinematic data set, excluding stars from the three fields that proved too difficult to photometrically calibrate (010.1n03.2, 020.1n06.1, 020.5p00.1). The colors of the survey stars range from 0.03–1.32 magnitudes, which

Table 5.4: Color to Absolute Magnitude Conversion for Main-sequence Stars

$(V-I)$	M_V	$(V-I)$	M_V	$(V-I)$	M_V	$(V-I)$	M_V	$(V-I)$	M_V
B0 –0.31	–3.80	0.24	2.55	0.79	6.01	1.34	7.79	1.89	9.44
B1 –0.30	–3.20	0.25	2.59	0.80	6.04	1.35	7.82	1.90	9.46
B2 –0.29	–2.60	0.26	2.63	0.81	6.07	1.36	7.85	1.91	9.49
–0.28	–2.10	0.27	2.66	K1 0.82	6.10	1.37	7.88	1.92	9.52
B3 –0.27	–1.60	F0 0.28	2.70	0.83	6.14	1.38	7.90	1.93	9.55
–0.26	–1.51	0.29	2.83	0.84	6.19	1.39	7.93	1.94	9.57
–0.25	–1.43	0.30	2.97	0.85	6.23	1.40	7.96	1.95	9.60
B5 –0.24	–1.25	0.31	3.10	0.86	6.27	1.41	7.99	1.96	9.63
–0.23	–1.13	0.32	3.20	0.87	6.31	1.42	8.02	1.97	9.65
–0.22	–1.02	0.33	3.30	0.88	6.36	1.43	8.04	1.98	9.68
B6 –0.21	–0.90	0.34	3.40	K2 0.89	6.40	1.44	8.07	1.99	9.71
–0.20	–0.75	F2 0.35	3.50	0.90	6.43	K7 1.45	8.10	2.00	9.74
B7 –0.19	–0.60	0.36	3.51	0.91	6.45	1.46	8.13	2.01	9.76
–0.18	–0.50	0.37	3.52	0.92	6.48	1.47	8.16	2.02	9.79
–0.17	–0.40	0.38	3.53	0.93	6.50	1.48	8.20	2.03	9.82
B8 –0.16	–0.20	0.39	3.54	0.94	6.53	1.49	8.23	2.04	9.85
–0.15	–0.13	0.40	3.56	0.95	6.55	1.50	8.26	2.05	9.87
–0.14	–0.07	0.41	3.57	0.96	6.58	1.51	8.29	M2 2.06	9.90
–0.13	0.00	0.42	3.58	K3 0.97	6.60	1.52	8.32	2.07	9.93
–0.12	0.07	0.43	3.59	0.98	6.66	1.53	8.35	2.08	9.96
–0.11	0.13	F5 0.44	3.60	0.99	6.71	1.54	8.39	2.09	9.98
B9 –0.10	0.20	0.45	3.67	1.00	6.77	1.55	8.42	2.10	10.01
–0.09	0.30	0.46	3.73	1.01	6.83	1.56	8.45	2.11	10.04
–0.08	0.40	0.47	3.80	1.02	6.89	1.57	8.48	2.12	10.07
–0.07	0.45	0.48	3.87	1.03	6.94	1.58	8.51	2.13	10.09
–0.06	0.50	0.49	3.93	K4 1.04	7.00	1.59	8.55	2.14	10.12
–0.05	0.55	F8 0.50	4.00	1.05	7.03	1.60	8.58	2.15	10.15
A0 –0.04	0.60	0.51	4.10	1.06	7.05	1.61	8.61	2.16	10.18
–0.03	0.80	0.52	4.20	1.07	7.08	1.62	8.64	2.17	10.21
A1 –0.02	1.00	0.53	4.30	1.08	7.10	1.63	8.67	2.18	10.23
–0.01	1.15	G0 0.54	4.40	1.09	7.13	1.64	8.70	2.19	10.26
A2 0.00	1.30	0.55	4.48	1.10	7.15	1.65	8.74	2.20	10.29
0.01	1.40	0.56	4.55	1.11	7.18	1.66	8.77	2.21	10.32
A3 0.02	1.50	0.57	4.63	1.12	7.20	M0 1.67	8.80	2.22	10.34
0.03	1.57	G2 0.58	4.70	1.13	7.23	1.68	8.83	2.23	10.37
0.04	1.63	0.59	4.90	1.14	7.25	1.69	8.86	M3 2.24	10.40
0.05	1.70	0.60	5.00	1.15	7.28	1.70	8.89	2.25	10.45
0.06	1.75	G5 0.61	5.10	1.16	7.30	1.71	8.92	2.26	10.49
0.07	1.80	0.62	5.18	1.17	7.33	1.72	8.95	2.27	10.54
0.08	1.85	0.63	5.26	1.18	7.35	1.73	8.98	2.28	10.59
A5 0.09	1.90	0.64	5.34	1.19	7.38	1.74	9.01	2.29	10.64
0.10	1.95	0.65	5.42	K5 1.20	7.40	1.75	9.04	2.30	10.68
0.11	2.00	G8 0.66	5.50	1.21	7.43	1.76	9.06	2.31	10.73
0.12	2.05	0.67	5.54	1.22	7.46	1.77	9.09	2.32	10.78
0.13	2.10	0.68	5.59	1.23	7.48	1.78	9.12	2.33	10.83
0.14	2.15	0.69	5.63	1.24	7.51	1.79	9.15	2.34	10.87
A7 0.15	2.20	0.70	5.68	1.25	7.54	1.80	9.18	2.35	10.92
0.16	2.24	0.71	5.72	1.26	7.57	1.81	9.21	2.36	10.97
0.17	2.28	0.72	5.77	1.27	7.60	1.82	9.24	2.37	11.02
0.18	2.32	0.73	5.81	1.28	7.62	1.83	9.27	2.38	11.06
0.19	2.36	0.74	5.86	1.29	7.65	M1 1.84	9.30	2.39	11.11
A8 0.20	2.40	K0 0.75	5.90	1.30	7.68	1.85	9.33	2.40	11.16
0.21	2.44	0.76	5.93	1.31	7.71	1.86	9.35	2.41	11.21
0.22	2.48	0.77	5.96	1.32	7.74	1.87	9.38	2.42	11.25
0.23	2.51	0.78	5.99	1.33	7.76	1.88	9.41	M4 2.43	11.30

Note: The correspondence between $(V-I)$ color and spectral type was adopted from Ducati et al. (2001) using the transformation equations of Bessell (1979). The correspondence between absolute V-band magnitude (M_V) and spectral type was taken from Carroll & Ostlie (1996). Absolute V-band magnitudes were estimated at all other values of $(V-I)$ using linear interpolation.

corresponds to a range in spectral types from approximately A3 to K5, and a range in absolute magnitudes from 1.57 to 7.74, respectively. These limits are shaded in grey in Figure 5.22. The most commonly observed spectral type was G5, and ∼92% of the observed stars have spectral types in the range F5–K2.

The uncertainty in distances calculated using the distance modulus equation (Equation 5.5b) can be estimated using standard error analysis methods. Since the distance, d, is a function of V and M_V, its uncertainty, δd, can be estimated in terms of the uncertainties of its two independent variables, δV and δM_V:

$$\delta d = \sqrt{\left(\frac{\partial d}{\partial V}\right)^2 (\delta V)^2 + \left(\frac{\partial d}{\partial M_V}\right)^2 (\delta M_V)^2} \tag{5.6a}$$

$$= \sqrt{\left(d\,\frac{\ln 10}{5}\right)^2 (\delta V)^2 + \left(d\,\frac{\ln 10}{5}\right)^2 (\delta M_V)^2} \tag{5.6b}$$

$$= d\,\frac{\ln 10}{5}\sqrt{(\delta V)^2 + (\delta M_V)^2}. \tag{5.6c}$$

The relative uncertainties in the distance estimates are then given by:

$$\frac{\delta d}{d} = \frac{\ln 10}{5}\sqrt{(\delta V)^2 + (\delta M_V)^2} \tag{5.7a}$$

$$\simeq 0.46\sqrt{(\delta V)^2 + (\delta M_V)^2}. \tag{5.7b}$$

The uncertainty in V is fairly straightforward. In Section 2.3 the typical uncertainty

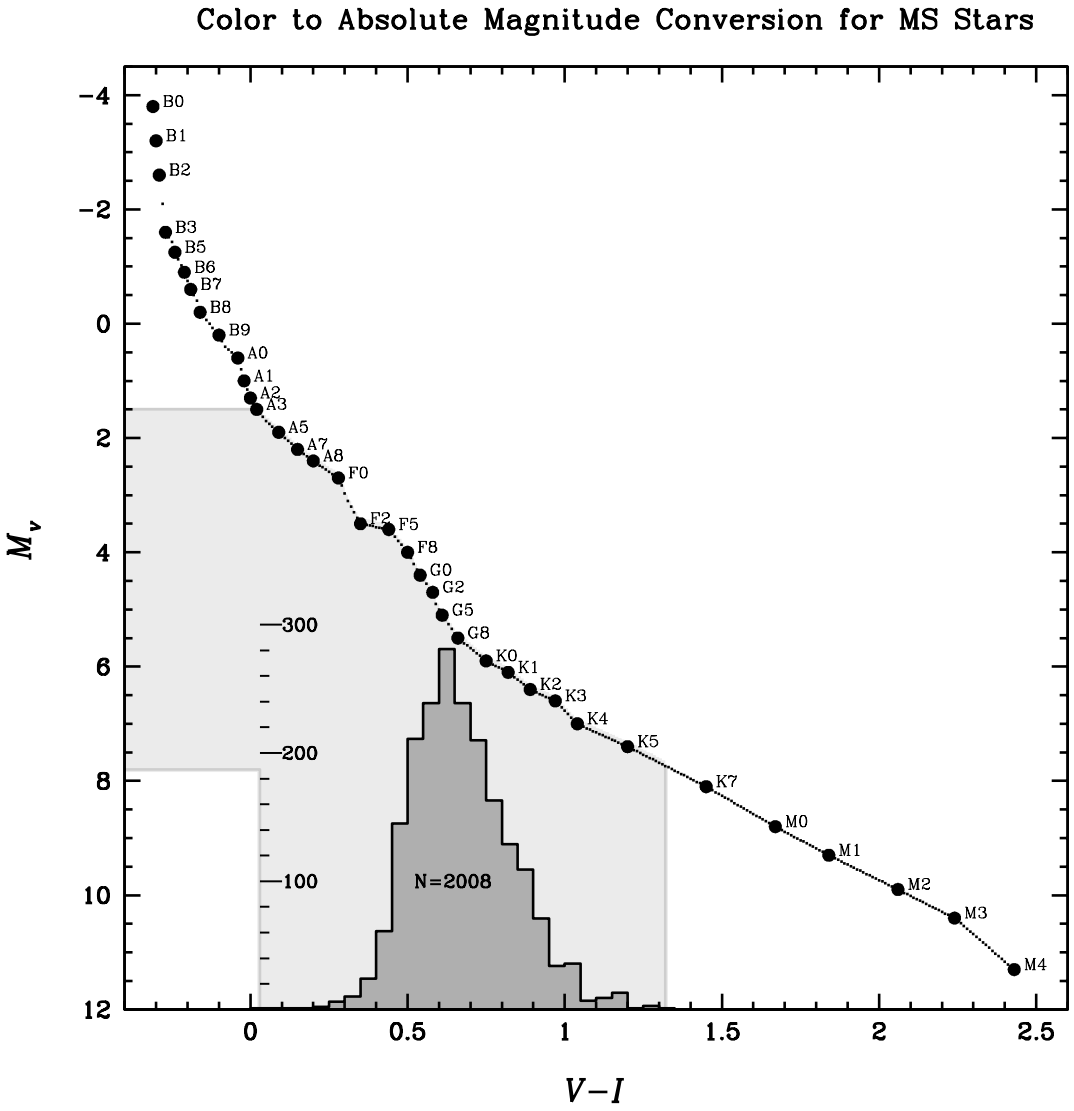

Figure 5.22: Color to Absolute Magnitude Conversion for MS stars. Solid black circles are plotted at the $(V-I, M_V)$ values published in the referenced literature, and are labeled with their corresponding spectral type. The small dots between the labeled circles at intervals of 0.01 magnitudes denote points whose absolute magnitudes were estimated via linear interpolation. Also shown is a histogram of the $(V-I)$ colors of all 2008 unique stars in the final kinematic data set, excluding stars from the three fields that proved too difficult to photometrically calibrate (010.1n03.2, 020.1n06.1, 020.5p00.1). A vertical scale for the histogram is offset to the left of it. The histogram's bin size is 0.05 magnitudes. The shaded grey regions indicate the maximum extent of the observed stars in both color (0.03–1.32 magnitudes, corresponding approximately to spectral types A3–K5) and absolute magnitude (1.57–7.74).

in V was estimated to be $\delta V \sim 0.07$ magnitudes (see Figure 2.7). This alone would be responsible for producing a 3% uncertainty in the distance estimates (using Equation 5.7b). However, the dominant source of uncertainty in the distance calculations is due to the absolute magnitude term, M_V. The uncertainty in M_V is derived from the uncertainty in the color. The typical uncertainty in $V - I$ can be estimated as:

$$\delta(V - I) = \sqrt{(\delta V)^2 + (\delta I)^2} \tag{5.8a}$$

$$\simeq \sqrt{(0.07)^2 + (0.09)^2} \tag{5.8b}$$

$$= 0.11 \text{ magnitudes.} \tag{5.8c}$$

But given the nonlinear way in which the color of a main-sequence star corresponds to its absolute magnitude (see Figure 5.22), an uncertainty of 0.11 magnitudes in $V - I$ can lead to an uncertainty in M_V that ranges from 0.23–1.10 magnitudes. This yields a combined relative uncertainty in the distance estimates (from Equation 5.7b) that can range from 11–51%.

5.2.2.3 Applying a Distance Cut to the Models

When making future comparisons between the kinematic results of this survey and the predictions of the models it is important to exclude the model stars with distances beyond the limits of the observations. The inclusion of these stars could lead to misidentifications of observed kinematic features. We therefore apply a $\Lambda_\odot$-dependent distance cut to the model stars as depicted in Figure 5.23.

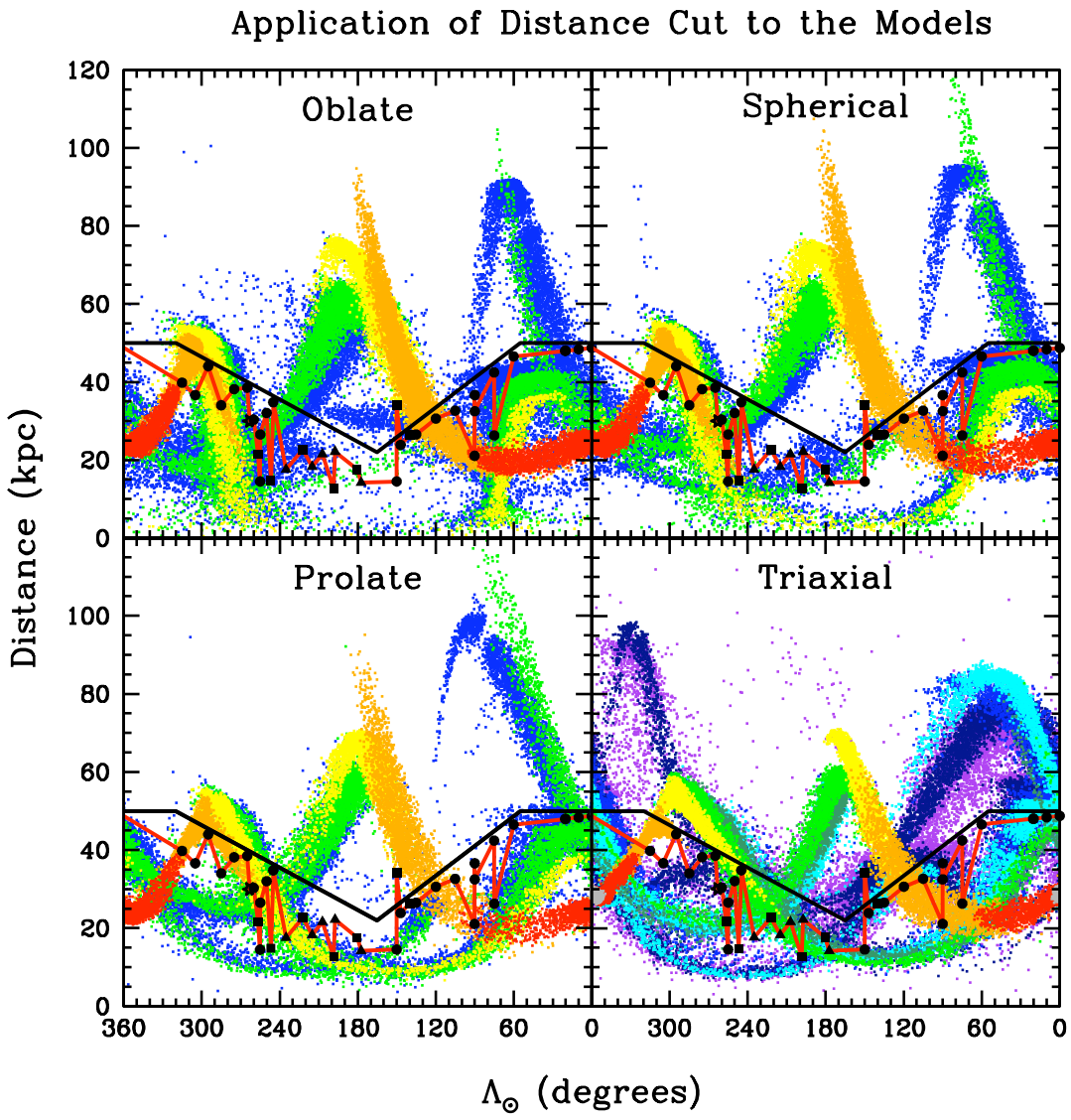

Figure 5.23: Application of distance cut to the models. The distances of all 10^5 stars are plotted as a function of their Sgr longitude for each of the four models. The name of each model is centered near the top of its panel. The model particles are color-coded as before to indicate on which orbit they became unbound. Black data points are placed at the distance of the second most distant star in each field, which is taken to be representative of the observational distance limit for each field. The five solid black triangles with $177^\circ < \Lambda_\odot < 235^\circ$ represent the Hectospec fields. The seven solid black squares with $140^\circ < \Lambda_\odot < 257^\circ$ represent the fields along the northern hemisphere bifurcation in the stream (Belokurov et al., 2006). The black star at $\Lambda_\odot = 263^\circ$ denotes the Virgo field discussed in Chapter 4. The 26 solid black circles represent the remaining fields. These data points are connected by a red line to help accentuate the overall trend as function of $\Lambda_\odot$. The solid black line in each panel represents the distance cut that will be applied to the model stars henceforth. It has vertices at ($\Lambda_\odot$,d) = (0,50) , (55,50) , (165,22) , (320,50) and (360,50).

In Figure 5.23 the distances of all 10^5 stars are plotted as a function of their Sgr longitude for each of the four models. The model stars are color-coded in accordance with the system adopted in Section 5.2.1, which uses the orbit on which the particles became unbound from the core as an indicator of their dynamical age. In each panel black data points are placed at the distance of the second most distant star in each field, which is taken to be representative of the observational distance limit for each field. This convention was adopted to exclude a very small number of stars (no more than one per field) with very blue colors, whose corresponding absolute magnitudes made them extreme distance outliers relative the other stars in their field. These data points are connected by a red line to help accentuate the overall trend as function of $\Lambda_\odot$.

The solid black line in each panel represents the distance cut that will henceforth be applied to the model stars. The model stars above this line exceed the distance limits of the observed fields, and will thus be discarded. The specific shape of the employed distance cut was designed to simultaneously cross just above the distance limit for as many fields as possible, undercut the limit in as few fields as possible, and maintain a simplistic, easy to implement form.

Table 5.5 summarizes the effects of applying this cut to the models. It lists, for all four models, the initial number of stars, N_i, before the cut is applied, the final number of stars, N_f, after the cut is applied, and their ratio %Kept $\equiv \frac{N_f}{N_i}$. These numbers are provided for the total number of stars in each model as well as for the number of stars unbound on each orbit (i.e. color).

Table 5.5: Effects of Applying the Distance Cut to the Models

Orbit	Age[a]	Oblate			Spherical			Prolate			Triaxial		
	(Gyr)	N_i	N_f	%Kept	N_i	N_f	%Kept	N_i	N_f	%Kept	N_i	N_f	%Kept
Bound[b]	0.0–0.0	···	···	···	···	···	···	···	···	···	27522	27522	100.0
0[b]	0.0–0.5	39168	39168	100.0	51172	51172	100.0	61593	61593	100.0	3560	3560	100.0
1	0.5–1.3	11997	6928	57.7	8576	3695	43.1	5160	2211	42.8	5033	4152	82.5
2	1.4–2.3	10467	2856	27.3	8484	2446	28.8	7367	1819	24.7	5658	294	5.2
3	2.4–3.2	13947	7011	50.3	12833	6804	53.0	11819	6284	53.2	7738	1971	25.5
4	3.2–4.2	24421	14290	58.5	18935	11545	61.0	14061	9185	65.3	5217	1917	36.7
5	4.2–5.0	···	···	···	···	···	···	···	···	···	10029	5445	54.3
6	5.1–6.0	···	···	···	···	···	···	···	···	···	6186	3421	55.3
7	6.0–6.9	···	···	···	···	···	···	···	···	···	14418	4895	34.0
8	6.9–7.8	···	···	···	···	···	···	···	···	···	14639	5389	36.8
Total		100000	70253	70.3	100000	75662	75.7	100000	81092	81.1	100000	58566	58.6

Note: N_i refers to the initial number of stars in the model. N_f refers to the final number of stars remaining after applying the described distance cut to the model stars. %Kept is the percentage of stars that remain after applying the distance cut and is defined as %Kept $\equiv \frac{N_f}{N_i}$.

[a] The ages listed are for the triaxial model. Ages for the three axisymmetric models are very similar, but differ by 0.1–0.2 Gyr for some of the orbit age boundaries.

[b] The triaxial model specifically lists the bound particles separate from the stripped debris. The axisymmetric models include the still bound particles with those lost on the current (zeroth) orbit.

5.2.3 Velocity Trends Along the Streams

The principal observational result of the spectroscopic survey described in this dissertation is the trend of characteristic velocities in the observed fields along the Sgr streams. These results were summarized in Table 5.2. In this section we compare the kinematic results of our survey with predictions from the models of LJM05 and LM10.

In Figures 5.24 to 5.27 the Galactic standard of rest radial velocities of the model stars are plotted as a function of their Sgr longitude, $\Lambda_\odot$, for the oblate, spherical, prolate, and triaxial models, respectively. Only model stars that satisfy the distance cut introduced in Section 5.2.2.3 are included[3]. The model stars are color-coded in accordance with the system adopted in Section 5.2.1, which uses the orbit on which

[3]Plots of $V_{\rm gsr}$ as a function of $\Lambda_\odot$ that include all 10^5 model stars were presented in Figure 5.16.

the particles became unbound from the core as an indicator of their dynamical age. Overplotted in each of these figures are the primary velocity peaks from all 39 of our observed fields. The peak velocities and the sizes of the asymmetric error bars are listed for every field in Table 5.2. To make visual comparisons between the different models easier, Figure 5.28 combines Figures 5.24 to 5.27 in to a single figure.

In the adopted Sgr coordinate system (Majewski et al., 2003) the leading stream of tidal debris originates at the core of Sgr (at $\Lambda_\odot = 360°$) and extends out in the direction of decreasing $\Lambda_\odot$. Similarly, the trailing stream of tidal debris originates at the core of Sgr (at $\Lambda_\odot = 0°$) and extends out in the direction of increasing $\Lambda_\odot$. It is therefore expected that the regions just in front of ($360° > \Lambda_\odot > 180°$) and just behind ($0° < \Lambda_\odot < 180°$) the core of Sgr will be dominated by the young (red/orange/yellow) leading and trailing debris streams, respectively. The models predict this, and our data confirm it.

5.2.3.1 Primary Velocity Peaks

Trailing Stream

First consider the young trailing stream. The models' predictions for the velocity trend along the first two-thirds of the trailing stream ($0° < \Lambda_\odot < 120°$) are all nearly identical. These model stars (shown in red and orange) have not been orbiting freely in the Milky Way's halo for a sufficiently long time to exhibit noticeable differences in their positions and motions due to the mass distribution in the halo.

The observed peak velocities in the twelve survey fields along this stretch are an excellent match to the model results. The observed velocity of the Sgr core (163 km s^{-1})